





## Contents

Foreword	2
CEO Welcome	5
Beamline Development and Technical Summary	6
Macromolecular Crystallography Group	8
Biological Cryo-Imaging Group	22
Structures and Surfaces Group	28
Magnetic Materials Group	36
Imaging and Microscopy Group	46
Crystallography Group	56
Spectroscopy Group	66
Soft Condensed Matter Group	74
Phase III Overview	84
Integrated Facilities and Collaborations	86
Machine Operation and Development	90
Optics and Metrology Group	92
Detector Group	94
Scientific Software, Controls and Computation	96
Key Facts and Figures	100
Industrial Liaison	102
Engaging with Diamond Light Source	104
Governance and Management	106
Staffing and Financial Information	107
Committee Membership	108

## Foreword

**T**he past 12 months have seen an increase in the complementary capabilities and facilities that Diamond is able to offer its over 10,000 users. With the operations of the electron Bio-Imaging Centre (eBIC) now fully integrated into the user programme, researchers can access a one-stop shop for structural biology right here at Diamond. The unique offer enabled by further integrated facilities such as the electron Physical Science Imaging Centre (ePSIC), the MPL (Membrane Protein Lab), the XChem Fragment Screening service and the XFEL Hub, put Diamond at the leading edge of transformative science on the world stage.



An increase in Diamond's scientific output naturally leads to a demand to further develop our data analysis capabilities. Progress in this area is extensive, with efficient data analysis pipelines delivering results in close-to-real time. One particular project is focusing on citizen science as a means to help train Artificial Intelligence systems, which is a key focus of the UK's industrial strategy.

Located on a world-leading site for scientific discovery, Diamond aims to be a cornerstone of the Harwell Campus. We are pleased to have seen key investments in our new neighbours, the Rosalind Franklin Institute (RFI) and Faraday Institution (FI), further increasing the impact of the Harwell Campus on UK science and innovation. We will continue to strengthen our relationships with these institutes and act as a catalyst for the activities they are undertaking.

**Professor Sir Adrian Smith**  
*Chairman of the Board of Directors*

“An increase in Diamond's scientific output naturally leads to a demand to further develop our data analysis capabilities. Progress in this area is extensive, with efficient data analysis pipelines delivering results in close-to-real time.”



“To remain at the cutting edge of science, we need to ensure we continue to attract people from all over the world because they bring their different perspectives and skills.”

## CEO Welcome

**A**s we close the financial year 2018-19, it is good to reflect upon the achievements of this period. 2018 was the Year of Engineering and this saw an increase in news and features from the engineering team resulting in some striking headlines. For example, the Daily Express showcased the work done with Martian Meridianites within the facility. These minerals were named after the place they were discovered on Mars and provide direct evidence that there used to be surface water on this planet. This wonderful and engaging science was made possible by the design of a special cold cell built by our talented engineers.

The Year of Engineering has left a legacy of enhanced engagement, which we can now build on ensuring that career opportunities are more widely promoted, and staff continue to be good role models helping to attract the best talents into our organisation.

With the investment made in Diamond over the past 18 years, funded by the taxpayers through the Science and Technology Facilities Council (STFC) - UK Research & Innovation (86%) and the Wellcome Trust (14%), our institute now offers access to 32 beamlines and five complementary facilities (eBIC, ePSC, MPL, XFEL Hub and XChem). The final beamline of the current phase of construction – DIAD – saw first light in the past year and will take first users in the next twelve months. All are pushing the boundaries of visualisation of molecules and materials at the atomic level, and enabling high quality science for both industry and academia. An indication of the role Diamond plays in establishing the UK at the forefront of science worldwide is the high impact of its work embodied in almost 8,000 peer review scientific articles published since the organisation was created, with citation rates significantly higher than the national average across the spectrum of science it serves.

A great illustration of the impact we are having is the work by an international team led by the University of Portsmouth and the US National Energy Research Laboratory that will enable a natural plastic digesting enzyme to be exploited more effectively in waste treatment. The unique visualisation tools used to elucidate the way the enzyme works were provided by several of our beamlines. The research made the headlines all over the world, generating the equivalent of over £23M of advertising spend in press and broadcast coverage.

This review contains many more examples of high impact science drawn from across the broad range of areas of fundamental science that Diamond serves, and the societal challenges it helps address. These include health and wellbeing, the environment, transport and energy challenges of the future, as well as new functional materials, including electronic devices and high-performance engineering alloys, and new processing technology for innovative manufacturing.

All of these achievements reflect the skills, hard work and commitment of the dedicated staff that we have within our walls. They also reflect the strong engagement of a vibrant and growing user community in academia and industry. In the last financial year, we received 1,788 proposals for experiments on our instruments via peer reviewed access routes, requesting a total of 22,117 shifts. After peer review, 1,191 proposals were awarded beamtime. This resulted in 12,497 experimental shifts being awarded across 30 beamlines and eight electron microscopes. We welcomed 6,332 onsite user visits from academia across all instruments, with an additional 4,459 remote user visits. The machine continues to perform to the highest standard with 98.4% uptime and 90.3 hours mean time between failures (MTBF).

However, we cannot afford to rest on our laurels. The pace of technical development is rapid and relentless so if we are to continue to offer the scientific community the best opportunities for world-leading research, we need to plan

to take advantage of such advances. We have already started a very substantial rolling programme of upgrades to beamlines supported by a considerable uplift in capital from our shareholders. We aim to complement this programme with the Diamond-II upgrade of the machine and instruments, which with a factor of 20 times reduction in emittance coupled with an increase in electron beam energy from 3.0 to 3.5 GeV will provide up to a factor of 70 increase in brightness



and coherence of Diamond's photon beams at the higher energies. A new lattice geometry will allow us to not only keep and enhance all current beamlines, but offers the opportunity for up to five new additional beamlines to be created. The science case has been well received and approved by our Science Advisory Committee (SAC) and Diamond Industrial Science Committee (DISCo). The

Conceptual Design Report (CDR) has also been approved by an international expert panel, clearing the way to work on the Technical Design Report (TDR) for which we will need an increase in staff and resources for much more detailed planning.

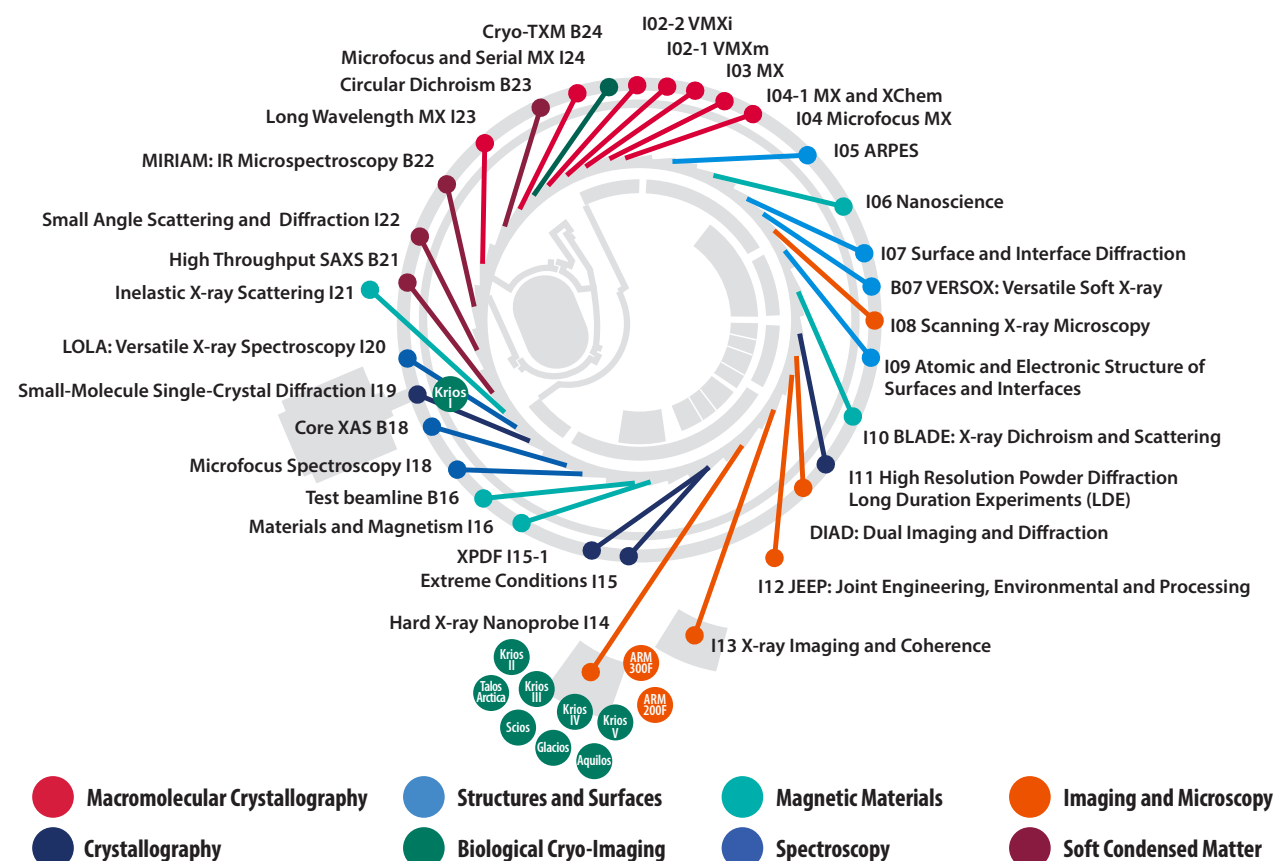
To remain at the cutting-edge of science, we need to ensure we continue to attract people from all over the world because they bring their different perspectives and skills. We also need to engage more closely with other facilities that provide complementary technical expertise. These are global endeavours, but the highest density of world-class light source facilities and suitably trained scientists and engineers are in Europe, so it is more critical than ever that we maintain close and effective ties with our closest and strongest allies. To this end, in 2017 we became Members of LEAPS – the League of European Accelerator-based Photon Sources – an organisation that brings together every synchrotron and Free Electron Laser (FEL) facility in Europe. Over the past year, the collaboration has developed a collection of projects for enabling technology, from new sources and optics to detectors and data analysis tools, that we will work on together to ensure that we are all able to support the most brilliant science and innovation well into the future.

**Prof Andrew Harrison**  
CEO Diamond Light Source

## Beamline Development and Technical Summary

In its twelfth year of experiments, Diamond is now operating with 32 beamlines and 11 electron microscopes. The next year will see the completion of the latest phase of construction when the DIAD beamline welcomes first users. Of the electron microscopes, nine are cryo-electron microscopes specialising in life sciences, with two provided for industry use in partnership with Thermo Fisher Scientific, and make up eBIC (electron Bio-Imaging Centre). The two remaining microscopes dedicated to advanced materials research are supplied by Johnson Matthey and the University of Oxford. These microscopes form ePSIC (electron Physical Science Imaging Centre) and are operated under strategic collaboration agreements to provide for substantial dedicated peer reviewed user access. Both the eBIC and ePSIC centres are next to the Hard X-ray Nanoprobe beamline (I14). For academic research, Diamond instruments (beamlines and microscopes) are free at the point of access through peer review. For proprietary research, access can be secured through Diamond's industry team.

Following a restructure in 2018, the instruments are organised into eight science groups as described below.



### Electron Microscopes

Microscope	Main Capabilities	Accelerating Voltages	Operational Status
Titan Krios I	Cryo-EM, Cryo-ET	80, 120, 200, 300 kV	Operational since 2015
Titan Krios II	Cryo-EM, Cryo-ET	80, 120, 200, 300 kV	Operational since 2016
Titan Krios III	Cryo-EM, Cryo-ET	80, 120, 200, 300 kV	Operational since 2017
Titan Krios IV	Cryo-EM, Cryo-ET	80, 120, 200, 300 kV	Operational since 2017
Titan Krios V	Cryo-EM, Cryo-ET	80, 120, 200, 300 kV	Operational since 2018
Talos Arctica	Cryo-EM, Cryo-ET	200 kV	Operational since 2016
Glacios	Cryo-EM, Cryo-ET	200 kV	Installed, March 2019
Scios	Cryo-SEM, Cryo-FIB	3 to 30 kV	Operational since 2017
Aquilos	Cryo-SEM, Cryo-FIB	3 to 30 kV	Operational since 2019
JEOL ARM200F	Atomic scale STEM imaging, EELS, EDX, electron diffraction	80, 200 kV	Operational since 2017
JEOL ARM300F	Atomic scale TEM and STEM imaging, electron diffraction, 4D-STEM, EDX	30, 60, 80, 160, 200, 300 kV	Operational since 2017

### Diamond's beamlines: current operational status April 2019

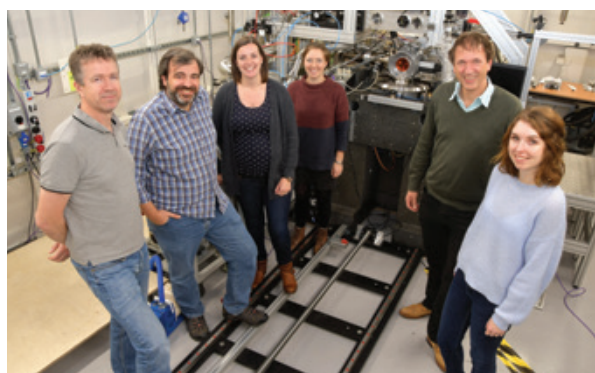
Beamline Name and Number	Main Techniques	Energy / Wavelength Range	Status
I02-1 - Versatile MX micro (VMXm)	Micro- and nano-focus in vacuum cryo-macromolecular crystallography (VMXm)	7 - 28 keV	Commissioning
I02-2 - Versatile MX <i>in situ</i> (VMXi)	<i>In situ</i> microfocus macromolecular crystallography, Serial Synchrotron Crystallography	10 - 25 keV	Commissioning
I03 - MX	Macromolecular crystallography (MX), Multiwavelength Anomalous Diffraction (MAD)	5 - 25 keV	Operational
I04 - Microfocus MX	MX, MAD	6 - 18 keV	Operational
I04-1 - Monochromatic MX	MX, XChem fragment screening	13.53 keV (fixed wavelength)	Operational
I05 - ARPES	Angle-Resolved PhotoEmission Spectroscopy (ARPES) and nano-ARPES	18 - 240 eV; 500 eV	Operational
I06 - Nanoscience	X-ray Absorption Spectroscopy (XAS), X-ray photoemission microscopy and X-ray magnetic circular and linear dichroism	80eV - 2200eV	Operational
I07 - Surface and Interface Diffraction	Surface X-ray diffraction, Grazing Incidence X-ray Diffraction (GIXD), Grazing Incidence Small Angle X-ray Scattering (GISAXS), X-ray Reflectivity (XRR)	6 - 30 keV	Operational
B07 - VERSOX: Versatile Soft X-ray	Ambient Pressure XPS and NEXAFS NEXAFS and High-Throughput XPS	250 - 2800 eV 50 - 2200 eV	Operational Commissioning
I08 - Scanning X-ray Microscopy	Scanning X-ray microscopy, NEXAFS/ XANES, X-ray fluorescence	I08 branch: 250 eV - 4.4 keV	Operational
		J08 - Soft and Tender X-ray Ptychography branch: 250 - 2000 eV	Construction
I09 - Atomic and Electronic Structure of Surfaces and Interfaces	XPS (including HAXPES), X-ray Standing Waves (XSW), Near Edge X-ray Absorption Fine Structure (NEXAFS), energy-scanned photoelectron diffraction	Hard X-rays: 2.1 - 18+ keV Soft X-rays: 0.1 - 2.1 keV (currently 0.1 - 1.9 keV)	Operational
I10 - BLADE: Beamline for Advanced Dichroism Experiments	Soft X-ray resonant scattering, XAS and X-ray magnetic circular and linear dichroism	Circular: 400-1600eV; Linear Horizontal: 250-1600eV; Linear Vertical: 480-1600eV	Operational
I11 - High Resolution Powder Diffraction	X-ray powder diffraction	6 - 25(30) keV (0.5 - 2.1 Å)	Operational
DIAD: Dual Imaging and Diffraction	Simultaneous imaging and diffraction	8 - 38 keV	Construction
I12 - JEEP: Joint Engineering, Environmental and Processing	Time-resolved imaging and tomography (phase- and attenuation-contrast), time-resolved powder diffraction, single crystal diffraction, diffuse scattering, energy dispersive X-ray diffraction (EDXD), high-energy small angle X-ray scattering (under development)	53 keV - 150 keV monochromatic or continuous white beam	Operational
I13 - X-ray Imaging and Coherence	Phase contrast imaging, tomography, full-field microscopy (under commissioning), coherent diffraction and imaging (CXRD, CDI), ptychography and photocorrelation spectroscopy (XPCS) (under commissioning), innovative microscopy and imaging	Imaging branch: 8 - 30keV	Operational
		Coherence branch: 7 - 20keV	Operational
I14 - Hard X-ray Nanoprobe	Scanning X-ray fluorescence, X-ray spectroscopy, ptychography and transmission diffraction	5 - 23 keV	Optimisation
I15 - Extreme Conditions	Powder diffraction, single crystal diffraction	Monochromatic and focused 20 - 80 keV White beam	Operational
I15-1 - XPDF	X-ray Pair Distribution Function (XPDF)	40, 65, and 76 keV	Operational
I16 - Materials and Magnetism	Resonant and magnetic single crystal diffraction, fundamental X-ray physics	2.5 - 15 keV	Operational
B16 - Test beamline	Diffraction, imaging and tomography, topography, reflectometry	4 - 20 keV monochromatic focused 4 - 45 keV monochromatic unfocused White beam	Operational
I18 - Microfocus Spectroscopy	Micro XAS, micro Extended X-ray Absorption Fine Structure (EXAFS), micro fluorescence tomography, micro XRD	2.05 - 20.5 keV	Operational
B18 - Core XAS	X-ray Absorption Spectroscopy (XAS)	2.05 - 35 keV	Operational
I19 - Small-Molecule Single-Crystal Diffraction	Small-molecule single-crystal diffraction	5 to 25 keV / 0.5 to 2.5 Å	Operational
I20 - LOLA: Versatile X-ray Spectroscopy	X-ray Absorption Spectroscopy (XAS), X-ray Emission Spectroscopy (XES) and Energy Dispersive EXAFS (EDE)	Dispersive branch: 6 - 26 keV	Optimisation
		Scanning branch: 4 - 20 keV	Operational
I21 - Inelastic X-ray Scattering	Resonant Inelastic X-ray Scattering (RIXS), X-ray Absorption Spectroscopy (XAS)	Currently 250 - 1500 eV (to be upgraded to 250 - 3000 eV)	Optimisation
B21 - High Throughput SAXS	BioSAXS, solution state small angle X-ray scattering	8 - 15 keV (set to 13.1 keV by default)	Operational
I22 - Small Angle Scattering and Diffraction	Small angle X-ray scattering and diffraction: SAXS, WAXS, USAXS, GISAXS. Micro-focus.	7 - 20 keV	Operational
B22 - MIRIAM: Multimode InfraRed Imaging And Microspectroscopy	IR micro- & nano-spectroscopy, IR imaging, THz spectroscopy	nanoFTIR: 4000-900 cm <sup>-1</sup> (2.5-11 μm) microFTIR: 10,000-100 cm <sup>-1</sup> (1-100 μm) Spectroscopy (FTIR): 10,000-10 cm <sup>-1</sup> (1-1000 μm) Imaging (FPA): 10,000-900 cm <sup>-1</sup> (1-11 μm)	Operational
I23 - Long Wavelength MX	Long wavelength macromolecular crystallography	3 - 8 keV (1.5 - 4.1 Å)	Optimisation
B23 - Circular Dichroism	Circular Dichroism (CD)	125-500 nm & 165-650 nm for CD Imaging at 50 μm resolution, 96-cell High-Throughput CD (HTCD) and High-Pressure CD up to 200 MPa	Operational
I24 - Microfocus and Serial MX	Macromolecular crystallography, MAD, Serial Crystallography	6.5 - 25.0 keV	Operational
B24 - Cryo Transmission X-ray Microscopy (TXM)	Full field X-ray imaging	200eV - 2600eV	Optimisation

## Macromolecular Crystallography Group

Dave Hall, Science Group Leader

**M**acromolecular crystallography (MX) is a key technique in the structural biologist's toolkit for understanding the function of biologically relevant molecules by revealing their shape and interactions at atomic resolution. The information derived from MX experiments can be complemented by many other techniques at Diamond for life science research (see the Soft Condensed Matter and Imaging and Microscopy sections of this review), coupled with experiments in the researcher's lab, to give deeper insight adopting an integrated structural biology approach.

At Diamond, seven beamlines (I03, I04, I04-1, I23, I24, VMXi, and VMXm), alongside the XChem fragment screening facility, the UK XFEL Hub, and the Membrane Protein Facility, are dedicated to exploiting the technique of MX for the benefit of the UK structural biology community, alongside researchers from Europe and further afield.



First users and beamline team on VMXm, from left to right: Gwyndaf Evans (PBS), Jose Trincao, Anna Warren, Emma Beale, Diamond, and Ivo Tews and Rachel Bolton, University of Southampton.

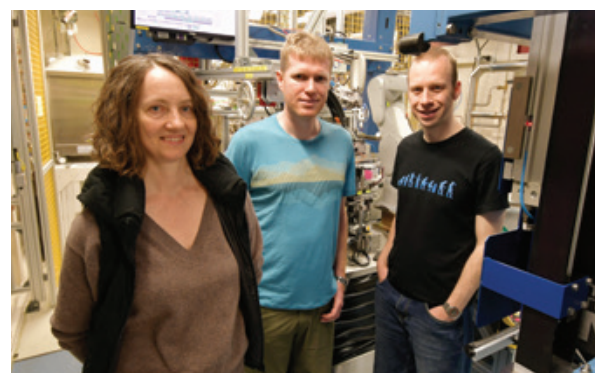
It has been an exciting year for the VMXm micro/nanofocus MX beamline. After performing the first protein diffraction experiments at room temperature and in vacuum back in May 2018, first user experiments followed in October 2018. The group of Dr Ivo Tews from University of Southampton measured data from their sample crystals mounted on cryoelectron microscopy grids held at cryogenic temperatures in the evacuated sample environment. The compact sample space incorporates an on-axis video microscope and a Scanning Electron Microscope (SEM) for sample visualisation. The SEM has already proved invaluable in identifying the location, size, and shape of micron sized crystals. The smallest X-ray beam size measured to date on VMXm is currently 0.4 x 1.2  $\mu\text{m}$ , and further commissioning and optimisation will take place throughout 2019.

Beamline VMXi provides a highly intense X-ray beam for the study of crystals at room temperature, particularly in the media in which the crystals are grown. Through 2018, significant upgrades have been made that enable VMXi to progress to a full user programme, with the beamline being the test bed for the first 2<sup>nd</sup> generation Eiger2 X detector (4M), which is capable of collecting data at very fast rates with extremely high count rates - perfectly matched to room temperature data collection with a very intense X-ray source. A new sample viewing system, and improved alignment configuration, now enable accurate automatic collection of data sets from many 10s, if not 100s of crystals per hour. Early experiments with serial crystallography delivery methods have been trialled and will add a further strength to the beamline capabilities in the coming years.

In the push to increase throughput across the beamlines, upgrades and methods are continuously being rolled out across the facilities. One such development in the last year is a significant improvement in grid scans - the ability to raster a sample in the X-ray beam and collect data. Fast grid scans have

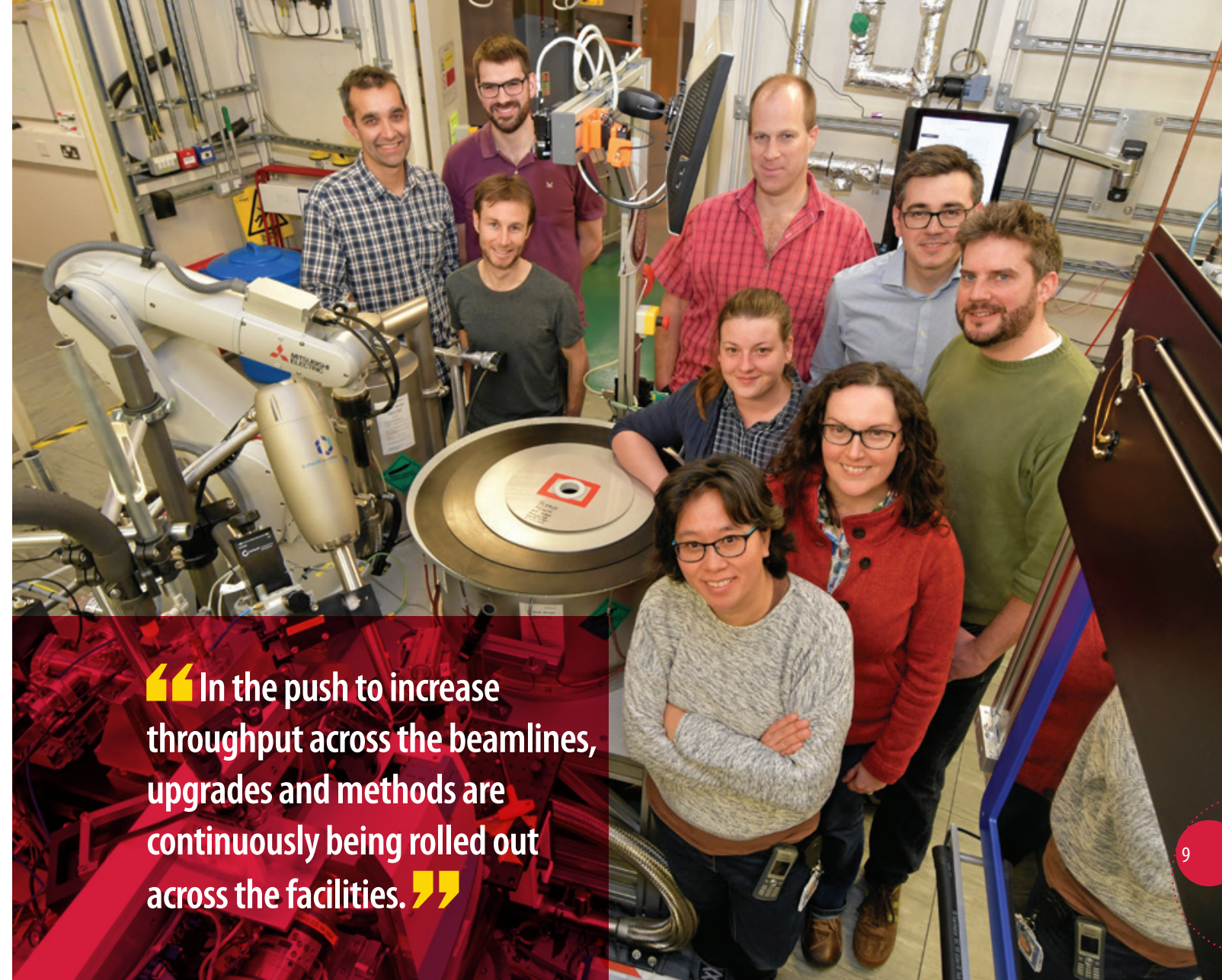
been developed by beamline I24, and are already rolled out to the beamline as well as I03 and I04. Building on the approach used on I24 for fixed-target serial crystallography, samples can now be moved continuously during grid scans allowing data collection at the maximum frame-rate of the detector, with no compromise on positional accuracy. With grid scans now running at >100 Hz, many more samples can be rastered over during a shift, and the throughput of automated X-ray centering will significantly increase. Data collection using this approach on the hard X-ray Imaging and Coherence beamline I13 has reached rates of 600 Hz, with a positional accuracy of 50 nm, illustrating that detectors are now the limiting step in raster scanning.

Building on the work for Eiger detectors on VMXi, the first of the Eiger2 X 16M series detector model has been installed on beamline I04 recently. It replaces the first generation Pilatus2 detector, and provides a significant number of advantages and improvements that are benefitting the user community and science output. Data acquisition rates have increased five-fold over the previous detector, and a typical data set can now be collected in less than 15 seconds. The Eiger2 detector's much smaller pixel size, coupled with no read-out time and vastly increased count rate capability, is leading to high dynamic range data with reduced background noise, improving data quality, and is beneficial in resolving large unit cells. Recently we installed the second Eiger2 X 16M detector on beamline I03 to complement the MX beamline suite's capabilities.



Katherine McAuley (PBS), Neil Paterson and Mark Williams on I03.

Remote data collections are routine on the cryo-MX beamlines at Diamond and, over the last few years, there has been a steady increase in the numbers of samples shipped to Diamond for remote sessions, with more recently up to 90 dewars (or 10,000 sample mounts) on-site at any one time. Consequently, the logistics of managing users' dewars and pucks has become more complicated, requiring new systems for tracking and streamlining the process of setting up for remote experiments. Tracking has been resolved by barcoding pucks and shipping dewars, and utilising the experiment database ISPyB. In this



“ In the push to increase throughput across the beamlines, upgrades and methods are continuously being rolled out across the facilities. ”

The I04-1 beamline team, clockwise from left: Jose Brandao-Neto, Richard Gillams, Frank von Delft (PBS), Alex Dias, Romain Talon, Ailsa Powell, Alice Douangamath, Anthony Aimon, Rachel Skyner.

way, every experiment is tracked, and the responsible Diamond scientist is automatically informed which dewars are needed and where they are. The puck barcodes are scanned as they are loaded into the robot storage dewar and, consequently, the user is presented with a list of their samples when they start the data acquisition software. All these tools will be essential over the next few months as sample throughput is likely to increase further following the installation of new, faster detectors and, when automated, queued data collections become more widely used.

Automated collection of data on beamline I04-1 has underlined the success of the crystal-based fragment screening facility, XChem, which to date has supported more than 130 new screens from academia and industry for fragment-based drug discovery. In October 2018, the I04-1/XChem team hit the milestone of the 100,000<sup>th</sup> XChem crystal collection - just three and half years since the XChem programme started. To meet the MX user's increasing demands for XChem, the platform has been expanded, and a dedicated XChem support team has been put in place. More information on the XChem facility can be found in the Integrated Facilities section.

The team of beamline I23 has been working to establish MX in a wavelength range which hasn't been accessible before, and has required building the first MX beamline operating in vacuum. This has necessitated a completely new approach to sample delivery being developed. A variety of studies have already been published, mainly for experimental native phasing,

however, one recent highlight has been the study of potassium binding in the selectivity filter for potassium channels (*Nature Communications*, DOI 10.1038/s41467-018-06957-w), where access to the potassium K-edge at I23 unequivocally identified the biologically relevant state without recourse to complex substitution experiments. I23 can access the absorption edges of calcium, potassium and chlorine allowing unambiguous identification of the nature of these atoms even at low resolution. Over the next few years we will be able to give further insight into binding of these important elements in biology, information which remains elusive in cryo-EM. In the coming months, significant improvements to the beamline will be made to facilitate user mode and, to optimise best use of time on I23, adaptors for the I23 sample holders have been developed that enable fast sample screening on beamline I03.

Serial crystallography experiments at MX beamlines are complemented by Diamond hosting the UK XFEL Hub, a Wellcome funded initiative. It has a remit to develop hardware and software for Serial Femtosecond Crystallography (SFX), alongside supporting user training and access to SPB/SFX (single particles, clusters and biomolecules SFX) at the European XFEL and other hard X-ray facilities worldwide. Recently the XFEL Hub was internationally reviewed, with strong backing of the work and research the Hub is doing, and its support of the UK life science community who are awarded XFEL beamtime around the world. More details on the XFEL Hub can be found in the Integrated Facilities section.

## Using structure-based design to engineer chimeric protein vaccines

**Related publication:** Hollingshead S., Jongerius I., Exley R. M., Johnson S., Lea S. M. & Tang C. M. Structure-based design of chimeric antigens for multivalent protein vaccines. *Nat. Commun.* **9**, 1051 (2018). DOI: 10.1038/s41467-018-03146-7

**Publication keywords:** Meningococcal; Vaccine; Serogroup B; fHbp; PorA

**A** major World Health Organisation objective is to develop vaccines against pathogenic bacteria. However, vaccine development is often hindered by variation in the molecules at the surface of the bacteria, and the manufacturing challenges inherent to working with such molecules. Researchers conducted a proof-of-principle study to assess the feasibility of taking portions of intractable molecules and creating chimeras by splicing them into well-behaved molecules, with the ultimate goal of producing vaccines that raised immune responses against both types of molecule.

They used Macromolecular Crystallography beamlines I02 and I04-1 to carry out structural investigations to confirm that this chimera-generating approach doesn't compromise key structural features of the molecules. This is especially important when it comes to molecules with the potential for use in therapeutic drugs. The study demonstrated that the approach is valid. Structures of the chimeric molecules revealed that both molecules retained the structure observed in their native context, or in immune-relevant complexes. Immunisation studies revealed that the chimeric molecules were able to elicit immune responses against each component.

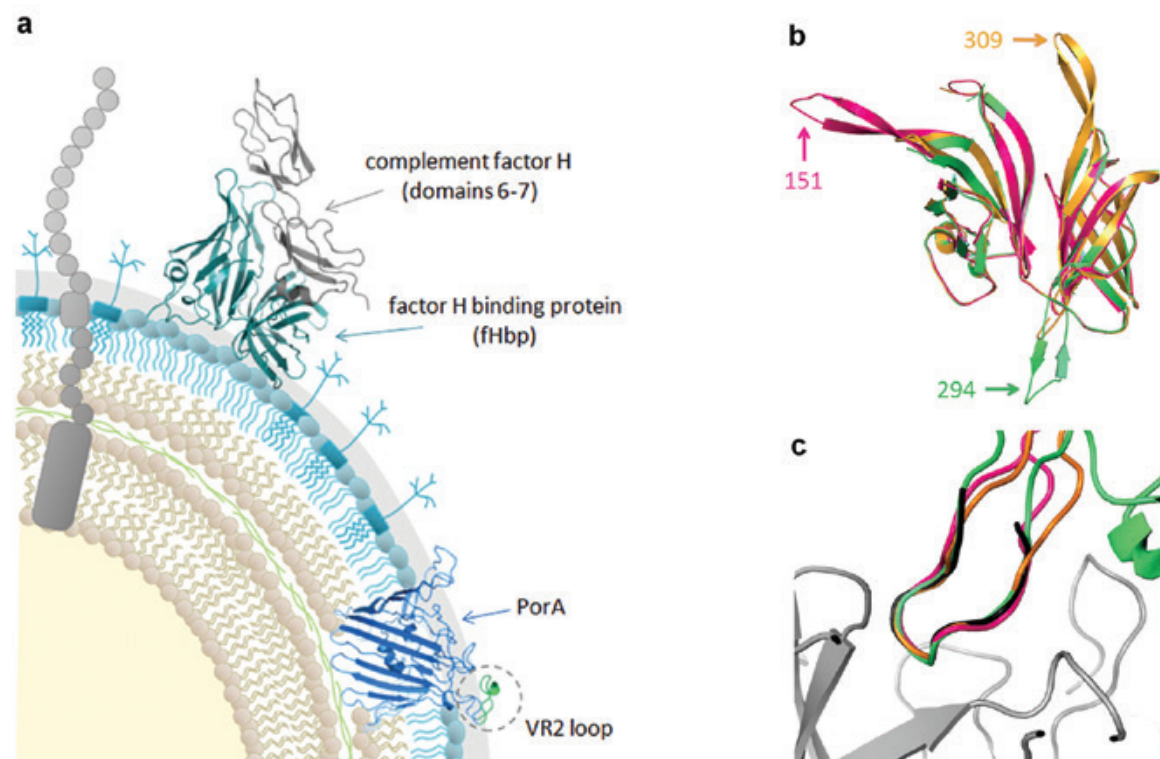


**Figure 1:** (a) Schematic of *N. meningitidis* cell surface, shown are the major antigens fHbp (in a complex with human complement factor H domains 6-7) and PorA. (b) Structural alignment of fHbp scaffolds from V1 fHbp peptides with a PorA loop inserted at residue 151 (pink, PDB: 5NQP), 294 (green, PDB: 5NQX) or 309 (orange, PDB: 5NQY). (c) Structural alignment of the PorA VR2 epitopes in the fHbp scaffold (151, pink; 294, green; 309, orange) with a linear peptide of PorA VR2 P1.16 (black) in a complex with a bactericidal Fab fragment (grey) from monoclonal antibody MN12H2 (PDB: 2MPA).

To combat the rise in multi-drug resistant bacteria, the World Health Organisation is advocating the development of vaccines against bacterial pathogens. Historically, vaccines were based on protein toxoids, polysaccharide capsules, or outer membrane vesicles. However, these approaches are not feasible for many pathogens, and immune evasion mechanisms, such as antigenic diversity, further limit the strategies available to develop successful vaccines. In addition, many vaccine candidates are integral membrane proteins which can present manufacturing problems, and issues such as generating

immune responses against epitopes that are masked in the whole organism. To circumvent these issues, we used structure-based design to engineer chimeric antigens (ChAs), and developed a next generation vaccine for prevention of meningococcal disease.

The meningococcal ChAs produced for our study are composed of two major *N. meningitidis* antigens, factor H binding protein (fHbp), a surface exposed lipoprotein<sup>1</sup>, and PorA, an integral outer membrane porin<sup>2</sup> (Fig. 1a). In the

a.

Antisera			<i>N. meningitidis</i> strain used in SBA			PorA dependent SBA titre
fHbp	PorA	position	Isolate	fHbp peptide	PorA VR2	
V1.4	P1.10_1	151	M11.240189	V3.84	P1.10_1	1/20
V1.4	P1.14	151	M15.240853	V3.45	P1.14	1/640
V3.45	P1.4	151	M11.240123	V1.92	P1.4	1/160
V3.45	P1.9	151	M11.240431	V2.19	P1.9	1/1280

b.

Antisera			<i>N. meningitidis</i> strain used in SBA			fHbp dependent SBA titre
fHbp	PorA	position	Isolate	fHbp peptide	PorA VR2	
V1.1	P1.16	151	H44/76 Δ PorA	V1.1	N/A	1/1024
		294				1/4096
		309				1/2048

**Figure 2:** Serum bactericidal assay titres. (a) a-PorA SBA titres generated using ChA/alum antisera and serogroup B *N. meningitidis* isolates with mismatched fHbp variants. (b) a-fHbp SBA titres generated using ChA/alum antisera and serogroup B *N. meningitidis* isolate H44/76 Δ porA.

ChAs, fHbp is exploited as a molecular scaffold to display an immunogenic surface exposed loop from PorA, known as the variable region 2 (VR2, Fig. 1a). Both fHbp and the VR2 loop exhibit antigenic diversity, with fHbp peptides falling into three variant groups or two subfamilies depending on the classification system: V1 (subfamily B), V2, and V3 (both subfamily A). In general, immunisation with a particular fHbp induces cross-protection against strains that express an fHbp belonging to the same, but not a different, variant group, although there can be cross-protection between fHbp variant groups V2 and V3 (subfamily A). Unlike fHbp, the PorA VR2 offers limited or no cross-protection against strains expressing a PorA peptide with a different VR2. Therefore to optimise coverage of the vaccine, the fHbp and PorA VR2 peptides used must be carefully selected. This was achieved using the comprehensive epidemiology data available in the meningococcal genome library<sup>3</sup>.

A proof of principle study was designed to ascertain: i) the introduction of a PorA VR2 loop did not alter the overall architecture of fHbp, ii) functional immune responses could be elicited against both fHbp and PorA antigens, iii) ChA composition can be manipulated to adapt to circulating fHbp and PorA antigens.

Structures were determined of ChAs with PorA VR2 P1.16 inserted into position 151, 294, or 309 of a V1 fHbp (Fig. 1b). These structures were solved using molecular replacement to resolutions of 2.9 Å, 3.7 Å, and 2.6 Å, respectively. All ChA scaffolds align with good agreement to native fHbp (Fig. 1b), demonstrating that the structure of fHbp is not perturbed by insertion of VR2 loop P1.16. In each structure, the VR2 loop adopts a β-turn conformation that extends away from the fHbp scaffold, and mimics an identical free VR2 peptide in a complex with a bactericidal Fab fragment (Fig. 1c).

The adaptability of the ChA approach was tested by generating ChAs composed from different combinations of fHbp and PorA VR2. The comprehensive meningococcal genome data available for strains isolated in the UK enable design of ChAs that have exact sequence matches to the most common antigens in a given region<sup>3</sup>. Prevalent PorA VR2s in circulating serogroup B *N. meningitidis* isolates are P1.4, P1.9, P1.14, P1.16 and P1.10\_1, and prevalent fHbp peptides are V1.4 and V3.45. Five different ChAs were constructed, in which a VR2 peptide was inserted into position 151 in V1.4 or V3.45. The ability of these ChAs to elicit immune responses was examined by immunising groups of CD1 mice with each ChA, followed by the use of a serum bactericidal assay (SBA), to assess the ability of the immune sera to

initiate complement-mediated lysis of *N. meningitidis*. This assay demonstrated PorA specific SBA titres ranging between  $\geq 20$  and  $\geq 1280$  (Fig. 2a) (above the  $\geq 8$  threshold for an accepted correlate of protective immunity against *N. meningitidis*). Furthermore, fHbp specific SBA titres, obtained from ChAs composed of fHbp V1.1 and VR2 P1.16, range between  $\geq 1024$  and  $\geq 4096$  (Fig. 2b).

Previous studies had found that linear PorA VR2 peptides failed to elicit antibodies that recognised native PorA, while cyclic VR2 peptides, with identical residues fixed in a β-turn, elicited PorA specific bactericidal antibodies. In the ChAs generated in this study, the VR2 N- and C- termini are effectively locked into a "biological" β-turn peptide mimetic by neighbouring fHbp β-strands, as confirmed by our atomic structures.

This study provides proof of principle that ChAs can be used to display selected antigens from a soluble protein, which forms a scaffold, and an epitope from an integral membrane protein. The structural data conclusively demonstrates that fHbp is not perturbed by insertion of a PorA VR2, and that the VR2 loop P1.16 adopts a conformation known to induce bactericidal antibody responses. The immune response data demonstrates that correlates of protection are elicited by both antigens in the ChA, and that ChA composition can be adapted to provide protection against relevant circulating *N. meningitidis* strains.

### References:

- Pizza M. *et al.* Identification of vaccine candidates against serogroup B meningococcus by whole-genome sequencing. *Science* (80-. ). 287, 1816–1820 (2000). DOI: 10.1126/science.287.5459.1816
- van der Ley P. *et al.* Topology of outer membrane porins in pathogenic *Neisseria* spp. *Infect. Immun.* **59**, 2963 LP-2971 (1991)
- Meningitis Research Foundation Meningococcus Genome Library ([https://pubmlst.org/bigsub?db=pubmlst\\_neisseria\\_mrfgenomes](https://pubmlst.org/bigsub?db=pubmlst_neisseria_mrfgenomes))

### Funding acknowledgement:

Action Medical Research (Award number GN2205).

### Corresponding author:

Prof Susan Lea, University of Oxford, susan.lea@path.ox.ac.uk

## Understanding human sleeping sickness

**Related publication:** Zoll S., Lane-Serff H., Mehmood S., Schneider J., Robinson C. V., Carrington M. & Higgins M. K. The structure of serum resistance-associated protein and its implications for human African trypanosomiasis. *Nat. Microbiol.* **3**, 295–301 (2018). DOI: 10.1038/s41564-017-0085-3

**Publication keywords:** African trypanosomes; Innate immunity; Apolipoprotein L1; SRA

**T**he worst forms of human sleeping sickness (African trypanosomiasis) are caused by a species of trypanosome (single-celled parasite) known as *T. b. rhodesiense*. Most African trypanosomes are unable to infect humans as they are killed by a component of human blood, known as trypanolytic factor, and only two trypanosome subspecies are able to infect humans. *T. b. rhodesiense* is able to do so due to the presence of a single molecule called SRA. Although it was clear that SRA is the sole molecule responsible for allowing this parasite to develop human resistance, we did not know how it worked, or what it looked like. We also did not know how it binds to the active component of the trypanolytic factor, a molecule called ApoL1.

A team of researchers from the Universities of Oxford and Cambridge investigated how SRA stops the trypanolytic factor from working, using the Macromolecular Crystallography beamlines I03 and I04-1 to collect diffraction data from crystals of SRA bound to an antibody, and to determine the structure of the molecule. They were able to work out what SRA looks like, and to map onto the structure the regions of SRA that bind to the trypanolytic factor. This provides a first view of how SRA gives a trypanosome the ability to infect humans. However, it still leaves many questions, and understanding exactly how ApoL1 interacts with SRA remains an exciting future research challenge.

African trypanosomes are single-celled eukaryotic pathogens that are transmitted by tsetse flies, and live within the blood streams and tissue spaces of infected mammals. Infection causes disease, including the debilitating wasting illness of cattle, nagana, which restricts the productivity of livestock in sub-Saharan Africa. While there are numerous species of African trypanosome, only two subspecies, *T. b. gambiense* and *T. b. rhodesiense*, can proliferate in humans. This is due to lytic factors, present only in humans and some other primates, which are taken up by trypanosomes and causes their death<sup>1</sup>. Human-infective species are able to negate the action of this lytic factor. This confers the ability to grow within infected humans, and to cause the disease Human African trypanosomiasis, also known as sleeping sickness. The aim of our work is to understand how human-infective trypanosomes inactivate the lytic factor, and then to determine whether we can make them susceptible to lytic factor mediated killing.

Our first contribution towards these goals used beamline facilities at Diamond Light Source to understand how lytic factor is taken up by trypanosomes. The lytic factor is a complex of several components, including the pore-forming protein, apolipoprotein L1 (ApoL1), which acts as the toxin and a complex of haptoglobin related-protein bound to haemoglobin (HprHb). Trypanosomes have a receptor on their cell surface that binds to haptoglobin-haemoglobin (HpHb), allowing them to scavenge this valuable nutrient from the blood. However, the presence of HprHb in lytic factor allows this toxin to hitch a ride on the receptor, taking it into the trypanosome cell, where it mediates its toxic effect. We used beamlines I03 and I04-1 to solve structures of HpHb receptors from human-infective and non-infective trypanosomes, alone and also bound to HpHb<sup>2-4</sup>. This revealed how the lytic factor is recognised by trypanosomes. It also helped us to understand how *T. b. gambiense* becomes human-infective, as it has a mutation of the HpHb receptor which reduces lytic

factor uptake. Our structures revealed how this mutation decreases the affinity of the receptor for lytic factor, and how it helps to protect this trypanosome subspecies from destruction<sup>2-3</sup>.

We more recently turned our attention to *T. b. rhodesiense*, which counteracts the action of lytic factor by expressing an anti-toxin that binds to, and inactivates, ApoL1. The anti-toxin, known as the serum resistance associated protein (SRA), is found primarily within the lysosome of trypanosomes, and is sufficient to allow a trypanosome to become human infective. Our goal was to determine the structure of SRA, and to investigate how it binds to, and inactivates, ApoL1.

Determining the structure of SRA proved challenging. As we later discovered, a large loop at one end of SRA is flexible, and prevented the formation of well-ordered crystals. We were able to solve this problem by producing a panel of monoclonal antibodies that bind to SRA, and discovered that the complex of SRA with one of these antibodies formed crystals of sufficient quality<sup>5</sup>. Armed with data collected from beamline I03 at Diamond, we were then able to determine the structure of SRA. Together with data from hydrogen-deuterium exchange mass spectrometry, and validated by mutagenesis, this allowed us to map onto SRA the residues that interact with ApoL1.

This provided the first detailed structural insight into SRA and its mode of interaction with ApoL1<sup>6</sup>. It also revealed that prevailing models for how SRA prevents ApoL1 function were not compatible with our structural findings. However, it still leaves many questions, and understanding exactly how ApoL1 forms pores, and how the binding of SRA prevents these pores from forming, remains an exciting future research challenge.

### References:

1. Pays E. *et al.* The molecular arms race between African trypanosomes and humans. *Nat. Rev. Microbiol.* **12**, 575 (2014). DOI: 10.1038/nrmicro3298.
2. Higgins M. K. *et al.* Structure of the trypanosome haptoglobin-hemoglobin receptor and implications for nutrient uptake and innate immunity. *Proc. Natl. Acad. Sci.* **110**, 1905–1910 (2013). DOI: 10.1073/pnas.1214943110
3. Lane-Serff H. *et al.* Structural basis for ligand and innate immunity factor uptake by the trypanosome haptoglobin-haemoglobin receptor. *Elife* **3**, e05553 (2014). DOI: 10.7554/eLife.05553

4. Lane-Serff H. *et al.* Evolutionary diversification of the trypanosome haptoglobin-haemoglobin receptor from an ancestral haemoglobin receptor. *Elife* **5**, e13044 (2016). DOI: 10.7554/eLife.13044
5. Zoll S. *et al.* The structure of serum resistance-associated protein and its implications for human African trypanosomiasis. *Nat. Microbiol.* **3**, 295–301 (2018). DOI: 10.1038/s41564-017-0085-3

### Funding acknowledgement:

MRC (MR/L008246/1 and MR/P001424/1); Wellcome Trust.

### Corresponding authors:

Prof Matt Higgins, University of Oxford, matthew.higgins@bioch.ox.ac.uk and Prof Mark Carrington, University of Cambridge, mc115@cam.ac.uk

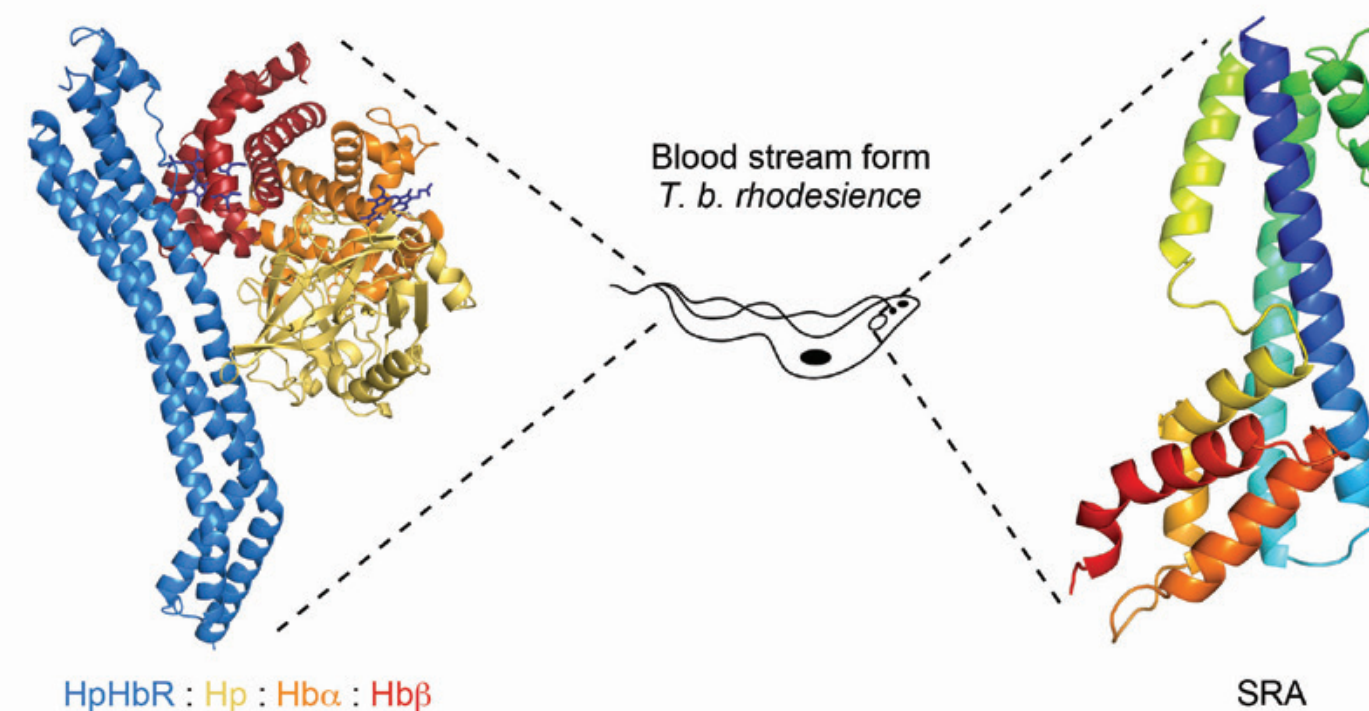


Figure: The centre of the figure shows a schematic of a blood stream form *T. b. brucei*. The left-hand side of the figure shows the *T. b. rhodesiense* haptoglobin-haemoglobin receptor (HpHbR, blue) bound to a complex of the SP domain of haptoglobin (Hp, yellow), the  $\alpha$ -subunit of haemoglobin (Hb $\alpha$ , orange) and the  $\beta$ -subunit of haemoglobin (Hb $\beta$ , red). This is found on the cell surface, and within the flagella pocket of trypanosomes. The right-hand panel shows the surface resistance associated protein (SRA, rainbow) of *T. b. rhodesiense*, which is found primarily in the lysosome of trypanosomes.

## Turning the plastic tide – engineering enzymes to tackle plastic pollution

**Related publication:** Austin H. P., Allen M. D., Donohoe B. S., Rorrer N. A., Kearns F. L., Silveira R. L., Pollard B. C., Dominick G., Duman R., El Omari K., Mykhaylyk V., Wagner A., Michener W. E., Amore A., Skaf M. S., Crowley M. F., Thorne A. W., Johnson C. W., Woodcock H. L., McGeehan J. E. & Beckham G. T. Characterization and engineering of a plastic-degrading aromatic polyesterase. *Proc. Natl. Acad. Sci.* **115**, E4350–E4357 (2018). DOI: 10.1073/pnas.1718804115

**Publication keywords:** Biodegradation; Polyethylene terephthalate (PET); Plastics recycling; Cutinase

**W**hile climate change has rightly received significant global attention in recent years, we have only just awoken to the sheer magnitude of plastic pollution. Eight million tons of plastic waste enters our oceans annually, impacting the environment, wildlife, and human health. Programmes like Blue Planet II have changed our perceptions about the effects of plastic, but we currently lack effective solutions to deal with the scale of the problem.

We need to find a way to recycle plastic in a circular fashion. 93% of plastic bottles are never made into new plastic bottles, but are instead ‘downcycled’ into lower grade plastic, incinerated, or buried in landfill. Polyethylene terephthalate (PET) is one of the most common polluting plastics, and is used for single-use plastic bottles, textiles and carpets.

Biological enzymes have the potential to break down solid PET into its original building block monomers, and an international team of researchers used the state-of-the-art Long-Wavelength Macromolecular Crystallography (MX) beamline (I23) to investigate the 3D structure of a newly-discovered PETase enzyme to see how it works, and how to make it more efficient.

They discovered that the PETase enzyme is closely related to a cutinase enzyme produced by bacteria to digest the protective natural polyester coating on plant leaves. The 3D structure allowed them to design an improved enzyme that can digest PET faster, which offers great potential for future engineering of this enzyme for industrial recycling applications.

Plastic pollution has reached alarming levels in the environment, particularly in our oceans. From documentary programmes such as Blue Planet II, through to media from around the globe, the sheer scale of the problem is now receiving the attention that it deserves. Many plastics were only patented in the 1940s, but have gained such traction in our everyday lives that their production has reached truly staggering rates. The plastics industry is worth \$1 trillion, and in the UK it represents our second largest manufacturing sector. Few could have predicted that in only a few decades huge plastic waste patches would be found floating in our oceans, and once pristine beaches would be contaminated all over the world (Fig. 1). Recent studies indicate the pervasive nature of these materials, and plastics have now been discovered in our polar sea ice and in the deepest parts of our oceans. The flow of plastic into the environment continues to grow, and it is now with some urgency that we need to find sustainable alternatives and reduce our reliance on plastics for single-use applications.

Plastics have incredible properties and have revolutionised many industries. They are cheap to manufacture, strong, light, transparent, waterproof, inert,



Figure 1: Single-use materials such as PET plastic bottles can persist for hundreds of years in the oceans, concentrating in huge ocean gyres such as the Great Pacific Garbage Patch. Photo credit: DAVID JONES.

and can be moulded into highly complex solids. From films to the ubiquitous fizzy drink bottle, they protect and extend the lifetime of many products. So why then have they created such a global scourge? It is the very properties that the chemists were asked to create, low cost and durability, that have had unforeseen consequences. To understand why, we need to look at the nature of common plastics.

Plastic polymers such as polyethylene terephthalate, or PET, are made from simple monomer building blocks that are linked together via ester bonds, hence the name polyesters. Most monomers are extracted from petroleum, although more recent developments have seen building blocks produced directly from plants. Petroleum based monomers are very cheap because of low oil prices, and it is therefore often cheaper to manufacture virgin-PET than to use recycled material. PET also suffers from down-cycling, and in the case of single-use plastic bottles, only a small percentage will be turned back into new plastic bottles. A reduction in chemical properties results in most recycled PET being used for clothing fibres, eventually reaching an end-of-cycle use as fillings or carpet. From these low value products, there is little financial incentive to recycle further and much ends up in landfill or is incinerated. While burning plastic can be used to generate electricity, this practice contributes to greenhouse gases with the release of carbon dioxide. Of course, any recycling process can only take place when there is a proper infrastructure for the collection and treatment of waste; infrastructure that is severely lacking in many parts of the world. The consequence is that much of the plastic that is not dumped into landfill or incinerated will eventually find its way into rivers and oceans, feeding the already giant plastic-waste islands from the gyres created by global ocean currents. We must reduce our reliance on single-use plastic, and develop better collection and recycling methods that are truly circular and sustainable.

In 2016, a team of scientists in Japan published an exciting research paper describing the discovery and isolation of a strain of bacteria, *Ideonella sakaiensis*, which has the remarkable ability to survive on a diet of PET<sup>1</sup>. It was



Figure 2: Some of the team that solved the PETase crystal structure on I23 – Armin Wagner, John McGeehan, Mark Allen, Ramona Duman and Kamel El-Omari.

shown that these bacteria secreted two enzymes that can break apart the ester bonds holding the PET monomers together, providing a food and energy source for the growing organisms. This study highlights the diversity of bacteria and shows how they can adapt to new substrates, even man-made materials. Given that PET has only been in the environment for around 60 years, it is incredible that these bacteria have evolved to tackle this difficult material in such a short timeframe. The big questions for us were: how did these enzymes evolve, how do they work, and can we utilise them as part of a recycling solution?

In addition to researchers at the Centre for Enzyme Innovation at the University of Portsmouth, we worked across multiple scientific disciplines and countries with teams led by Dr Gregg Beckham at the National Renewable Energy Laboratory, Colorado, Dr Lee Woodcock at the University of South Florida, Tampa, Dr Munir Scaf at the University of Campinas, Sao Paulo, Brazil and Dr Armin Wagner at Diamond Light Source, UK (Fig. 2). We were able to produce and isolate the enzyme in our laboratories, follow the digestion of PET plastic directly from a single-use drinks bottle over several days, and measure the production of the monomer building blocks being produced.

Utilising the exceptional I23 beamline at Diamond, not only could we solve the structure of the PETase enzyme from native crystals, but we could collect a very high-resolution structure extending to 0.9 Å (Fig. 3)<sup>2</sup>. This provided initial structural insights, and we employed computer modelling to further understand how this enzyme binds to PET and breaks the ester-bonds. We found that the enzyme has a similar shape to a family of naturally occurring enzymes called cutinases. Cutin is a natural polyester found in plants and forms a protective and waterproof barrier that can be observed by simply running

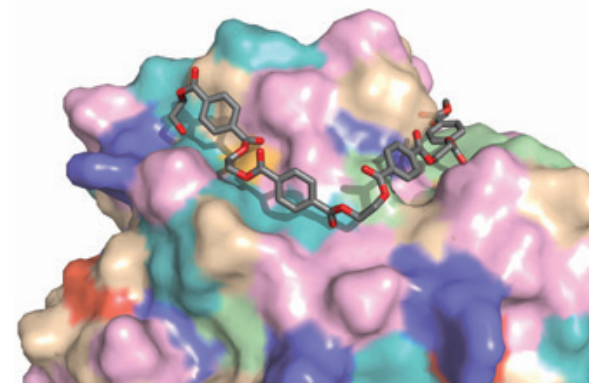


Figure 3: The PETase enzyme structure is shown bound to a polymer of PET plastic. Image credit: H.L. Woodcock.

broccoli under the tap. This waxy layer is also made of monomers that are linked together by ester bonds, thus bacteria have been evolving polyester-degrading enzymes to invade plant cells for millions of years. We were interested to see if we could turn PETase back to an ancestral cutinase by changing the DNA sequence. To our surprise, rather than reduce PET-degrading activity, we actually improved it. While only a modest increase, this does indicate that PETase has the potential to be further engineered to be faster and more efficient at digesting PET. This opens up the exciting possibility of turning polyester plastics back to monomers so that they can be directly reused for new plastic bottles or even upcycled to improved materials.

We now need to engineer an even faster enzyme and produce it at large scale. Fortunately, the technology exists, and there are many large industrial companies that have the capacity to generate large quantities of enzymes. Examples include those currently used in biological washing powders, biofuels production, and food and drink manufacturing. We are now working in partnership between academia and industry to provide us with the best chance of reaching a real-world solution. We must be mindful though that any real solution will involve a reduction in our reliance on plastics by innovative alternatives and implementation of a global recycling infrastructure. Responsibilities lie with both industry and consumers, and now that we are acutely aware of the problem, we can all play a positive role in reducing our environmental impact and developing solutions.

### References:

- Yoshida S. *et al*; A bacterium that degrades and assimilates poly(ethylene terephthalate). *Science* (80-. ). **351**, 1196–1199 (2016). DOI: 10.1126/science.aad6359
- Austin H. P. *et al*. Characterization and engineering of a plastic-degrading aromatic polyesterase. *Proc. Natl. Acad. Sci.* **115**, E4350–E4357 (2018). DOI: 10.1073/pnas.1718804115

### Funding acknowledgment:

BBSRC (BB/P011918/1); National Renewable Energy Laboratory (NREL); US DOE Office of Energy Efficiency and Renewable Energy. US National Science Foundation; University of Portsmouth.

### Corresponding author:

Prof John McGeehan, University of Portsmouth, john.mcgeehan@port.ac.uk

## Insc:LGN tetramers revert breast cancer stem cell expansion by promoting asymmetric cell divisions

**Related publication:** Culurgioni S., Mari S., Bonetti P., Gallini S., Bonetto G., Brennich M., Round A., Nicassio F. & Mapelli M. Insc:LGN tetramers promote asymmetric divisions of mammary stem cells. *Nat. Commun.* **9**, 1025 (2018). DOI: 10.1038/s41467-018-03343-4

**Publication keywords:** Mammary stem cells; Cell divisions; Asymmetric fate

In stem cells, asymmetric cell division (ACD) generates two distinct cells: a stem cell, and a cell committed to differentiate. Defects in this delicate and extremely coordinated process can cause cell over-proliferation and cancer. How stem cell ACDs are executed remains largely unclear. The knowledge of the architecture of key ACD players constitutes a remarkable advance in the understanding of the operational principles of asymmetric divisions. An international research group determined the three-dimensional structure of the Insc:LGN complex, which revealed that oligomerisation and clustering of LGN (spindle orientation protein) and Insc are essential for ACDs.

To obtain an optimal structural characterisation of this complex, several tens of crystals obtained in different conditions were tested on the Macromolecular Crystallography (MX) beamlines I04 and I04-1, but only two diffracted to 3.4 Å and 4.0 Å resolution. The final combination of the two datasets allowed the structural determination. The group showed that LGN forms intertwined tetramers with Insc, which are markedly stable. Most importantly, in mammary stem cells, the tetrameric molecular assembly suffices to promote asymmetric cell divisions, and reverts the over-proliferation caused by loss of the tumour suppressor gene p53.

Stem cells are characterised by two unique properties: (I) the ability of engendering all differentiated cell types, and (II) the capacity of self-renewal through several rounds of cell divisions keeping an undifferentiated state. Specifically, stem cells divide asymmetrically, generating a daughter stem cell (identical to the mother) attached to the maternal niche, and a daughter cell inclined to relocate and differentiate. This asymmetric cell division (ACD) requires the spatial coordination between the division plane and cell polarity cues. The current view is that cell polarity is established by Par proteins (Par3:Par6:aPKC) at the apical site, while the division plane is defined by the position of the mitotic spindle regulated by the Gcc:LGN:NuMA spindle orientation complex. The protein Inscuteable (Insc) links these two cellular processes as a result of its concomitant binding to Par3 and LGN.

Initial structural characterisation of the LGN TPR-domain (LGN<sup>TPR</sup>) in complex with a 35-residue Insc peptide (Insc<sup>PEPT</sup>), showed that the association is mutually exclusive with NuMA, and revealed a nanomolar binding affinity<sup>1</sup>. However, no information was available for the entire operational domain of Insc, which is able to recapitulate all its functions in stem cell divisions (the so-called asymmetric domain, Insc<sup>ASYM</sup>). Therefore, we set out to determine the structure of the LGN<sup>TPR</sup>:Insc<sup>ASYM</sup> complex, which would constitute a valuable advance in the understanding of the molecular principles of asymmetric cell division and stem cell replication, with substantial implications for cancer.

The *Drosophila melanogaster* LGN<sup>TPR</sup> and Insc<sup>ASYM</sup> polypeptides were coexpressed in bacteria and purified as a 2:2 stoichiometry complex with an experimentally measured mass of 180 kDa (Fig. 1a). After the identification of the first crystal hits, extensive efforts dedicated to the optimisation of the crystallisation condition yielded plate-shaped crystals diffracting to 3.3–4.0 Å. Despite the low resolution, the good data quality and the consistency across the whole data collection resulted in high redundancy datasets, and permitted the generation of electron density maps that were suitable for structure determination. The overall architecture of the LGN<sup>TPR</sup>:Insc<sup>ASYM</sup> complex consists of an intertwined hetero-tetramer, where each Insc chain contacts one TPR domain (LGN-A) through its Insc<sup>PEPT</sup> region, and the other (LGN-B) with its four-helix bundle. The final portion of each Insc<sup>ASYM</sup> is organised in Armadillo repeats that contact one another, further stabilising the assembly (Fig. 1b and 1d). The two TPR domains are complementarily juxtaposed in a head-to-head interaction, forming a cylinder

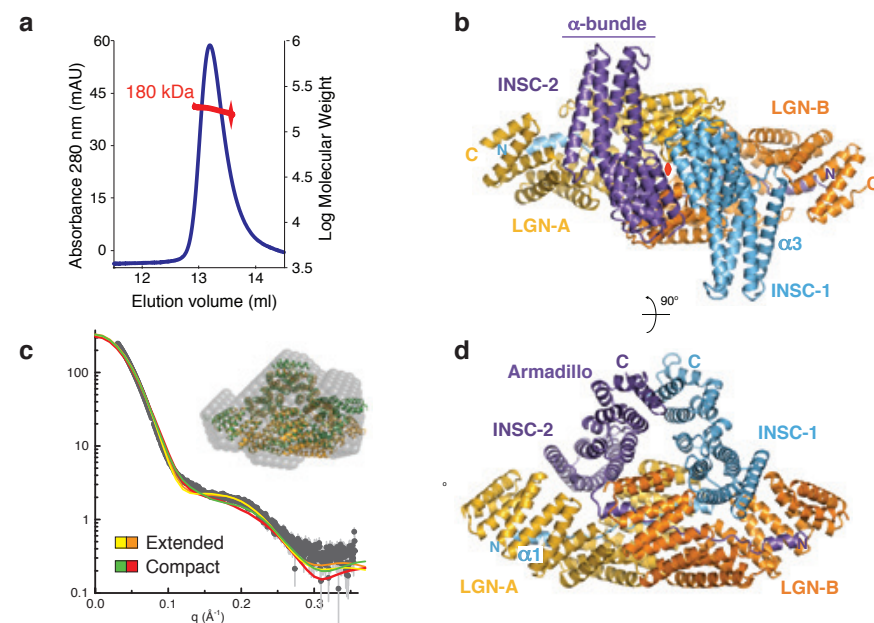


**Figure 1:** Structure of *Drosophila* LGN<sup>TPR</sup>:Insc<sup>ASYM</sup> complex. (a) Static-Light-Scattering profile of the LGN<sup>TPR</sup>:Insc<sup>ASYM</sup> tetramer. (b-d) Cartoon representation of the LGN<sup>TPR</sup>:Insc<sup>ASYM</sup> tetramer in two orthogonal orientations. The two protomers of LGN<sup>TPR</sup> are coloured gold and orange, while the two Insc<sup>ASYM</sup> copies are in cyan and purple. The two-fold symmetry axis of the tetramer is marked as a red oval in b. (c) SAXS data of the *Drosophila* LGN<sup>TPR</sup>:Insc<sup>ASYM</sup> complex, and *ab initio* model of the SAXS-derived envelope superposed to the crystallographic structures of extended and compact tetramers.

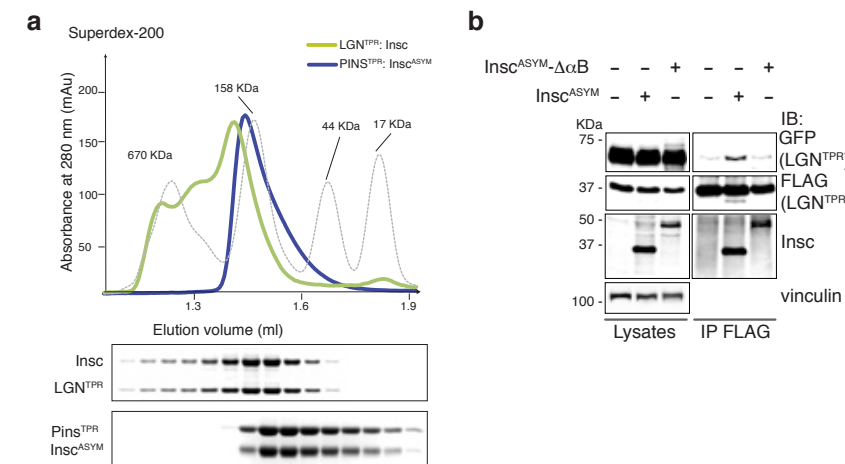


**Figure 2:** Human LGN:Insc complex oligomerisation. (a) SEC elution profiles of *Drosophila* LGN<sup>TPR</sup>:Insc<sup>ASYM</sup> (blue trace) and human LGN<sup>TPR</sup>:Insc (green trace) with associated Coomassie-stained SDS-PAGE separations of peak fractions. The elution profile of globular markers is reported as a dashed gray line. (b) Immunoprecipitation experiments (IPs) from HEK293T cells transfected with human GFP-LGN<sup>TPR</sup> and FLAG-LGN<sup>TPR</sup> alone or in combination with human Insc<sup>ASYM</sup> or Insc<sup>ASYM</sup>:ΔαB (lacking residues 62–191). IPs with anti-FLAG antibodies were immunoblotted (IB) with the indicated antibodies. FLAG-LGN<sup>TPR</sup> co-immunoprecipitates with GFP-LGN<sup>TPR</sup> only when bound to Insc<sup>ASYM</sup>, but not to Insc<sup>ASYM</sup>:ΔαB.

open on one side; the cylinder is closed by the Insc helix bundle, increasing the steadiness of the complex.

The LGN<sup>TPR</sup>:Insc<sup>ASYM</sup> tetramers are present in the crystals in two slightly different conformations: one is extended and symmetric, and the other is slightly more compact and asymmetric. Small Angle X-ray Scattering (SAXS) analyses indicated that the LGN<sup>TPR</sup>:Insc<sup>ASYM</sup> complex in solution is flexible and can acquire both conformations (Fig. 1c, the extended and compact tetramers are shown in yellow and green ribbons respectively, and fitted into the SAXS envelope). We speculate that this intrinsic structural plasticity of LGN<sup>TPR</sup>:Insc<sup>ASYM</sup> might be functional to the scaffolding role of the complex at the plasma membrane, which is intrinsically flexible.

The human LGN<sup>TPR</sup> and Insc<sup>ASYM</sup> counterparts were coexpressed in insect cells and in mammalian cells, but the poor yield did not enable any structural characterisation. Size-exclusion chromatography analyses of the human purified LGN<sup>TPR</sup>:Insc complex agreed with a 2:2 stoichiometry (Fig. 2a). In addition, the ability of human LGN to pull down another copy of LGN only in presence of Insc<sup>ASYM</sup> demonstrated that the hetero-tetrameric assembly observed in flies is conserved in humans (Fig. 2b). The 2:2 stoichiometry of the LGN:Insc assembly is lost when the region encompassing the four-helix bundle of human Insc is deleted (Fig. 1b), confirming that this region is essential for oligomerisation (and not for LGN association).

To determine the functional relevance of the Insc<sup>ASYM</sup>-dependent LGN oligomerisation for stem cell asymmetric divisions, we analysed the ectopic expression of different constructs of Insc in murine mammary stem cells (MaSCs) depleted of the tumour suppressor gene p53 (p53-KO). Notably, p53-KO MaSCs show low Insc expression, and replicate abnormally through cycles of symmetric divisions, causing over-proliferation<sup>2</sup>. Restoring Insc expression in p53-KO MaSCs increases the number of ACDs (Fig. 3a), and consistently

decreases the number of mammospheres formed in sphere-forming assays (Fig. 3b). Notably, the Insc region encompassing the ASYM domain is sufficient to reduce the sphere-forming efficiency, while the the Insc<sup>ASYM</sup> domain lacking the four-helix-bundle, and forming a 1:1 complex with LGN, is not (Fig. 3b). These results clearly demonstrate that the oligomerisation of Insc<sup>ASYM</sup> with LGN is essential for the asymmetric functions of Insc in stem cell divisions.

Conclusively, the crystallographic structure of the LGN<sup>TPR</sup>:Insc<sup>ASYM</sup> complex revealed a stable hetero-tetrameric assembly with intertwined architecture, which is conserved throughout evolution. The steadiness of the LGN:Insc structural organisation suggests that the association of LGN with Insc is constitutive, and that the LGN:Insc interaction promotes asymmetric fate specification without exchanging with the NuMA-bound pool of LGN that associates with the microtubule motor dynein. Most importantly, the LGN:Insc structure revealed that the tetrameric organisation of the complex is essential to promote asymmetric divisions of mammary stem cells, and suffices to revert aberrant stem cell over-proliferation caused by p53 loss, with important therapeutic implications.

### References:

- Culurgioni S. *et al.* Inscuteable and NuMA proteins bind competitively to Leu-Gly-Asn repeat-enriched protein (LGN) during asymmetric cell divisions. *Proc. Natl. Acad. Sci.* **108**, 20998–21003 (2011). DOI: 10.1073/pnas.1113077108
- Cicalese A. *et al.* The Tumor Suppressor p53 Regulates Polarity of Self-Renewing Divisions in Mammary Stem Cells. *Cell* **138**, 1083–1095 (2009). DOI: 10.1016/j.cell.2009.06.048

### Funding acknowledgement:

Italian Foundation for Cancer Research (AIRC) (IG18692, IG14085); Italian Ministry of Health (RF-2013-02357254); BioStruct-X (FP7/2007-2013, grant agreement N°283570).

### Corresponding authors:

Dr Marina Mapelli, European Institute of Oncology, marina.mapelli@ieo.it and Dr Simone Culurgioni, Exscientia, sculurgioni@exscientia.co.uk

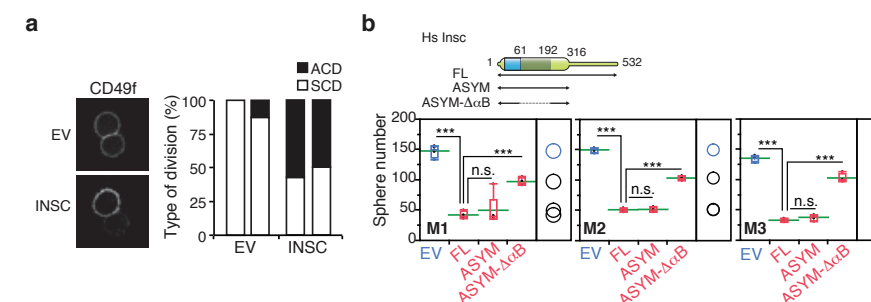


**Figure 3:** Insc promotes asymmetric cell divisions of murine mammary stem cells. (a) Quantification of the division mode of mammary epithelial cells isolated from p53-KO mice evaluated by pair-cell assay. Cells were infected with empty lentivirus (EV) or virus expressing full-length Insc (INSC) and imaged after the first division by staining with the CD49f surface marker of the mammary basal lineage. (b) Sphere-forming assays performed with p53-KO mammospheres infected with empty lentivirus (EV) or viruses expressing Insc (FL), Insc<sup>ASYM</sup> (ASYM), or Insc<sup>ASYM</sup>:ΔαB. The sphere-forming efficiency (SFE) was quantified over three subsequent passages M1–M2–M3.

## Toward remote control of an 'undruggable' dynamic enzyme with structure-based fragment screening

**Related publication:** Keedy D. A., Hill Z. B., Biel J. T., Kang E., Rettenmaier T. J., Brandão-Neto J., Pearce N. M., von Delft F., Wells J. A. & Fraser J. S. An expanded allosteric network in PTP1B by multitemperature crystallography, fragment screening, and covalent tethering. *eLife* 7, e36307 (2018). DOI: 10.7554/eLife.36307

**Publication keywords:** X-ray crystallography; Allostery; Phosphatase; Fragment screening; Allosteric inhibition; Multiconformer modelling; Multitemperature crystallography

**M**any treatments for human diseases use small-molecule drugs that target protein molecules. It is sometimes quite difficult to target the active site within the protein (or 'business end') with such molecules. An international team of researchers set out to find new sites on a particular medically promising protein - PTP1B - where drug-like small molecules might bind and alter how the protein behaves, with the longer-term goal of treating diseases such as diabetes and breast cancer.

Their goal was to expose the protein of interest, called PTP1B, to nearly 2,000 small molecules, and to use X-ray crystallography to learn which parts of PTP1B are most prone to having molecules bind to them. They used the automated XChem fragment screening facility on beamline I04-1, followed by computer-based analysis to process the large amount of data collected during this work.

Their research at Diamond Light Source identified dozens of small-molecule fragments that stick to various 'hot spots' that are surprisingly widespread throughout the surface of PTP1B. Excitingly, the hot spots with the most fragments coincided with promising hot spots that had also been identified by a different, complementary approach to X-ray crystallography. The hope is that these fragments can later be stitched together into a more potent drug-like molecule.

Proteins are dynamic molecules whose motions are important for their biological functions. In allostery, for example, protein motions between alternative conformations can propagate a signal from one part of a protein structure to another part where it can affect structure, dynamics, and function. Because protein energy landscapes are complex and inevitably give rise to alternative conformations, allostery is increasingly thought to be a property of potentially all proteins<sup>1</sup>. However, allostery remains incompletely understood, in part because we lack structural biology approaches that allow us to interrogate how different parts of a protein structure are 'wired' together, and which surface sites can act as inputs to this wiring network by binding small-molecule allosteric modulators.

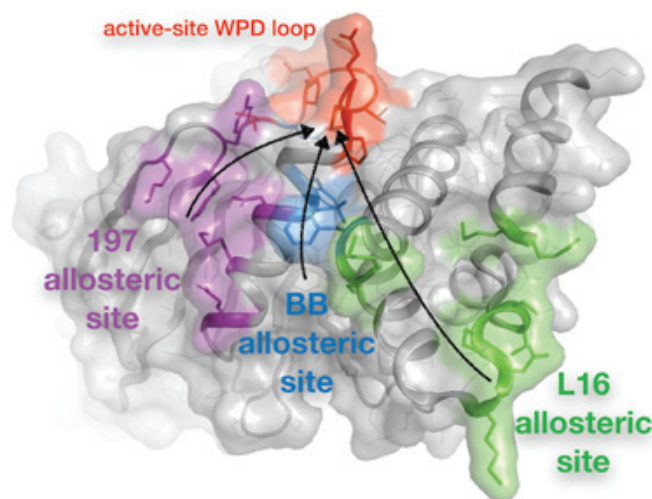


**Figure 1:** An expanded allosteric network in PTP1B. Multitemperature crystallography and multiconformer modelling of the apo protein revealed one previously reported allosteric site, the BB site (blue), as well as two new allosteric sites, the 197 site (purple) and the L16 site (green). Each site is thought to allosterically communicate via conformational motions (arrows) with the dynamic WPD loop that is adjacent to the active site (red).

Protein Tyrosine Phosphatase 1B (PTP1B) exemplifies the opportunities associated with an improved understanding of the physical mechanisms of allostery. PTP1B is a highly validated drug target for several diseases, most notably diabetes and obesity<sup>2</sup>, yet it remains difficult to target PTP1B's active site with small-molecule inhibitors because of specificity and bioavailability limitations, resulting in its reputation as 'undruggable'. Allosteric inhibitors could overcome these technical hurdles. However, despite some preliminary successes, such as a benzobromarone-based series of allosteric inhibitors<sup>3</sup> that was clinically abandoned, there have been no clinically approved allosteric inhibitors for PTP1B.

The work described here sought to identify new allosteric sites in PTP1B and small molecules that bind to them to modulate enzyme activity. Three primary methods were used. First, multitemperature crystallography of apo PTP1B was used to elucidate networks of residues with putatively energetically coupled alternative conformations, which could participate in allosteric communication. Second, and of most interest for this report, a high-throughput facility at Diamond was used to solve cocrystal structures of PTP1B bound to hundreds of different small-molecule fragments, to determine which surface sites are 'ligandable'. Third and finally, covalent tethering was used to increase the occupancy of molecules at an allosteric site to confirm a functional link to the active site. Each of these approaches and the associated results are discussed below, with particular emphasis placed on the work performed at Diamond.

The first part of this work, performed separate from Diamond, sought to elucidate the allosteric network inherent to unliganded PTP1B. To do so, multitemperature crystallography<sup>4</sup> – instead of the more traditional cryogenic-temperature crystallography – was used to reveal redistributions of electron density for particular residues as a function of temperature. Multiconformer modelling algorithms were then used to model the corresponding alternative conformations in atomic detail. Connecting the dots between the interacting, flexible residues in PTP1B revealed a substantial putative allosteric network that included three main allosteric sites (Fig. 1). One of these sites, the BB

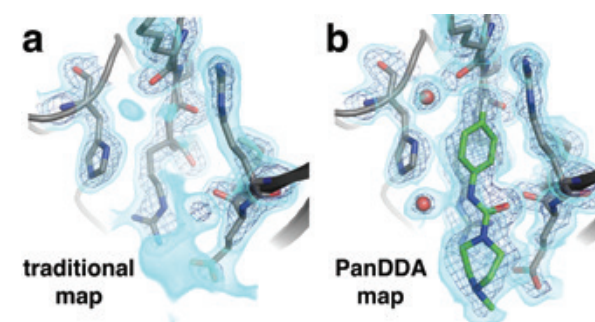


**Figure 2:** PanDDA analysis reveals low-occupancy allosteric fragments bound to PTP1B. (a) For one example fragment, a traditional  $2F_o - F_c$  map contoured at  $1.25\sigma$  (cyan volume) and at  $3.5\sigma$  (blue mesh) provides no clear evidence for a bound fragment; (b) By contrast, a background-subtracted PanDDA event map (85% background subtraction in this case) contoured at the same levels clearly reveals the precise pose of the bound fragment, plus additional ordered water molecules that accompany it (red spheres).

site, coincides with the binding site for the previously reported but abandoned allosteric inhibitor<sup>3</sup>. The other sites had not been identified previously, though similar regions were implicated by concurrent analyses based on Nuclear Magnetic Resonance (NMR) spectroscopy and mutagenesis.

Having identified putatively allosteric sites in PTP1B, the subsequent challenge was to test whether they were capable of binding small molecules that allosterically modulate enzyme activity. To tackle this challenge, first the 'ligandability' of each site was assessed using the new high-throughput XChem facility at Diamond for small-molecule fragment soaking, X-ray data collection, and structure determination. This facility was used to soak 1,966 apo crystals of PTP1B with small-molecule fragments, almost all of which were unique. Of these crystals, 1,774 yielded diffraction data that were successfully processed. These data were generally high-resolution: 65% were better than  $2.0\text{ \AA}$ . All of this was performed very efficiently, in less than two weeks.

Importantly, by virtue of their small size, small-molecule fragments typically bind at low occupancy, and are therefore often undetectable using traditional  $2F_o - F_c$  electron density maps (Fig. 2a). However, this work took advantage of the recently developed Pan-Dataset Density Analysis (PanDDA) algorithm<sup>5</sup>, which exploits large numbers of datasets, like those collected at XChem, to compute an average 'background' model for the unbound state and computationally subtract it, thus yielding a clear view of the low-occupancy bound state. For our PTP1B datasets, PanDDA yielded excellent density maps for low-occupancy fragment binding events (Fig. 2b) scattered across the protein surface; these binding events would not have been evident without this special analysis.

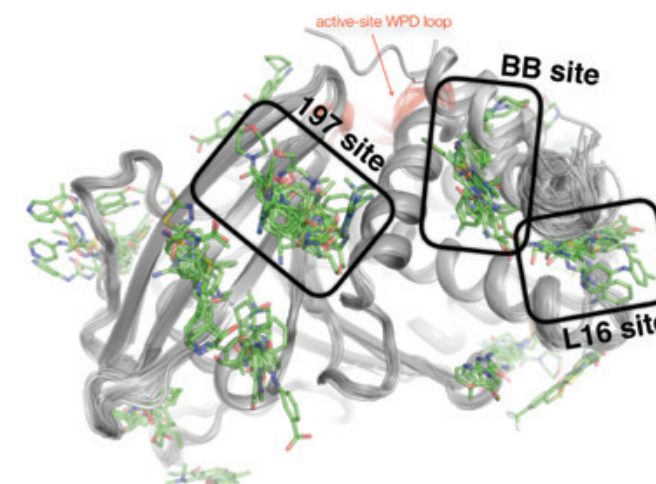


**Figure 3:** Overview of bound fragments across the PTP1B surface, including several fragment-binding hotspots: the 197 site, BB site, and L16 site. The view is similar to Fig. 1.

Overall, most fragments did not bind, as was expected given the naively constructed fragment library. However, using PanDDA, 110 of the 1,774 datasets yielded all-atom structures of PTP1B bound to unique small-molecule fragments. These fragments' binding sites were spread across the surface of PTP1B – but they clustered at three primary 'hot spots' (Fig. 3) which coincided remarkably well with the putative allosteric sites discovered by multitemperature crystallography of the apo enzyme (Fig. 1). This convergence was encouraging that these sites in PTP1B would perhaps be capable of binding potent allosteric inhibitors.

To separately validate the functional relevance of the putative allosteric sites identified by XChem fragment screening of PTP1B, a covalent tethering experiment was also performed outside of Diamond. One molecule, compound 2, significantly inhibited PTP1B catalysis ( $K_i$  of  $7.1 \pm 1.1\ \mu\text{M}$ ) when tethered to a K197C mutation at the new 197 allosteric site, confirming that at least this site is truly allosterically linked to the catalytic site.

Overall, this work pinpointed exciting new footholds for allosteric inhibition or 'remote control' of a daunting but promising therapeutic target, PTP1B. Future efforts can explore at least two avenues related to this work. First, the fragments identified here by XChem and PanDDA may be fruitfully linked and optimised into higher-affinity binders, which could yield potent allosteric inhibitors of PTP1B. Second, although the conformational heterogeneity underlying the allosteric network in apo PTP1B was identified via multitemperature crystallography at temperatures ranging from  $\sim 100\text{ K}$  to  $\sim 300\text{ K}$ , the XChem fragment screening of PTP1B described here which was used to validate that network was performed at cryogenic-temperature,  $\sim 100\text{ K}$ . Future work may productively combine aspects of both these approaches by performing room-temperature fragment screening. Such an approach could elucidate how the conformational motions underlying allostery in PTP1B are perturbed by binding of specific ligands at specific allosteric sites. Such work could also clarify whether ligand binding observed at cryogenic-temperature is still relevant at near-physiological temperature.

### References:

- Gunasekaran K. *et al.* Is allostery an intrinsic property of all dynamic proteins? *Proteins Struct. Funct. Bioinforma.* **57**, 433–443 (2004). DOI: 10.1002/prot.20232
- Elchebly M. *et al.* Increased Insulin Sensitivity and Obesity Resistance in Mice Lacking the Protein Tyrosine Phosphatase-1B Gene. *Science*. **283**, 1544–1548 (1999). DOI: 10.1126/science.283.5407.1544
- Wiesmann C. *et al.* Allosteric inhibition of protein tyrosine phosphatase 1B. *Nat. Struct. & Mol. Biol.* **11**, 730 (2004). DOI: 10.1038/nsmb803
- Keedy D. A. *et al.* Mapping the conformational landscape of a dynamic enzyme by multitemperature and XFEL crystallography. *eLife* **4**, e07574 (2015). DOI: 10.7554/eLife.07574
- Pearce N. M. *et al.* A multi-crystal method for extracting obscured crystallographic states from conventionally uninterpretable electron density. *Nat. Commun.* **8**, 15123 (2017). DOI: 10.1038/ncomms15123

### Funding acknowledgement:

A.P. Giannini Foundation (Postdoctoral Fellowship).

### Corresponding authors:

Prof Daniel A. Keedy, CUNY Advanced Science Research Center, daniel.keedy@asrc.cuny.edu and Zachary B. Hill, University of California, San Francisco, zachary.hill@ucsf.edu

## Parkinson's: Completing the Parkin activation puzzle

**Related publication:** Gladkova C., Maslen S. L., Skehel J. M. & Komander D. Mechanism of parkin activation by PINK1. *Nature* **559**, 410–414 (2018). DOI: 10.1038/s41586-018-0224-x

**Publication keywords:** Ubiquitin; Parkinson's disease; Parkin; E3 ligase; PINK1; Mitophagy

**A**lthough Parkinson's disease is the second most common neurodegenerative disorder, current diagnosis is subjective and there is no cure. Studying inherited, young-onset forms of the disease has helped to identify defective cellular processes that give rise to disease symptoms. Understanding these could help design more effective diagnostic tools or therapeutic strategies.

Parkin is an enzyme commonly defective in inherited forms of Parkinson's disease. To maintain cellular health, Parkin attaches a small protein to damaged mitochondria, marking them for degradation. Although stabilising the active form of Parkin could form the basis of therapy, this state has evaded structural characterisation. Researchers therefore set out to capture the structure of active Parkin, using the Microfocus Macromolecular Crystallography (MX) beamline (I24), as their best crystals only reached 40 µm in two of the dimensions.

They found that dramatic structural rearrangements occur upon Parkin activation on damaged mitochondria, and identified a novel element essential for full Parkin activation. Being able to compare the active Parkin structure with previously resolved inactive forms is the first step to designing novel Parkinson's disease therapies.

Although the work described here provides the final piece of the Parkin activation conundrum, Diamond Light Source has been instrumental in understanding the whole mechanism. This research group and others have previously resolved inactive Parkin states on beamlines I04 and I02 (highlighted in the 'Insights into Parkinson's disease from crystal structures of Parkin' article in the Diamond Light Source Annual Review 2015/16).

Parkinson's Disease (PD) is the second most common neurodegenerative disorder; it is characterised by neuronal loss and a subsequent decrease of dopamine levels in the brain. While most cases of PD arise sporadically, 10% of patients carry mutations giving rise to a young-onset inherited form of the disease. Among genes mutated in young-onset PD are the kinase PINK1 and the E3 ubiquitin ligase Parkin, an enzyme which attaches the small signalling protein ubiquitin (Ub) to substrates. In cells PINK1 and Parkin orchestrate clearance of damaged mitochondria by a specialised form of autophagy, known as mitophagy<sup>1</sup>.

Under resting conditions, PINK1 is continuously turned-over, while Parkin resides in the cytosol. Previous structural work by others and us has explained how the activity of cytosolic Parkin is restrained by several autoinhibitory elements. To induce mitophagy, PINK1 is stabilised on the outer mitochondrial

membrane of damaged mitochondria and phosphorylates Ub as its first substrate. Mitochondrially anchored phosphorylated Ub (phospho-Ub) binds to Parkin and triggers Parkin translocation to the damaged organelles. There, the N-terminal Ub-like (Ubl) domain of Parkin becomes a second substrate for PINK1. Only phosphorylated Parkin is fully active, although the nature of the Parkin rearrangement upon phosphorylation remained a key unanswered question in the field<sup>1</sup>.

Before transferring Ub to mitochondrial substrates, Parkin receives an activated Ub-molecule onto its active site Cys residue from an upstream E2 Ub-conjugating enzyme. However, in cytosolic Parkin the conserved binding site for the E2 enzyme is blocked and the catalytic Cys is buried in a hydrophobic interface between the catalytic RING2 domain and the unique Parkin domain (UPD), (Fig. 1a). To enable E2 binding the Repressor Element of Parkin (REP) and

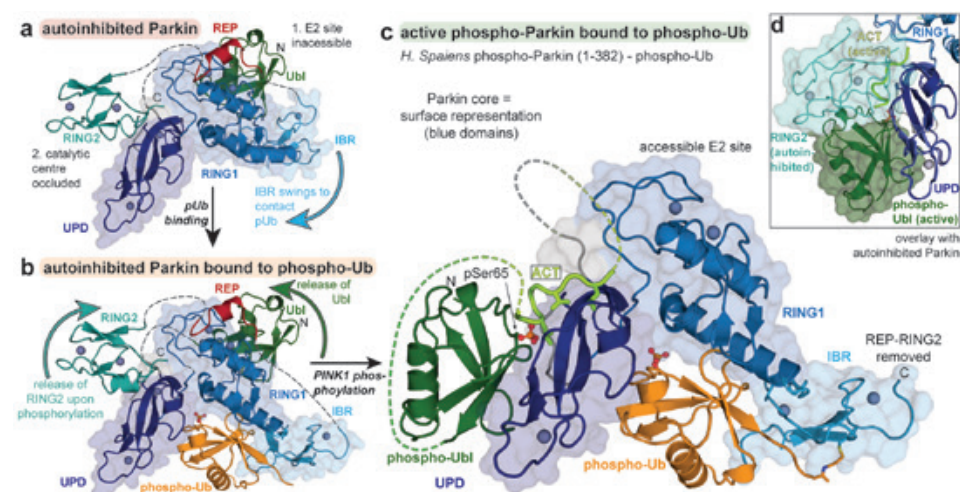


**Figure 1:** Completing the structural picture of Parkin activation. a) Autoinhibited Parkin, PDB ID: 5C1Z<sup>2</sup>. The surface of core Parkin domains (blue) is shown. The positions of the Ubl (green), REP (red) and RING2 (cyan) domains disable Ub transfer; b) Autoinhibited Parkin bound to phospho-Ub (orange), PDB ID: 5N2W<sup>3</sup>. Although core Parkin domains rearrange to bind phospho-Ub, autoinhibitory elements persist; c) Active phospho-Parkin bound to phospho-Ub, PDB ID: 6GLC. The phospho-Ubl and ACT (light green) displace the catalytic RING2 domain, thus activating Parkin; d) An overlay between b) and c) showing surface of the phospho-Ubl and RING2 domains, coloured as above.

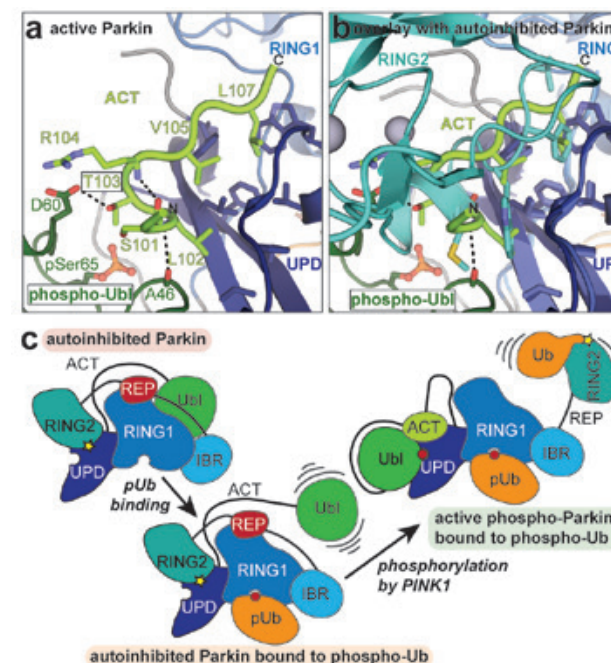


**Figure 2:** Activating Parkin. a) The ACT linchpin (light green) stabilises the new activating Parkin interface by contacting both the UPD (dark blue) and the phospho-Ubl domain (green); b) Overlay with autoinhibited Parkin (PDB ID: 5N2W<sup>3</sup>) shows how the ACT mimics autoinhibitory interactions between the catalytic RING2 domain (cyan) and the UPD domain to activate Parkin; c) A schematic representation of the Parkin activation cascade, domains coloured as above.

the N-terminal Ubl domain must be displaced from their autoinhibitory binding sites. Furthermore, release of the catalytic Cys residue requires a large-scale rearrangement where the catalytic RING2 domain is entirely displaced from its autoinhibitory binding site on the UPD<sup>2,3</sup>.

Our group has previously reported a structure of Parkin bound to phospho-Ub<sup>4</sup>. While phospho-Ub binding mediates Parkin translocation to mitochondria and primes Parkin for phosphorylation, most autoinhibitory elements remain intact (Fig. 1b). Helix straightening necessary to create an optimised phospho-Ub binding site weakens the autoinhibitory Ubl interface. The Ubl is therefore released upon phospho-Ub binding and becomes accessible for phosphorylation. Despite these rearrangements, the resolved complex of Parkin bound to phospho-Ub remains inactive, as the catalytic Cys residue remains buried and the REP remains in place<sup>4,5</sup>.

Although previous Parkin structures do not capture the active state of the enzyme, they provide a structural basis for many disease-linked mutations. Intriguingly, some mutations could not be explained to date as they likely disrupt the unknown active state. Among these are mutations of a phosphate-binding pocket previously identified on the UPD as well as mutations in a linker region between the Ubl domain and the rest of Parkin. Although partially conserved, this linker region had previously been omitted from analysis due to its intrinsic flexibility.

Dynamic and proteolytic studies suggested that upon activation, the catalytic RING2 domain is released and the catalytic Cys becomes accessible, consistent with a fully active state of Parkin. To overcome the difficulties of crystallising full-length activated phospho-Parkin with a flexible RING2 domain, a cleavage site within the protein was designed so that the flexibly linked RING2 can be removed following activation by PINK1 phosphorylation *in vitro*.

The 1.8 Å structure of human phospho-Parkin(ΔRING2), determined from data collected at the Microfocus MX beamline, finally revealed the extensive domain rearrangements required to release the catalytic domain from its autoinhibitory position and enable Parkin activity (Fig. 1c). While the core domains remained unperturbed upon phosphorylation, the phospho-Ubl domain shifted by over 50 Å compared to previous structures. In the activated

form of the protein, the phospho-Ubl binds to a new activating interface, which partially overlaps with the previously observed RING2 autoinhibitory binding site (Fig. 1d). Simultaneous binding of both domains is sterically impossible. In a carefully balanced system, intramolecular binding of the phospho-Ubl, therefore, displaces the catalytic RING2 domain to activate phospho-Parkin. The phosphorylated residue in the Ubl is placed in the mutation-lined phosphate pocket on the UPD, elucidating the basis of active-state specific pathogenic Parkin mutations.

Most strikingly, a conserved portion of the linker region which follows the N-terminal Ubl domain could be resolved. Since mutation or deletion of the region led to severely diminished Parkin activity, we termed the conserved region the Activating Element of Parkin (ACT). The ACT binding mode mimics the interactions which keep the RING2 domain in its autoinhibitory position (Fig. 2a,b). The amphipathic nature of the ACT allows insertion of hydrophobic residues into the groove of the UPD, while polar residues contact the phospho-Ubl domain, stabilising the novel activating interface. Interestingly, Arg104, which electrostatically interacts with the phospho-Ubl, is mutated in patients suffering from young-onset PD.

Our structure contributes the last missing piece of the Parkin activation cascade. Only now can we fully appreciate the scale of domain rearrangements necessary to activate Parkin specifically on the surface of damaged mitochondria (Fig. 2c). Initially, Parkin adopts an almost serpentine arrangement, where regions linking Ubl and catalytic RING2 domains to the Parkin core cross over to enable the domains to adopt their autoinhibitory positions. Upon phospho-Ub binding, the Ubl domain is released for phosphorylation by PINK1, although the catalytic RING2 domain remains sequestered. Upon phosphorylation the phospho-Ubl domain together with the ACT element liberate the catalytic RING2 domain, enabling Ub transfer activity and completely unravelling Parkin.

Now that the relevant Parkin states have been structurally characterised, it is clear that structural facets unique to the active state exist and could be exploited translationally. Modulating Parkin conformations by designing conformation-specific molecules might benefit PD sufferers in the future.

### References:

- Harper J. W. *et al.* Building and decoding ubiquitin chains for mitophagy. *Nat Rev Mol Cell Biol.* **19**, 93–108 (2018). DOI: 10.1038/nrm.2017.129
- Wauer T. *et al.* Structure of the human Parkin ligase domain in an autoinhibited state. *EMBO J.* **32**, 2099–2112 (2013). DOI: 10.1038/emboj.2013.125
- Kumar A. *et al.* Disruption of the autoinhibited state primes the E3 ligase parkin for activation and catalysis. *EMBO J.* **34**, 2506–2521 (2015). DOI: 10.15252/emboj.201592337
- Wauer T. *et al.* Mechanism of phospho-ubiquitin-induced PARKIN activation. *Nature* **524**, 370–374 (2015). DOI: 10.1038/nature14879
- Kumar A. *et al.* Parkin-phospho-ubiquitin complex reveals cryptic ubiquitin-binding site required for RBR ligase activity. *Nat. Struct. Mol. Biol.* **24**, 475–483 (2017). DOI: 10.1038/nsmb.3400

### Funding acknowledgement:

Access to Diamond Light Source was supported in part by the EU FP7 infrastructure grant BIOSTRUCT-X (contract no. 283570).

Work at the Komander laboratory was supported by the Medical Research Council (U105192732), the European Research Council (724804), the Michael J. Fox Foundation and the Lister Institute for Preventive Medicine.

### Corresponding authors:

Christina Gladkova, MRC Laboratory of Molecular Biology, gladkova@mrc-lmb.cam.ac.uk and Dr David Komander, Walter and Eliza Hall Institute of Medical Research, dk@wehi.edu.au

## Biological Cryo-Imaging Group

Martin Walsh, Deputy Director of Life Sciences

**The Biological Cryo-Imaging Group was established a little over a year ago and brings together dedicated facilities for X-ray, light and electron microscopy at Diamond. The bending magnet B24 is the source of X-rays for the full field cryo-transmission X-ray microscope dedicated to biological X-ray imaging. The beamline has also established a cryo-super resolution fluorescence microscopy facility, which is a joint venture between Diamond and the University of Oxford. Exploiting electrons for imaging, the electron Biolmaging Centre (eBIC) is the national centre for cryo-Electron Microscopy (cryo-EM) in the UK and provides a range of capabilities and supporting facilities for cryo-EM. The first year of the Biological Cryo-Imaging Group at Diamond has been a busy one, with both B24 and eBIC developing and expanding their capabilities. This has meant installation, commissioning of new instrumentation, and a major focus on recruitment.**

The resolution revolution in cryo-EM has made a massive impact on the world of structural biology and this has, in no small part, been driven by detector developments, in particular direct electron detectors for which the first commercial products were made available in 2012. Improvements in detector frame rates, detection quantum efficiency and active area are being pursued by a number of groups both in academia and industry. At the end of 2018, eBIC upgraded two of its Titan Krios microscopes with the K3™ direct electron detector from Gatan, which has been keenly anticipated by the community at large. The K3™ detector has a 1.6 times bigger active area than its predecessor and can operate at 1,500 frames/second, an increase in throughput of 3.75 over the previous fastest detector on the market (the K2™, also from Gatan). The capabilities offered by these upgrades are already making a significant impact, as the increased frame rates allow shorter counting acquisition times leading to a two-fold increase in the number of movies collected per hour. This, in combination with the increased detector size of the K3, means that substantially more data can be collected in the same time than with the previous generation of detectors, maximising microscope output. The implementation of new data collection strategies, using the microscope image shift coils instead of stage movements to navigate between acquisition areas, have increased throughput further.

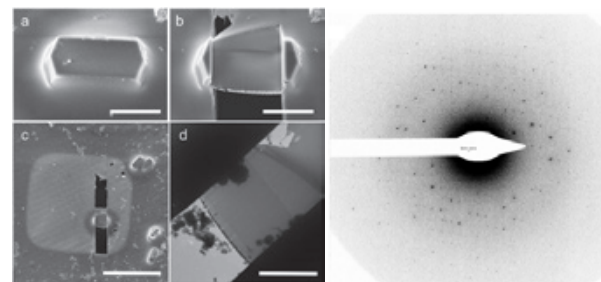


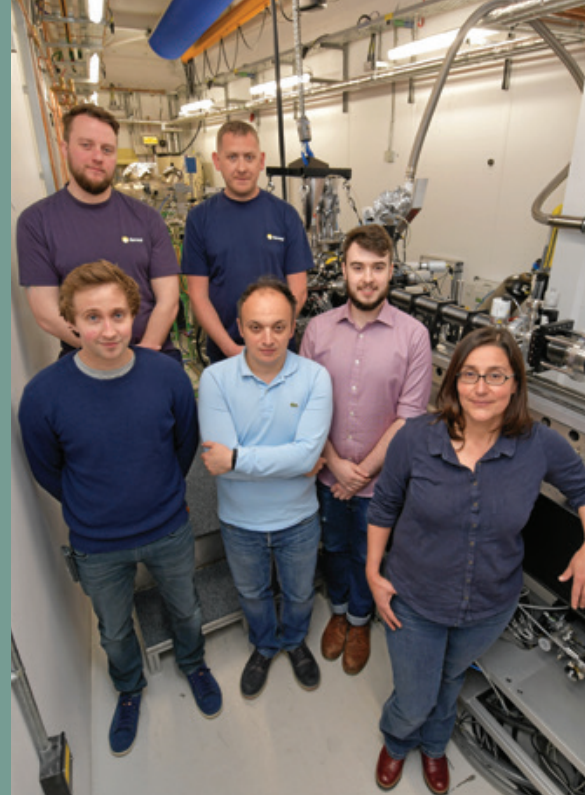
Figure 1: Micro Electron diffraction at eBIC. Left: Representative Images from the Scios™ cryo-FIB scanning electron microscope: (a) lysozyme crystal before milling and after (b, c). Transmission EM image of the milled Lamella (d). [Scale bars: a and b, 4 mm, c, 30 mm, d, 3 mm]. Right: An electron diffraction image from the lysozyme lamella. The edges of the image correspond to ~ 1.8 Å resolution.

eBIC has also been developing its capabilities for collecting electron diffraction data from micro-crystals (microED). Exploratory work in developing a user programme for microED is being carried out on the 200 kV Talos Artica cryo-TEM at eBIC. A highlight from this work during 2018 was the demonstration that thin lamella produced from Focused Ion Beam (FIB) milling of lysozyme crystals retained their crystallinity. The near-atomic resolution data collected showed that the milling did not disturb the very fine structure of the lamella<sup>1</sup>. Optimisation of the experimental setup and workflows for microED is ongoing. In late 2018, a new CetaD detector optimised for electron diffraction was installed. We hope to add microED to the offering to users within the next year.

The demand for access to high-end cryo-EM facilities has been a major driver for the rapid development and expansion of eBIC; in just over three years the facility has grown from offering a single high-end 300 kV Titan Krios transmission electron microscope to four fully operational Titan Krios<sup>®</sup> at the close of 2017. eBIC has hosted many users providing nearly 5,000 shifts at the end of AP24 resulting in 65 publications to date, of which over half are in journals with an Impact Factor >10. Although the majority of use has been for single particle cryo-EM, eBIC is developing an access route for cellular tomography and had its first commissioning call for users to access the Scios DualBeam™, a cryo-FIB scanning electron microscope early last year. This provided a mechanism for the first set of users to perform cryo-FIB milling of cells grown on EM grids to produce cellular lamella on the order of 100-200 nm thickness. The cryo-FIB milling sessions are linked to a cryo-Electron Tomography (cryo-ET) imaging session on one of the Titan Krios's thus allowing the users to prepare lamella from their cells grown on EM grids and then to carry out subsequent imaging with cryo-ET. A typical session currently takes up to five days. The workflows are time consuming and access to cryo-FIB milling is very limited with only a few EM centres around the world with the necessary infrastructure and expertise to drive developments forward. To underpin eBIC's commitment to providing peer reviewed access to this emerging technology, a second cryo-FIB scanning electron microscope – a Thermo Fisher Aquilos™, which has been designed specifically for FIB milling of biological samples, was delivered in March 2019 and is currently being commissioned for use with users. This will accelerate access and help build up expertise generally in the community for cellular tomography experiments.

Interest from industry in cryo-EM has also grown at a rapid rate. Access has been facilitated by the Industrial Liaison Office at Diamond, who have a strong track record in providing industry access to Diamond beamlines, in particular the suite of Macromolecular Crystallography (MX) beamlines. Thus, our first industry users followed shortly after the academic programme started in June 2015. The strong demand from industry led to the establishment in 2018 of an exciting new partnership between Diamond and Thermo Fisher Scientific to serve the needs of industry in parallel to our academic programme. This has enabled us to provide two new dedicated microscopes, a Thermo Fisher Scientific Krios G3i cryo-TEM and a 200 kV Glacios cryo-TEM. The industrial team at eBIC, together with embedded Thermo Fisher staff, will provide support and guidance to industrial researchers in sample preparation, cryo-EM sample screening, and high-end data collection. First users of the industry Titan Krios were welcomed in November 2018.

A full user programme was delivered from April 2018 at B24 and the interest from user groups continues to grow steadily (the beamline was heavily oversubscribed in the last call for proposals). The X-ray microscope has benefitted from the incorporation and full commissioning of a 25 nm zone plate which is currently available to users. The integration of a bespoke cryo-super resolution fluorescence module at B24 (an international first!) is also in high



B24 beamline team, from left to right: (Front) Matt Spink, Ilias Kounatidis, Maria Harkiolaki (PBS). (Behind) Adam Prescott, Adam Taylor, Thomas Fish.

demand and has been developed to offer both cryo-Structured Illumination Microscopy (cryo-SIM) and dSTORM. This allows a unique correlative imaging workflow, whereby B24 users first collect 3D fluorescence imaging data at optical resolutions beyond the diffraction limit. This allows areas of biological and chemical interest to be identified before the same sample is taken to the cryo-transmission X-ray microscope where 3D X-ray data can be taken on the same areas of interest and directly correlated with the existing 3D fluorescent microscopy data. The B24 team are working with the data analysis team at Diamond to improve tomographic reconstruction results, and with the developers of easy cell-correlative light to electron microscopy (eC-CLEM) an open source software for Correlative Light Electron Microscopy (CLEM) to improve correlative microscopy workflows to improve correlative workflows, which has led to a collaborative PhD project due to start in September 2019. Currently all fiducialised X-ray data is automatically processed into tomograms

allowing users to interactively evaluate samples and refine data collection strategies during their visit. All fluorescence data is also processed on site during data collection, and the focus is now on automation of data correlation across modalities.

Training for users continues to be a major activity at B24 and eBIC. At B24, a focus has been on hands-on sessions covering sample preparation, data collection, data processing and imaging data correlation. Software training at eBIC has been carried out in collaboration with CCP-EM, which has meant a busy schedule of basic and specialised courses in cryo-EM software such as Relion 3. The third instalment of eBIC's 'hands-on' training workshops in sample preparation for cryo-EM was again heavily oversubscribed and well received. This was complemented by focused training of eBIC users and Block Allocation Groups (BAGs).

Finally, looking to the future and the potential benefits and opportunities that will arise from the Diamond-II machine upgrade for imaging, were avidly discussed at a joint workshop between the Biolmaging and Imaging and Microscopy groups at Diamond. The workshop's aims were to introduce the scope of the Diamond machine upgrade, bring together experts in the field and Diamond users to identify key science areas that would benefit from the upgrade as a contribution to the development of the science case. The workshop provided a timely forum for experts and Diamond users to discuss the potential for upgrading existing instruments and the opportunities for new beamlines. Of particular interest for the Biolmaging community were discussions centred around the potential science drivers for a dedicated cryo-imaging beamline for biology, which would exploit cryo-ptychography, holography and fluorescence microscopy.

In summary, the Biolmaging group at Diamond continued to grow in 2018, as has the impact on biology of the user programme. We look forward to further expanding both our Biolmaging capabilities and their impact in 2019.

### Reference:

1. Duyvesteyn, H. M. E. *et al.* Machining protein microcrystals for structure determination by electron diffraction. *Proc Natl Acad Sci USA* **115**, 9569–9573 (2018). DOI: 10.1073/pnas.1809978115

“The first year of the Biological Cryo-Imaging Group at Diamond has been a busy one, with both B24 and eBIC developing and expanding their capabilities.”



Participants of the Diamond-II workshop 'Benefits & opportunities of the Diamond upgrade for Biological Cryo-Imaging and Imaging and Microscopy' held in September 2018.

## Unveiling RNA polymerase III transcription initiation with cryo-EM

**Related publication:** Abascal-Palacios G., Ramsay E. P., Beuron F., Morris E. & Vannini A. Structural basis of RNA polymerase III transcription initiation. *Nature* **553**, 301 (2018). DOI: 10.1038/nature25441

**Publication Keywords:** RNA Polymerase III; tRNAs; gene transcription; TFIIB

**R**NA polymerase (Pol) III is a major determinant of lifespan in eukaryotes (organisms whose cells have a nucleus enclosed within membranes, unlike bacteria). The level of Pol III transcription is tightly linked to the rate of growth, as it is known to play a role in cancer, and neurodegenerative diseases. A better understanding of the structure of Pol III could lead to new therapies for these diseases. However, Pol III is the most complex nuclear RNA polymerase.

A team of researchers from the Institute of Cancer Research in London used cryogenic electron microscopy (cryo-EM) at the electron Bio-Imaging Centre (eBIC) to obtain high-resolution maps of a core RNA Pol III pre-initiation complex, which is the minimum essential complex capable of faithfully initiating Pol III transcription *in vitro*.

Their results show that the transcription factor TFIIB recruits Pol III at its target genes and activates it to enable melting of the DNA - the initial process of gene transcription. This explains why Pol III transcription is so efficient. This work unravels the molecular mechanisms underlying the first stages of Pol III transcription, and the general conserved mechanisms of gene transcription initiation.

The eukaryotic nuclear genome is transcribed by the multisubunit enzymes RNA Polymerase (Pol) I, II and III, which catalyze DNA-dependent RNA synthesis. Pol III transcribes genes encoding short non-coding essential RNAs, such as the entire pool of transfer RNAs (tRNAs), the 5S ribosomal RNA (rRNA) and the spliceosomal U6 small nuclear RNA (snRNA). Pol III genes are essential in all cells and involved in fundamental processes such as ribosome and protein biogenesis, RNA processing, and protein transport. Pol III transcription is tightly co-regulated with Pol I activity, accounting together for up to 80% of nuclear gene transcription in growing cells<sup>1</sup>. Pol III activity influences TORC1-dependent lifespan in yeast, flies and worms and, given its conservation, it is likely to exert the same effect in vertebrates<sup>2</sup>. Pol III deregulation has been associated with a series of neurodegenerative diseases and with cancer onset<sup>3</sup>.

Pol III, with its 17 subunits and nearly 700 kDa mass, is the most complex

nuclear RNA polymerase. Recruitment of Pol III at its target promoters rely on a specific subset of transcription factors, including TFIIA, TFIIB and TFIIC. TFIIA and TFIIC complexes can be regarded as 'peripheral' recruiting factors for the core transcription factor TFIIB. At all Pol III-transcribed genes, TFIIB ultimately recruits Pol III resulting in the formation of a closed pre-initiation complex (PIC) and subsequently, assists Pol III in melting the DNA and inserting the template strand at the active site, which is the transition to an open PIC<sup>1,3</sup>. While Pol I and Pol II requires additional transcription factors, Pol III only requires TFIIB in order to drive specific transcription from a TATA-box containing U6 promoter *in vitro* and does not require the ATP-dependent helicase activity of TFIIF for the closed- to open-PIC transition *in vivo*, as in the case of Pol II<sup>1,3</sup>.

The core Pol III transcription factor TFIIB is a trimeric complex which consists of TBP, Bdp1 and Brf1. Bdp1 is required for nucleation of the

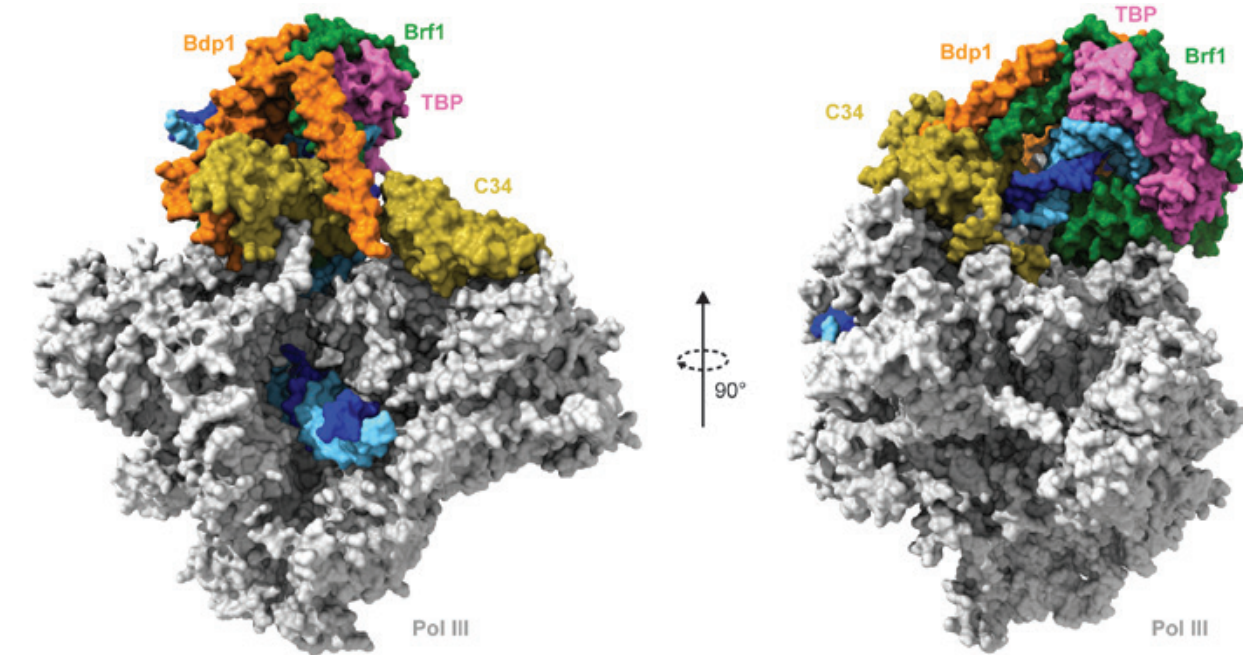


**Figure 1:** Two orthogonal views of the core Pol III PIC, represented as a molecular surface. The template and non-template strands of the promoter DNA are coloured in blue and cyan, respectively. The Pol III enzyme is depicted in grey, with the exception of subunit C34 which is depicted in yellow. TFIIB components, Brf1, TBP and Bdp1 are depicted in green, pink and orange, respectively.

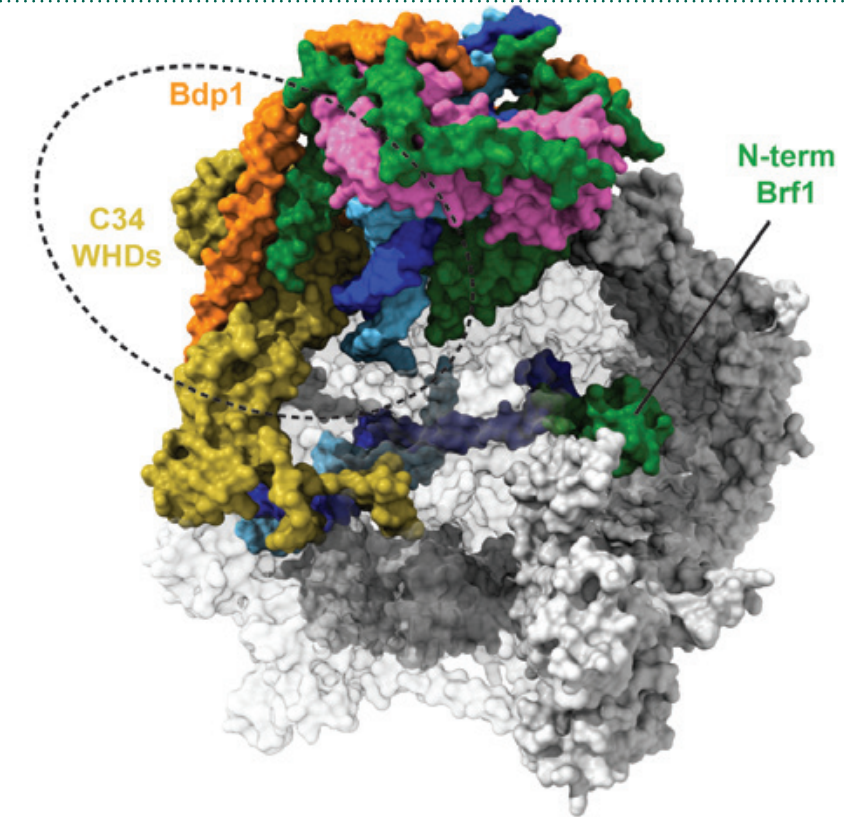


**Figure 2:** Zoom in of the DNA path within the core Pol III PIC. The initial DNA melting is generated in the upstream part of the transcription bubble (dashed line) where the C34 winged-helix domains (WHDs) are repositioned upon Bdp1 binding. Final expansion of the transcription bubble occurs upon binding of the Brf1 N-terminal domain (N-term Brf1) that clears the template strand loading path.

transcription bubble (initial DNA melting) while the N-terminal domain of Brf1 is required for the full extension of the transcription bubble, which results in template strand loading in the active site.

Cryo-EM analysis of a core Pol III PIC, reconstituted *in vitro* using endogenous *S. cerevisiae* Pol III, recombinant TFIIB and a 70 base-pairs double-stranded DNA scaffold encompassing the yeast U6 snRNA promoter, resulted in reconstructions of Pol III PIC in different states in the 3.4–4.0 Å resolution range. In particular, an atomic model of a core Pol III PIC in its open state, where the DNA has been spontaneously melted and loaded in the active site of the Pol III enzyme could be built (Fig. 1).

The structure reveals how the transcription factor TFIIB tightly encapsulates the promoter DNA around the TATA box, explaining the unusually high stability of the Pol III PIC (Fig. 2). The initial DNA melting in the upstream region of the transcription bubble is elicited by a concerted allosteric mechanism involving Pol III subunits C37 and C34 and the Bdp1 subunit of the transcription factor TFIIB. Upon binding, Bdp1 and a mobile region of subunit C37, the initiation/termination loop, rigidly position the winged-helix domains of subunit C34, that are highly mobile in the unbound Pol III enzyme, in a conformation competent for the initial DNA melting (Fig. 2). Concomitantly, the unwound DNA strands are stabilised by binding to conserved pockets on opposite sides of the Pol III cleft. Finally, binding of the N-terminal domain of Brf1 allows the DNA template strand to be loaded in the active site (Fig. 2). The conformation of the active site in the open Pol III PIC is virtually identical to the one of elongating Pol III, suggesting that immediately after recruitment Pol III adopts an elongation-ready conformation. Thus, TFIIB efficiently performs two functions at once: TFIIB effectively recruits Pol III at its target genes and, concomitantly, activates Pol III for initiation of gene transcription, resulting in RNA synthesis.

In summary, cryo-EM reconstructions allowed us to rationalise the molecular basis of the observed high transcriptional efficiency of the Pol III transcription apparatus and allowed for a comparison with the Pol I and Pol

II PICs. The Pol III PIC is topologically related to the Pol II PIC while the Pol I PIC is more divergent.

We are now focussing on obtaining cryo-EM reconstructions of a full Pol III PIC, including the multi-subunit transcription factor TFIIC, which binds promoter elements within the coding region. This structure will reveal how Pol III can efficiently transcribe a gene without deleteriously colliding with TFIIC.

### References:

- Vannini A. A structural perspective on RNA polymerase I and RNA polymerase III transcription machineries. *Biochim. Biophys. Acta - Gene Regul. Mech.* **1829**, 258–264 (2013). DOI: 10.1016/j.bbagr.2012.09.009
- Filer D. *et al.* RNA polymerase III limits longevity downstream of TORC1. *Nature* **552**, 263–267 (2017). DOI: 10.1038/nature25007
- Arimbasseri A. G. *et al.* RNA Polymerase III Advances: Structural and tRNA Functional Views. *Trends Biochem. Sci.* **41**, 546–559 (2016). DOI: 10.1016/j.tibs.2016.03.003
- Kassavetis G. A. *et al.* Transcription factor TFIIB and transcription by RNA polymerase III. *Biochem. Soc. Trans.* **34**, 1082–1087 (2006). DOI: 10.1042/BST0341082

### Funding acknowledgement:

Biotechnology and Biological Sciences Research Council (BBSRC) New Investigator Award (BB/K014390/1), Cancer Research UK Programme Foundation (CR-UK C47547/A21536) and Wellcome Trust Investigator Award (200818/Z/16/Z).

### Corresponding author:

Dr Alessandro Vannini, The Institute of Cancer Research, [alessandro.vannini@icr.ac.uk](mailto:alessandro.vannini@icr.ac.uk)

## Insight into work of molecular machines supporting genome stability

**Related publication:** Willhoft O., Ghoneim M., Lin C.-L., Chua E.Y.D., Wilkinson M., Chaban Y., Ayala R., McCormack E.A., Ocloo L., Rueda D.S., & Wigley D.B. Structure and dynamics of the yeast SWR1-nucleosome complex. *Science* (80-.). **362**, eaat7716 (2018). DOI: 10.1126/science.aat7716

**Publication keywords:** Chromatin remodelling; SWR1; Nucleosome; DNA translocation; cryo-Electron Microscopy

**T**he work recently published in the journal *Science* by a team of scientists from Imperial College London featured the structure of the SWR1:nucleosome complex at 3.6 Å resolution, determined using cryo-Electron Microscopy (cryo-EM) data collected at the UK national electron Bio-Imaging Centre (eBIC).

In a eukaryotic cell, DNA is wrapped around millions of histone protein octamers into structures called nucleosomes. Such wrapping compresses DNA into a superstructure called chromatin, and plays an important role in the regulation of gene expression. Nucleosomes, however, are not static entities - they can be slid along DNA or dislodged; histone tails can be chemically modified; histones themselves can be replaced with a different variant by specialised enzymes. The SWR1 chromatin remodelling complex exchanges histone variants in nucleosomes, playing an important role in preventing genome instability - a hallmark of cancer.

SWR1 is a large ATP dependent macromolecular machine. Part of the complex appears to be highly flexible, which may be required for the mechanics of the histone exchange reaction. Researchers from Imperial College London prepared specially designed nucleosomes with DNA overhangs, and used a non-hydrolysable ATP analogue in order to trap the SWR1:nucleosome complex at the initial stage of the reaction.

High throughput cryo-EM data collection at eBIC using the Falcon III detector was crucial for obtaining sufficient data to resolve the intrinsic structural heterogeneity of the SWR1:nucleosome complex and to obtain a high resolution structure. The structure of the complex revealed for the first time the molecular interactions between SWR1, the nucleosome, and DNA required for the initiation of the histone exchange.

The "Histone Code" theory, proposed at the turn of the century, stated that coordinated patterns of modifications to DNA-packaging histones may be a key factor in turning specific genes on or off<sup>1</sup>. Currently, two distinct classes of chromatin alterations are identified, and usually performed by different types of enzymes: 1) chemical modification of histone tails, and 2) active modification of chromatin structure, or chromatin remodelling. Both processes appear to be interlinked and tightly controlled throughout the cell cycle. Deregulation of these processes results in abnormalities in gene expression patterns that can lead to significant changes in cell chemistry, and subsequent tissue degeneration, or cancer. Yeast SWR1 complex (related to SRCAP and Tip60 complexes in human) mediates the incorporation of conserved Htz1 variant of H2A histone into chromatin. Htz1 has been implicated in transcriptional regulation, and prevention of the spread of the condensed form of chromatin, heterochromatin<sup>2</sup>.

Replacing histones in a nucleosome core is a complex task, which requires at least partial unwrapping of the supercoiled DNA, while maintaining nucleosome integrity. The cryo-EM structure of the SWR1:nucleosome complex has demonstrated how that can be achieved. The interaction of the Swr1 subunit N-terminal ATPase domain with the nucleosome at the SHL2 binding site is displaced by one base pair in comparison to other currently reported structures for other remodellers, such as Chd1:nucleosome complex<sup>3</sup>. This results in a tight interaction of the second Swr1 ATPase domain with the adjacent DNA gyre (Fig.1). As a result, DNA makes a sharp kink and is pulled away from the histone core (Fig. 2). Formation of a DNA bulge during chromatin remodelling has long been predicted, but is observed for the first time in such detail.

The Swc6 subunit of the complex is seen interacting with DNA on the opposite side to the Swr1 ATPase motor domain. DNA is unwrapped from

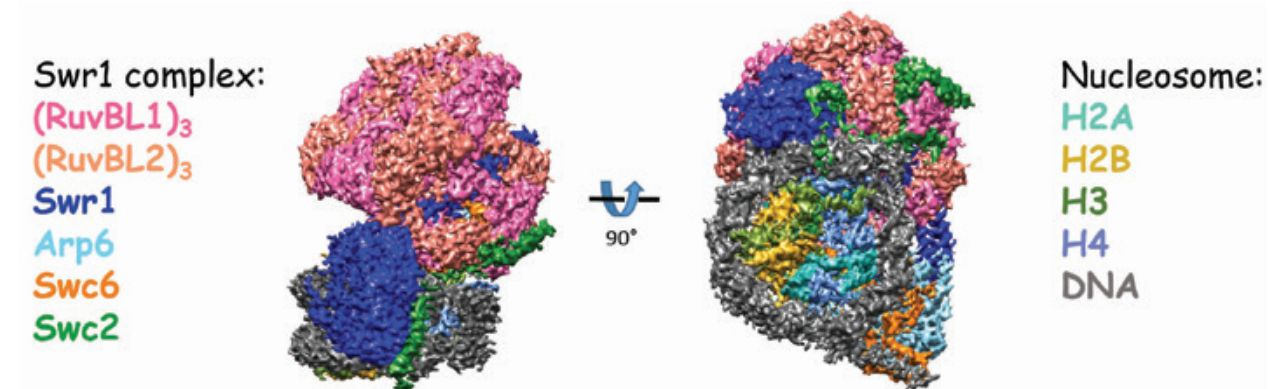


Figure 1: Overview of cryo-EM 3D map of SWR1:nucleosome complex at 3.6 Å resolution.

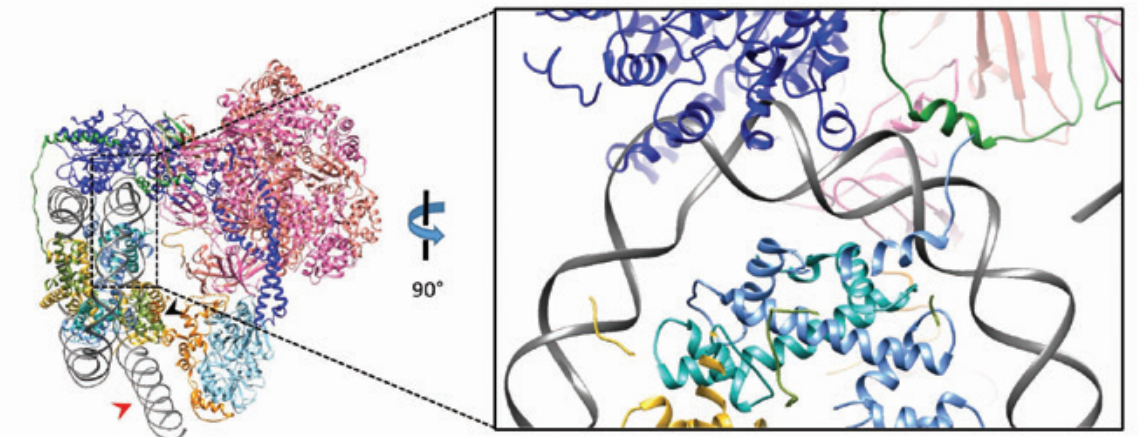


Figure 2: Left panel: atomic model of SWR1:nucleosome built into cryo-EM map. The map is rotated with the nucleosome diad axis towards viewer. Red arrowhead shows interaction between DNA overhang and Swc6; black arrowhead points towards Swc6-H2A contact. Right panel: inset showing bulging of nucleosomal DNA caused by interaction with Swr1 subunit. SWR1 complex and the nucleosome are depicted with the same colours as in Figure 1.

the canonical nucleosome path, exposing 2.5 turns of the wrap. A single alpha helix of Swc6 interacts with the surface of H2A histone (Fig. 2). The interaction site involves histone residues which differ between H2A and Htz1, and thus may contribute to enzyme specificity.

The SWR1:nucleosome structure was stabilised in the presence of the non-hydrolysable ATP analogue ADP·BeF<sub>3</sub>. Dynamics of nucleosome remodelling were tested with single molecule Förster Resonance Energy Transfer (smFRET) using labeled nucleosomes. These experiments have confirmed that ATP binding, but not hydrolysis, is required to initiate DNA unwrapping.

The recent "resolution revolution" led to the emergence of cryo-EM as a powerful tool in structural biology. The developments were recognised by the award of the 2017 Nobel prize in Chemistry to Jacques Dubochet, Joachim Frank, and Richard Henderson. The great strength of cryo-EM is in enabling the study of complex biological molecules without the need for crystallisation. This, however, can also lead to difficulties, since the collected data may represent a mixture of molecules in different conformations and ligand bound states - the issue which was affecting previous studies of the SWR1 complex<sup>4</sup>. The problem is currently addressed by: 1) improvements in speed and automation of data collection, in order to collect larger data sets; 2) the emergence of powerful techniques for computational sorting of heterogeneous data into homogeneous groups (sometimes referred as "in silico" purification/crystallisation). Established thanks to a joint grant from the Wellcome Trust, Medical Research Council (MRC), and Biotechnology and Biological Sciences Research Council (BBSRC), eBIC is a leading, high-end automated cryo-EM data acquisition facility, which allows users free-of-charge data collection using state-of-the-art equipment and methods<sup>5</sup>. Despite opening only in 2015, eBIC is continuously improving. A research and development programme is in place to implement the most current technical, software, and methodological advances. This has allowed eBIC to more than double the average speed of data acquisition in the past two years.

The upgrades and improvements in the speed of data acquisition at eBIC proved their value during the analysis of the SWR1:nucleosome complex. Using the recently installed (at the time of data acquisition) Falcon III direct electron detector in linear mode, the Imperial College team was able to collect 5,517 movies of specimen in a single user session. The automated data pre-processing pipeline available at eBIC provided real-time feedback on data quality and properties, allowing on-the-fly optimisation of data acquisition

parameters. During subsequent data processing at Imperial College, ~193,000 molecular projections were extracted from the movies, from which only 51% were homogeneous enough to be included into the final high resolution SWR1:nucleosome complex 3D-reconstruction.

The current model of SWR1:nucleosome complex reveals how nucleosome remodelling is initiated. However, the mechanism of histone exchange itself is not yet clear. Moreover, part of the SWR1 complex thought to be involved in nucleosome targeting is disordered in the current structure. The team will build on their great success to further explore the structural mechanism and dynamics of chromatin remodelling.

### References:

- Jenuwein T. Translating the Histone Code. *Science* (80-.). **293**, 1074–1080 (2002). DOI: 10.1126/science.1063127
- Talbert P. B. *et al.* Histone variants on the move: Substrates for chromatin dynamics. *Nat. Rev. Mol. Cell Biol.* **18**, 115–126 (2017). DOI: 10.1038/nrm.2016.148
- Farnung L. *et al.* Nucleosome-Chd1 structure and implications for chromatin remodelling. *Nature* **550**, 539–542 (2017). DOI: 10.1038/nature24046
- Lin C. L. *et al.* Functional characterization and architecture of recombinant yeast SWR1 histone exchange complex. *Nucleic Acids Res.* **45**, 7249–7260 (2017). DOI: 10.1093/nar/gkx414
- Clare D. K. *et al.* Electron Bio-Imaging Centre (eBIC): The UK national research facility for biological electron microscopy. *Acta Crystallogr. Sect. D Struct. Biol.* **73**, 488–495 (2017). DOI: 10.1107/S2059798317007756

### Funding Acknowledgement:

Wellcome Trust (095519/Z/11/Z & 209327/Z/17/Z (DBW)); Cancer Research UK (C6913/A21608 (DBW)); Medical Research Council (MR/N009258/1 and MR/R009023/1 (DBW)); Imperial College London.

### Corresponding authors:

Prof Dale B Wigley, Imperial College London, d.wigley@imperial.ac.uk and Dr Yuriy Chaban, Diamond Light Source, yuriy.chaban@diamond.ac.uk

## Structures and Surfaces Group

Chris Nicklin, Science Group Leader

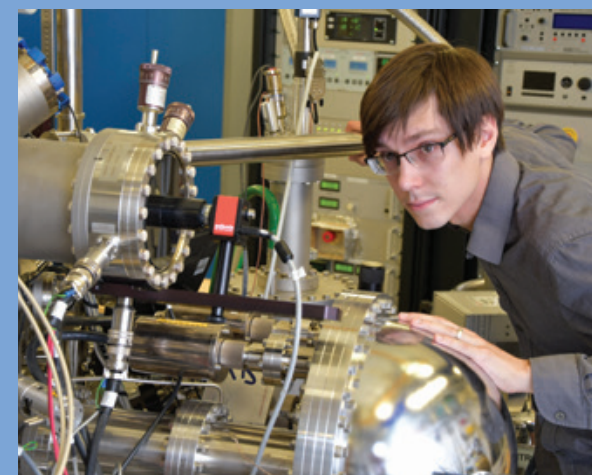
**T**he Structures and Surfaces Group consists of four beamlines: I05 (Angle Resolved Photoelectron Spectroscopy – ARPES), I07 (Surface and Interface X-ray Diffraction), B07 (Versatile Soft X-ray Scattering – VERSOX), and I09 (Atomic and Electronic Structure of Surfaces and Interfaces). There has been a great deal of activity this year; continuing to develop the beamlines, working closely with the user groups, and looking to the future opportunities enabled by the Diamond-II upgrade. The group held a successful workshop in September 2018, with a focus on Diamond-II and the new science that could be enabled including potential new techniques or beamlines. Outcomes from the workshop were incorporated into the science case for the upgrade, highlighting in particular the important role that surfaces and interfaces play in broader research areas such as battery technology, photovoltaic structures, and catalytic/electrochemical systems under *operando* conditions. Expanding the techniques to these communities is a key objective for the group.

The new group structure enables the science team to work much more closely with engineering colleagues and software developers that are aligned with the science groups, leading to common solutions across the beamlines. It also encourages cross group developments, and we are strengthening interactions with the Magnetism Group, spectroscopy beamlines, and the Soft Condensed Matter Group in a number of science areas such as energy materials and catalysis. This cooperation enhances our ability to work more closely with user groups, offering a comprehensive range of techniques to non-specialists that aids understanding of their science problems.

The beamlines within the group continue to develop through a number of major and minor upgrade projects, whilst maintaining active user and in-house programmes. VERSOX (B07) is in the process of installing a second branch, to enable high-throughput X-ray Photoelectron Spectroscopy (XPS) measurements on multiple samples, and Near-edge Extended X-ray Absorption Fine Structure (NEXAFS) Spectroscopy in ambient-pressure environments up to several bar. Together with the Near Ambient Pressure XPS/NEXAFS capabilities of the existing branch, the beamline will cover a

wide range of non-vacuum sample environments for soft X-ray experiments. It thus provides excellent opportunities to study the electronic and structural properties of materials relevant to science areas such as atmospheric chemistry, pharmaceuticals, catalysis, or cultural heritage, etc. Future development plans include expanding the sample environment capabilities to enable studies of solid-liquid interfaces and liquid surfaces.

Beamline I09 is continuing to develop optimised end stations for Hard X-ray Photoelectron Spectroscopy (HAXPES) to improve studies of the electronic states of buried interfaces, and a momentum microscope to produce images of the electron band structure directly in momentum space. The HAXPES system has been transferred to its final home on the hard X-ray branch. As it has already been utilised in user experiments on the soft X-ray branch, only a limited amount of commissioning is required to optimise the system for the higher energies. The system will be available for user experiments from early 2020. The soft X-ray ARPES system (the momentum microscope) is being designed in collaboration with two user groups (Gerd Schönhense's, Johannes Gutenberg-Universität and Ralph Claessen's, Universität Würzburg), with



Luke Rhodes, joint PhD student with Royal Holloway and Diamond, using the ARPES facility on beamline I05.

the key development being to implement a novel electron analyser. It is a complex system that will require extensive commissioning and optimisation; the aim is to have it available for user experiments in 2021. Future upgrades to I09 are likely to include new optics to improve the energy resolution of the spectroscopic measurements and prepare the beamline to fully exploit Diamond-II.

Beamline I05 has two branches, the first a high resolution facility that has proven to be a very successful addition to the suite of beamlines, since it became operational in 2014. The high resolution (HR) branch has contributed to a number of research areas, including the discovery of Weyl semimetal behaviour in tantalum arsenide (TaAs), and studies of iron-based superconductors, such as iron selenide (FeSe). Whilst most experiments have made use of *in situ* cleaving to study the electronic band structure in novel crystals, there is also a fully equipped molecular beam epitaxy (MBE) system attached to the end station that can be used to produce samples *in situ*, and is particularly suited to the growth of thin film oxide samples. The Nano-ARPES branch is now operational, enabling investigators to understand not only the electronic structure on a macroscopic scale, but also to establish the real space distribution of those states with sub-micrometre resolution. Specific developments on I05 include adding another grating to enable higher flux over the whole energy range, and replacing the current electron analyser in the HR branch with one with integrated deflection, to enable ARPES measurements without having to rotate the sample. A new micromirror system is being developed for the Nano-ARPES branch to reduce the spot size and improve the spatial resolution; a solution that will likely also be rolled out to the HR branch.

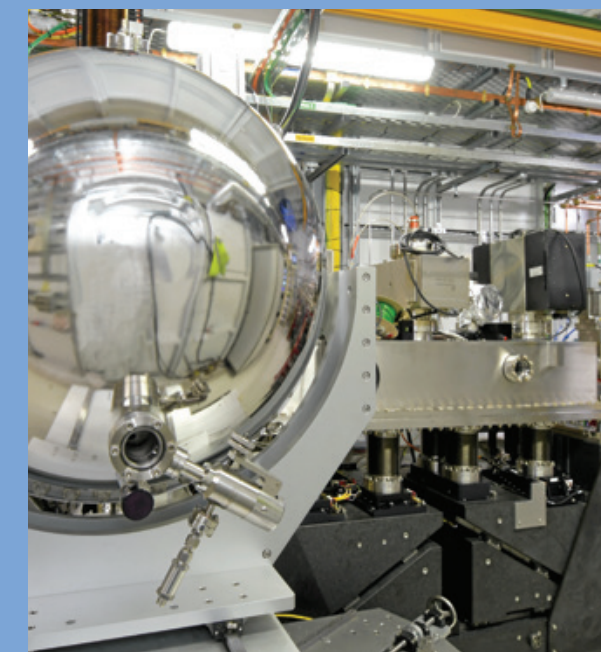
Beamline I07 has been in a period of stable operation for the last few years, but is now entering its next stage of development. There is a new Diamond-designed monochromator (planned installation in June 2019) that will improve the beam stability in preparation for a transition to use smaller X-ray beams (reduce the beam dimensions to a planned size of  $\sim 10\mu\text{m}$ ), and to exploit Diamond-II. Plans are also underway to upgrade the sample environments, in particular the Ultrahigh Vacuum (UHV) system for *in situ* MBE studies, and to expand the electrochemistry provision. Other developments are focusing on improving the usability of the beamline through the introduction of fly-scanning, auto-attenuation, and more versatile (and automated) data reduction software. New detectors with smaller pixel sizes and higher dynamic range (integrating detectors) are also part of the beamline roadmap in order to exploit the new source.

The diversity of the science programme is a strength of the Structures and Surfaces Group, with studies ranging from the observation of novel electronic states in complex crystals, to experiments on the structure of lipid

layers at the air-liquid interface. This year's science highlights cover a broad range of applications, including understanding the structural modification of Metal Organic Frameworks (MOFs), thin films, studying the Mott-transition in an oxide sample, and the observation of polaron behaviour in molybdenum disulphide.

Rubio-Giménez *et al.* used I07 to highlight the two-dimensional stacking arrangement formed through deposition using either a liquid-liquid method or Langmuir-Blodgett transfer after organising the molecules at a water surface. Relating the electronic behaviour to the structural arrangement in this conductive MOF was essential to understand the transport behaviour that may be relevant in devices for photovoltaics or photocatalysis. The correlation between the experiments clearly indicated that the charge preferentially travelled along the 2d layers rather than between them.

On beamline I09, the group from University of Würzburg studied the metal-insulator Mott transition in lanthanum titanate driven by a change in the oxygen doping of the material. The clear signature of a peak at the Fermi level was seen to develop with excess O doping, in comparison to the band gap in the stoichiometric compound. Such studies could be used in a transistor type device to act as a switch or sensor. These experiments were made possible by using a vacuum suitcase to transfer samples grown in the user's home laboratory to Diamond for the electron spectroscopy study, a system available to all I09 user groups.



The I09 HAXPES end station from the viewpoint of the hemispherical electron analyser.

The intrinsic high resolution of beamline I05 was essential in the ARPES measurements undertaken by the group of Prof K. S. Kim. They were looking for the signature of Holstein polarons in molybdenum disulphide, caused by interaction between the electrons and the lattice through localised distortions. This was only observable by running the beamline and analyser in a very high (energy) resolution mode, where small discontinuities in the bands became visible. Understanding the mechanism by which the polarons form is important as they are predicted to play a key role in high-temperature superconductivity or solar cells.

The members of the Structures and Surfaces Group are committed to continuing the high quality scientific output from the beamlines, through enhanced interaction with our user community. Please contact us if you would like to discuss any of the techniques or possible experiments, and how the synchrotron studies could help in your research.

“The beamlines within the group continue to develop through a number of major and minor upgrade projects, whilst maintaining active user and in-house programmes.”

The VERSOX team on the beamline, from left to right: Federica Venturini, Dave Grinter, Kanak Roy, Pilar Ferrer, Georg Held (PBS), Wilson Quevedo Garzon, and Andrew Watts.

## A quantum bead rolling on a lattice cushion

**Related publication:** Kang M., Jung S. W., Shin W. J., Sohn Y., Ryu S. H., Kim T. K., Hoesch M. & Kim K. S. Holstein polaron in a valley-degenerate two-dimensional semiconductor. *Nat. Mater.* **17**, 676–680 (2018). DOI: 10.1038/s41563-018-0092-7

**Publication keywords:** Holstein polaron; Two-dimensional semiconductor; ARPES

If you imagine a solid bead rolling on a soft cushion, it leaves distortions in the cushion in its wake. Transfer this analogy to the quantum-mechanical realm, and the condensed matter physics version of the rolling bead is a polaron.

Holstein polarons are small composite particles composed of an electron dragging a cloud of lattice distortions. Although they were predicted to play a key role in high-temperature superconductivity and solar cells, the spectroscopic signature of Holstein polarons, despite its importance, has not yet been observed.

Recent advances in theoretical models and computational techniques have made it possible to predict a spectroscopic hallmark of Holstein polarons. A potential candidate for the experimental observation was a surface-doped 2D semiconductor, where an anomalous superconductivity with the transition temperature as high as 12 Kelvin (K) was recently reported.

The energy resolution is a critical factor for resolving the subtle signature of Holstein polarons in spectroscopy experiments, and so a team of Korean researchers chose Diamond Light Source's ARPES (Angle-Resolved Photoemission Spectroscopy) beamline (I05) – one of the best experimental stations in terms of the energy resolution. It allowed them to make the first experimental discovery of the spectroscopic signature of Holstein polarons, as predicted by theory. They found that the coupling strength between electrons and lattice distortions gradually increases with the charge carrier density, which is suggestive of their relevance.

In nature, one can often find an entity strongly interacting with its surrounding environments. A familiar example is a solid bead rolling on a soft cushion, which is accompanied by some distortions left along the moving path. The quantum-mechanical version of this rolling bead in condensed-matter physics is a composite particle called the polaron. The theoretical basis of polarons was founded by Soviet Physicist Landau back in the early 1930s. An electron residing in an ionic crystal would attract the positively charged ions towards it and push the negatively charged ions away from it by electric forces. This can be viewed as a composite particle of an electron dragging a cloud of lattice distortions (or phonons) with it (Fig. 1). This electron-phonon interaction can be approximately described by two standard models, one is the Fröhlich-type and the other is the Holstein-type<sup>1</sup>. The Holstein-type polaron is

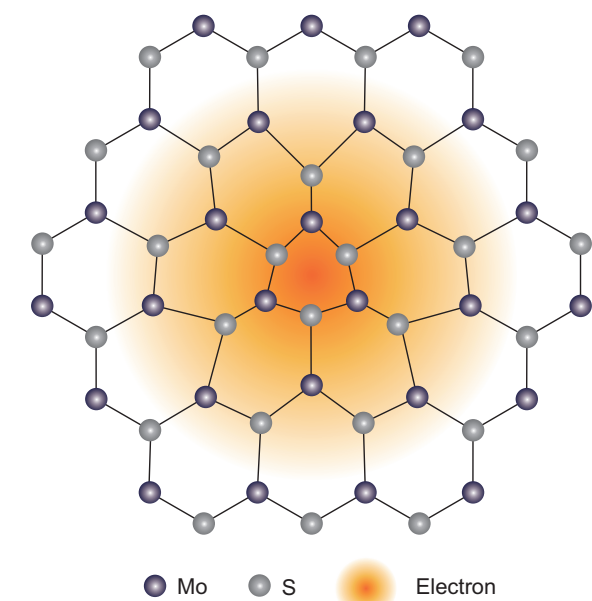


Figure 1: Schematic illustration of a polaron in MoS<sub>2</sub>. The blue and grey balls represent Mo and S atoms, respectively. The yellowish envelop represent the electron that carries a cloud of lattice distortions.

the lattice model that has been widely employed to describe the mechanism of high-temperature superconductivity and the limiting factor of carrier mobility in solar-cell devices. Despite such potential importance in both fundamental physics and device applications, the Holstein polaron has remained elusive, because it is extremely difficult to solve analytically. Only recently, the energy spectrum of Holstein polarons, which is key to understanding their fundamental properties, was successfully calculated owing to the recent advances in theoretical models and computational techniques<sup>2</sup>. These theoretical predictions laid a ground for experimentalists to hunt for the energy spectrum of Holstein polarons that have remained undiscovered for more than 50 years.

On the other hand, since the discovery of graphene, atomically thin two-dimensional (2D) crystals have emerged as a class of materials that may impact our future electronics technologies. Owing to their atomic scale thickness, the carrier density can be tuned by electrostatic gating over the range of 10<sup>12</sup> cm<sup>-2</sup>, which is highly useful not only for device applications, but also for the study of many-body correlations. This range of carrier density can be further increased by ionic liquid gating up to 10<sup>14</sup> cm<sup>-2</sup>, where a variety of exotic quantum states of matter may emerge. This level of carrier doping was indeed achieved in MoS<sub>2</sub>, a 2D semiconductor with promising device characteristics. Surprisingly, electron doping to the surface of multilayer MoS<sub>2</sub> was found to develop a superconducting dome that typically appears in the phase diagram of high-temperature superconductors<sup>3</sup>. The maximum critical temperature was reported as high as 12 K, which is the record among transition-metal dichalcogenides. This previous work made it ideal to explore a signature of electron-phonon interaction (or polaron) and its possible relevance to the superconductivity.

The electron density of 10<sup>14</sup> cm<sup>-2</sup> was achieved by ionic liquid gating<sup>3</sup>, where the spatial separation of positively charged and negatively charged ions forms an electric double layer in the surface of multilayer MoS<sub>2</sub>. The similar atomic-scale dipole layer can also be formed by the deposition of alkali-metal (Rb) atoms that donate electrons to MoS<sub>2</sub> and become positively charged ions<sup>4</sup>.

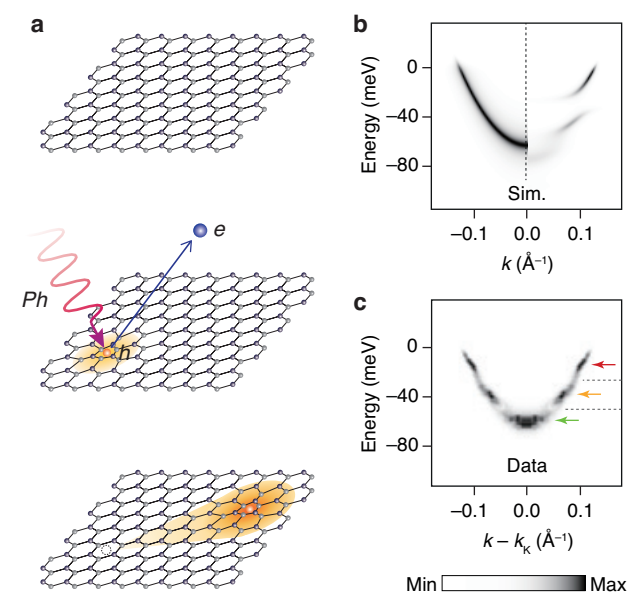


Figure 2: (a) Process of detecting a signature of Holstein polarons using ARPES. The photons generate electron-hole pairs and the photoholes left in solids experience the interaction with other degrees of freedom; (b) Simulated energy-momentum spectrum (left) without and (right) with considering Holstein polarons based on the momentum-average approximation<sup>2</sup>; (c) Experimental energy-momentum spectrum of Holstein polarons measured by ARPES from Rb-doped MoS<sub>2</sub>.

This surface chemical doping was employed in our study to experimentally explore a signature of Holstein polarons in the superconducting regime of MoS<sub>2</sub>. The energy spectrum of Holstein polarons can be detected by an experimental technique called ARPES<sup>5</sup>. The high-flux photons generated by the synchrotron radiation is incident on the samples, and photoelectrons are generated leaving photoholes behind (Fig. 2a). By recording the energy and angle of the emitted photoelectrons by an electron spectrometer, one can learn about the energy-momentum relation of initial-state electrons in the samples. This process is basically a quantum-mechanical transition, and information on the interaction of photoholes left in the samples to other degrees of freedom, such as phonons, is recorded together in the energy-momentum relation measured by ARPES. The strong interaction of electrons to phonons (polarons) appears as a series of abrupt changes in the energy-momentum spectrum (Fig. 2b). The typical energy scale of electron-phonon coupling is in the order of a few tens of milli-electronvolts, which is comparable to the energy resolution of ARPES. In this respect, the energy resolution was expected to be critical in

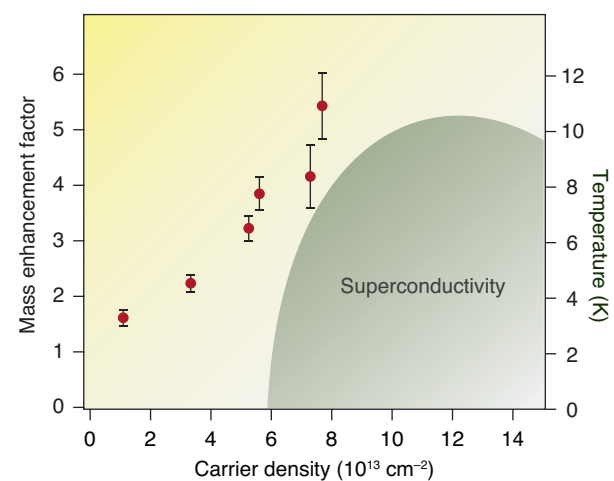


Figure 3: The mass enhancement of electrons by the interaction to phonons is plotted as a function of carrier density. The overlaid green region is the superconducting dome reported before<sup>3</sup>.

resolving the signature of Holstein polarons, and our first choice of beamline was I05 at Diamond.

Our team had tried with help from the beamline scientists at I05 to find a signature of electron-phonon interactions in MoS<sub>2</sub> doped by Rb atoms up to the carrier density at which the superconducting dome was observed. The energy-momentum spectrum of doped electrons in MoS<sub>2</sub> shown below the Fermi energy by surface doping and measured by ARPES was overall parabolic. At that time, the yield of photoelectrons was anomalously high with the photon energy of 50–60 eV. At beamline I05, there is a safety rule that one has to keep the number of photoelectrons below a certain limit to prevent the detector from being burned out. As restricted by this safety rule, we had to reduce the number of photoelectrons at detector by narrowing the slit of the electron analyser (the narrower the slit is the better the energy resolution, but usually not used for poor yield of photoelectrons). With the narrowest slit (the best energy-resolution condition), we found something totally unexpected in the energy-momentum spectrum of MoS<sub>2</sub>. That is, we could observe a subtle signature of abrupt kinks (indicated by arrows in (Fig. 2c)) which is collectively identified as a hitherto unobserved energy spectrum of Holstein polarons predicted in theory<sup>2</sup>. To the best of our knowledge, this is the first experimental observation of the spectral function of Holstein polarons, which would not be possible without the superior energy resolution of beamline I05.

The observed energy spectrum of Holstein polarons allows us to closely scrutinise the doping evolution of electron-phonon coupling. We found an interesting tendency that the strength of electron-phonon coupling increases along with the superconducting dome in surface-doped MoS<sub>2</sub> (Fig. 3). This is suggestive of bipolaronic pairing that has been hotly debated as a possible mechanism of high-temperature superconductivity. Although a correlation of Holstein polarons to the 2D superconductivity is yet to be made by further studies, we anticipate that the energy spectrum of Holstein polarons revealed here may contribute as a stepping stone to solve relevant grand challenges in condensed matter physics.

### References:

- Friedman L. *et al.* Studies of polaron motion. *Ann. Phys. (N. Y.)* **21**, 494–549 (1963). DOI: 10.1016/0003-4916(63)90130-1
- Goodvin G. L. *et al.* Green's function of the Holstein polaron. *Phys. Rev. B - Condens. Matter Mater. Phys.* **74**, 245104 (2006). DOI: 10.1103/PhysRevB.74.245104
- Ye J. T. *et al.* Superconducting dome in a gate-tuned band insulator. *Science (80-. )* **338**, 1193–1196 (2012). DOI: 10.1126/science.1228006
- Damascelli A. *et al.* Angle-resolved photoemission studies of the cuprate superconductors. *Rev. Mod. Phys.* **75**, 473–541 (2003). DOI: 10.1103/RevModPhys.75.473
- Kang M. *et al.* Universal Mechanism of Band-Gap Engineering in Transition-Metal Dichalcogenides. *Nano Lett.* **17**, 1610–1615 (2017). DOI: 10.1021/acs.nanolett.6b04775

### Funding acknowledgement:

NRF (grants no. 2017R1A5A1014862 and no. 2017R1A2B3011368), Yonsei University (2017-22-0059), POSCO TJ Park Foundation.

### Corresponding author:

Professor Keun Su Kim, Yonsei University, keunsukim@yonsei.ac.kr

## X-rays help to unravel the structure and orientation of semiconductive porous ultrathin films

**Related publication:** Rubio-Giménez V., Galbiati M., Castells-Gil J., Almora-Barrios N., Navarro-Sánchez J., Escorcía-Ariza G., Mattera M., Arnold T., Rawle J., Tatay S., Coronado E. & Martí-Gastaldo C. Bottom-Up Fabrication of Semiconductive Metal-Organic Framework Ultrathin Films. *Adv. Mater.* **30**, 1704291 (2018). DOI: 10.1002/adma.201704291

**Publication keywords:** Electrical conductivity; Metal-organic frameworks; Self-assembled monolayers; Ultrathin films

**E**lectrically conductive Metal-Organic Frameworks (MOFs) are promising materials for electronic devices, owing to their unique capability to adsorb guest molecules. Processing them as ultrathin films is one of the key requirements for the development of electronic devices, and might offer new perspectives in fields of key environmental value such as photovoltaics, photocatalysis or sensing.

A team of researchers from the Universitat de València prepared ultrathin films of a conductive MOF composed of 2D layers (Cu-CAT-1), and characterised their thickness and chemical purity. To unravel the pathway that charges were taking when going through the Cu-CAT-1 films, they needed detailed information about the crystallinity and preferential orientation with respect to the surface of the substrate, and to combine this information with electrical conductivity measurements.

To study the structure and relative orientation of the MOF ultrathin films they used the Surface and Interface Diffraction beamline (I07), which has the capability to perform Grazing Incidence X-ray Diffraction (GIXD) measurements.

Their results showed that the Cu-CAT-1 films were preferentially oriented with the 2D layers laying parallel to the surface of the substrate instead of being perpendicular or having a random orientation. This meant that, in the electrical conductivity measurements, charges were preferentially travelling along the Cu-CAT-1 layers instead of across them. These results will inform our ability to produce high-quality MOF films on a wide variety of substrates with control over their orientation, crystallinity, homogeneity and thickness; an exciting development in the production of new electronic devices.

MOFs combine the extended structure and high crystallinity of inorganic solids with the synthetic versatility, and easy processability and mechanical flexibility, of organic materials. Furthermore, their porous structures offer the possibility of indirectly manipulating their properties by infiltration with active guests. Nevertheless, most consolidated applications employ MOFs as electronically innocent frameworks, as most of them are electrical insulators. However, the appearance in recent years of various examples of conductive MOFs has opened a pathway of integration of MOF materials as active elements in electronic devices<sup>1,2</sup>. A fundamental difference from other applications is the fact that a very small amount of material is needed for electronic devices, in other words, they have to be prepared or processed as thin films. In this regard, this constitutes the very first step in device integration; materials must be carefully processed to achieve nanometric thicknesses with exquisite control over several factors that play an important role in the device performance, such as film thickness, substrate coverage, homogeneity, roughness, crystallinity, and crystalline orientation with respect to the substrate. Controlling these parameters

is necessary so that the designer properties of the original bulk material are equivalent in its nanostructured form. However, this nanostructuring also carries with it a challenge with regards to their characterisation.

After our first work, which involved the fabrication of the electronic properties of ultrathin films of a moderately conductive and non-intrinsically porous MOF<sup>3</sup>, we moved on to apply the acquired nanofabrication expertise to an intrinsically conductive and porous system. For that purpose, we chose a previously reported material: Cu-CAT-1<sup>4</sup>, a highly conductive MOF composed of hexagonal layers of 2, 3, 6, 7, 10, 11-hexahydroxytriphenylene (HHTP) ligands in the semiquinone form and square planar Cu<sup>2+</sup> ions (Fig. 1a). In order to produce ultrathin films of Cu-CAT-1, we employed two complementary deposition strategies, a facile and versatile liquid-liquid (LL) method (Fig. 1b), and a more demanding but highly controllable Langmuir-Blodgett (LB) procedure (Fig. 1c). In both routines, the Cu-CAT-1 ultrathin film is synthesised at the interphase between two immiscible liquid mediums, and then transferred

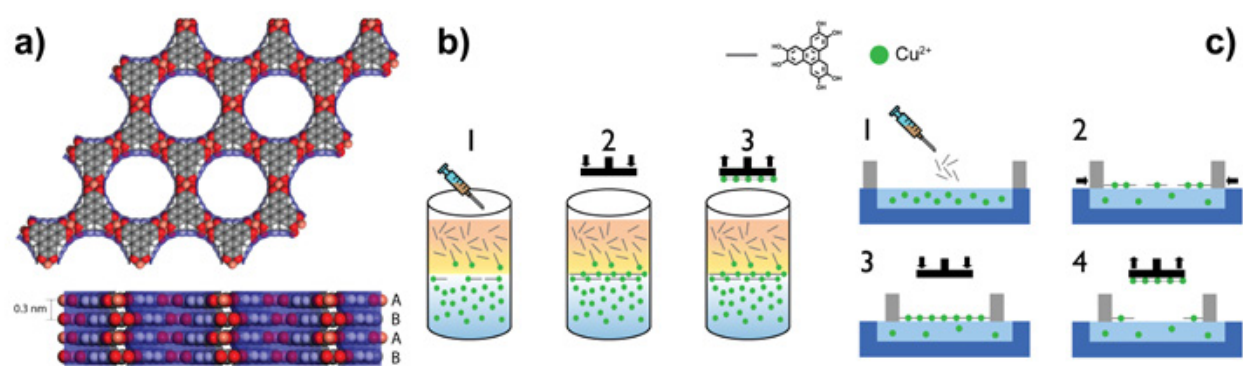


Figure 1: (a) Layered structure of Cu-CAT-1 formed by stacking of hexagonal layers of Cu<sup>2+</sup> and HHTP. Schemes for the formation and transfer to a solid substrate of Cu-CAT-1 ultrathin films via the LL (b) and LB (c) methods.

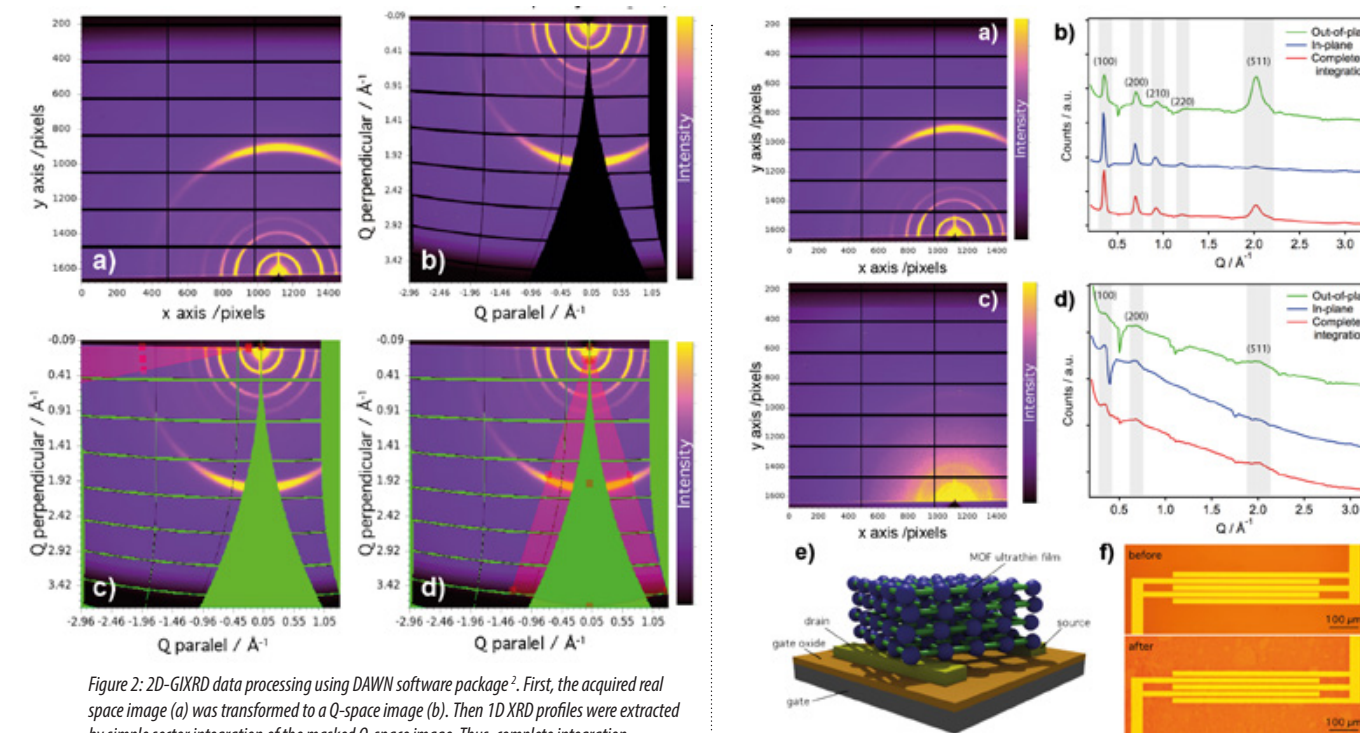


Figure 2: 2D-GIXRD data processing using DAWN software package<sup>2</sup>. First, the acquired real space image (a) was transformed to a Q-space image (b). Then 1D XRD profiles were extracted by simple sector integration of the masked Q-space image. Thus, complete integration including all spatial directions (0° to 180°), in-plane (150° to 180°) and out-of-plane (60° to 120°) diffractograms were obtained.

to a solid substrate. We used spectroscopic techniques like infrared reflectance absorption spectroscopy (IRRAS), UV-vis, or X-ray photoelectron spectroscopy (XPS) to confirm the successful formation and transfer of Cu-CAT-1 ultrathin films onto substrates, as well as microscopic ones such as optical microscopy, atomic force microscopy (AFM), and scanning electron microscopy (SEM) to assess the films' roughness, thickness and morphology. However, structural studies key to confirming their crystallinity and preferential orientation long-range order were still missing. Thus, we performed 2D grazing incidence X-ray diffraction (2D-GIXRD) at beamline I07.

Cu-CAT-1 ultrathin films fabricated onto Si/SiO<sub>2</sub> substrates, with both LL and LB procedures, were placed into a closed cell mounted on a multiaxis diffractometer, and measured under a continuous helium flow to minimise beam damage. We then collected 2D-GIXRD single shot images at room temperature using a Pilatus 2M area detector with a wavelength of 0.85 Å (beam energy of 14.53 keV), a sample-to-detector distance of 456 mm, and an incidence angle of 0.1° above the critical angle. Next, the resulting real space images were processed into Q-space images using the DAWN software, and complete in-plane and out-of-plane profiles were extracted by simple sector integration of the Q-space images (Fig. 2). As seen in Fig. 3, the complete 2D-GIXRD pattern for both LL and LB ultrathin films showed the characteristic peaks of Cu-CAT-1. Additionally, the higher intensity of the (001) peak in the out-of-plane XRD profiles with respect to the in-plane diffractograms indicates that the films are preferentially oriented with the hexagonal sheets (ab plane) laying parallel to the surface of the substrate. The difference in intensity between LL and LB diffractograms can be ascribed to the disparity in the thickness of the films analysed (~20–70 nm for LL vs. ~20 nm for LB).

Finally, we investigated the electrical properties by fabricating field effect transistor-type devices of Cu-CAT-1 ultrathin films, and measuring room-temperature conductivities through horizontal Au electrodes. The structural information collected via synchrotron 2D-GIXRD allowed us to determine that the charge transport was taking place along the Cu-CAT-1 2D layers, which laid preferentially parallel to the substrate (Fig. 3e,f). This demonstrates that correlating structural information with electronic measurements is of utmost importance for establishing structure-to-function parallelisms that might be key for the integration of porous and electro-active MOF scaffolds in electronic

Figure 3: 2D-GIXRD real space images and extracted complete, in-plane and out-of-plane profiles for Cu-CAT-1 ultrathin films made via the LL (a,b) and LB (c,d) methods. Scheme (e) and optical images (f) of the Cu-CAT-1 field effect transistor-type devices showing the relative orientation of the Cu-CAT-1 layer with respect to the Si/SiO<sub>2</sub> substrate and the Au electrodes.

devices. We later used this expertise to fabricate a Cu-CAT-1 chemiresistive sensing device<sup>5</sup>.

### References:

- Sun L. *et al.* Electrically Conductive Porous Metal-Organic Frameworks. *Angew. Chemie - Int. Ed.* **55**, 3566–3579 (2016). DOI: 10.1002/anie.201506219
- Stassen I. *et al.* An updated roadmap for the integration of metal-organic frameworks with electronic devices and chemical sensors. *Chem. Soc. Rev.* **46**, 3185–3241 (2017). DOI: 10.1039/c7cs00122c
- Rubio-Giménez V. *et al.* High-Quality Metal-Organic Framework Ultrathin Films for Electronically Active Interfaces. *J. Am. Chem. Soc.* **138**, 2576–2584 (2016). DOI: 10.1021/jacs.5b09784
- Hmadeh M. *et al.* New porous crystals of extended metal-catecholates. *Chem. Mater.* **24**, 3511–3513 (2012). DOI: 10.1021/cm301194a
- Rubio-Giménez V. *et al.* Origin of the Chemiresistive Response of Ultrathin Films of Conductive Metal-Organic Frameworks. *Angew. Chemie - Int. Ed.* **57**, 15086–15090 (2018). DOI: 10.1002/anie.201808242

### Funding acknowledgement:

EU (ERC Stg Chem-fs-MOF 714122, Horizon 2020 Marie Curie Action SPIN2D H2020/2014-659378); Spanish MINECO (Unit of Excellence María de Maeztu MDM-2015-0538, Ramón y Cajal fellowship RYC-2012-10894, FPI predoctoral fellowship CTQ2014-59209-P); Spanish MECD (FPU predoctoral fellowship FPU13/03203); Generalitat Valenciana (Grant for emergent research groups GV/2016/137, Santiago Grisolia predoctoral fellowship GRISOLIA/2015/007).

### Corresponding author:

Mr Víctor Rubio-Giménez, Instituto de Ciencia Molecular, Universitat de València, victor.rubio@uv.es

## Teaching 'failed metals' new tricks

**Related publication:** Scheiderer P., Schmitt M., Gabel J., Zapf M., Stübinger M., Schütz P., Dudy L., Schlueter C., Lee T. L., Sing M. & Claessen R. Tailoring Materials for Mottronics: Excess Oxygen Doping of a Prototypical Mott Insulator. *Adv. Mater.* **30**, 1706708 (2018). DOI: 10.1002/adma.201706708

**Publication keywords:** Electronic phase transitions; Mottronics; Photoelectron spectroscopy; Thin films; Transition metal oxides

**A** new class of electronic devices, often referred to by the term **Mottronics**, is based on charge correlations between the electrons. Transition metal oxides exhibit fascinating phenomena such as the Mott metal-to-insulator transitions, electronic phase transitions that are of potential interest for future device applications. However, further progress in material development is required to make high quality thin films of prototypical Mott materials available, and to establish methods to control their electronic phase, i.e. insulating or metallic.

A team of researchers from the Universität Würzburg in Germany, and Diamond Light Source, investigated the electronic properties of  $\text{LaTiO}_3$  (LTO) thin films, which tend to over-oxidise. This presents a challenge for the preparation of the thin films, however, it also allows for chemical doping by excess oxygen once control of the oxygen content has been gained. The team used an *in situ* vacuum suitcase supplied by beamline I09 to prevent exposure of the samples to air, and then used a combination of soft and hard X-ray photoelectron spectroscopy to monitor the oxygen stoichiometry via the titanium valence, and valence band photoemission to determine the electronic phase.

Based on the spectroscopic characterisation of the thin films, they developed a method to control the oxygen stoichiometry, and demonstrated that stoichiometric LTO films are insulating and that oxygen excess doping induces the filling controlled Mott transition into the metallic phase. This work identified a suitable channel material for Mottronics, characterised the Mott insulator-to-metal transition in LTO, and characterised a way to tune the electronic phase.

The strong electron correlations in transition metal oxides induce a rich electronic phase diagram that waits to be harnessed in the development of future electronic devices, often referred to as Mottronics. One of the most prominent potential applications of this field is the Mott transistor that uses the electronic phase transition between the Mott insulator phase (OFF-state) and the correlated metal phase (ON-state) as a switch.

Mott insulators are 'failed metals' in the sense that their charge carrier densities correspond to a half-filled narrow band (usually of  $d$  character) which, however, leads to strong on-site Coulomb interactions and thus localised electrons. As sketched in the phase diagram<sup>1</sup> in Fig. 1, tuning the band filling away from the half-fill ( $d^1$ ) condition by, e.g., an external electric field, may trigger a Mott transition (MT) into a metallic phase, rendering all previously localised electrons mobile. Therefore, a Mott transistor exhibits a large ON/OFF ratio and fast switching speed, and due to the high carrier concentration, miniaturisation of devices below the current limits of conventional semiconductors is possible. The downside of these high carrier densities are the large electric fields required to induce a sizable change of the band-filling. A solution to this problem has recently been suggested based on dynamical mean field theory simulations<sup>2,3</sup>. In Mott insulating materials that are already close to the phase transition, the electronic phase is highly sensitive to external stimuli including moderate electric fields. In order to reach such an operating point, well characterised Mott materials are required, and methods to adjust their properties within the electronic phase diagram need to be developed, both of which is the scope of this work.

Good candidates as Mott materials are the  $3d^1$  perovskite series:  $\text{SrVO}_3$ ,  $\text{CaVO}_3$ ,  $\text{LaTiO}_3$  and  $\text{YTiO}_3$ , which range from the metallic vanadates to the insulating titanates (Fig. 1) and exhibit a bandwidth controlled MT. From this series, the insulating compound closest to the phase transition,  $\text{LaTiO}_3$ , is selected and oxygen doping is demonstrated to tune the electronic properties in  $\text{LaTiO}_{3+x}$  thin films all the way from being Mott insulating to metallic. In view

of future device designs the samples are fabricated as thin films by pulsed laser deposition (PLD).

The electronic properties can be best investigated by photoelectron spectroscopy (PES), which allows us to monitor the titanium valence with the binding energy of the Ti  $2p$  core level, and the spectral weights of the Ti  $3d$  states near the Fermi level. Taking advantage of the wide photon energy range uniquely available at beamline I09, that covers both soft and hard X-rays, we examine the Ti valence near the surface and in the bulk of the thin films and probe both angle-integrated and -resolved valence electronic structures of  $\text{LaTiO}_{3+x}$  at the Ti  $L$  resonance.

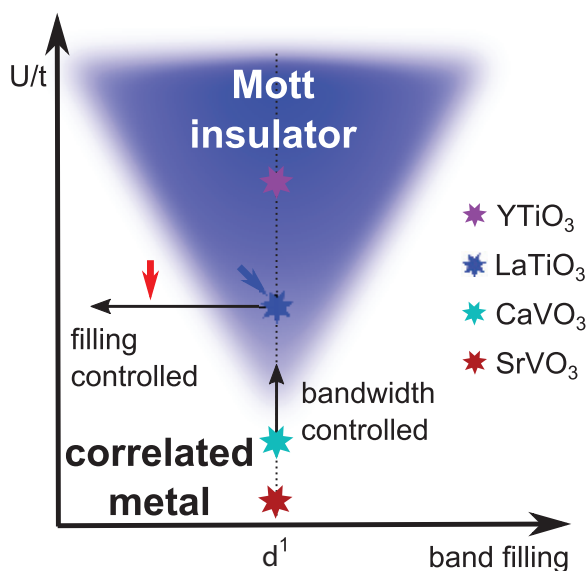


Figure 1: Sketch of the electronic phase diagram of Mott materials including some prototypical  $d^1$  materials.  $U$  is the on-site repulsion and  $t$  is the hopping term.

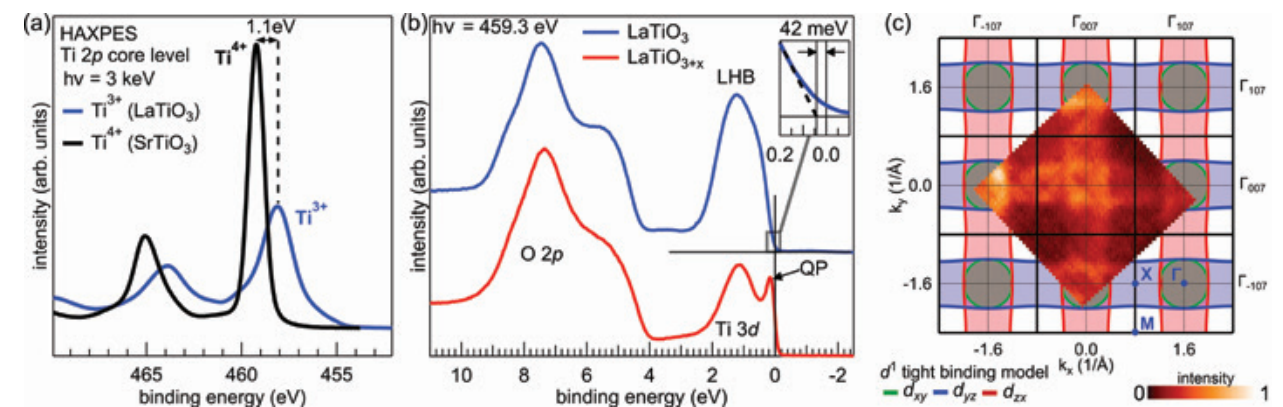


Figure 2: (a) The titanium valence is monitored by core-level photoelectron spectroscopy of the Ti  $2p$  line. The absence of any sizable  $\text{Ti}^{4+}$  signal in the spectrum from the  $\text{LaTiO}_3$  film (blue line) verifies the correct oxygen stoichiometry; (b) Resonant photoemission at the Ti  $L$  absorption threshold allows to investigate the Ti  $3d$  valence band states. Whereas the stoichiometric sample exhibits a gapped spectrum, the oxygen excess doped thin film is metallic as indicated by the quasiparticle peak (QP) and the Fermi cutoff; (c) Fermi surface measured by resonant SX-ARPES at the Ti  $L$  absorption threshold depicted together with a tight binding model for a filling of  $d^1$ .

Furthermore, I09 provides a UHV suitcase that allows *in situ* transfer of samples from the growth chamber in Würzburg to the end station at the beamline, which is crucial for the investigations of  $\text{LaTi}^{3+}\text{O}_3$  thin films since the material tends to over-oxidise towards  $\text{LaTi}^{4+}\text{O}_{3.5}$ , corresponding to a reduction of the valence band filling from  $3d^1$  to  $3d^0$ . In air the films oxidise in an uncontrolled way impeding any investigations of the dependence of the electronic phase on the oxygen content. Even when the samples are transferred in vacuum, the Ti oxidation state may deviate from its nominal value due to other sources of excess oxygen supplied by, e.g., the substrate, during the growth process, a major challenge that is overcome by a novel growth strategy developed in this study, as discussed in more detail in a related publication<sup>4</sup>. Therefore, the first experimental task is to verify the stoichiometry of the samples, which can be best characterised by analysing the Ti  $2p$  core level. The comparison of the corresponding spectrum with data obtained from the tetravalent reference material  $\text{SrTiO}_3$  (Fig. 2a) shows that no sizable amount of  $\text{Ti}^{4+}$  ions is present in the  $\text{LaTiO}_3$  thin films, thereby confirming the intended oxygen stoichiometry and band filling.

The electronic phase, i.e. Mott insulator or correlated metal, is investigated by measuring the Ti  $3d$  valence states using resonant photoelectron spectroscopy (ResPES) at the Ti  $L$  absorption threshold. The resonant conditions strongly and selectively enhance the Ti  $3d$  signal, providing a clear view of the valence states. The resulting spectrum of the stoichiometric sample (blue line in Fig. 2b) exhibits a single Ti  $3d$  feature around 1 eV identified as the lower Hubbard band (LHB) and an energy gap at the Fermi level (see the inset in Fig. 2b). Note that, for non-interacting electrons, the configuration of one electron per unit cell would result in a conduction band that crosses the Fermi level. Instead, due to the strong on-site Coulomb interactions between the  $3d$  electrons in a half-filled band, an LHB is formed in  $\text{LaTiO}_3$  and the material is in the Mott insulating phase.

Having demonstrated the Mott insulating phase in stoichiometric samples, the next challenge is to tune the electronic properties in order to reach the suggested operating point for a Mott transistor. As mentioned above,  $\text{LaTiO}_3$  thin films tend to over-oxidise. This behaviour can be harnessed to reduce the band filling, since every excess oxygen ion accepts two electrons from the Ti  $3d$  states, and thereby drive the Mott transition (see Fig. 1). The effectiveness of this method in  $p$  doping and in triggering the Mott transition into a metallic phase is again tested by ResPES. The red spectrum in Fig. 2b shows that, indeed, the  $\text{LaTiO}_{3+x}$  sample fabricated in higher oxygen pressure exhibits a Fermi cutoff with a quasiparticle peak (QP) characteristic for the correlated metal phase.

The momentum-dependence of the QP spectral weight is further

investigated by soft X-ray angular resolved PES (SX-ARPES, Fig. 2c). The corresponding Fermi surface matches approximately the tight binding model of the related correlated metal  $\text{SrVO}_3$  (Fig. 1). This confirms three important statements about the Mott transition in  $\text{LaTiO}_{3+x}$  that have been made above. First, the valence electrons form dispersing bands indicative of the metallic phase. Second, the required doping level to reach the metallic phase is rather low, i.e. of the order of only a few percent, since the Luttinger volume of the Fermi surface is still very close to one electron per unit cell ( $d^1$ ). Third, this large Fermi surface shows that indeed *all*  $3d$  electrons are rendered mobile in the metallic phase and the electronic transport is not related to the doping level as in semiconductor materials.

These findings are not only important steps in material research on the prototypical correlated compound  $\text{LaTiO}_3$ , they also demonstrate that it is a promising channel material for future Mott transistor devices.

## References:

- Imada M. *et al.* Metal-insulator transitions. *Rev. Mod. Phys.* **70**, 1039–1263 (1998). DOI: 10.1103/RevModPhys.70.1039
- Mazza G. *et al.* Field-Driven Mott Gap Collapse and Resistive Switch in Correlated Insulators. *Phys. Rev. Lett.* **117**, 176401 (2016). DOI: 10.1103/PhysRevLett.117.176401
- Zhong Z. *et al.* Electronics with Correlated Oxides:  $\text{SrVO}_3/\text{SrTiO}_3$  as a Mott Transistor. *Phys. Rev. Lett.* **114**, 246401 (2015). DOI: 10.1103/PhysRevLett.114.246401
- Scheiderer P. *et al.* Tailoring Materials for Mottronics: Excess Oxygen Doping of a Prototypical Mott Insulator. *Adv. Mater.* **30**, 1706708 (2018). DOI: 10.1002/adma.201706708

## Funding acknowledgement:

The authors are grateful for funding support from the Deutsche Forschungsgemeinschaft (FOR 1162 and SFB 1170 "ToCoTronics") and acknowledge Diamond Light Source for time on beamline I09 under proposals SI14106, SI15200, SI15856, and NT18372. The authors would also like to thank D. McCue for his superb technical support at the I09 beamline, and also acknowledge fruitful discussions with M. Bibes and R. Aeschlimann.

## Corresponding author:

Philipp Scheiderer, Physikalisches Institut und Röntgen Center for Complex Material Systems (RCCM), Universität Würzburg, philipp.scheiderer@physik.uni-wuerzburg.de

## Magnetic Materials Group

Sarnjeet Dhesi, Science Group Leader

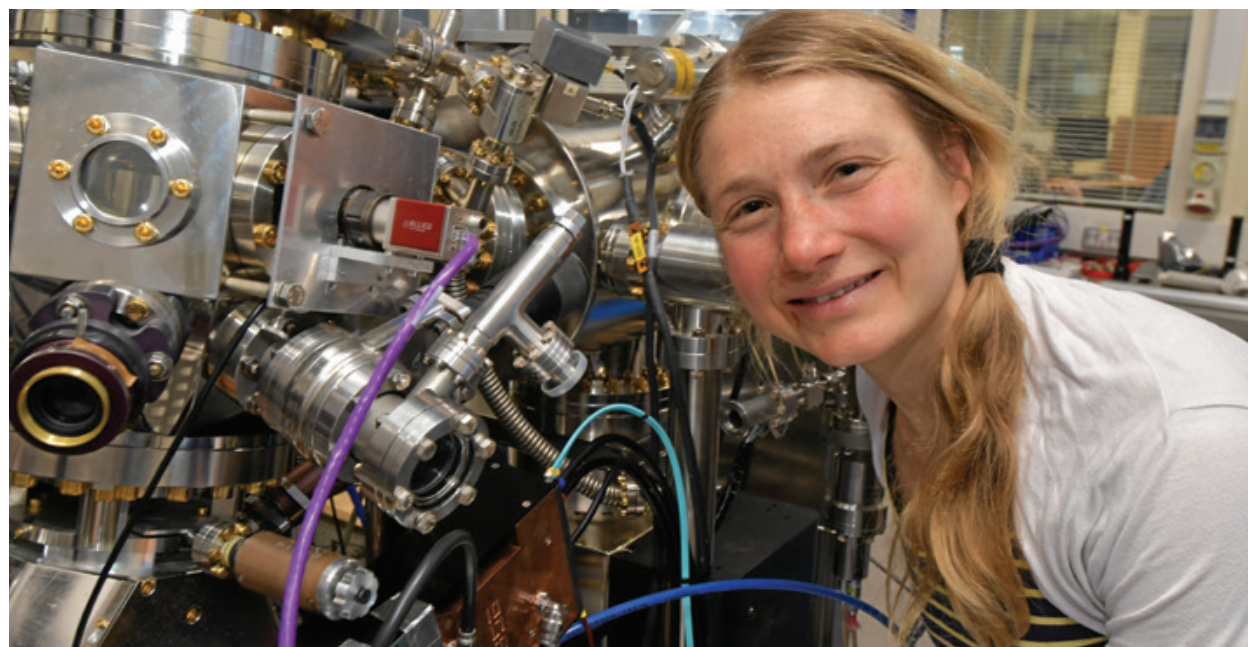
**T**he Magnetic Materials Group comprises scientists and engineers working across five beamlines (I06, I10, I16, B16 and I21) covering the soft to hard X-ray range, and a variety of techniques, from resonant X-ray scattering, coherent diffraction imaging, photoemission electron microscopy to absorption spectroscopy. Over the last year, our research community has explored the fundamental properties of a wide range of naturally occurring and fabricated materials to discover a wealth of fascinating new phenomena. In this contribution, we present research from the beamlines demonstrating how X-ray diffraction and imaging can isolate surface effects in chiral spin structures, and how confined volumes can dramatically enhance the growth of single-crystals. We also present the development of a new form of non-linear X-ray spectroscopy, which has enormous potential as an atomic probe of valence states. The results, as a whole, highlight the need for improved theoretical models to underpin technique and material development.

Vortices are naturally occurring structures that form on cosmic as well as microscopic length scales. On the other hand, vortices in magnetic materials are rare since they are generally destroyed by long-range interactions. On beamline I06 (see page 38), researchers have discovered such structures in antiferromagnetic (AF) thin films of iron oxide ( $\text{Fe}_2\text{O}_3$ ) for which the destructive, long-range interactions are absent due to the lack of a net magnetic moment. Using X-ray Magnetic Linear Dichroism (XMLD) based high-resolution vector magnet imaging in the Photoemission Electron Microscope (PEEM), vortex-antivortex pairs have been discovered and their interactions with a ferromagnetic cobalt overlayer determined. Furthermore, since  $\text{Fe}_2\text{O}_3$  exhibits a spin flop transition, which aligns the magnetic moments along the  $c$ -axis, it naturally provides new opportunities to test theoretical models of chiral structures formed by nucleation rather than fluctuations. The I06 PEEM has also been used by researchers to understand how AF domain wall motion can depend on the polarity of an injected current (see Fig. 1). In previous work, orthogonal in-plane current pulses were used to induce  $90^\circ$  rotations of AF domains that were not polarity dependent. In the new work, researchers have demonstrated that AF domain walls can be manipulated to realise stable and reproducible domain changes using just two electrical contacts. This represents a major breakthrough in switching AF materials since the effect can occur at much lower current densities than those needed for coherent domain rotation.

Skyrmions are topologically protected spin textures that arise from a subtle balance between the energies associated with the exchange interaction, the

spin-orbit interaction and magnetic anisotropy. Generally speaking, there are two types of skyrmions (Néel and Bloch), but recent theoretical work has predicted a chiral twist to this story at the surface of a material. By utilising the unique properties of the RASOR diffractometer on beamline I10 (see page 40) researchers have revealed how skyrmion structures change close to the surface using extinction effects in polarised soft X-ray resonant elastic scattering. The magnitude of these distortions is much larger than predicted by theory, indicating the need to include surface effects more accurately in theoretical models.

Spectroscopic probes of semiconductor band gaps or phenomena associated with states close to the Fermi energy have had a rich history of development at optical wavelengths. On beamline I16 (see page 42) researchers have combined the highly monochromatic and collimated X-ray beam with a carefully designed experimental setup to detect Parametric Down Conversion (PDC) of X-ray photons at energies corresponding to optical photons. The importance of PDC is that it detaches the spatial resolution limit from the wavelength of the probe light used. The breakthrough on I16 means that, for instance, local valence-electron charge maps can be generated using the sensitivity of visible light spectroscopy, but with atomic scale resolution. Moreover, numerical simulations predict that the PDC effect is two orders of magnitude weaker than that measured in the experiment, implying significant opportunities for a more detailed theoretical understanding of resonant and non-resonant effects in non-linear X-ray spectroscopy.



Sonka Reimers, a joint Nottingham and Diamond PhD student, using I06 to investigate how to store and read information in antiferromagnets.



“Over the last year, our research community has explored the fundamental properties of a wide range of naturally occurring and fabricated materials to discover a wealth of fascinating new phenomena.”

The Magnetic Materials Group Mechanical & Electrical Technicians that underpin the research across the facilities of the group, from left to right, back: Tom Rice, Chris Callaway, Andy Malandain, Ryan Russell. Front: Matthew Hilliard, Lee White, Mark Sussmuth, Richard Mott, Mike Matthews, Sam Embling.

The Magnetic Materials Group has had a busy year improving and extending the capabilities of its facilities for X-ray research. I21 accepted first users in October 2017 and has been operating in optimisation mode with

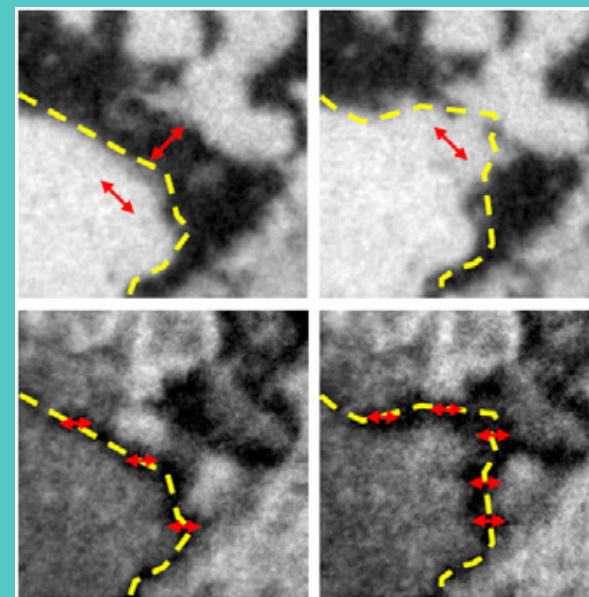


Figure 1: XMLD-PEEM images showing AF domain rotation and domain wall motion after current injection into a  $\text{CuMnAs}$  film grown on  $\text{GaP}$ . (Top) sample oriented to show AF domains before (left) and after (right) current injection. (Bottom) sample oriented to show the corresponding AF domain wall before (left) and after (right) current injection. The field of view is  $4 \mu\text{m}$ . The red arrows indicate the local AF axis and the broken yellow lines indicate the position of the AF domain wall. Adapted from P. Wadley et al., *Nat. Nanotech.* **13**, 362 (2018).

~50% of available beamtime allocated to the user programme. Towards the end of 2018, the beamline spectrometer was transformed from a discrete-port setup to a continuous-rotation configuration allowing, amongst other things, studies of emergent phenomena throughout the Brillouin zone. The exceptional efficiency of I21 has meant that the user community, together with the beamline team, have been able to measure magnon dispersion at

the O  $K$ -edge, detect extremely weak signals from thin films of only a few unit cells, and resolve  $f$ - $f$  excitations in heavy fermion systems. On I16, a new polarisation analyser stage and detector manifold has been installed, along with a Pilatus in vacuum area detector allowing improved efficiency at photon energies down to the S  $K$ -edge ( $\sim 2.5 \text{ keV}$ ). On I10, a new feedback system allows improved spatial resolution when mapping, for instance, electronic and magnetic domain structures. The new 1.6T electromagnet end station is now in the commissioning phase and will enable much faster absorption spectroscopy studies complementing the existing 14T superconducting facility. A new direct-electron detector has been installed on the I06 PEEM improving the quantum efficiency and increasing the frame rate to  $>1000\text{fps}$ . The PEEM manipulator has also been upgraded to reach lower temperatures ( $<60 \text{ K}$ ) whilst maintaining rapid azimuthal rotation of the sample. On B16, an X-ray imaging system has been developed and combined with on-the-fly scanning tomography enabling data acquisition times to be reduced from hours to seconds using the intense white beam available. In addition, a new Merlin quad-detector chip, based on the Medipix3, has been added, which further increases the efficiency of the diffraction and imaging facilities of the beamline. The remarkable imaging capabilities of B16 are demonstrated (see page 44) by recent work on the formation of aragonite in confined membranes. Using commercial filtration membranes, researchers were able to determine that precipitation of single-crystal aragonite in 25 nm diameter membranes could be significantly enhanced in the presence of Sulphur and Magnesium ions.

The Magnetic Materials Group is dedicated to continually developing and improving its facilities and off-line laboratories and would welcome further input from our user community. We organise regular workshops to explore new scientific and technical opportunities together with our user community. In the past year we have run workshops on Resonant Inelastic and Elastic X-ray Scattering (June 2018), Opportunities for Quantum Materials Research at Diamond-II (September 2018) and a workshop for the new Aberration-Corrected PEEM at Diamond (January 2019). Our objective is to run a suite of state-of-the-art polarised X-ray beamlines with leading edge software, along with access to advanced on-site sample characterisation facilities.

## Magnetic knots suggest a pathway to energy-efficient computers

**Related publication:** Chmiel F. P., Waterfield Price N., Johnson R. D., Lamirand A. D., Schad J., Van Der Laan G., Harris D. T., Irwin J., Rzchowski M. S., Eom C. B. & Radaelli P. G. Observation of magnetic vortex pairs at room temperature in a planar  $\alpha$ -Fe<sub>2</sub>O<sub>3</sub>/Co heterostructure. *Nat. Mater.* **17**, 581–585 (2018). DOI: 10.1038/s41563-018-0101-x

**Publication keywords:** Absorption; Spectra; Vortices

Computers based on silicon are energy-hungry, and the search for energy-efficient alternatives is increasingly important. Electronic components based on insulating magnetic oxides should be much more efficient at storing and manipulating information. In order to operate at room temperature, such devices would rely on the presence of 'magnetic knots' (vortices), which would protect stored information from thermal fluctuations.

A team of researchers from Diamond Light Source, the University of Oxford, and the University of Wisconsin-Madison predicted that magnetic vortices could exist in a very simple form of iron oxide, known as haematite, which is abundant in common rust. Vortices are amongst the simplest topological structures, but in some systems (such as crystals) long-range interactions hamper their formation. This is true for microscopic magnetic vortices, which are not commonly found in ferromagnetic materials. Haematite is an antiferromagnet; it has the same magnetic moments as a ferromagnet, combined in a way that does not produce a long-range effect.

The team also expected to be able to 'imprint' the vortices found in haematite onto a ferromagnetic material - cobalt. On the Nanoscience beamline (I06) they were able to use X-ray Photoemission Electron Microscopy (X-PEEM) to visualise vortices in both the haematite and cobalt simultaneously but independently, with a resolution of a few tens of nm. They also managed to manipulate the vortices with a magnetic field, and observed the presence of what could be interpreted as 'bits' of magnetic information in the cobalt layer, in the form of a different type of magnetic knot known as a 'meron'.

In spite of its extraordinary success in fuelling the IT revolution, silicon (CMOS) technology is intrinsically energy-inefficient. The heat flux generated by microprocessors is comparable to that on the Sun's surface, and their clock speeds stopped growing a decade ago to prevent complete meltdown. At the core of the problem is the fact that CMOS relies on the movement of electrical charge, which is associated with Joule heating. Although its commercial success seems unstoppable, power-hungry CMOS is ultimately doomed, and IT companies are actively scouting for new energy-efficient technologies to replace it. A nominal target of 1 attojoule/operation ought to be possible – after all, the human brain uses up approximately 1.5 attojoule/operation, and the ultimate physical limit (dictated by the so-called Landauer principle) is ~0.003 attojoule/operation at room temperature. However, we would have to improve by a factor of 1,000,000 to reach this target.

Several novel technologies are being investigated to address this crucial issue. One of the front runners among these 'beyond-CMOS' technologies is spintronics, which relies on spins rather than charges to process information.

However, much of the energy-efficiency of spintronics is lost if spin flipping – the elementary spintronic operation – must itself be performed by electrical currents. For this reason, voltage control of magnetic components is widely considered to be the key to large-scale commercialisation of spintronics. The field of oxide electronics emerges precisely from the consideration that oxides can display a multitude of intriguing multi-functional properties in their insulating states. Moreover, oxides are already integrated with CMOS, are generally stable, and are compatible with other spintronic components. Insulating oxides of magnetic transition metals such as iron, cobalt, and manganese, have many of the required properties to achieve voltage control of spins, since their charge, orbital, and magnetic states are intertwined. This can be further enhanced by exploiting the power of topology. It is well known that ordinary magnetic 'bits' are thermally unstable when very small in size, but this can be overcome, quite literally, by tying the spins into 'magnetic knots'. Very recently, topological structures such as skyrmions, vortices, and 'merons' (see below) have shown enormous potential to enhance the performances of both spintronics and oxide materials, since they can be stable at room temperature and above even when very small, and can be manipulated at very low energy cost.

Work recently published in *Nature Materials*<sup>1</sup> presented what could be a major breakthrough in this field<sup>2</sup>: for the first time, small-scale hybrid oxide/metal topological magnetic objects were created, consisting of spin vortices in antiferromagnetic iron oxide (Fe<sub>2</sub>O<sub>3</sub>), tightly coupled with spin 'merons' in ferromagnetic metallic cobalt (Co). One particularly appealing feature of this system is that it employs cheap and readily available materials – Fe<sub>2</sub>O<sub>3</sub> is the most abundant constituent of common rust! Moreover, the film fabrication method was relatively simple, raising hopes that it could be deployed on a commercial scale.

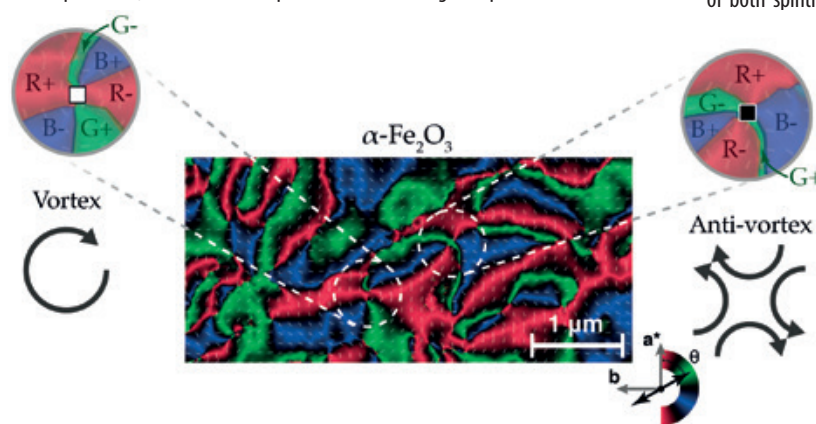


Figure 1: Map of the antiferromagnetic spins in the Fe<sub>2</sub>O<sub>3</sub> layer. Colour represents the axis of the antiferromagnetic moments (colour bar bottom right). The two insets (left and right) highlight a vortex and anti-vortex respectively. The three colours (red, green, blue) represent the three possible spin directions allowed by the magnetic symmetry of Fe<sub>2</sub>O<sub>3</sub>.

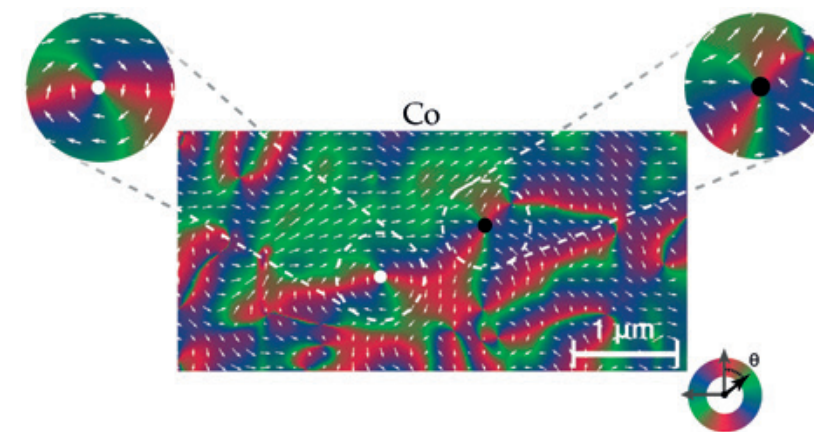


Figure 2: Map of the ferromagnetic spins of the Co layer. Colour and arrows represents the direction of the ferromagnetic moments (colour bar bottom right). The two insets (left and right) highlight a vortex and anti-vortex respectively.

The journey towards this discovery illustrates the power of analogies and generalisations in physics. Vortices are common in nature at all length scales, from galaxies (~10<sup>5</sup> light years), through to hurricanes and ordinary sink whirlpools, down to sub-micron objects. The visual similarity between all these objects belies a much deeper topological analogy – for example, all vortices 'swirl' around a one-dimensional singularity (a core), regardless of what exactly is the swirling field. In the early 70s, the famous British physicist Tom Kibble discussed in great detail the topology of vortices, and also pointed out that these structures can often be described by an 'effective' phenomenological theory<sup>3</sup>. Although primarily concerned with the formation of cosmic strings (thereby providing inspiration to countless science fiction stories), Kibble's theory was later applied to describe the tiny quantum vortices that form in superfluid helium.

As Kibble remarked, vortices are generally destroyed by long-range interactions, so they would be extremely difficult to stabilise in ordinary magnets. The only known method to create magnetic vortices is to fabricate tiny (sub-micron) magnetic disks – an expensive process that is difficult to scale up commercially. One possible solution is to use an antiferromagnet, in which spins are exactly compensated at the atomic scale, and do not generate a long-range field. As it turns out, Fe<sub>2</sub>O<sub>3</sub> is almost perfect in this respect, because it can be described by a phenomenological theory that is very close to Kibble's 'cosmic strings' theory. However, the advantage of Fe<sub>2</sub>O<sub>3</sub>, and all antiferromagnets, comes with a major drawback: they do not have a net magnetic moment that can be detected or modified with external magnetic fields, and therefore their vortices are extremely difficult to observe. To overcome this issue, the ideal technique is synchrotron X-ray Photoemission Electron Microscopy (X-PEEM), which is able to resolve magnetic structures as small as a few tens of nanometres by measuring the light polarisation dependency of the X-ray Absorption (XAS) coefficient of a material. An added bonus of this method is that it is element-specific, and can measure ferromagnets and antiferromagnets independently, even when they are stacked on top of each other. This led to the idea of depositing a very thin layer of ferromagnetic Co on top of Fe<sub>2</sub>O<sub>3</sub>, in a sense mimicking a typical spintronic device configuration.

The experiments were performed using the I06 beamline at Diamond, reconstructing a single spin map by merging polarisation dependent X-PEEM images recorded across a range of different sample orientations. This technique, known as vector mapping, takes advantage of the anisotropic nature of XAS in ferromagnets or antiferromagnets. This method was first applied to image the antiferromagnetic spin map of the Fe<sub>2</sub>O<sub>3</sub> layer (Fig. 1) revealing a network of whirling magnetic vortices hundreds of nanometres in size, as well as more exotic anti-vortices. Based on Kibble's theory, vortices and anti-vortices can annihilate, and they were seen occasionally to do so in the experiment (perhaps under the influence of the X-ray beam), although most of

the vortex-antivortex network remained very stable. Later, the instrument configuration was switched to observe the Co over-layer. What was seen confirmed the team's predictions: the Fe<sub>2</sub>O<sub>3</sub> had 'imprinted' itself onto the adjacent metallic layer, forming tiny ferromagnetic vortices/antivortices exactly on top of the antiferromagnetic counterparts (Fig. 2). But – one may ask – what happens at the exact centre of the vortex? Once again, the power of analogy – helped by powerful finite-element simulations – provided the answer. The analogy here is with the 'eye of the storm' in a hurricane: whereas throughout the storm the wind whirls parallel to the ground, in the eye the flow is downwards towards the ground, whence the high pressure and clear

skies. Likewise, at the centre of a ferromagnetic vortex, the spins are expected to lift out of the plane of the film, forming a topological structure known as a 'meron' (Fig. 3). Hints of 'meron' cores could be seen in the data, although the resolution of the measurements was not quite sufficient to confirm them unambiguously. Finite-element simulations confirmed that 'merons' with very small cores (10 nm) should form in these conditions. If corroborated by higher-resolution data, the existence of 'merons' would be extremely exciting; a 'meron' core would in effect act as an extremely small memory bit, which would be topologically protected against thermal fluctuations by the surrounding vortex. Further beamtime at Diamond has been allocated for a new experimental campaign to control the density of magnetic vortices, and to investigate their presence in other materials and architectures.

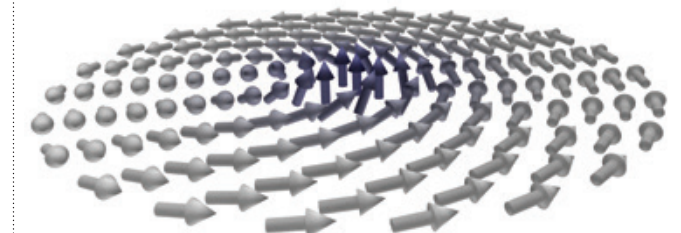


Figure 3: Artistic rendering of a 'meron'. A spin 'meron' is characterised by a swirling of magnetic spins, which rise out of their plane of rotation at the 'meron' core. Finite-element simulations indicate that vortices observed in the Co core are likely to be 'merons'.

### References:

- Chmiel F. P. *et al.* Observation of magnetic vortex pairs at room temperature in a planar  $\alpha$ -Fe<sub>2</sub>O<sub>3</sub>/Co heterostructure. *Nat. Mater.* **17**, 581–585 (2018). DOI: 10.1038/s41563-018-0101-x
- Fiebig M. Symmetry and magnetism allied. *Nat. Mater.* **17**, 567–568 (2018). DOI: 10.1038/s41563-018-0113-6
- Kibble T. W. B. Topology of cosmic domains and strings. *J. Phys. A Gen. Phys.* **9**, 1387–1398 (1976). DOI: 10.1088/0305-4470/9/8/029

### Funding acknowledgement:

The work done at the University of Oxford was funded by EPSRC grant no. EP/M020517/1, entitled Oxford Quantum Materials Platform grant, and by a Royal Society University Research Fellowship. The work at University of Wisconsin-Madison was supported by the Army Research Office through grant nos W911NF-13-1-0486 and W911NF-17-1-0462.

### Corresponding author:

Prof Paolo G. Radaelli, University of Oxford, p.g.radaelli@physics.ox.ac.uk

## Next-gen memory: How skyrmions behave at surfaces

**Related publications:** Zhang S. L., van der Laan G., Wang W. W., Haghighirad A. A. & Hesjedal T. Direct Observation of Twisted Surface skyrmions in Bulk Crystals. *Phys. Rev. Lett.* **120**, 227202 (2018). DOI: 10.1103/PhysRevLett.120.227202; Zhang S., van der Laan G., Müller J., Heinen L., Garst M., Bauer A., Berger H., Pfleiderer C. & Hesjedal T. Reciprocal space tomography of 3D skyrmion lattice order in a chiral magnet. *Proc. Natl. Acad. Sci.* **115**, 6386–6391 (2018). DOI: 10.1073/pnas.1803367115

**Publication keywords:** Resonant elastic X-ray scattering (REXS); Magnetic skyrmions; Surface reconstruction

**M**agnetic skyrmions are promising candidates for the next generation of memory devices as they allow increased storage density, and require less energy. The established methods for studying skyrmions, e.g. neutron diffraction and electron microscopy, are not sensitive to the near-surface region of a sample, which is the area most relevant for applications.

In order to characterise the 3D structure of the skyrmion lattice for the first time, an international team of researchers established a new X-ray technique for the direct measurement of the helicity angle – a quantity that is characteristic for the different types of skyrmions. They then made use of the uniquely tunable surface-sensitivity of soft X-rays, tuning the energy of the incident X-rays across the absorption edge, while carrying out circular dichroism of resonant elastic X-ray scattering peak technique. This allowed them to fully reconstruct the detailed structure of the skyrmion lattice as a function of depth, information crucial for enabling future skyrmion-based devices.

The soft X-ray diffractometer RASOR on the Beamline for Advanced Dichroism (I10) is extremely well-suited for characterising skyrmion structures. It offers ultra-high reciprocal space resolution, allowing clear observation of magnetic signals, with an advanced sample environment (ultra-high vacuum (UHV), high temperature stability, magnetic vector field, and multi-axis goniometer).

The discovery of skyrmions in chiral magnets, featuring non-trivial topological winding described by a highly unusual emergent electrodynamics, has inspired tremendous efforts to read, write, and manipulate individual skyrmion bubbles, as well as skyrmionic textures in tailored nano-systems amenable for data storage, transmission, and processing<sup>1</sup>. So far, skyrmions have been mostly treated as two-dimensional objects that extend into the third dimension forming tubular structures. However, it is well-known that the abrupt change of boundary conditions (truncated crystal) can lead to a shift in atomic positions in order to lower energy, commonly known as a (structural) surface reconstruction. Similarly, magnetic structures at or in the vicinity of a

surface may be fundamentally different from the bulk, resulting from broken symmetry or non-continuous properties. Different mechanisms have been discussed as the underlying cause of magnetic surface effects, which depend on the intrinsic and extrinsic properties of the system, and which may be present at the same time, leading to a magnetic surface reconstruction. Their presence has far-reaching implications for the creation of skyrmions in surface-dominated systems. More generally, it identifies surface-induced magnetic effects as an uncharted scientific territory, in particular due to the lack of experimental tools allowing for their study.

Magnetic skyrmions are characterised by the topological winding number  $N$ , radial profile, polarity, and helicity angle  $\chi$ . Prior to our work, only two types of  $N = 1$  skyrmions with different helicity angles were experimentally confirmed, i.e., Néel-type skyrmions ( $\chi = 0^\circ$  or  $180^\circ$ ) that exist at the surface/interface of thin film systems with strong spin-orbit coupling, and Bloch-type chiral skyrmions which are found in chiral magnets, such as MnSi and  $\text{Cu}_2\text{OSeO}_3$  ( $\chi = \pm 90^\circ$ ). We recently developed a set of new resonant elastic X-ray scattering (REXS) based methods<sup>2</sup> with which the winding number  $N$ , and the exact value of the helicity angle  $\chi$ , can be unambiguously determined, making use of circular dichroism. The hexagonally long-range ordered skyrmion lattice phase gives rise to a six-fold-symmetric diffraction pattern in REXS<sup>2</sup> (see Fig. 1).

Circular dichroism (CD), the difference between the intensities obtained using left- and right-circularly polarised incident light, is known to be sensitive to the chirality of a

*Figure 1: It's skyrmion time! Look-up 'clock' illustrating the one-to-one correspondence of the extinction direction (red arrow) and the skyrmion helicity angle. The circular dichroism (CD) of the diffraction peaks is obtained by taking the difference of the diffraction intensities with left- and right-circularly polarised incident light. The CD-REXS pattern for a skyrmion lattice state exhibits positive and negative peaks (yellow and blue spots), separated by the indicated extinction direction at which the CD intensity vanishes. Adapted from Phys. Rev. Lett. 120, 227202 (2018).*

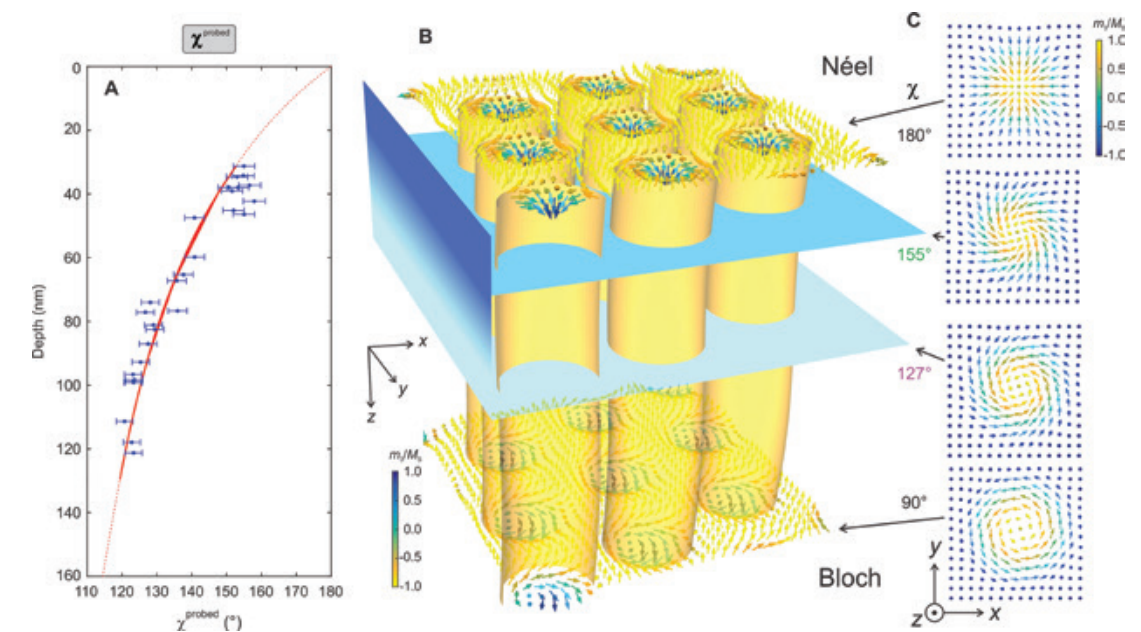
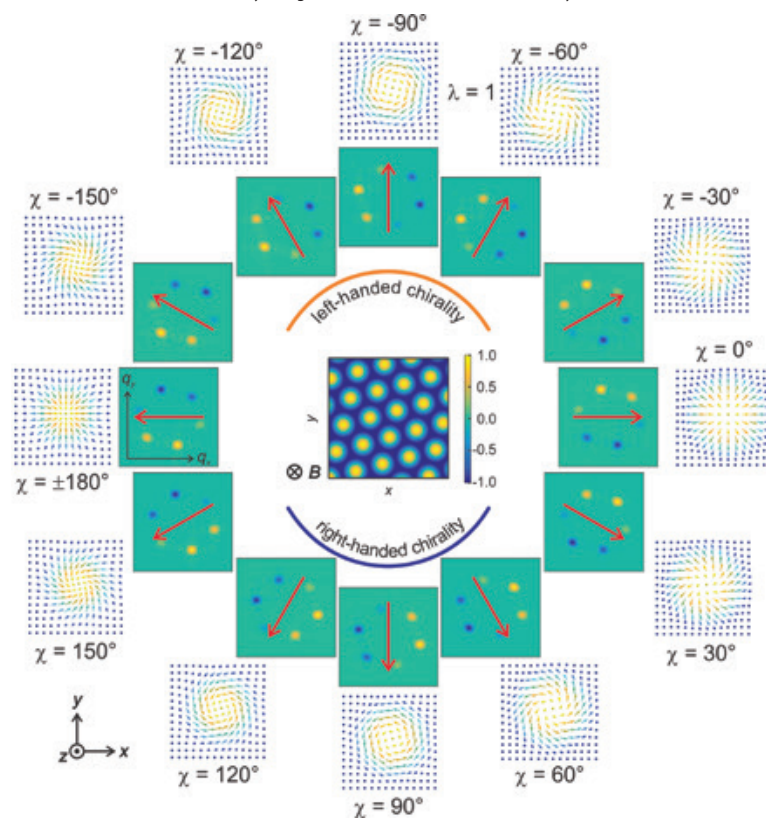


*Figure 2: Depth-dependent probing and model of the skyrmion surface state in  $\text{Cu}_2\text{OSeO}_3$ . (a) Depth-dependence of the averaged helicity angle ( $\chi^{\text{probed}}$ ) and fit to the data (red curve) using the model in (b). At the top surface, the skyrmions are Néel-type with  $\chi = 180^\circ$ . The helicity angle continuously decreases when probing deeper into the crystal, eventually reaching the well-characterised bulk skyrmion state with  $\chi = 90^\circ$ . (b) Illustration of the skyrmion crystal with its surface state. In (c), the corresponding skyrmion magnetisation patterns for the indicated helicity angles are shown. Adapted from PNAS 115, 6386–6391 (2018).*

material. In our experiment, the CD-REXS was obtained by integrating a series of reciprocal-space-map scans for each polarisation separately, followed by normalisation and subsequent subtraction of the left- and right-circularly polarised patterns<sup>4</sup>. The direct CD-REXS pattern shows six magnetic peaks with varying CD intensities, and a distinct boundary that separates the positive and negative halves. Each  $\chi$  corresponds to a characteristic CD-REXS pattern, in which a dichroism extinction vector can be defined as illustrated by the red arrows in Fig. 1. Consequently, the orientation of the dichroism extinction vector exclusively reveals the helicity angle, which is a unique characteristic of a skyrmion.

The RASOR diffractometer on beamline I10 is uniquely suited for soft X-ray resonant magnetic diffraction experiments of the skyrmion lattice state. RASOR has ultra-high reciprocal space resolution – a necessary condition for the observation of these magnetic structures – and its large UHV chamber allows for the incorporation of a magnetic vector field setup, which is essential for stabilising the skyrmion lattice state.

Furthermore, by tuning the energy of the incident X-rays, it is possible to systematically vary the probing depth to perform a depth-dependent mapping of the magnetic state. At the  $2p$  absorption edge of a  $3d$  transition metal, the soft X-rays are particularly surface-sensitive as the absorption is large, whereas away from the absorption maximum, increasingly deeper layers are probed as well. In the case of the investigated material,  $\text{Cu}_2\text{OSeO}_3$ , the probing depth was tuned from  $\sim 31$  nm (at  $\text{Cu } L_2$  resonance at 931.25 eV) to  $\sim 77$  nm at 932.45 eV. In a CD-REXS experiment, the spectroscopic measurement therefore provides a strategy to obtain the helicity angle as a function of depth in a three-dimensional skyrmion crystal. From measurements as a function of the photon energy, we obtain the probed helicity angle as a function of depth (see Fig. 2a). Very much in contrast to the expected Bloch-type skyrmion ( $\chi = 90^\circ$ ),  $\chi(z)$  shows a smooth variation of the skyrmion type with depth (Fig. 2b). Most interestingly, on the top surface of  $\text{Cu}_2\text{OSeO}_3$ , the skyrmions have  $\chi \approx 180^\circ$ , which is not expected for a chiral magnet in any existing theoretical framework. Deep below the surface in the bulk, Bloch-type skyrmions are found as expected, however, pushed an order of magnitude further down than predicted by recent models.

In conclusion, we present the observation of a new topological surface state, and a new form of skyrmion ordering. By using a novel X-ray diffraction

technique (CD-REXS), we were able to determine the skyrmion helicity angle as a function of depth along the skyrmion tubes. Our study surprisingly reveals Néel-type surface skyrmions, and a continuous transformation into the well-established Bloch-type bulk state with increasing depth. The recently developed theoretical 3D skyrmion models, which have predicted minute surface effects, greatly underestimate its magnitude, emphasising the unexpected significance of the surface. Our findings further highlight the fact that the helicity angle is a degree of freedom for magnetic skyrmions, which can take different values. A detailed knowledge of surface effects will allow us to tailor nanostructures<sup>5</sup>, thereby unlocking the door for the engineering of new skyrmion devices.

### References:

- Fert A. *et al.* Magnetic skyrmions: advances in physics and potential applications. *Nat. Rev. Mater.* **2**, 17031 (2017). DOI: 10.1038/natrevmats.2017.31
- Zhang S. L. *et al.* Resonant elastic x-ray scattering from the skyrmion lattice in  $\text{Cu}_2\text{OSeO}_3$ . *Phys. Rev. B* **93**, 214420 (2016). DOI: 10.1103/PhysRevB.93.214420
- Zhang S. L. *et al.* Topological Winding Number of Skyrmions. *Nat. Commun.* **8**, 14619 (2017). DOI: 10.1038/ncomms14619
- Zhang S. L. *et al.* Direct experimental determination of spiral spin structures via the dichroism extinction effect in resonant elastic soft x-ray scattering. *Phys. Rev. B* **96**, 94401 (2017). DOI: 10.1103/PhysRevB.96.094401
- Zhang S. *et al.* Real-Space Observation of Skyrmionium in a Ferromagnet-Magnetic Topological Insulator Heterostructure. *Nano Lett.* **18**, 1057–1063 (2018). DOI: 10.1021/acs.nanolett.7b04537

### Funding acknowledgement:

We acknowledge financial support by the Semiconductor Research Corporation (SRC), and the Engineering and Physical Sciences Research Council under grant EP/N032128/1.

### Corresponding author:

Dr Shilei Zhang, University of Oxford,  
Shilei.Zhang@physics.ox.ac.uk

## Nonlinear spectroscopy with X-rays

**Related publication:** Schori A., Bömer C., Borodin D., Collins S. P., Detlefs B., Moretti Sala M., Yudovich S. & Shwartz S. Parametric Down-Conversion of X Rays into the Optical Regime. *Phys. Rev. Lett.* **119**, 253902 (2017). DOI: 10.1103/PhysRevLett.119.253902

**Publication keywords:** Spectroscopy; Nonlinear optics; Second order nonlinear optical processes; Parametric down-conversion; Valence electrons

**A**n international team of researchers has demonstrated a novel method for studying the microscopic structure of chemical bonds, the valence electron density of crystals, and light-matter interactions at the atomic scale resolution, with synchrotron radiation. The goal of the work was to develop a technique that provides spectroscopic and structural information on valence electrons in a single measurement, this new approach enables the measurements of atomic scale interactions of valence electrons, providing access to microscopic scale effects.

The team chose the Materials and Magnetism beamline (I16) at Diamond Light Source for their experiments due to its high photon flux, the high collimation of the X-ray source, and the combined energy resolution of the monochromator-analyser setup. They combined spectroscopic information with structural information to enhance understanding of microscopic inter-molecular processes.

Their results provide the first observation of parametrically down-converted (PDC) X-ray signal photons at photon energies that correspond to idler photons at optical wavelengths. They demonstrate that the conversion of X-rays into optical photons may be used as a new tool to probe microscopic valence charge densities and optical properties of materials on the atomic scale with synchrotron radiation. This novel tool can be used to test and improve the understanding of condensed matter physics.

The understanding of the interactions of valence electrons with light, and with each other, is essential for the understanding of many phenomena in physics, chemistry, and biology. However, although optical radiation has been extensively used to study the properties of valence electrons, optical radiation spectroscopy methods do not provide atomic scale information due to their long wavelengths. While X-ray Bragg diffraction can reveal structural information at the atomic scale, those types of experiments cannot provide spectroscopic information on valence electrons. Thus, the understating of the microscopic nature of valence electron interactions remains a great challenge.

Nonlinear interactions of X-rays and long wavelengths can provide insight into the microscopic structure of chemical bonds, the valence electron density

of crystals, and light-matter interactions at the atomic scale resolution<sup>1</sup>. In essence, the high resolution stems from the short wavelengths of X-rays, whereas the long wavelength field is used to probe the interactions with the valence electrons. The effect could be considered as X-ray diffraction from optically modulated charge densities. In analogy to Bragg diffraction, the atomic scale resolution can be achieved by measuring the intensities for different atomic planes but, in contrast to Bragg diffraction, in the nonlinear process the intensity is proportional to the Fourier coefficient of the valence electrons, and not to the coefficient of the core electrons.

To date, there was only one observation of nonlinear interactions between X-rays and optical radiation. Glover *et al.* measured nonlinear wave mixing

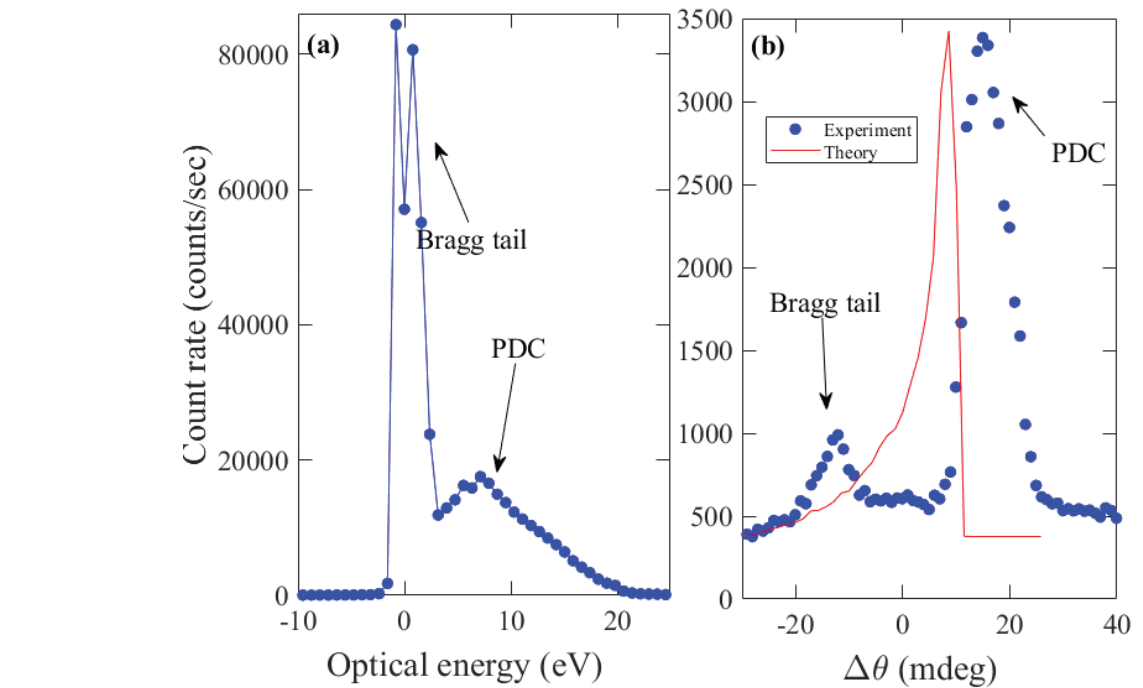


Figure 2: (a) X-ray signal count rate as a function of the analyser detuning from the photon energy of the input beam. (b) X-ray count rate as a function of the pump deviation angle from the phase matching angle. The blue dots are the experimental results and the solid red line is calculated from theory.

between X-rays and optical radiation by using the first hard X-ray free-electron laser<sup>2</sup>, and an optical laser. However, it is very challenging to perform further progress with this effect, mainly because it requires high optical intensities, which are above the radiation damage threshold of most materials.

In this work, we have demonstrated the nonlinear effect of parametric down-conversion (PDC) of X-rays into the optical regime. In this nonlinear effect, which is another wave mixing effect that relies on the same nonlinear mechanism, the input photons interact with vacuum fluctuations to generate correlated X-ray and optical photon pairs. Since the photons are always generated in pairs, and since the process conserves energy and momentum, the generation rate, the photon energy, and the angle of propagation of the generated X-ray photons are perfectly correlated with the long wavelength photons. Consequently, it is sufficient to measure only the X-ray signal to probe the properties of the sample at energies corresponding to long wavelength photons. Several demonstrations of PDC into extreme ultraviolet were reported<sup>3,4</sup>, but the extension of this method into the optical regime is more challenging due to the proximity of the photon energy to the input photon energy.

The experiments were conducted at ID-20 (ESRF) and at I16. The measurements were performed with a highly collimated monochromatic beam at 9 and 11 keV, to illuminate a diamond crystal for the generation of the PDC. The emitted X-ray photons were collected by a system that contains slits, a crystal analyser, and a detector (Fig. 1). The diffraction was from the C(220) atomic planes.

Fig. 2a shows the spectrum of the effect. The peak on the left corresponds to the elastic scattering, and the broad peak is the PDC signal. The peak is observed at 7.1 eV, where the efficiency of the PDC is the largest. This energy is near the bandgap of the diamond crystal, where the density of states of the valence electrons is the highest. This observation demonstrates the ability to measure the valence electron spectral dependencies.

To demonstrate the ability to calculate the Fourier component of the nonlinear susceptibility, the rocking curve of X-ray signal of PDC at an optical wavelength that corresponds to 2.2 eV was measured (Fig. 2b). The small peak

on the left is the residual elastic, and the peak centred at 15 mdeg from the origin is the PDC signal. The Fourier coefficient of the susceptibility obtained from the measurement is comparable to the theoretical prediction, and to the result of X-ray and optical mixing experiment<sup>2</sup>.

The first observation of PDC of X-ray into optical radiation is reported. The results advance the possibility to use the effect as a new tool to probe microscopic valence charge densities, and optical properties of materials on the atomic scale. This novel tool can be used to test and improve the understanding of condensed matter physics.

### References:

- Freund I. *et al.* Optically modulated X-ray diffraction. *Phys. Rev. Lett.* **25**, 1241–1245 (1970). DOI: 10.1103/PhysRevLett.25.1241
- Tamasaku K. *et al.* Visualizing the local optical response to extreme-ultraviolet radiation with a resolution of  $1\lambda/380$ . *Nat. Phys.* **7**, 705–708 (2011). DOI: 10.1038/nphys2044
- Hastings J. B. *et al.* X-ray and optical wave mixing. *Nature* **488**, 603–608 (2012). DOI: 10.1038/nature11340
- Borodin D. *et al.* High energy-resolution measurements of x-ray into ultraviolet parametric down-conversion with an x-ray tube source. *Appl. Phys. Lett.* **110**, 131101 (2017). DOI: 10.1063/1.4979413

### Funding acknowledgement:

Israel Science Foundation (ISF) (1038/13); Marie Curie FP7 Integration Grant within the 7th European Union Framework Programme (PCIG13-GA-2013-618118); Ministry of Aliyah and Immigrant Absorption of Israel; Deutsche Forschungsgemeinschaft (DFG) via SFB925 (Teilprojekt A4).

### Corresponding author:

Dr Sharon Shwartz, Bar-Ilan University, sharon.shwartz@biu.ac.il

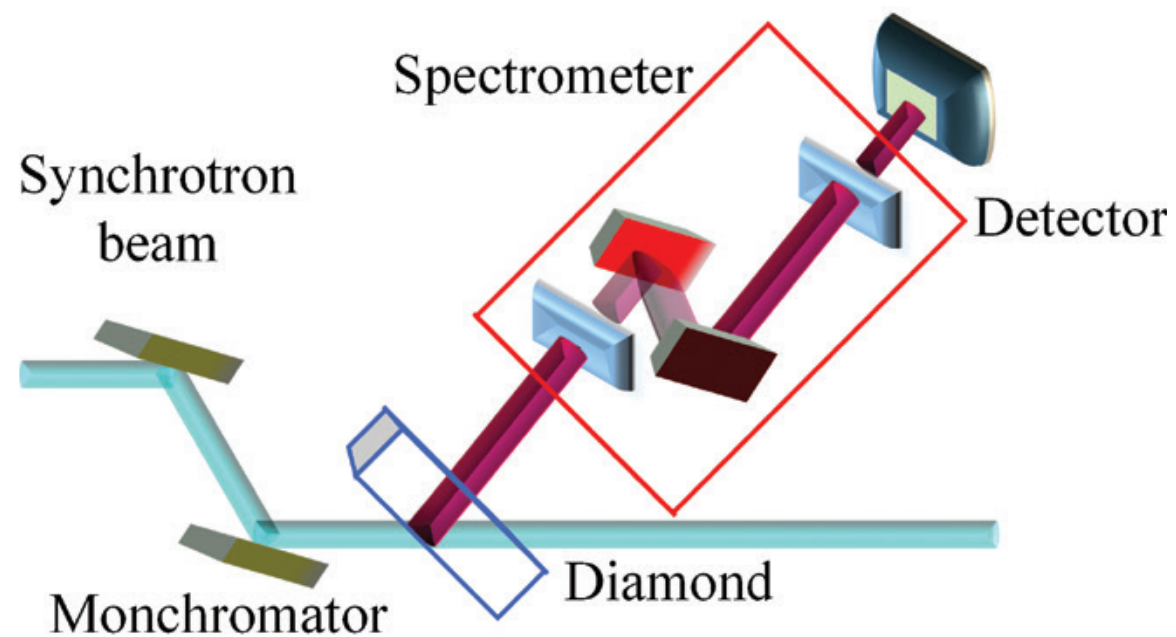


Figure 1: Experimental setup. The scattering plane of the analyser was normal to the scattering plane of the sample. S1 and S2 are the slits before the analyser and before the detector. The analyser was a Si(440) crystal and the detector was an avalanche photodiode.

## Confinement effects promote the formation of aragonite

**Related publication:** Zeng M., Meldrum F. C., Kim Y.-Y., Laundry D., Frontera C., Anduix-Canto C., Kapur N. & Christenson H. K. Confinement generates single-crystal aragonite rods at room temperature. *Proc. Natl. Acad. Sci.* 115, 7670–7675 (2018). DOI: 10.1073/pnas.1718926115

**Publication keywords:** Calcium carbonate; Biomineralisation; Bio-inspired crystallisation; Biomimetic; Confinement

**A**ragonite is a common crystalline form (polymorph) of calcium carbonate, an important biomineral found, for example, in seashells. Outside of the natural environment, aragonite usually only crystallises from solution at high temperatures, or in the presence of magnesium ions. However, although organisms can readily form aragonite, the way in which they do so remains unclear.

A team of researchers from the University of Leeds, the Institut de Ciència de Materials de Barcelona, and Diamond Light Source explored whether the confined volumes in which all biomineralisation occurs allows organisms to control calcium carbonate production.

To investigate how confined volumes affect the precipitation of calcium carbonate, they precipitated calcium carbonate in the cylindrical pores of commercially-available filtration membranes. As these membranes are available with a wide range of pore diameters, the researchers were able to systematically investigate the relationship between the pore diameter and the calcium carbonate polymorph formed.

The team only had small volumes of sample material to work with, and so used the micro-focus capability of the Test beamline (B16) to obtain powder X-ray diffraction patterns. They found that oriented single crystals of aragonite were the sole product from additive-free solutions in 25 nm pores, and significant quantities of aragonite formed in pores as large as 200 nm in the presence of low concentration of magnesium and sulphate ions. This study shows that confinement effects can promote the formation of aragonite, and suggests that organisms may exploit confinement effects to control calcium carbonate formation.

Organisms exhibit remarkable control over mineralisation processes, generating biominerals with complex morphologies, hierarchical structures, and outstanding mechanical properties<sup>1</sup>. However, while many of nature's strategies for controlling biomineralisation are known, the mechanisms by which organisms control crystal structure are poorly understood. While it was long believed that the proteins entrapped within biominerals would hold the key, precipitation of calcium carbonate in the presence of proteins extracted from calcite or aragonite biominerals (where these are "polymorphs" of calcium carbonate, having the same composition but different crystal structure) failed to deliver polymorph control. The work described here explores an alternative explanation. It is well known that biominerals invariably form within small volumes, and that these can strongly influence crystallisation processes<sup>2,3</sup>. A simple system – crystallisation within the cylindrical pores of commercial filtration membranes – was therefore used

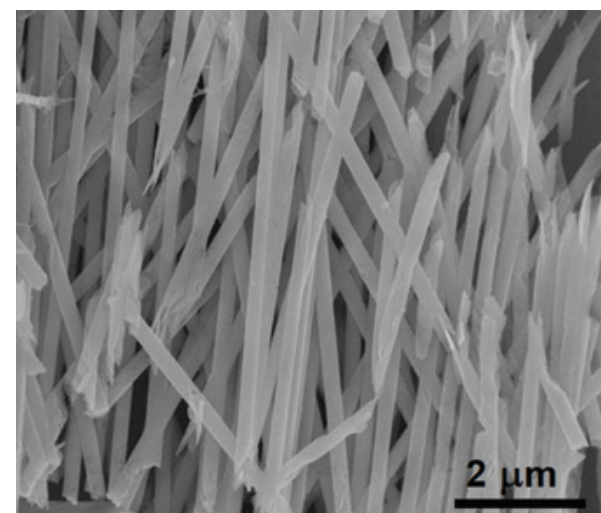


Figure 1: Calcium carbonate rods precipitated within pores of diameter 200 nm.

to systematically investigate how confinement influences calcium carbonate polymorph.

Experiments were conducted in the absence of additives, and in the presence of low concentrations of sulphate and magnesium ions. These are significant components of the seawater in which many organisms live, and can promote aragonite formation. It would therefore be surprising if they do not contribute to aragonite formation *in vivo*. Calcium carbonate was precipitated within track-etched membranes by placing membranes between two half U-tube arms, one which was filled with a solution containing calcium and magnesium ions, and the other with a solution containing carbonate and sulphate ions. Calcium carbonate is precipitated when the calcium and carbonate ions meet in the pores<sup>4</sup>.

Reaction conditions containing low concentrations of magnesium and sulphate ions were used, where these produced only a few percent aragonite in bulk solution. Rod-shaped crystals with lengths comparable to the membrane thickness formed in the pores (Fig. 1). The structure of these crystals was then investigated. For crystals formed in the larger pores, it was possible to extract sufficient material to carry out powder X-ray diffraction – a method that fingerprints the structure of crystals – using a laboratory instrument. This showed that the crystals formed within the 1,200 nm pores were almost entirely calcite, while those in the 800 nm pores were 81% calcite and 19% aragonite. Further reduction in the pore size to 200 nm increased the proportion of aragonite to 69%.

In order to characterise the polymorphs of the crystals formed in smaller pores, however, it was necessary to use synchrotron micro-beam XRD, where this was conducted at beamline B16. The analysis showed that aragonite was the only polymorph present in the 50 nm and 25 nm pores (Fig. 2). Individual rods grown in the 200, 50 and 25 nm pores were also investigated using electron diffraction (performed in a transmission electron microscope)

to gain further information on their structures, and to identify if they were oriented with respect to the pore. The aragonite crystals grown in the 200 nm pores were polycrystalline and showed no preferential orientation. Those in the 50 nm pores, in contrast, were almost single crystals, while the 25 nm rods were single crystals (Fig. 3). These aragonite crystals were also preferentially oriented with their crystallographic *c*-direction parallel to the pore axis, such that 50% and 100% of rods in the 50 and 25 nm pores were oriented in this way.

Finally, experiments were conducted in the absence of magnesium and sulphate ions. Very little aragonite formed in the 1,200 and 800 nm pores, just 8% in the 200 nm pores, and a significant increase to 47% was recorded in the 50 nm pores. Precipitation within the 25 nm pores, however, yielded a most unexpected result – aragonite single crystals formed in the absence of any additives in these very small pores.

These results therefore demonstrate that confinement can promote the formation of aragonite such that all of the crystals precipitated in 25 nm pores were aragonite under additive-free conditions. This effect is enhanced in the presence of low concentrations of magnesium and sulphate ions. But what are the origins of these effects? Calcite/aragonite polymorphism is a complex problem that has challenged researchers for decades. The production of these mineral phases from solution is dependent on kinetics as well as thermodynamics, and thus on variables including temperature, concentration, and the presence of additives. While aragonite is only slightly less thermodynamically stable than calcite at room temperature, it typically only appears as a minor product on precipitation from additive-free solutions at room temperature.

The possibility that the small pores affect the transport of ions to growing crystals – which may influence polymorph<sup>5</sup> – was explored by modelling the diffusion of ions through the membrane pores. This showed that the calcium and carbonate solutions were fully mixed in under 0.1 sec, where mixing is rapid due to the short length of the pores. This cannot then be the origin of the polymorph change. The membrane surface may also have a significant influence on crystal formation. This was explored by analysing our data to explore the relationship between the aragonite fraction and the pore diameter. A graph of the aragonite fraction versus the inverse of the pore diameter revealed a roughly linear relationship between these quantities. This is expected if the number of aragonite nucleation sites is proportional to

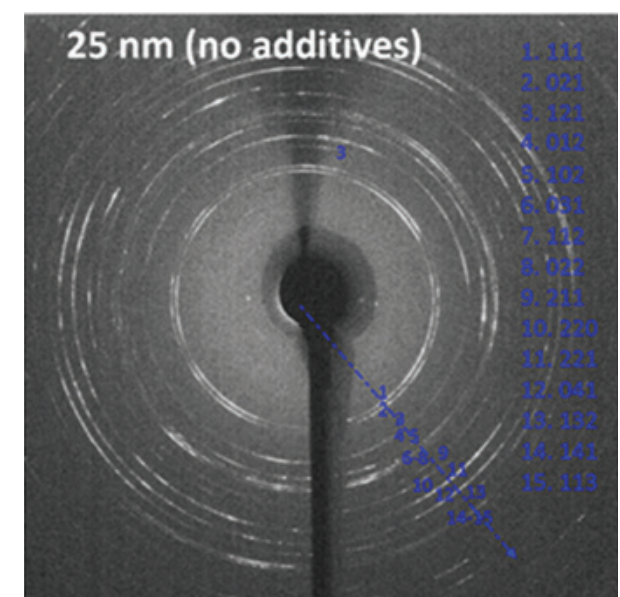


Figure 2: Synchrotron micro-beam pXRD pattern of aragonite crystals precipitated in 25 nm pores in the absence of additives.

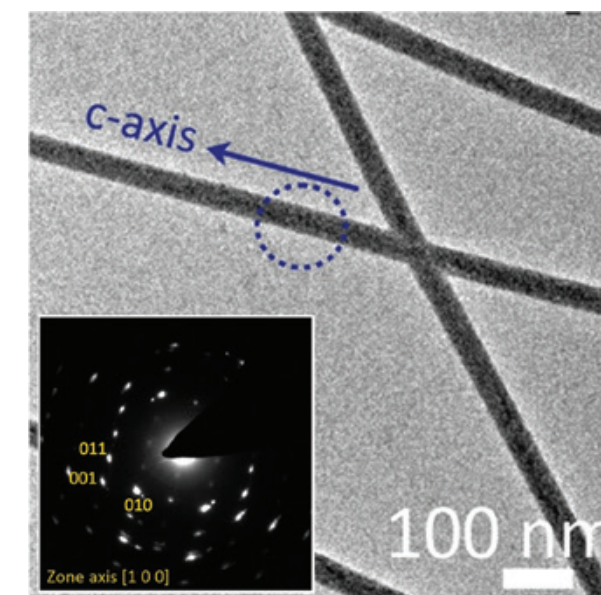


Figure 3: Transmission Electron Microscope (TEM) image and electron diffraction pattern (inset) of an aragonite rod precipitated within a 50 nm pore.

the surface area. Thus, as the surface increases in importance relative to the bulk with the degree of confinement, the proportion of aragonite increases. The distribution of ions adjacent to a charged membrane surface can also differ significantly in a membrane pore as compared to a planar surface, which may contribute to the effects seen.

This study demonstrates that confinement can promote the formation of aragonite, and that this is intimately linked to the properties of the confining surface. These results are of particular significance to calcium carbonate biomineralisation, which invariably occurs in privileged environments bound by organic matrices. Confinement effects may enhance the influence of such organic frameworks on crystallisation, enabling organisms to achieve superior control over characteristics such as polymorph or orientation.

### References:

1. Biomineralization: Principles and Concepts in Bioinorganic Materials Chemistry (2002). ISBN:9780198508823
2. Stephens C. J. *et al.* Amorphous calcium carbonate is stabilized in confinement. *Adv. Funct. Mater.* **20**, 2108–2115 (2010). DOI: 10.1002/adfm.201000248
3. Anduix-Canto C. *et al.* Effect of nanoscale confinement on the crystallization of potassium ferrocyanide. *Cryst. Growth Des.* **16**, 5403–5411 (2016). DOI: 10.1021/acs.cgd.6b00894
4. Loste E. *et al.* Precipitation of calcium carbonate in confinement. *Adv. Funct. Mater.* **14**, 1211–1220 (2004). DOI: 10.1002/adfm.200400268
5. Prieto M. Nucleation and supersaturation in porous media (revisited). *Mineral. Mag.* **78**, 1437–1447 (2015). DOI: 10.1180/minmag.2014.078.6.11

### Funding acknowledgement:

Engineering and Physical Sciences Research Council (EPSRC) (EP/N002423/1 and EP/J018589/1); Leverhulme Trust.

### Corresponding author:

Fiona Meldrum, University of Leeds, F.Meldrum@leeds.ac.uk

## Imaging and Microscopy Group

Paul Quinn, Science Group Leader

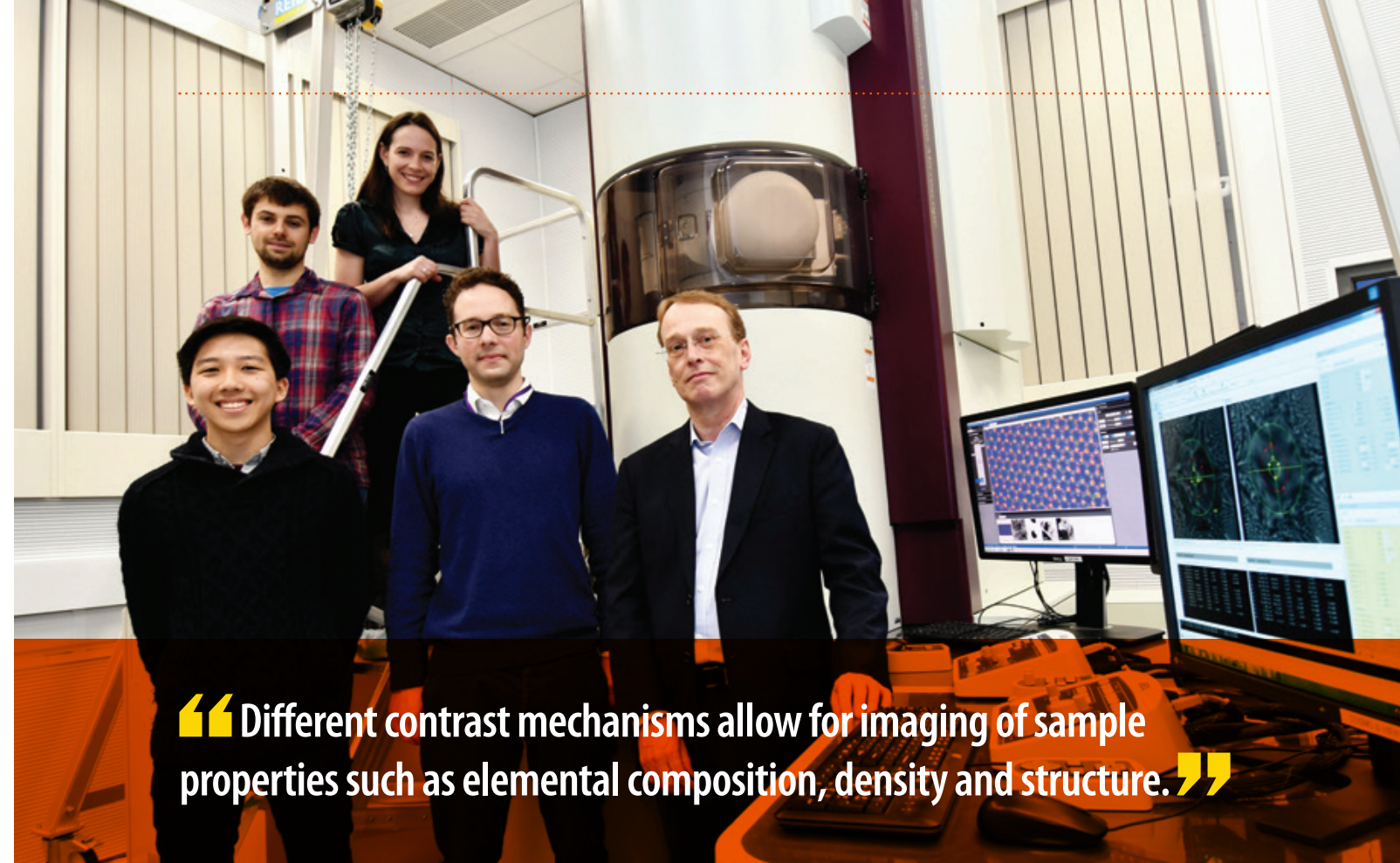
**The Imaging and Microscopy Group brings together eight experimental facilities (I08, J08, DIAD, I12, I13-1, I13-2, I14 and ePSIC) which use electrons and X-rays to image samples under different experimental conditions across a diverse range of length scales and time scales. Different contrast mechanisms allow for imaging of sample properties such as elemental composition, density and structure. This ability to extract image sample properties in minute detail lends itself to a wide range of scientific areas, from chemistry and catalysis to environmental science, materials science, biology, medicine and cultural heritage.**

The Scanning X-ray Microscopy (SXM) beamline (I08) is for morphological, elemental and chemical speciation on a broad range of organic-inorganic interactions in a 250 - 4400 eV photon energy range, and sample investigations under ambient or cryogenic conditions. I08 has a range of applications including biological and biomedical sciences, earth and environmental science, geochemistry, and materials science. The main activity on I08 over the past year has been designing, constructing and testing various aspects of a new soft X-ray spectro- and tomo-ptychography branchline (J08). This new branchline is expected to be available for experiments in early 2020 and will provide spatial resolutions down to a few nm, providing a step change in imaging performance.

The Dual Imaging and Diffraction (DIAD) beamline will be the first beamline to offer two X-ray microscopy techniques (imaging and diffraction) applied synchronously with a switching time of 0.1s. This enables *in situ* structural characterisation experiments taking advantage of both techniques simultaneously. DIAD is being built to use light from a ten pole permanent magnet wiggler. The diffraction technique is conducted using monochromatic light, whereas the imaging technique can be performed with monochromatic or polychromatic ('pink') beam. The X-ray energy can be chosen separately for both techniques in the range from 8 - 38 keV. The beamline has completed construction of the Optics Hutch and took first light in December 2018. Next to a standard tomography setup, a mechanical test-rig for diffraction and tomography will be one of the main instruments to allow *in situ* experiments for a variety of scientific disciplines such as engineering and materials science, bio-materials and hard tissues, geology and mineralogy, and soil-

plant interactions. The commissioning activities and construction of the experimental end station are ongoing with first users expected in early-mid 2020.

The Joint Engineering, Environmental and Processing (JEEP) beamline (I12) uses a 4.2 T superconducting wiggler to provide polychromatic and monochromatic X-rays in the energy range 50 - 150 keV. The high photon energies provide good penetration through large or dense samples. The beamline offers beam sizes ranging from 50 x 50  $\mu\text{m}$  for diffraction, up to 90 x 25 mm for imaging. These beam characteristics enable the study of materials and processes inside sample environments without unacceptable attenuation of the beam, using macro-scale samples that are more representative of the process under study. X-ray techniques available are radiography, tomography, energy-dispersive diffraction, monochromatic and white-beam 2D diffraction/scattering and small-angle X-ray scattering. The beamline's two flexible experimental hutches allow users to bring their own rigs and sample chambers. I12 has a diverse user community (materials science and engineering; chemical processing; biomedical engineering; geoscience; environmental science; physics; palaeontology) who make full use of the beamline's versatility. High-speed imaging and tomography has benefited from the integration of the Phantom Miro camera into the beamline data acquisition and processing pipelines. High-speed tomography of natural and artificial volcanic minerals during heating, cooling and compression at temperatures up to 1,300 °C have been undertaken by different groups, using this new capability, yielding insight into the development of gas bubbles and mineral precipitation during volcanic eruption. For diffraction and scattering measurements, a new Pilatus



“Different contrast mechanisms allow for imaging of sample properties such as elemental composition, density and structure.”

ePSIC first users from the National Graphene Institute at The University of Manchester, left to right: Lan Nguyen, Aidan Rooney, Sarah Haigh, Manchester, with Christopher Allen and Angus Kirkland, Oxford.

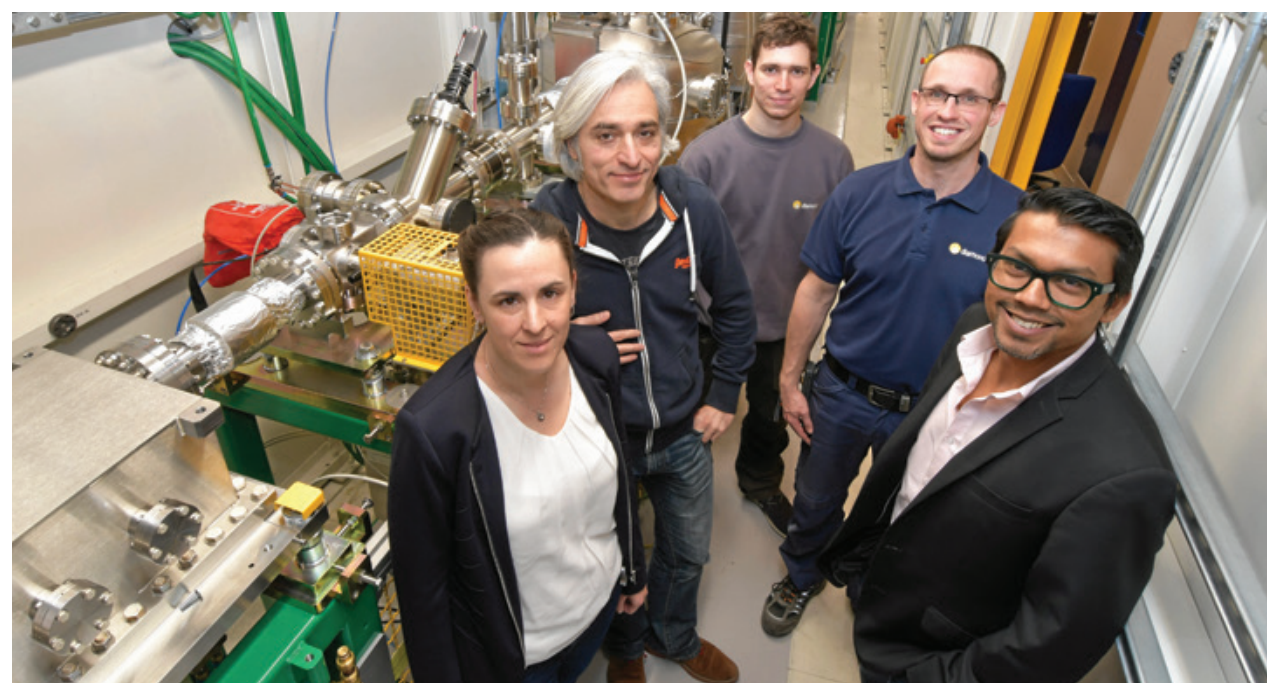
2M Cd-Te detector has been commissioned and has entered user service, allowing faster and more sensitive detection of X-rays by photon-counting technology. The phase changes, strain and texture during friction welding of nickel alloys has been studied successfully with this method, enabling the changes at previously unreachable time-scales to be observed.

The I13 Imaging and Coherence beamline is for multiscale imaging in the energy range of 6 - 30 keV. The achievable resolution ranges from several microns to some tens of nanometers with two branchlines operating independently for this purpose. The Diamond Manchester Imaging branchline performs mainly in-line phase contrast tomography with a strong emphasis on dedicated sample environments. A new full-field microscope using Zernike phase contrast imaging over a field of view of 50-100  $\mu\text{m}$  and a resolution of 50 - 100 nm is now in operation, with a growing user community, allowing us to identify nano-sized structures under dynamic conditions. The highest spatial resolution, of 30 nm, is achieved on the coherence branch with ptychographic imaging. Continuous improvements such as new piezo stages and improved detector interfaces have reduced ptycho-tomography scans from days to a few hours, and ongoing fly-scanning developments aim to reduce this even further. Ptychography is now a routine standard user experiment and more advanced imaging modes such as 3D Bragg ptychography and simultaneous transmission and Bragg geometry measurements have been demonstrated and developed with users.

I14, the Hard X-ray Nanoprobe beamline, offers a small beam of 60 - 200 nm for high resolution imaging. I14 has entered its second year of operation and has developed and expanded its capabilities in X-ray fluorescence, diffraction and X-ray Absorption Near Edge Structure (XANES) mapping. The integration of the Excalibur detector on I14 now enables diffraction data to be acquired at sampling times down to 10 ms. For XANES mapping, there have been a number of developments in automated drift correction to improve data quality. Corroded metal interfaces, metallic particles in cells and photovoltaic

films are just a sample of the many science areas and successful experiments conducted. The beamline is still in its optimisation phase and new techniques and facilities such as ptychography are in development, and an increasing emphasis on *in situ* studies is driving a number of developments.

The electron Physical Science Imaging Centre (ePSIC) at Diamond consists of two transmission electron microscopes, a JEOL ARM 200 and a JEOL GRAND ARM 300, which were brought to Diamond through a collaboration with Johnson Matthey and the University of Oxford respectively. The ARM 200 is a state-of-the-art probe-corrected analytical microscope capable of atomic resolution electron energy loss and X-ray spectroscopy. The ARM 300 is a dedicated imaging instrument aligned across a wide range of accelerating voltages (30 - 300 keV). It is both probe- and imaging-corrected and has numerous detectors, including a fast direct electron detector (operating at up to 2000 fps). These combined capabilities make this a unique resource for electron microscopy within the UK. With *in situ* sample holders, users at ePSIC can perform variable temperature measurements from 100 to 1600 K to directly image the atomic structure of materials during thermally driven transitions. This *in situ* capability will be expanded upon over the coming year. An Oxford Instruments Energy Dispersive X-ray (EDX) detector has been added to the ARM 300 to allow combined X-ray spectroscopy and high-resolution imaging. The state of the art instrumentation available at ePSIC has attracted both established electron microscopists looking to develop new techniques, and scientists with limited previous electron microscopy experience interested in the atomic structure of their samples. The collaboration of the expert staff at ePSIC with this range of users is helping to bring cutting-edge microscopy techniques to the wider material science community. A science highlight from the last year has been the resolution of the structure of platelets in type 1a diamonds using the low voltage imaging capabilities of the ARM 300. The growing importance of ptychography has led to a project aimed at harmonising and improving the acquisition and analysis processes across the different X-ray and electron instruments.



DIAD beamline team, early 2019, left to right: Christina Reinhard, Michael Drakopoulos, Tom Yates, Pete Garland, Sharif Ahmed.

## Single atom catalysts boost efficiency and cut waste in fine chemical production

**Related publication:** Chen Z., Vorobyeva E., Mitchell S., Fako E., Ortuño M. A., López N., Collins S. M., Midgley P. A., Richard S., Vilé G. & Pérez-Ramírez J. A heterogeneous single-atom palladium catalyst surpassing homogeneous systems for Suzuki coupling. *Nat. Nanotechnol.* **13**, 702–707 (2018). DOI: 10.1038/s41565-018-0167-2

**Publication keywords:** Heterogeneous catalysis; Atomic resolution imaging

**T**he chemical industry produces a tremendous amount of waste. Often this arises from the need to separate the product from a solution containing by-products and a dissolved catalyst. 85% of all industrial chemical processes use catalysts, chemicals that speed up a reaction but do not get used up in the process, and they are often expensive metals such as palladium.

An international team of researchers sought an efficient solid catalyst that would avoid waste. They investigated a material designed to contain individual atoms of palladium supported by carbon nitride, which showed improved performance in a reaction to produce new carbon-carbon bonds.

The E02 microscope at the electron Physical Science Imaging Centre (ePSIC) is capable of seeing individual atoms, without causing excessive damage to the sample. Using E02, the team were able to obtain high-quality images of the individual palladium atoms, before and after use in chemical reactions. Their results confirmed that the atoms occurred as isolated single atoms and were retained throughout the use of the catalyst. With additional computational work, they were able to show that the single palladium atoms on the carbon nitride hit the sweet spot: they are available to interact with molecules in the desired chemical reaction, but they are stable enough to be used over and over again.

Industrial production of fine chemicals depends critically on catalysis. In fact, 85% of all industrial processes in the chemical industries are catalytic processes<sup>1</sup>. Catalysts operate by reducing activation energies in key mechanistic steps during a chemical reaction, leading to increases in the rate of reaction at accessible temperatures. The catalyst, often relying on a transition metal species for carrying out key steps, is not used up during the reaction, and a relatively small quantity of the catalyst can participate in reactions, in principle, many times over to convert starting materials to a specific product.

Broadly, catalysts can be further subdivided into homogeneous and heterogeneous catalysts. Homogeneous catalysts occur as molecules in solution, such as in the form of organometallic complexes. Heterogeneous

catalysts are solids with which gaseous or liquid-phase reagents interact. In many heterogeneous catalysts, transition metal nanoparticles, clusters of metal atoms, or molecular complexes constitute the active catalyst, and are anchored to an inert support material. Common support materials are oxides such as silica and alumina.

Homogeneous catalysts are associated with higher levels of waste production during catalysis due to the requirement to separate the catalyst from the final product, as well as from any by-products. While heterogeneous catalysts can be used in processes that intrinsically segregate the flowing products from the stationary solid catalyst, there are many reactions where the homogeneous catalysts significantly outperform heterogeneous systems.

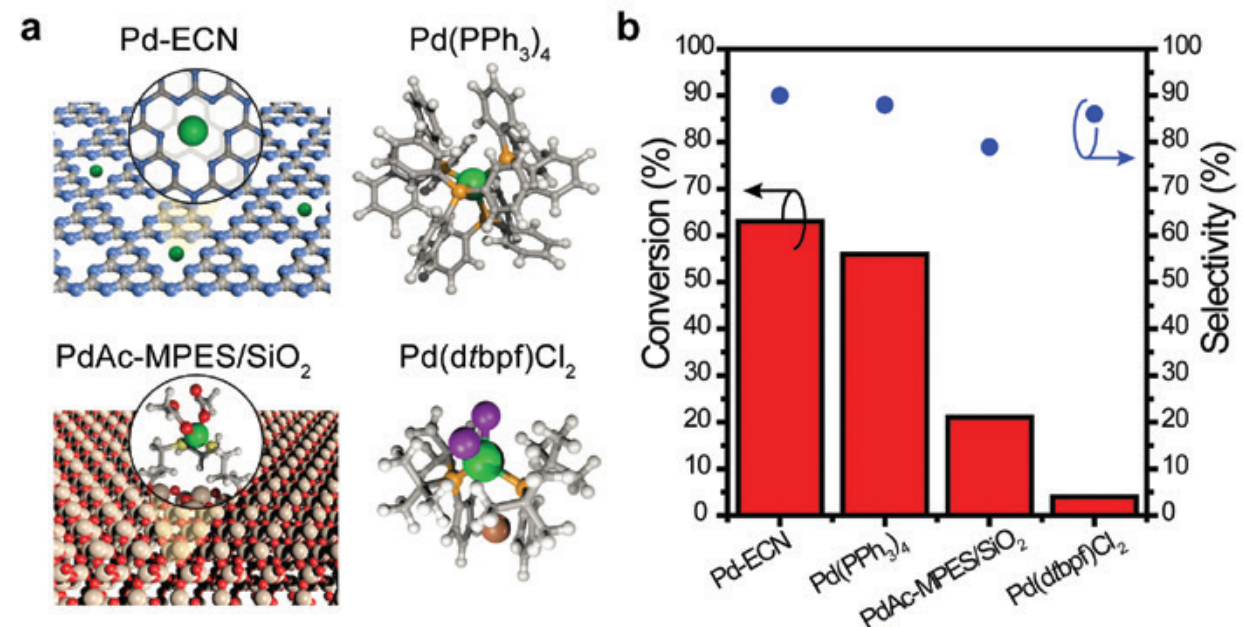


**Figure 1:** (a) Structural models for four Pd catalysts studied for C-C coupling reactions. (b) Conversion efficiency and selectivity for the four Pd catalysts in a selected test reaction producing biphenyl. Adapted by permission from Springer Nature: *Nature Nanotechnology*, see Related Publication, copyright 2018.

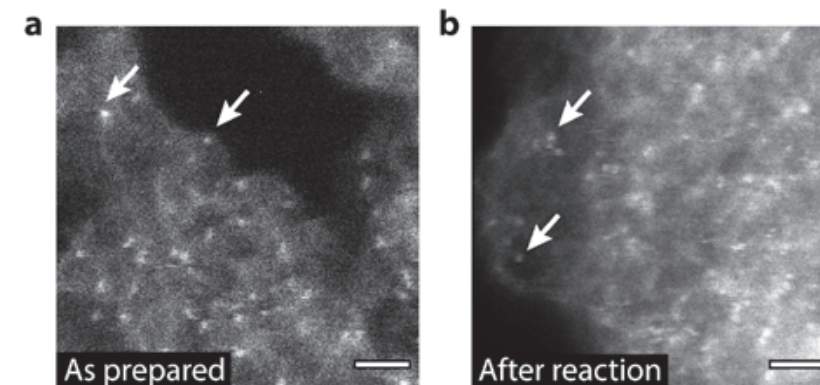


**Figure 2:** Atomic resolution aberration-corrected electron micrographs (a) before and (b) after reaction. White arrows highlight a selection of single Pd atoms, appearing as isolated bright spots in the micrographs. The scale bars are 1 nm. Adapted by permission from Springer Nature: *Nature Nanotechnology*, see Related Publication, copyright 2018.

Both heterogeneous and homogeneous catalysts may also suffer from catalyst degradation, reducing their catalytic activity over time.

A particular class of reactions requiring the formation of carbon-carbon bonds, known as cross-coupling reactions, have been carried out most successfully with homogeneous catalysts. The Suzuki coupling reaction, recognised by the 2010 Nobel Prize in Chemistry, is traditionally carried out with palladium (Pd) organometallic complexes in solution<sup>2</sup>, such as Pd(PPh<sub>3</sub>)<sub>4</sub> (tetrakis(triphenylphosphine)palladium), and Pd(dtbpf)Cl<sub>2</sub> ([1,1'-bis(di-tert-butylphosphino)ferrocene] dichloropalladium (Fig. 1). Alternatives using solid supports for organometallic complexes have been proposed, including silica functionalised by 3-mercaptopropyl sulphide to anchor a Pd acetate complex<sup>3</sup>. However, the most successful heterogeneous catalysts exhibit significantly lower conversion rates in many cross-coupling reactions in comparison with their homogeneous counterparts.

An alternative to homogeneous catalysts, and those heterogeneous designs anchoring Pd complexes to an inorganic support, has emerged with the development of single atom catalysts on carbon and nitrogen derived materials, such as graphitic carbon nitride<sup>4</sup>. Graphitic carbon nitride is a polymeric material consisting of sheets of carbon and nitrogen atoms analogously to graphene. Conceptually, the ability of graphitic carbon nitride to form bonds with bare, single Pd atoms suggests a design chemically very similar to the coordination environment of the most active homogeneous Pd cross-coupling catalysts.

To examine the performance of this proposed catalyst, Pd atoms were deposited onto exfoliated graphitic carbon nitride (ECN) using a microwave-irradiation assisted method. For a particular Suzuki coupling reaction to form biphenyl, the conversion rate and the selectivity were recorded for a number of candidate catalysts (Fig. 1). The Pd-ECN catalyst exhibited the highest figures of merit among the top performing heterogeneous and homogeneous catalysts. Additionally, the Pd-ECN catalyst retained its conversion efficiency for more than 12 hours of reaction, whereas the conversion efficiency of the next best catalyst (the homogeneous Pd(PPh<sub>3</sub>)<sub>4</sub> catalyst) decreased by more than a factor of two, after four hours. The catalyst was also studied for many other cross-coupling reactions and showed comparable or higher conversion efficiency and selectivity relative to the best performing Pd(PPh<sub>3</sub>)<sub>4</sub> homogeneous catalyst.

In order to understand these performance characteristics, a microscopic study of the catalyst, as originally prepared and after reaction, was carried out (Fig. 2). Electron microscopy is one of the few, if not only, methods capable of resolving individual atoms in these materials. Light microscopes are unable to resolve atoms due to the diffraction limit associated with the wavelength of light. High-energy electrons accelerated to a significant fraction of the speed of light, however, have associated wavelengths much smaller than the size of an

atom. The lenses used in electron microscopes, though, are limited by aberrations arising from the physics of focusing electrons with magnetic fields. Sophisticated aberration correctors comprising several small magnetic elements are required to offset the lens aberrations sufficiently to focus electron beams to the size required to resolve single Pd atoms supported on carbon nitride.

Moreover, carbon- and nitrogen-based materials are easily damaged by high-energy electrons. ePSIC houses a state-of-the-art aberration corrected electron microscope which is capable of high spatial resolution at electron energies as low as 60 keV. This capability for operating at

relatively low electron beam energy enabled high-quality images to be formed from Pd single atoms on graphitic carbon nitride (Fig. 2).

In tandem with this experimental work, Density Functional Theory calculations were carried out to model the mechanisms associated with Pd-ECN and Pd(PPh<sub>3</sub>)<sub>4</sub>. These computational results point to how the Pd atoms on ECN are located within an adaptive coordination environment necessary for catalysing several key mechanistic steps. At the same time, the Pd atoms on ECN are bound with sufficient strength to preclude detachment and loss of Pd during the reaction or aggregation of Pd atoms which might otherwise result in fewer catalytically active Pd sites over time.

The development of catalysts with reduced waste and improved atom economy are two objectives at the core of green chemistry, the effort to minimise harmful environmental effects of chemical processing. Moreover, the identification of catalysts that require lower loadings of precious metals with improved lifetime offers key commercial benefits as well. The newly developed single atom Pd catalyst supported on graphitic carbon nitride capitalises on each of these aspects by improving yield, selectivity, and durability. The conclusive demonstration of the single atom character of this catalyst hinged on advanced imaging capabilities for resolving individual atoms made possible through cutting-edge electron microscopy.

### References:

- Thomas J. M. *et al.* Some Turning Points in the Chemical Electron Microscopic Study of Heterogeneous Catalysts. *ChemCatChem* **5**, 2560–2579 (2013). DOI: 10.1002/cctc.201200883
- Miyaura N. *et al.* Palladium-Catalyzed Cross-Coupling Reactions of Organoboron Compounds. *Chem. Rev.* **95**, 2457–2483 (1995). DOI: 10.1021/cr00039a007
- Molnár Á. Efficient, Selective, and Recyclable Palladium Catalysts in Carbon–Carbon Coupling Reactions. *Chem. Rev.* **111**, 2251–2320 (2011). DOI: 10.1021/cr100355b
- Chen Z. *et al.* Stabilization of Single Metal Atoms on Graphitic Carbon Nitride. *Adv. Funct. Mater.* **27**, 1605785 (2017). DOI: 10.1002/adfm.201605785

### Funding acknowledgement:

ETH Zurich; Swiss National Science Foundation (200021-169679); MINECO (CTQ2015-68770-R); Severo Ochoa Excellence Accreditation 2014-2018 (SEV-2013-0319); Juan de la Cierva-Incorporación postdoctoral program (JCI-2016-29762); Girton College (Cambridge, UK); EPSRC (EP/R008779/1).

### Corresponding author:

Dr Sean M Collins, Department of Materials Science and Metallurgy, University of Cambridge, smc204@cam.ac.uk

## Discovering the nanoscale iron and calcium compounds that form in Alzheimer's disease senile plaques

**Related publication:** Everett J., Collingwood J. F., Tjendana-Tjhin V., Brooks J., Lermyte F., Plascencia-Villa G., Hands-Portman I., Dobson J., Perry G. & Telling N. D. Nanoscale synchrotron X-ray speciation of iron and calcium compounds in amyloid plaque cores from Alzheimer's disease subjects. *Nanoscale* **10**, 11782–11796 (2018). DOI: 10.1039/c7nr06794a

**Publication keywords:** Spectromicroscopy; STXM; Alzheimer's disease; Senile plaques; Amyloid; Iron; Calcium

**A**lzheimer's disease is the most common form of dementia, yet its cause is unclear and there is no effective treatment. A hallmark of Alzheimer's disease is the formation of amyloid plaques in the brain that disrupt its normal function. There is also an imbalance of metals, with increased levels of iron and harmful reactive iron forms being associated with amyloid plaques.

Researchers wanted to examine Alzheimer's disease plaques to see if there was evidence of the protein-derived amyloid peptide converting non-reactive iron forms into reactive states. They also wanted to investigate the distribution of calcium in the plaques, as disruptions to brain functions associated with calcium have also been reported in Alzheimer's disease.

They used X-ray spectromicroscopy on the Scanning X-ray Microscopy beamline (I08) to characterise the precise distribution and chemical state of iron and calcium compounds within amyloid plaques derived from the brains of Alzheimer's patients. They needed to examine the plaques with a resolution of tens of nanometres, whilst simultaneously accessing superb chemical sensitivity, to identify differences in metal chemistry within highly localised regions of interest. They also used X-ray Magnetic Circular Dichroism (XMCD) to probe the magnetic states of the forms of iron present within the amyloid plaques. This level of characterisation of inorganic compounds associated with amyloid plaques has not been possible in the past, and was here enabled by development and establishment of these synchrotron microscopy techniques with nanoscale resolution.

They observed iron in multiple different states within the amyloid plaque, with calcium in at least two different forms. Their results advance prior work by defining the precise properties of iron and calcium in the plaques, and show that reactive iron might serve as a target for therapies. The presence of magnetic iron forms and calcium inclusions also supports developments in non-invasive diagnosis of Alzheimer's disease using innovative and existing clinical techniques such as Magnetic Resonance Imaging (MRI).

This study reveals, in unprecedented detail at nanoscale resolution, the properties of iron and calcium compounds in senile plaques from individuals who had Alzheimer's disease. The findings extend current hypotheses about the way in which these and other metallic species may contribute to the pathogenesis of Alzheimer's disease and could help direct future innovative diagnosis and treatment of the disease.

Alzheimer's disease (AD) is the most common form of dementia, affecting ~850,000 people in the UK, with the number of cases on the increase it creates tremendous social and economic costs, and there is no cure at present.

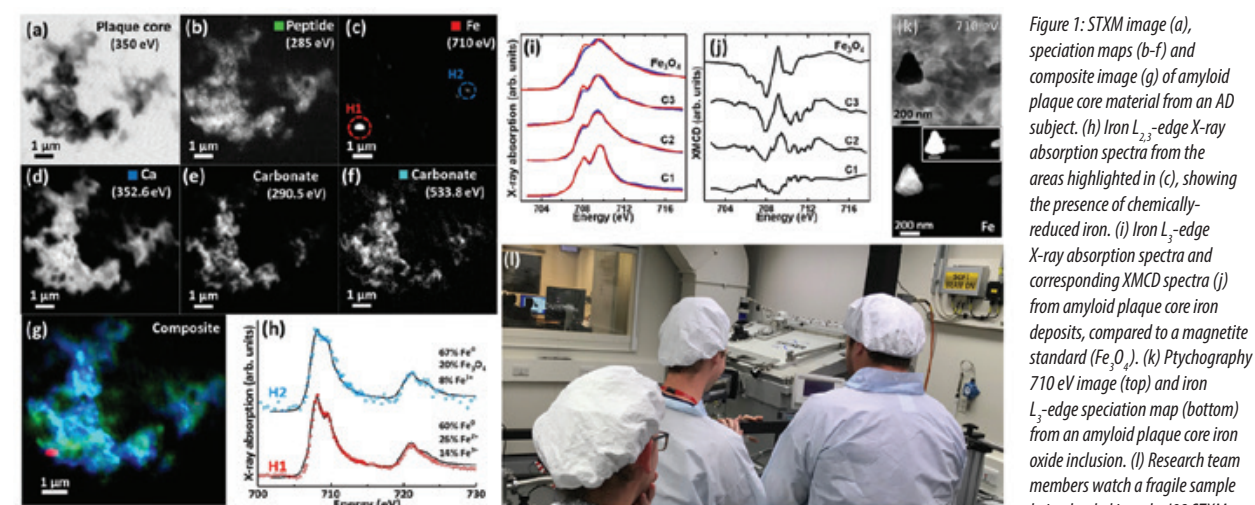
AD is traditionally characterised by the presence of two hallmark lesions of abnormal protein aggregates: (i) intracellular neurofibrillary tangles of tau protein, and (ii) extracellular amyloid plaques, primarily comprised of amyloid- $\beta$  peptides, which are small hydrophobic protein fragments (39 to 42 residues) from the transmembrane protein APP. The accumulation of amyloid plaques in AD brain tissue is thought to be fundamental to the development of the disease, affecting normal neuronal activities with intra and extracellular accumulations associated with impaired cognitive and memory function.

Alongside amyloid plaque formation, disrupted metal homeostasis is frequently observed in AD brains. For example, disrupted calcium-dependent processes have been observed in AD. Iron levels are significantly increased in several regions of AD-affected brains when compared to disease-free age-matched controls<sup>1</sup> and over time these chemically-reduced forms of iron, including mixed-valence iron oxides<sup>2</sup>, are associated with pathological features of the disease. Iron is vital for brain function, but if it is not properly transported or stored in cells and tissues, it can catalyse the formation of free radicals. Chemically-reduced iron can produce excessive levels of these free radical species, contributing to the damage observed in AD via elevated oxidative stress and triggering of cell death processes.

This study examined the distribution and material properties of iron and calcium within amyloid plaques extracted from the brains of two AD patients. The work was underpinned by the hypothesis that the chemical reduction of iron occurs when co-localised to aggregating amyloid- $\beta$  *in vivo*, a hypothesis supported by prior-published *in vitro* experiments showing amyloid- $\beta$  induces the chemical reduction of ferric ( $\text{Fe}^{3+}$ ) iron to ferrous ( $\text{Fe}^{2+}$ ) states<sup>3</sup>.

With ethical approval, amyloid plaque cores were extracted and isolated from two deceased patients who had a formal diagnosis of AD. Plaques were embedded and sectioned before being examined using X-ray spectromicroscopy in the form of Scanning Transmission X-ray Microscopy (STXM), at beamline I08, and the Advanced Light Source beamline 11.0.2 (ALS; Berkeley USA). No dyes, contrast agents or aldehyde fixatives were used, which is critical as these could alter or contribute to the signal from the samples.

Nanoscale maps of the distribution of chemical species found in the plaques were created from images obtained at approximately 50 nm spatial resolution. The maps were computed from paired images, one collected at the X-ray energy corresponding to the peak absorption for a material of interest (e.g.  $\text{Fe}^{3+}$  L<sub>2,3</sub>-edge absorption at 709.5 eV), and a second image collected over the same area but at a slightly lower energy (the off-peak image). The off-peak image was subtracted from the peak image, providing an artefact-free map of the distribution of the material of interest. These speciation maps were calculated using data collected at X-ray absorption edges for carbon, calcium, oxygen, and iron.



Once the overall distributions had been determined, detailed information was obtained from each area of interest by collecting a series of images (a 'stack') at multiple energies through an X-ray absorption edge, not just the peak/off-peak pair. For example, image stacks were acquired over the carbon K-edge (280-320 eV) and iron L<sub>2,3</sub>-edge (700-740 eV), followed by iron L<sub>3</sub>-edge (700-718 eV) X-ray Magnetic Circular Dichroism (XMCD) spectra revealing the magnetic properties of iron-rich regions from paired stacks obtained with left- and then right-circularly-polarised X-rays. This powerful method of spectromicroscopy produces stack images where every pixel contains detailed information about chemical and magnetic properties. In this example, the spectromicroscopy enabled detailed characterisation of individual iron deposits within the plaques.

I08 and Advanced Light Source (ALS) 11.0.2 were vital to this study for several reasons. To obtain spectromicroscopy at a length scale relevant to structures within amyloid plaque cores, spatial resolution of tens of nanometres was essential. The soft X-ray operational energy range of the beamlines enabled both organic and bioinorganic metal components of the plaques to be determined. The chemical sensitivity of these beamlines was vital in distinguishing closely-related iron species at the nanoscale, and the pioneering application of nanoscale XMCD analysis to these plaques was enabled by senior beamline scientist Dr Tohru Araki at beamline I08.

STXM analysis at the iron L<sub>2,3</sub>-edge revealed multiple iron phases in the amyloid plaque cores ranging from ferric, mixed valence ( $\text{Fe}^{2+}/\text{Fe}^{3+}$ ), to ferrous and even zero-valent ( $\text{Fe}^0$ ) iron (Fig. 1h). The presence of low-oxidation-state iron (<3<sup>+</sup>) suggests that excessive chemical reduction of iron occurred at the amyloid plaque sites. Extended damage from free radicals has been reported at sites of amyloid aggregation, so amyloid-associated toxicity to neurons may arise from this chemical reduction of iron. XMCD spectra (Fig. 1j) revealed the presence of the magnetic mixed-valence iron phase magnetite within the plaque cores<sup>4</sup>. Advanced imaging with ptychography, performed at ALS beamline 11.0.2, generated images at 2 nm resolution (Fig. 1k), revealing the morphology of a maghemite-like inclusion consistent with crystalline iron of biogenic origin (as opposed to magnetite derived from pollutants of industrial origin<sup>5</sup>).

Calcium L-edge speciation mapping (Fig. 1d) showed evidence for at least two distinct calcium phases in the amyloid plaques, new observations that might be associated with known disruption to neuronal calcium regulation and signalling in AD.

Information was also collected regarding the organic components of the plaques by examining protein content at the carbon K-edge (Fig. 1b) and oxygen K-edge. This allowed the distribution of metals within the protein-rich organic materials of the amyloid plaque cores to be visualised for the first time at nanoscale resolution without the need to introduce any kind of labelling such as staining agents.

Conclusion: These findings associate atypical iron reduction with amyloid plaque formation, and raise challenging questions about the critical contribution of disrupted metal homeostasis to AD pathogenesis. The next step is to extend this analysis to intact sections of human brain tissue, and to characterise a wider range of the metal elements that are present. These results may prove important for clinical trials currently underway elsewhere with Alzheimer's patients that are seeking to determine if iron-modifying drugs alter compartmental iron levels, markers of iron-associated toxicity in the brain, or clinical measures of disease progression.

### References:

- Tao Y. *et al.* Perturbed Iron Distribution in Alzheimer's Disease Serum, Cerebrospinal Fluid, and Selected Brain Regions: A Systematic Review and Meta-Analysis. *Journal of Alzheimer's Disease* **42**, 679-690 (2014). DOI: 10.3233/JAD-140396
- Plascencia-Villa G. *et al.* High-resolution analytical imaging and electron holography of magnetite particles in amyloid cores of Alzheimer's disease. *Sci. Rep.* **6**, 8868 (2016). DOI: 10.1038/srep24873
- Everett J. *et al.* Ferrous iron formation following the co-aggregation of ferric iron and the Alzheimer's disease peptide  $\beta$ -amyloid (1-42). *J. R. Soc. Interface* **11**, 20140165 (2014). DOI: 10.1098/rsif.2014.0165
- Collingwood J. F. *et al.* Iron Oxides in the Human Brain. *Iron Oxides: From Nature to Applications* 143-176 (John Wiley & Sons, Ltd, 2016). DOI: 10.1002/9783527691395.ch7
- Allsop D. *et al.* Magnetite pollution nanoparticles in the human brain. *Proc. Natl. Acad. Sci.* **113**, 10797-10801 (2016). DOI: 10.1073/pnas.1605941113

### Funding acknowledgement:

This work was supported by: EPSRC grants EP/K035193/1 (JFC), EP/N033191/1-EP/N033140/1 (JFC-NDT); the Alzheimer's Association (AARFD-17-529742); University of Warwick alumni donations (VTT, JE); the RCMI Program from NIH at UTSA (5G12RR013646, G12MD007591), San Antonio Life Sciences Institute (SALSI)-Clusters in Research Excellence Program, Semmes Foundation; The Advanced Light Source, supported by the Director, Office of Science, Office of Basic Energy Sciences, of the U.S. Department of Energy under Contract No. DE-AC02-05CH11231.

### Corresponding authors:

Dr James Everett, Keele University, j.everett@keele.ac.uk and Dr Joanna Collingwood, University of Warwick, J.F.Collingwood@warwick.ac.uk

## High-speed X-ray imaging reveals complex behaviour during metal 3D printing

**Related publication:** Leung C. L. A., Marussi S., Atwood R. C., Towrie M., Withers P. J. & Lee P. D. In situ X-ray imaging of defect and molten pool dynamics in laser additive manufacturing. *Nat. Commun.* **9**, 1355 (2018). DOI: 10.1038/s41467-018-03734-7

**Publication keywords:** Additive manufacturing; Defect; Molten pool dynamics; High-speed X-ray imaging

A type of 3D printing called laser additive manufacturing (LAM) uses a high-energy laser beam to melt powder particles into a solid structure in under 1/1000<sup>th</sup> of a second. The powder melting process controls how materials are formed, governing the overall product performance. However, the fast laser-material interaction makes it difficult to optimise the processing conditions, resulting in defects. The presence of defects slows down the adoption of LAM for safety-critical engineering components such as turbine blades, energy storage, and biomedical devices.

A team from Diamond Light Source and the University of Manchester used a specially designed 3D printer to observe the LAM process in action, using high-speed X-ray imaging. The aim of the research was to record the entire process of metal powder fusion, providing detailed information on how melt features form and evolve. The Joint Engineering, Environmental and Processing (JEEP) beamline (I12) provides high-energy X-rays able to penetrate the high-density metallic materials used to make engineering components, including iron-based and nickel-based alloys. In this case, the team studied Invar 36, an iron-nickel alloy. The beamline is equipped with a high-speed X-ray imaging system, which allows researchers to record the entire LAM process at up to 10,000 frames per second.

The team's results provide detailed information on the formation and evolution of the melt track during LAM, in particular the formation of porosity and the ejection of powder and molten material. This work clarifies aspects of the physics behind LAM, which are critical for its development, and provides a 'map' that enables manufacturers to select the optimum process parameters for making quality products.

Laser additive manufacturing (LAM), or metal 3D printing, transforms a 3D digital design into a real-life component by fusing metallic, ceramic, or other powders using a laser beam, layer-upon-layer. It has been used for a wide range of product applications, including jewellery, sports equipment, dental implants, and fuel nozzles. The adoption of LAM in the production of safety-critical engineering structures, such as turbine blades, biomedical, and energy storage devices, is hampered by many technical challenges<sup>1</sup>, including complex laser-matter interactions<sup>2</sup>, powder oxidation<sup>3</sup>, and defects<sup>4</sup>, such as porosity and spatter. These defects may act as stress initiators, deteriorating the performance of LAM components during use. A better understanding of how these defects are formed and evolved during LAM is crucial for process and product optimisation.

At present, the underlying defect formation mechanisms are inadequately understood, because the laser-matter interaction, and subsequent thermophysical phenomena, occur on very short time scales ( $10^{-6}$  -  $10^{-3}$  s). Although some phenomena at the powder bed surface have been revealed by *in situ* process monitoring devices during LAM, the evolution of defects inside a molten pool (or melt tracks) has not been observed, hindering our understanding of LAM.

Third-generation synchrotron radiation sources, such as Diamond Light Source, provide high-energy and high-flux X-ray beams for high-speed imaging with high temporal ( $\sim 10^{-3}$ s) and spatial ( $\sim 10^{-6}$ m) resolution. They have been used to provide insights into a wide range of dynamic processes, including semi-solid forming, laser processing, battery failure, and volcanic eruptions. In this study, a LAM process replicator<sup>2</sup> and synchrotron X-ray imaging were used to investigate defect and molten pool dynamic behaviour during LAM of Invar 36 powder. Invar 36 is a material of interest for precision instruments, optical devices, and aircraft tooling owing to its low coefficient of thermal expansion.

The key stages of LAM were captured by high-speed X-ray imaging at 5100 frames per second in beamline I12<sup>5</sup> (Fig. 1), including the evolution of the molten pool, melt track, defects, and denuded zone. The results demonstrate that melt tracks are formed and extended by molten pool wetting and powder entrainment. Hot powder particles and metal vapour are hypothesised to heat the surrounding argon gas at the laser-matter interaction zone, inducing a rapid gas expansion radially upwards from the molten pool surface, leading to powder

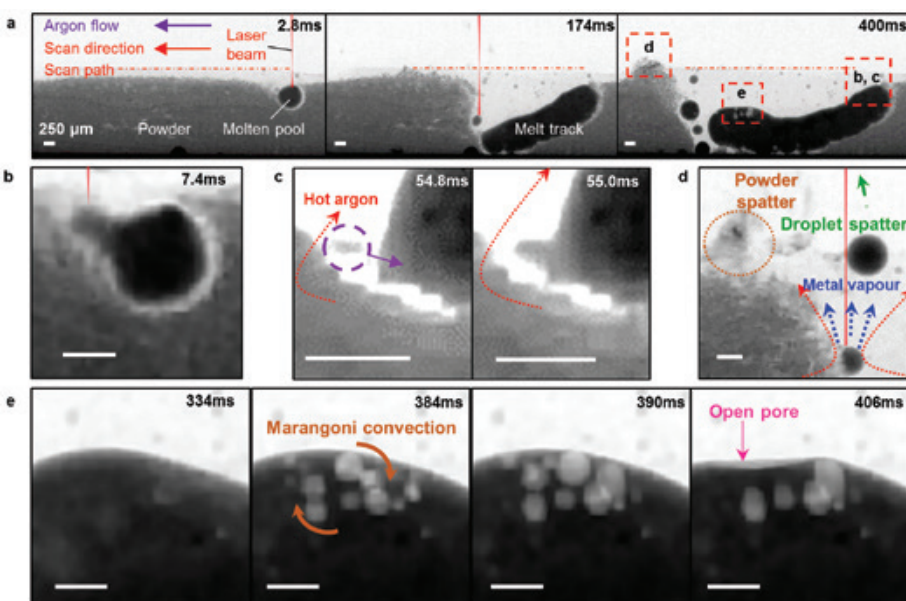


**Figure 1:** Time series radiographs showing (a) the evolution of a single layer Invar 36 melt track, whereby the melt track formation is driven by (b) molten pool wetting and (c) powder entrainment, and the evolution of (d) spatter and (e) porosity.

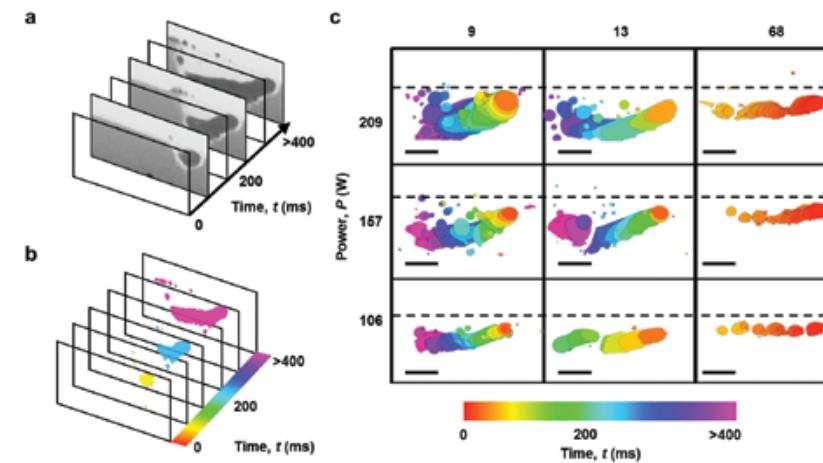


**Figure 2:** Melt pool dynamics of Invar 36 under overhang conditions. (a) The melt pool features were extracted from the time-series radiographs and then (b) labelled with time, and subsequently flattened to create a time integrated image. (c) A mechanism map is formed by collating these time integrated images with respect to their process parameters.

spatter and droplet spatter. A new series of pore evolution mechanisms are also uncovered during LAM. Firstly, pores are formed as the melt track undergoes solidification. Secondly, they move in a circular motion inside the melt track via the centrifugal Marangoni convection, and towards the direction of the laser beam. Some pores coalesce to form larger ones and some escape into the atmosphere via pore bursting, leaving an open pore at the surface of the melt track. The results show the formation mechanism of open pores is driven by pore bursting rather than by incomplete melting or insufficient liquid feeding, as previously hypothesised.

A mechanism map (Fig. 2) is developed to encapsulate the evolution of melt features, and the underlying thermophysical phenomena occur in a systemic set of LAM trials. It highlights an increase in laser power that would transfer more laser energy to the powder particles and the melt track, resulting in a violent movement of liquid metal, a frequent spatter ejection, and a deeper melt track. With increasing scan speed, less laser energy is delivered to the powder bed, lowering the temperature of the melt features while increasing their surface tension. As a consequence, the track morphology changes from a continuous hemi-cylindrical track to disconnected beads. This map emphasises the relationship between processing parameters, molten pool dynamics, and track morphology. It can be applied to other materials, processing conditions, or manufacturing processes, helping end-users to develop a more efficient processing environment.

While much can be learned from observing the complex behaviour in a single layer melt track, it is a common practice in LAM to build an additive manufactured component in a layer-by-layer manner. In the second layer melt track (Fig. 3), the molten pool wets onto the previous track

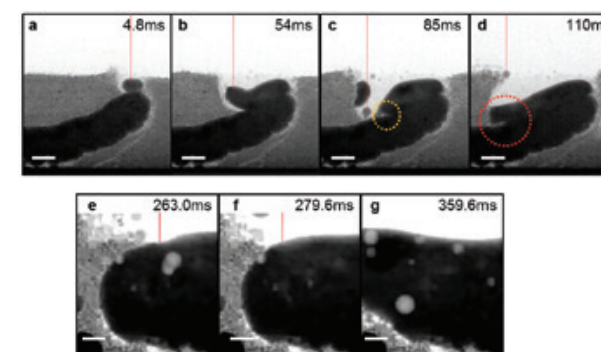


**Figure 3:** Time series radiographs showing a layer by layer LAM build. (a) Molten pool forms above the previous melt track and then (b) merges with previous track via molten pool wetting. Pore formation induced by entrapment of (c) gas porosity, and (d) powder particles. Three pore evolution mechanisms are revealed during laser re-melting, including (e) pore coalescence, (f) pore dissolution, and (g) pore dispersion into smaller pores.

and remelts it. The X-ray images show that porosity can be formed during LAM, including entrapment of gas porosity and powder particles. However, neither defects remain inside the melt track owing to the Marangoni flow that entrains the gas pores to other locations, and allows the hot liquid metal to melt the powder layer as LAM continues. We also uncover how pores coalesce together to form larger ones, dissolve back into the liquid metal due to an increase in gas solubility with increasing temperature, and then disperse into smaller pores as the temperature decreases, i.e. reduce in gas solubility.

Our results show the first example of high-speed X-ray imaging of LAM under layer-by-layer build conditions, providing insights into the molten pool and defect dynamics. This work highlights that the evolution of melt conditions strongly depends on

the temperature and chemistry of the molten pool, i.e. the surface tension effect, governed by the laser processing parameters. Future investigations should focus on effective ways to control the molten pool behaviour. The reported pore evolution process is rather complex compared to what has been hypothesised in the literature, such that pores can flow, coalesce, dissolve, and disperse into smaller ones inside melt tracks during melting and solidification. The mechanism map provides users with the ability to predict and control the molten pool behaviour and final track morphology. These valuable observations can only be captured using the methods presented in this study, and play a key role in the development of next-generation additive manufacturing processes, materials, and products.

### References:

- Sames W. J. *et al.* The metallurgy and processing science of metal additive manufacturing. *International Materials Reviews* **61**, (2016). DOI: 10.1080/09506608.2015.1116649
- Leung C. L. A. *et al.* Laser-matter interactions in additive manufacturing of stainless steel SS316L and 13-93 bioactive glass revealed by in situ X-ray imaging. *Addit. Manuf.* **24**, 647–657 (2018). DOI: 10.1016/j.addma.2018.08.025
- Leung C. L. A. *et al.* The effect of powder oxidation on defect formation in laser additive manufacturing. *Acta Mater.* **166**, 294–305 (2018). DOI: 10.1016/j.actamat.2018.12.027
- Leung C. L. A. *et al.* In situ X-ray imaging of defect and molten pool dynamics in laser additive manufacturing. *Nat. Commun.* **9**, 1355 (2018). DOI: 10.1038/s41467-018-03734-7
- Drakopoulos M. *et al.* I12: The Joint Engineering, Environment and Processing (JEEP) beamline at Diamond Light Source. *J. Synchrotron Radiat.* **22**, 828–838 (2015). DOI: 10.1107/S1600577515003513

### Funding acknowledgement:

EPSRC MAPP Future Manufacturing Hub (EP/P006566/1, www.mapp.ac.uk, EP/I02249X/1, EP/P006566/1, and EP/M009688/1); AMAZE (Additive Manufacturing Aiming towards Zero Waste and Efficient Production of High-Tech Metal Products) project funded by the 7th Framework Programme of the European Commission (contract FP7-2012-NMP-ICT-FoF-313781).

### Corresponding author:

Dr Chu Lun Alex Leung, University College London, alex.leung@ucl.ac.uk

## Maximising information from precious biological samples: Combining 3D X-ray imaging with traditional 2D histology

**Related publication:** Strotton M. C., Bodey A. J., Wanelik K., Darrow M. C., Medina E., Hobbs C., Rau C. & Bradbury E. J. Optimising complementary soft tissue synchrotron X-ray microtomography for reversibly-stained central nervous system samples. *Sci. Rep.* **8**, 12017 (2018). DOI: 10.1038/s41598-018-30520-8

**Publication keywords:** Spinal cord; Tomography; 3D imaging

**Complementary techniques that can maximise information derived from precious soft tissue samples are extremely valuable. A team from the Wolfson Centre for Age Related Diseases wanted to use 3D imaging to track how disease spreads through spinal tissue, followed by traditional 2D histology to probe the regions of interest identified in these scans at the molecular level. However, most 3D imaging methodologies require tissue preparation that prevents its subsequent use, or are too slow to practically image large sample sizes at a useful spatial resolution.**

**Synchrotron Micro-Computed Tomography (SR- $\mu$ CT) is a quasi-non-destructive 3D imaging technique, previously shown to be capable of achieving high-resolution imaging of soft tissues. To ensure they maintained the viability of tissue for later use, while also optimising imaging speed and spatial resolution, the team needed to directly compare a variety of tissue preparation methods and imaging parameters.**

**They chose the Diamond Manchester Imaging Branchline (I13-2), as its photon energy range and coherence make it suitable for imaging large soft biological tissues, with both absorption and phase contrast. I13-2 is equipped with high precision, high accuracy sample stages, and appropriate detector instrumentation to enable rapid, high resolution SR- $\mu$ CT.**

**They identified reversible wax embedding with contrast enhancing iodine staining as optimal for good absorption contrast, and subsequent histology, revealing gross internal spinal cord features and unprecedented cellular-level detail. Subsequent 2D histological stains and antibody markers used on these tissues could be aligned to 3D datasets, demonstrating the compatibility of the techniques.**

Histology is a widely-adopted technique in life science research that uses tissue staining and microscopy to address a multitude of questions in thin tissue slices. It can reveal the anatomical organisation of tissues, diagnose biopsy samples in the clinic, or probe molecular markers to reveal cell subtypes, subcellular features, and cell activation states. Studying different markers in adjacent tissue sections is a powerful approach to obtain multi-layered information from individual tissues, but these 2D snapshots of 3D tissues can risk overlooking key features. The desire to track 3D features such as a branching vasculature, or long-range neuronal projections and pathways across the nervous system, has spurred the development of novel 3D imaging technologies that are up to the task. In the last decade, the combination of fluorescent markers with tissue clearing and light-sheet microscopy has enabled imaging of tagged features of interest at cellular resolution across whole organs<sup>1</sup>, while more established technologies like magnetic resonance imaging show ever-improving spatial and temporal resolution. However, these approaches have notable disadvantages. The former is typically a 'one-shot' approach that limits subsequent use of tissue, while the latter suffers from extensive acquisition times (over 10 hours for high resolution of thin tissue slices) that prohibit imaging large sample sizes. It is desirable to extract maximal information from precious tissues by adopting methods that enable high-resolution imaging,

whilst also preserving tissue integrity for subsequent use. Synchrotron Micro-Computed Tomography (SR- $\mu$ CT) offers the potential to rapidly derive high-resolution 3D information from biological specimens, which could then be probed with standard 2D histology techniques.

Computed tomography reconstructs a 3D volume from a series of 2D images (projections) collected during sample (or detector) rotation across a range of equally spaced angles. The bright, coherent X-ray beam provided by a synchrotron enables short exposures (micro-millisecond) per 2D image acquisition, summing to rapid 3D imaging. Samples must not drift or deform during data acquisition (2D image collection), as this will compromise the final quality of tomography data. This is a problem for soft tissues, which lack the physical stability that is inherent to those sample types (e.g. bones, metals, and rocks) commonly probed by X-ray imaging. This study began by comparing various embedding agents used in standard histology procedures to confer tissue stability. Paraffin wax was identified as optimal for conferring sufficient SR- $\mu$ CT stability to rodent spinal cord soft tissue, while retaining the viability of samples for processing and probing with subsequent histology.

The next challenge was to increase SR- $\mu$ CT tissue contrast, which was

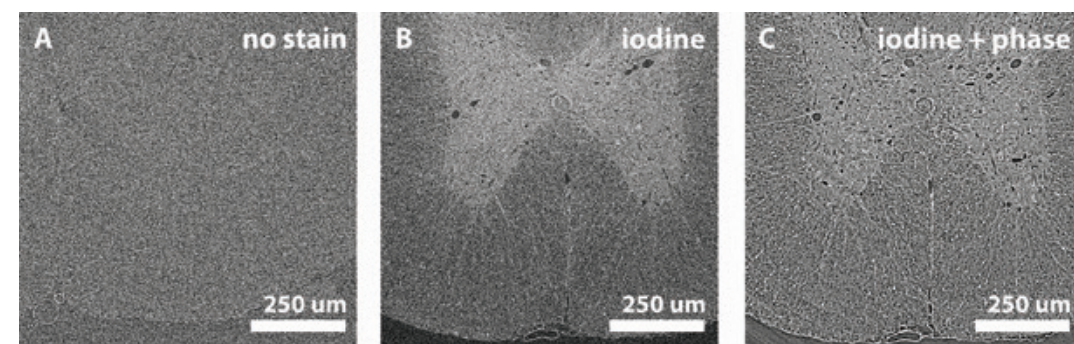


**Figure 1:** X-ray tomography of (a) unstained paraffin wax embed rat spinal cords with contrast improvements achieved by (b) iodine tissue stain, and further improved by (c) combining iodine stain with optimised in-line phase contrast.

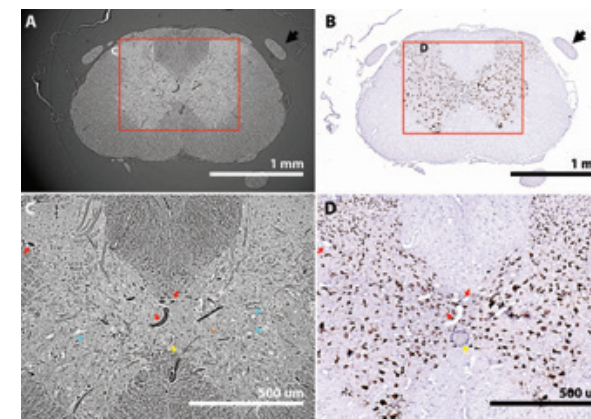


**Figure 2:** After 3D imaging a spinal cord sample by (a, c) SR- $\mu$ CT, tissue can be sectioned and probed by (b, d) 2D histology. Tomography and histology can be aligned by features within samples including vasculature (red arrows) and the central canal (yellow arrow). Cell bodies are also apparent (blue arrows). (b, d) Immunolabelling for NeuN (a marker for neuronal cell bodies) confirms tissue is viable for histology after 3D scanning.

initially very low (Fig. 1a). Signal was improved by a contrast enhancing iodine stain which - unlike other stains trialled - revealed the white-grey matter tissue boundary in spinal cord samples (Fig. 1b). This stain could be easily removed from dewaxed samples at a later stage after SR- $\mu$ CT, leaving tissues viable for subsequent histology. The more notable contrast improvements, however, came from combining this stain with the in-line phase contrast imaging capabilities available at the I13-2 branchline. Retreating the detector from the sample amplifies contrast derived from phase changes that occur as X-rays cross material boundaries within the sample, resulting in contrast enhancement of spinal cord internal fine features, including capillary level vasculature, and the large individual cell bodies of motoneurons found within spinal cord grey matter (Fig. 1c). This improvement was facilitated by screening propagation distances to optimise phase contrast - something hard to predict given the variety of different sized features present in the spinal cord that respond differently to phase propagation<sup>2</sup>. Reconstruction of phase contrast data was simplified by using Diamond's recently developed modular reconstruction software Savu, which incorporated a number of artefact correction modalities (including ring removal, zinger removal, and lens distortion) to improve accuracy of the final data reconstruction<sup>3</sup>. Features that emerged in the artefact corrected data could then be aligned to subsequent histology to confirm their identity (Fig. 2), and verify the compatibility of SR- $\mu$ CT with downstream tissue analyses.

Along with optimising sample preparation to make soft tissue SR- $\mu$ CT compatible with histology, this study outlined a single scan, iterative downsampling methodology that informs efficient SR- $\mu$ CT data collection more generally. This approach collects a single scan with an excessive number

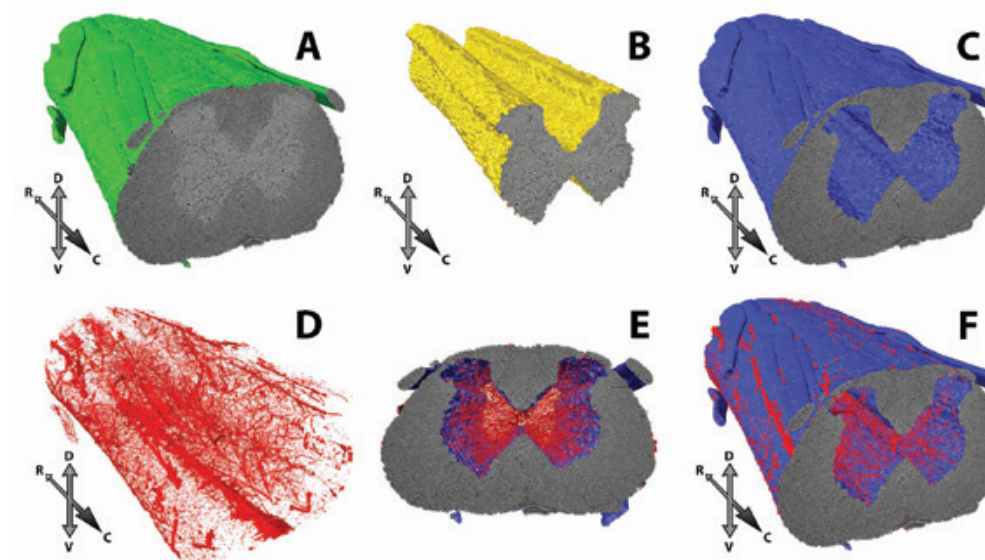


**Figure 3:** Tomography scans can be used to hierarchically extract tissue volumes including (a) the whole spinal cord, (b) grey matter, (c) white matter, and (d) spinal cord vasculature using the Super-Region Volume Segmentation (SuRVoS) software developed at Diamond. (e, f) Overlay of vasculature and white matter volume.

of 2D projections, then compares the image quality of reconstructions made from the full range, and an ever-smaller subset, of this 2D projection set. Image quality improvements delivered by increasing projection numbers can then be quantified, in this instance revealing how to deliver near-maximum signal-to-noise while keeping data acquisition times below just 12 minutes. Even with these rapid scan times, fine tissue features could still be identified across the tomographic volume, as shown by their volume extraction (Fig. 3) with the open source, semi-automated, shallow machine learning 3D segmentation software SuRVoS (Super-Region Volume Segmentation), developed at Diamond<sup>4</sup>.

The close collaboration between users and Diamond scientists to systematically optimise sample preparation, image acquisition, and data processing made high speed, high resolution, non-destructive 3D imaging of spinal cord soft tissue by SR- $\mu$ CT possible. Many of the lessons learnt should apply to soft tissue tomography more generally. This opens the door to future studies that could accurately characterise pathology in soft tissues across extended tissue regions, or compare large numbers of samples comprising multiple time points and treatments. Insights derived from these 3D data could then be enhanced by 2D histology.

### References:

- Richardson D. S. *et al.* Clarifying Tissue Clearing. *Cell* **162**, 246–257 (2015). DOI: 10.1016/j.cell.2015.06.067
- Wilkins S. W. *et al.* Simultaneous phase and amplitude extraction from a single defocused image of a homogeneous object. *J. Microsc.* **206**, 33–40 (2003). DOI: 10.1046/j.1365-2818.2002.01010.x
- Atwood R. C. *et al.* A high-throughput system for high-quality tomographic reconstruction of large datasets at diamond light source. *Philos. Trans. R. Soc. A Math. Phys. Eng. Sci.* **373**, 20140398 (2015). DOI: 10.1098/rsta.2014.0398
- Irvine S. *et al.* Volume Segmentation and Analysis of Biological Materials Using SuRVoS (Super-region Volume Segmentation) Workbench. *J. Vis. Exp.* e56162 (2017). DOI: 10.3791/56162

### Funding acknowledgement:

King's Bioscience Institute; Guy's and St Thomas' Charity Prize PhD Programme in Biomedical and Translational Science; Medical Research Council UK (SNCF Award G1002055).

### Corresponding authors:

Dr Merrick Strotton, Wolfson Centre for Age Related Diseases, King's College London, merrick.strotton@kcl.ac.uk and Dr Andrew Bodey, Diamond Light Source, andrew.bodey@diamond.ac.uk

## Crystallography Group

Joe Hriljac, Science Group Leader

**T**he Crystallography Science Group comprises the High Resolution Powder Diffraction beamline (I11), the Extreme Conditions beamline (I15), the X-ray Pair Distribution Function (XPDF) beamline (I15-1), and the Small-Molecule Single-Crystal Diffraction beamline (I19). Bringing these beamlines together into one science group means we can fully exploit the technical and scientific expertise within its teams to provide the basis for future development and pioneering experiments. The coming year will see many beamline upgrade projects, with the aim to further develop our tools, data analysis pipelines and strategic planning for the Diamond-II upgrade.

### I11 update

The high brightness beamline uses monochromatic X-rays in the range of 6 – 25 keV for high-resolution and time-resolved powder diffraction experiments in the first Experimental Hutch (EH1) or for Long Duration Experiments (LDEs) in EH2. Thanks to our dedicated beamline staff, I11 has continued to efficiently deliver beamtime, facilitating experiments to the busy user programme throughout the year, in particular for non-ambient applications and experiments requiring unusual hardware setups such as toxic/corrosive gas absorption studies at cryogenic temperatures, resonant diffraction at high temperature and time-resolved *in operando* lithium-ion (Li-ion) battery work. The continued success in terms of high quality research is clearly evidenced from record publications output, with an increase of 40% compared to the previous period.

As the I11 facility has now been running for more than 10 years, the main components of the original design such as the monochromator (DCM), diffractometer and X-ray source (in vacuum undulator), are starting to show signs of wear. We have therefore developed an upgrade plan, endorsed by the Scientific Advisory Committee (SAC) and the Diamond Industrial Science Committee (DISCO) at the end of 2017 to replace these components in order to maintain our competitiveness. The construction of the new high stability DCM

and the high-energy cryo-cooled undulator have already started and should be complete and ready for installation next year. We have also completed the design/specification for a new diffractometer, which will be delivered for installation late autumn. Finally, improvements of the detection systems (MAC and PSD) and the replacements of existing sample environments are also included in the project.

### I15 update

The Extreme Conditions beamline, I15, employs high energy X-rays to explore the structure of materials at high pressures, high and low temperatures, as well as other *in situ* and *in operando* conditions. The beamline receives an X-ray continuum from the superconducting wiggler; this allows for experiments which require monochromatic X-rays between 20 and 80 keV, as well as polychromatic beam. I15 was originally designed to serve the mineral physics community, which it has while also assisting material scientists, chemists and solid state physicists with their structural investigations, at pressure or otherwise.

I15 continues to offer capabilities and support that few extreme conditions beamlines do. I15 users have pre-experiment access to bespoke assistance and training from our highly skilled staff in diamond anvil cell (DAC) preparation

“Bringing these beamlines together into one science group means we can fully exploit the technical and scientific expertise within its teams to provide the basis for future development and pioneering experiments.”

*The I15 and I15-1 beamlines team and support group, clockwise from top left: Annette Kleppe, Maria Diaz Lopez, Philip Chater, Stuart Gurney, Dean Keeble, Dominik Daisenberger, Christine Beavers (PBS), Lawrence Gammond, Allan Ross, Volodymyr Khotkevych.*

and loading, as well as the loaning of DACs for I15 experiments. The high pressure gas loader available at I15 offers users the choice of many possible gases to use as their pressure transmitting media (PTM), allowing them to optimise for hydrostaticity with helium or neon, or choosing a PTM based on desired interactions with the sample at pressure. The recent addition of the laser heating system adds a further unique capability – the I15 system is capable of quickly ramping the laser power to perturb a sample without delivering too much heat to the bulk. The I15 team are actively working on the future development plans for the beamline.

### I15-1 update

The XPDF beamline, I15-1, is dedicated to producing high quality X-ray scattering data for Pair Distribution Function (PDF) analysis. Operational since 2017, I15-1 has illuminated samples from diverse fields, from Earth sciences to pharmaceuticals, as well as material science and chemistry. XPDF receives X-rays from the inside edge of the wiggler fan, and this light is monochromated and directed to the end station in three energies: 40, 65 and 76 keV. PDF data are collected at high energies to produce the low sample absorption and high Q range required for successful interpretation. Gaining structural information on amorphous samples is a primary goal of many XPDF experiments, but crystalline samples can also display local structure variations such as defects and disorder, which can be observed with PDF analysis.

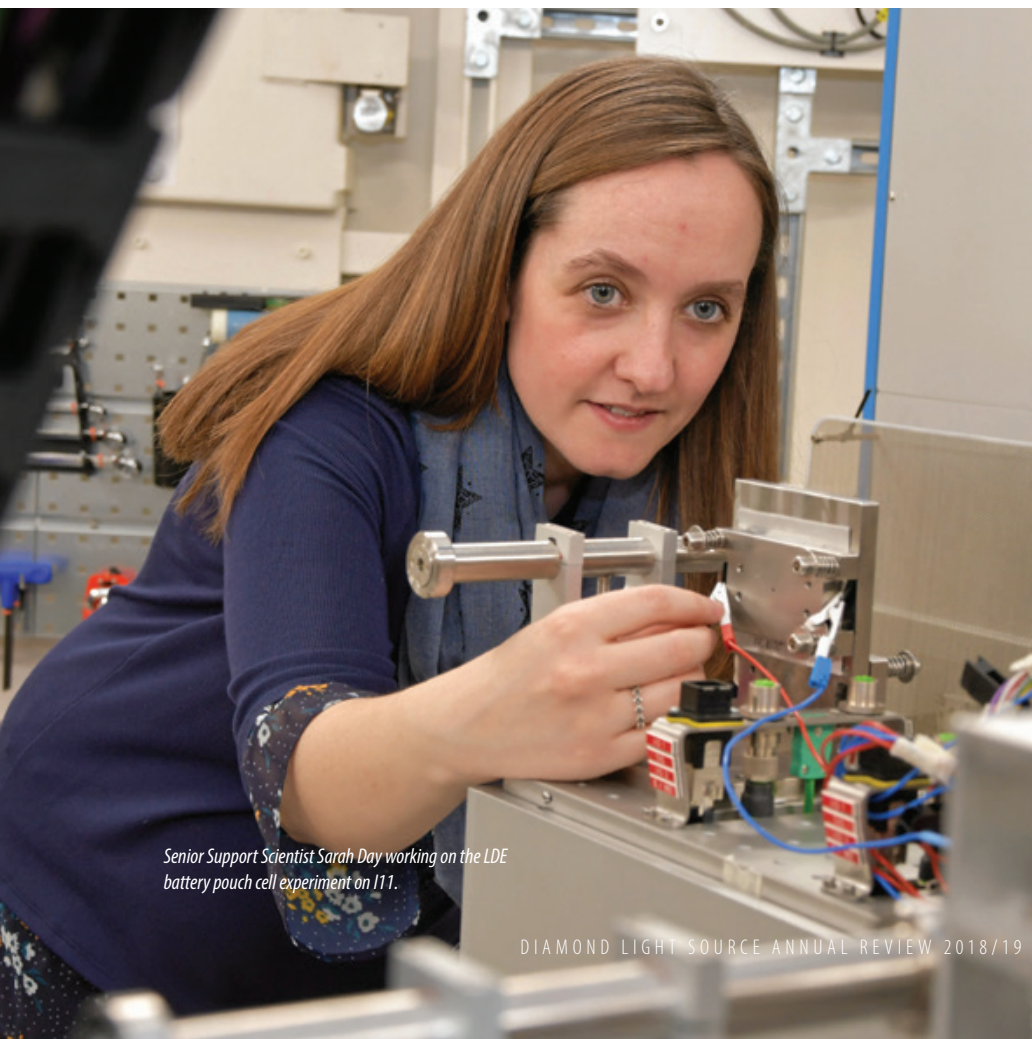
Consisting of a sample position, with an optional sample changing magazine, and two large area detectors, the end station is highly flexible and has been adapted to many *in situ* and *in operando* experiments, including variable temperature, gas flow, hydrothermal synthesis and electrochemical cycling. For more routine measurements, the 15 position sample changer has been a popular choice, allowing automatic data collection. A further automation improvement is currently underway; in spring 2020, a sample changing robot and an upgraded detector will be installed on I15-1. This upgrade will be a synergistic addition to the existing auto processing infrastructure, and will allow users to collect better data with less manual intervention.

### I19 update

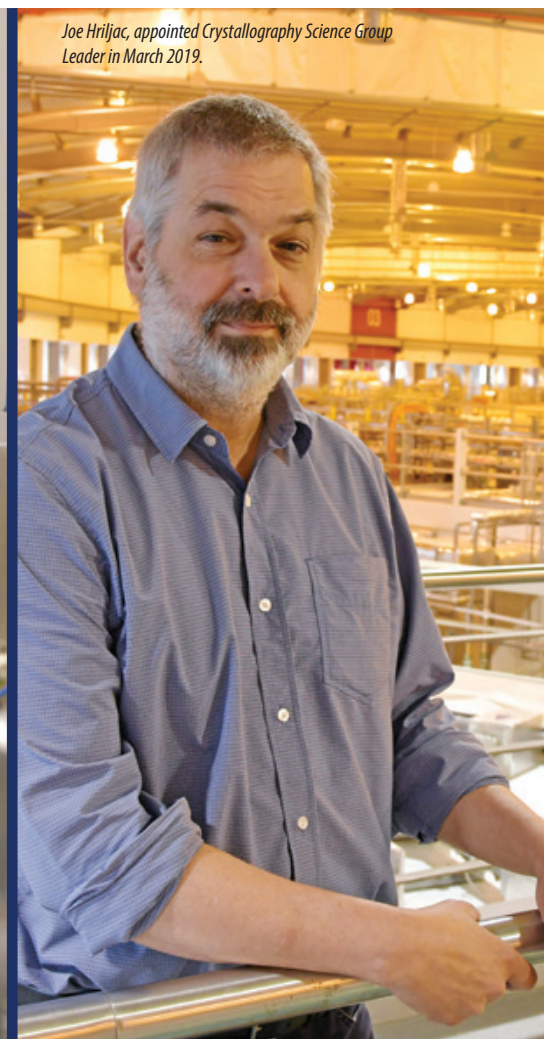
The Small-Molecule Single-Crystal Diffraction beamline, I19, uses X-rays in the 5 – 25 keV energy range to determine the structures of small-molecule systems with single-crystal diffraction techniques. This can be for characterisation of novel molecular materials or for investigating the variation in the structure of a crystalline material under an external physical influence such as change in temperature, the exposure to a gas, photo-excitation or through the application of high-pressure.

The use of the robotic sample changer, and remote access, is now well established in Experimental Hutch 1 (EH1) of the beamline, where pre-mounted samples are sent to Diamond under cryogenic storage and users then run their beamtime from their home institutions. This mode of operation makes it possible to carry out chemical crystallography studies in a more responsive manner as beamtime can be scheduled in more regular, and shorter, periods. From AP25 we will schedule individual shifts, rather than whole one-day (three shifts) blocks of beamtime, for those wishing to run their beamtime via the remote access route. For Experimental Hutch 2 (EH2) we have recently developed a cell which allows a high static electric field to be applied to the sample crystal. The application of electric fields to materials can result in a variety of responses that may have important technological applications, spanning electronic and ionic conductivity to piezo- and ferro-electricity.

In the near future, the control system for the Newport 4-circle diffractometer, housed in EH2, will be changed. This will not only improve the reliability of the instrument but will provide the foundation of further developments which will improve ease of use and allow better integration into the beamline's infrastructure. More significantly, perhaps, at the start of AP25 we will upgrade the monochromator to provide greater beam stability and allow data collections to be performed more quickly. The monochromator upgrade also promises a more automated approach to wavelength changes and will provide users a more direct control of this for the first time.



Senior Support Scientist Sarah Day working on the LDE battery pouch cell experiment on I11.



Joe Hriljac, appointed Crystallography Science Group Leader in March 2019.

## Understanding the origin of poor cycling stability in novel high capacity Li-ion battery materials: A long duration study

**Related publication:** Kleiner K., Strehle B., Baker A. R., Day S. J., Tang C. C., Buchberger I., Chesneau F. F., Gasteiger H. A. & Piana M. Origin of High Capacity and Poor Cycling Stability of Li-Rich Layered Oxides: A Long-Duration *in situ* Synchrotron Powder Diffraction Study. *Chem. Mater.* **30**, 3656–3667 (2018). DOI: 10.1021/acs.chemmater.8b00163

**Publication keywords:** Electrochemistry; Battery materials; Powder diffraction

**C**limate change, dwindling supplies of fossil fuels, and growing environmental awareness are all contributing to a surge of interest in electric vehicles. However, battery-powered electric vehicles cost more, and have a shorter range, than petrol/diesel vehicles, due to the energy density of lithium-ion batteries, for which cathode materials are currently a limiting factor.

Lithium-rich layered oxide cathode materials would fulfil the energy density requirements of the automotive industry, but commercial usage is hindered by poor capacity retention, and voltage fade, upon cycling (charge-discharge). Understanding the fading mechanism at a microscopic level is the first step to improving their cycling stability.

Using the High Resolution Powder Diffraction beamline (I11) allowed researchers to collect high-resolution, time-resolved measurements over the critical first cycle, followed by regular long-term data collections over the subsequent 100+ charge-discharge cycles. Powder diffraction is ideally suited to observing bulk structural changes occurring in battery materials, which allow for the processes leading to degradation to be better understood.

The group demonstrated, for the first time, that irreversible migration of transition-metal atoms occurs upon cycling: from octahedral sites in the transition-metal layers, via tetrahedral sites in the lithium layer, into octahedral lithium sites. Because both the reversible capacity and the cycling stability seem to be affected by this TM/Li disorder, future investigations will need to focus on how transition-metal motion can become completely reversible to ensure high capacity retention during cycling.

High-energy  $\text{Li}_{1.17}\text{Ni}_{0.19}\text{Co}_{0.10}\text{Mn}_{0.54}\text{O}_2$  (HE-NCM) is a lithium-rich layered oxide consisting of alternating Li and transition-metal (TM) layers in which excess lithium ions replace transition metals in the structure. HE-NCM offers a large, reversible discharge capacity of  $250 \text{ mAh g}^{-1}$ , at least  $50 \text{ mAh g}^{-1}$  higher than existing commercial battery materials. This improved energy density is key for meeting the requirements of the automotive industry for the large-scale commercialisation of electric vehicles, increasing the mileage range available on a single charge, and significantly reducing the cost of production. Unfortunately, these materials suffer from poor capacity retention, and voltage fade, upon cycling, limiting their lifetime and, therefore, reducing their appeal for commercialisation at present. It is, however, believed that this degradation can be overcome, but to achieve this it is first essential that the fading mechanism responsible for the degradation is well understood.

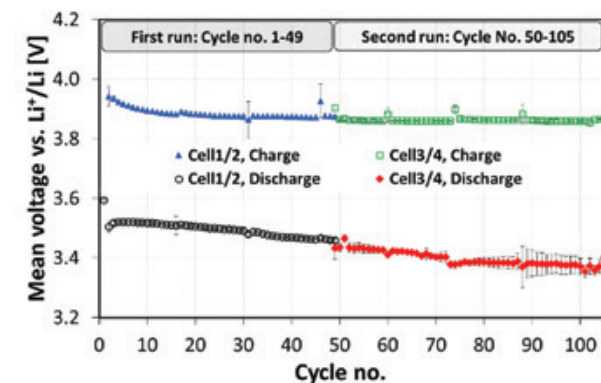


Figure 1: Mean charge and discharge voltages per cycle, measured with pouch cells on Beamline I11. The values presented are an average of two cells cycled simultaneously, and the error bars represent the standard deviation between the two cells. Reprinted (adapted) with permission from Kleiner et al., *Chem. Mater.* 2018, 30, 3656–3667. Copyright (2018) American Chemical Society.

The common understanding is that oxygen release from the host structure is the main reason for capacity loss and voltage fade<sup>1</sup>, however, Transmission Electron Microscopy (TEM) studies suggest that such an irreversible lattice-oxygen oxidation would be limited to near-surface parts of the particles<sup>2</sup>. Recent electrochemical data, obtained over a period of extended cycling, is inconsistent with this theory. Fig. 1 shows the mean voltage integrated over the number of exchanged charges for 105 cycles at a rate of C/5 (one complete charge-discharge cycle in 10 hours). The mean charge voltage stays relatively constant after the first ~30 cycles, but the discharge voltage decreases about 1 mV per cycle, indicating an asymmetric evolution of the overpotentials during cycling. This implies that a simple surface-related degradation mechanism (e.g. an impedance increase due to surface film formation), which would block both lithiation and delithiation of HE-NCM to the same extent, cannot be the only reason for the observed degradation. Instead, this suggests bulk structural changes (e.g. disorder, due to transition-metal migration) as the origin of the poor capacity retention, and theoretical calculations support the occurrence of transition-metal migration during cycling<sup>3</sup>. Synchrotron X-Ray Powder Diffraction (SXPd) is a technique ideally suited to study the bulk structure of materials such as these.

For this study, I11 was used as it offers both high-resolution (HR), time-resolved (TR) SXPd, and long-duration *in situ* studies. SXPd data (HR and TR) were collected in Experimental Hutch 1 (EH1) to study the evolution of the lattice parameters during the first charge, while *in situ* long-term studies (105 cycles) from two identical battery cells were performed on the recently commissioned Long Duration Experiment (LDE) facility<sup>4</sup>. SXPd patterns were taken once a week upon long-term cycling. Using pouch cells suitable for *in situ* SXPd, the first cycle was performed with a C-rate of C/20 to activate the material, and all subsequent cycles were performed at a rate of C/5 between 2.0 and 4.6 V, completing 14.5 cycles each week. From this data, it is possible

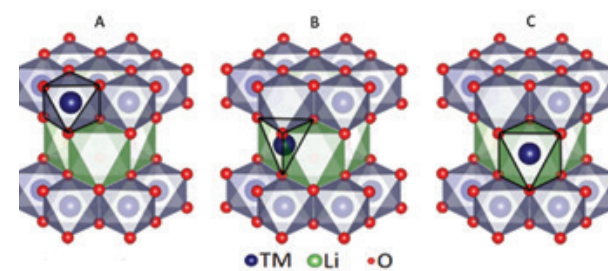


Figure 2: Schematic showing transition-metal migration in layered oxides. Transition metals can move from octahedral sites in the transition-metal layer (A) via tetrahedral sites in the lithium layer (B) into octahedral sites in the lithium layer (C). Reprinted (adapted) with permission from Kleiner et al., *Chem. Mater.* 2018, 30, 3656–3667. Copyright (2018) American Chemical Society.

to determine, and quantify, transition-metal (TM) migration upon cycling by detailed reflection profile analysis, and Difference-Fourier (DF) mapping. The relationship of reversible, and irreversible, TM disorder with the strain in the material can guide improvements in the cycling stability of lithium-rich cathodes, and potentially lead to the synthesis of new application-oriented materials. Although previous studies indicate only minor changes in the bulk material, long duration *in situ* SXPd measurements, in combination with difference Fourier analysis of the data, revealed an irreversible TM motion within the host structure.

TMs tend to occupy tetrahedral sites in the lithium layer (Fig. 2B) at highly delithiated (charged) states, since the occupation of tetrahedral sites in the TM layer is less favourable due to the occupation of neighbouring octahedral sites by cationic species. A TM in tetrahedral sites of the Li-layer can then either move back to the TM layer (Fig. 2A), or move on to occupy octahedral lithium sites (Fig. 2C), leading to a delithiated, disordered structure which is thermodynamically more stable and, therefore, energetically favourable<sup>5</sup>. This disorder is identified in diffraction patterns as a mismatch in the reflection

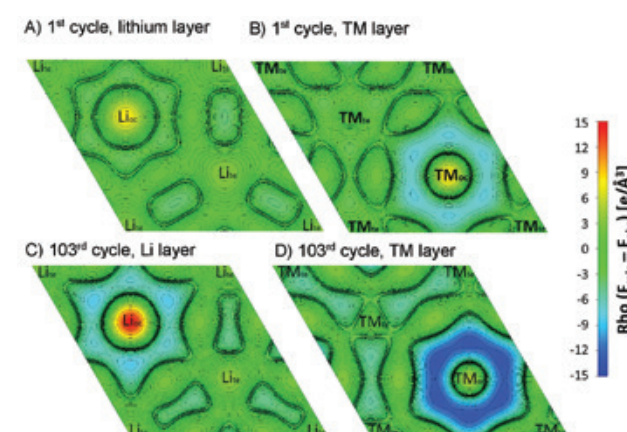


Figure 3: Difference Fourier maps of discharged HE-NCM after the 1st cycle (A and B) and after 103 cycles (C and D). The A, C and B, D projections are the Li and TM planes of the rhombohedral structure. Reprinted (adapted) with permission from Kleiner et al., *Chem. Mater.* 2018, 30, 3656–3667. Copyright (2018) American Chemical Society.

intensities, rather than changes in positions or the presence/absence of reflections. While a minor mismatch in the refined reflection intensities of the first cycle was observed, this became more significant as cycling progressed. If analysed further, the discrepancy in the measured, and refined, reflection intensities can provide useful information, as it originates from the difference between the measured, and calculated, electron density in the crystallographic structure. Due to their relatively high number of electrons, and thus their significant contribution to the X-ray diffraction profiles, TMs are the only elements in the HE-NCM structure that can cause such an effect. DF analysis of the diffraction data was performed to investigate which sites are occupied by

TMs upon cycling. The DF maps of the first discharged state (Fig. 3A and B) show that the electron density of octahedral sites ( $\text{Li}_{\text{oc}}$  and  $\text{TM}_{\text{oc}}$ ) are poorly described by the ideal rhombohedral structure, and the differences become even more significant by the 103<sup>rd</sup> cycle (Fig. 3C and D). Li/TM disorder is not observed in the first cycle of conventional layered oxides, supporting the assumption that lithium vacancies in the TM layer, created during the first charge (the so-called activation), accelerate transition-metal migration. During subsequent cycles, the disorder increases gradually, reaching roughly 5% of the transition metals in  $\text{Li}_{\text{oc}}$  sites after 100 cycles. This observed increase of disorder leads to the conclusion that this type of migration is to some extent irreversible. Equivalent DF maps of the 1.5 and 102.5 charged states show underestimated electron densities in  $\text{Li}_{\text{te}}$  sites (tetrahedral sites in the lithium layer). This confirms the migration of TMs via these sites in the charged state. Nevertheless, these results support the migration pathway shown in Fig. 3, and suggest that TM motion takes place at high states of charge. Migration of TMs into tetrahedral sites has to be largely reversible because no occupation of tetrahedral sites was observed in the discharged state throughout the 100 charge/discharge cycles, while ca. 8% of the TMs occupy tetrahedral sites in the charged state. At the end of discharge, 2–5% of the TMs are refined to be in octahedral Li-sites, while the tetrahedral sites are unoccupied, strongly indicating that 3–6% of the TMs migrate reversibly back from tetrahedral sites into octahedral TM sites upon lithiation.

These results experimentally demonstrated for the first time that the transition-metal migration in lithium-rich layered oxides proceeds upon cycling, moving from octahedral transition-metal sites to octahedral lithium sites via tetrahedral sites in the lithium layer. Prior to this work, these results were only claimed by theoretical investigations. The focus of future investigations should now be to determine how TM motion can become completely reversible, to ensure a high capacity retention during cycling, rather than attempting to suppress disorder, and retain the ideal rhombohedral structure.

### References:

- Lu Z. et al. Structure and Electrochemistry of Layered  $\text{Li}[\text{Cr}_x\text{Li}(1/3-x/3)\text{Mn}(2/3-2x/3)]\text{O}_2$ . *J. Electrochem. Soc.* **149**, A1454–A1459 (2002) DOI: 10.1149/1.1513557.
- Yan P. et al. Probing the degradation mechanism of  $\text{Li}_2\text{MnO}_3$  cathode for Li-ion batteries. *Chem. Mater.* **27**, 975–982 (2015). DOI: 10.1021/cm504257m
- Bréger J. et al. High-resolution X-ray diffraction, DIFFaX, NMR and first principles study of disorder in the  $\text{Li}_2\text{MnO}_3\text{-Li}[\text{Ni}_{1/2}\text{Mn}_{1/2}]\text{O}_2$  solid solution. *J. Solid State Chem.* **178**, 2575–2585 (2005). DOI: 10.1016/j.jssc.2005.05.027
- Murray C. A. et al. New synchrotron powder diffraction facility for long-duration experiments. *J. Appl. Crystallogr.* **50**, 172–183 (2017). DOI: 10.1107/S1600576716019750
- Chang K. et al. Thermodynamic description of the  $\text{LiNiO}_2\text{-NiO}_2$  pseudo-binary system and extrapolation to the  $\text{Li}(\text{Co,Ni})\text{O}_2\text{-}(\text{Co,Ni})\text{O}_2$  system. *Calphad Comput. Coupling Phase Diagrams Thermochem.* **37**, 100–107 (2012). DOI: 10.1016/j.calphad.2012.02.006

### Funding acknowledgement:

BASF SE (Network on Electrochemistry and Batteries); Diamond Light Source.

### Corresponding authors:

Dr Sarah Day, Diamond Light Source, sarah.day@diamond.ac.uk and Dr Karin Kleiner, Diamond Light Source, karin.kleiner@diamond.ac.uk

## Elastic porous crystals

**Related publication:** Henke S., Wharmby M. T., Kieslich G., Hante I., Schneemann A., Wu Y., Daisenberger D. & Cheetham A. K. Pore closure in zeolitic imidazolate frameworks under mechanical pressure. *Chem. Sci.* **9**, 1654–1660 (2018). DOI: 10.1039/C7SC04952H

**Publication keywords:** High pressure; Metal Organic Frameworks (MOFs); Phase transition

Over the past few years, responsive materials - materials that change their structure when chemical, thermal, or mechanical stimuli are applied - have been studied extensively. A team of researchers used high-pressure X-ray diffraction on the Extreme Conditions beamline (I15) to study stimuli-responsive metal-organic frameworks (MOFs), a class of synthetic, crystalline, and porous materials constructed from organic and inorganic building units. Some MOFs are known to be flexible, and to dramatically change their crystal structure upon adsorption of guest molecules or changes in temperature. The team wanted to investigate whether the responsive behaviour of MOFs can also be triggered by mechanical compression.

They focused on ZIF-4 materials, which are representative of an important subclass of MOFs called zeolitic imidazolate frameworks (ZIFs). They had previously shown that the Zn-based derivative ZIF-4(Zn) undergoes a remarkable phase transition from an open-pore form to a closed-pore form when cooled to cryogenic temperatures, and now wanted to investigate whether the same change could also be triggered by compressing the material. If so, the materials would have potential for shock absorbers, nanodampers, and cooling applications.

The data they obtained at Diamond Light Source helped to generate a full picture of the unusual phase behaviour of these framework materials, including the determination of macroscopic parameters such as their compressibility, and the critical pressures needed for pore closure.

Metal-organic frameworks (MOFs) are a class of crystalline porous materials constructed from molecular organic and inorganic building units. Some MOFs feature remarkable responsiveness towards external stimuli, enabling them to undergo reversible phase transitions as a function of guest molecule adsorption or changes in temperature<sup>1,2</sup>. Importantly, the crystalline order and internal connectivity (also known as topology) of the frameworks is retained in these processes, while volumetric changes of more than 20% occur. Such transitions typically involve large changes in pore volume, pore size, and pore shape. Chemical bonds between the building units remain fully intact, while bond and torsional angles change. In contrast to guest- and temperature-dependent structural changes, phase transitions as a function of mechanical pressure are much less common for MOFs<sup>3,4,5</sup>. However, pressure-driven framework flexibility is appealing for the application of such framework materials as shock absorbers, nanodampers, or for cooling applications (i.e. mechanocalorics).

Herein, the high-pressure phase behaviour of two isostructural zeolitic imidazolate frameworks (ZIFs) named ZIF-4(M), featuring the chemical composition  $M(\text{im})_2$  (with  $M^{2+} = \text{Zn}^{2+}$  or  $\text{Co}^{2+}$ ,  $\text{im}^- = \text{imidazolate}$ ), was studied. ZIF-4(M) crystallises in the orthorhombic space group  $Pbca$  and features the **ca**g topology. During a previous beamtime at the High Resolution Powder Diffraction beamline (I11) at Diamond, the team discovered that ZIF-4(Zn) undergoes a remarkable phase transition from its conventional open-pore (op)

phase to a closed-pore (cp) phase when cooled below 140 K (Fig. 1)<sup>2</sup>. The cp phase is about 30% denser than the porous op phase; space group symmetry and network topology, however, are unchanged. During the transition a concerted sequence of single-bond rotations results in an isotropic contraction of the framework by more than 20% in volume.

In the current study, High-Pressure Powder X-ray Diffraction (HP-PXRD) experiments were performed at beamline I15 at Diamond to investigate if ZIF-4(Zn), and its isostructural derivative ZIF-4(Co), undergo similar op-cp transitions when exposed to hydrostatic mechanical pressures. Finely ground and guest-free powders of the ZIF-4(M) materials were loaded into membrane diamond anvil cells (mDAC), together with a pressure transmitting fluid (PTF), and an alkali halide, as internal pressure standard. mDAC preparation had to be performed inside a glovebox (Ar atmosphere) in order to prevent adsorption of moisture inside the guest-free porous ZIF-4(M) compounds. Fluorinert FC-70, a liquid composed of molecules that are too large to penetrate into the microporous frameworks of the ZIF-4(M) compounds, was used as PTF. Subsequently, HP-PXRD patterns were recorded as a function of hydrostatic pressure. Surprisingly, the op-cp phase transitions of the ZIF-4(M) compounds were observed already at comparatively low hydrostatic pressures between 75 and 180 MPa (Fig. 2). Structureless profile fitting suggested that the high-pressure cp phases of ZIF-4(Zn) and ZIF-4(Co) are similar, but different to the previously reported low temperature cp phase of ZIF-4(Zn). The HP-

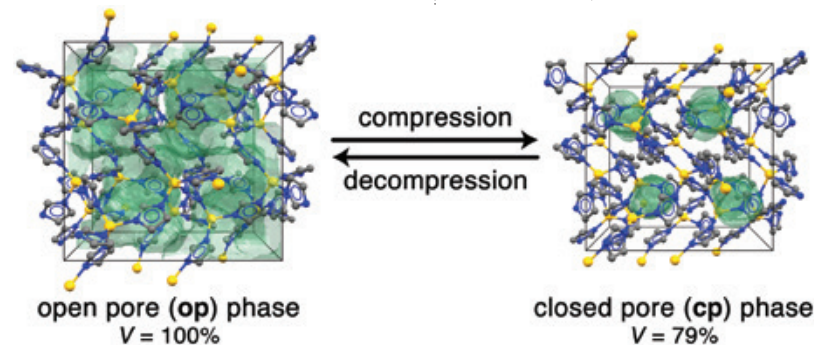


Figure 1: Representation of the op and cp phases of ZIF-4(M) materials.

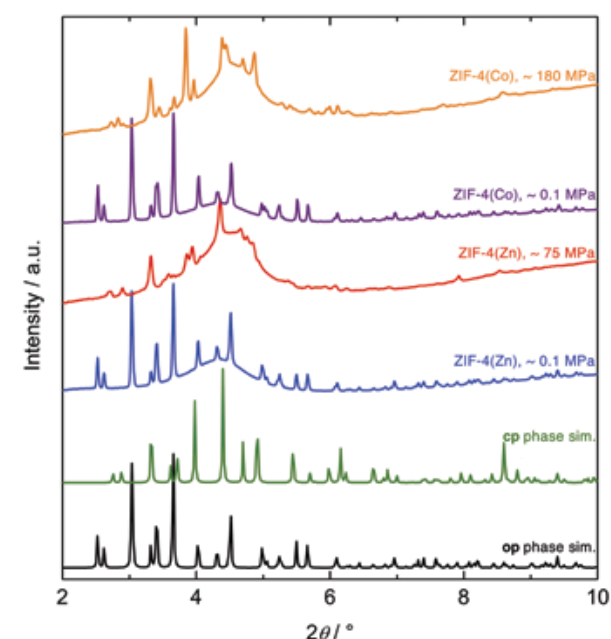


Figure 2: PXRD patterns of ZIF-4(M) materials at different hydrostatic pressures and room temperature. The simulated patterns of the op and cp phases are shown for comparison.

PXRD patterns could not be fitted satisfactory in the expected orthorhombic symmetry (space group  $Pbca$ ). However, a symmetry reduction involving a small shear element, and a transition to the monoclinic subgroup  $P2_1/c$ , yielded a reasonable fit to both experimental datasets. A volumetric compression by ~21% was found for ZIF-4(Zn), and by ~19% for ZIF-4(Co).

Additional mercury intrusion-extrusion experiments were performed to pinpoint the energetics and the reversibility of the unusual pressure-driven op-cp phase transformation of these materials (Fig. 3). It was found that ZIF-4(Zn) undergoes the op-cp transition already at a surprisingly low mechanical pressure of only ~28 MPa. The op-cp transition is visible as a pronounced step in the intrusion curve. The volume change corresponding to the step in the intrusion curve ( $\Delta V_{\text{intu}} = 0.16 \text{ cm}^3 \text{ g}^{-1}$ ) is very close to the value expected for the op-cp phase transition based on the crystallographic parameters extracted from the HP-PXRD data ( $\Delta V_{\text{crist}} = 0.169 \text{ cm}^3 \text{ g}^{-1}$ ). Noticeably, the following extrusion curve, and a second cycle of mercury intrusion-extrusion, do not show any further steps, indicating that the op-cp transition is irreversible for ZIF-4(Zn).

ZIF-4(Co) shows a different behaviour. The step associated to the op-cp phase transition is present at a much higher pressure of ~50 MPa, and the reverse cp-op transition is visible as a shallow but distinct step at

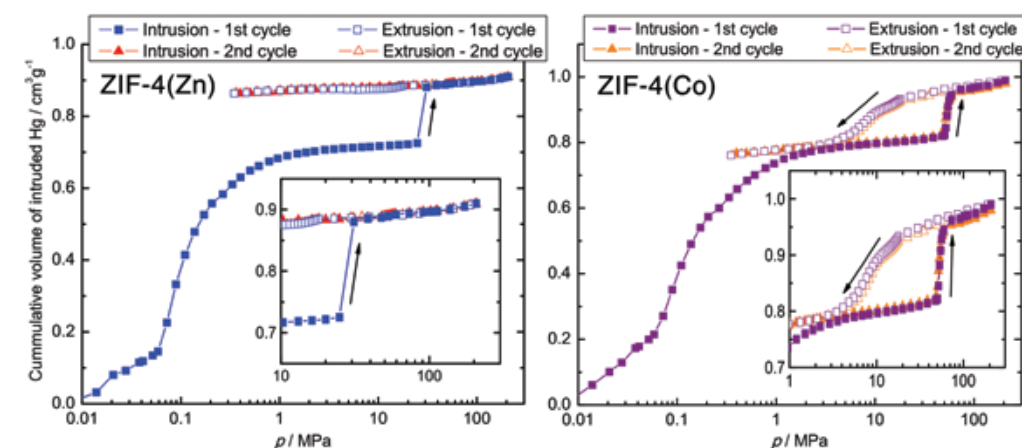


Figure 3: Mercury intrusion-extrusion curves recorded for ZIF-4(M) materials at room temperature. The insets reveal a closer look on the data in the region of the op-cp transition, which is irreversible for ZIF-4(Zn), and reversible for ZIF-4(Co).

pressures below 20 MPa. A second intrusion-extrusion cycle underlines the full reversibility of the phase transition process for ZIF-4(Co). The apparent differences of ZIF-4(Zn) and ZIF-4(Co) can be attributed to the specific valence electron configurations and electronegativities (ENs) of their respective metal ions ( $\text{Zn}^{2+}$ ,  $3d^{10}$ ,  $\text{EN} = 1.65$ ;  $\text{Co}^{2+}$ ,  $3d^7$ ,  $\text{EN} = 1.88$ ), which suggest a stronger and more directional ligand to metal bonding, as well as stiffer coordination tetrahedra for the Co-based derivative.

The discovery of pressure-driven op-cp phase transitions in ZIF-4(M) materials proposes novel applications of these microporous ZIFs as shock absorbers (i.e. irreversible transition of ZIF-4(Zn)), and nanodampers, or in mechanocalorics (i.e. reversible transition of ZIF-4(Co)). HP-PXRD and mercury intrusion experiments reveal that the detailed phase behaviour (critical pressure, volume change, reversibility) can be tuned by the selection of the appropriate metal ion. Furthermore, the obtained results suggest there may exist similar, or even more dramatic, phase transitions in other ZIF compounds.

### References:

- Schneemann A. *et al.* Flexible metal-organic frameworks. *Chem. Soc. Rev.* **43**, 6062–6096 (2014). DOI: 10.1039/c4cs00101j
- Mellot-Draznieks C. *et al.* Extreme Flexibility in a Zeolitic Imidazolate Framework: Porous to Dense Phase Transition in Desolvated ZIF-4. *Angew. Chemie Int. Ed.* **54**, 6447–6451 (2015). DOI: 10.1002/anie.201410167
- Yot P. G. *et al.* Mechanical energy storage performance of an aluminum fumarate metal-organic framework. *Chem. Sci.* **7**, 446–450 (2016). DOI: 10.1039/c5sc02794b
- Serre C. *et al.* Large breathing of the MOF MIL-47(VIV) under mechanical pressure: a joint experimental–modelling exploration. *Chem. Sci.* **3**, 1100 (2011). DOI: 10.1039/c2sc00745b
- Llewellyn P. L. *et al.* Using Pressure to Provoke the Structural Transition of Metal-Organic Frameworks. *Angew. Chemie Int. Ed.* **49**, 7526–7529 (2010). DOI: 10.1002/anie.201003048

### Funding acknowledgement:

We gratefully acknowledge support from the Alexander von Humboldt Foundation (Fellowship for S. Henke), and the Priority Program 1928 COORNETS of the German Research Foundation (Start-Up Grant to S. Henke).

### Corresponding author:

Prof Dr Sebastian Henke, Technische Universität Dortmund, sebastian.henke@tu-dortmund.de

## Mixing advanced materials to make hybrid glasses

**Related publication:** Longley L., Collins S.M., Zhou C., Smales G.J., Norman S.E., Brownbill N.J., Ashling C.W., Chater P.A., Tovey R., Schönlieb C.-B., Headen T.F., Terrill N.J., Yue Y., Smith A.J., Blanc F., Keen D.A., Midgley P.A. & Bennett T.D. Liquid phase blending of metal-organic frameworks. *Nat. Commun.* **9**, 2135 (2018). DOI: 10.1038/s41467-018-04553-6

**Publication keywords:** Metal-organic framework (MOF); Liquid; Glass; Blend; Pair Distribution Function (PDF)

**M**etal-organic frameworks (MOFs) are a class of crystalline materials with a structure of inorganic nodes connected by organic ligands. There are currently more than 60,000 known MOFs, and they are being investigated as promising materials for gas storage, including CO<sub>2</sub> sequestration, and hydrogen storage, and can even be used to harvest water in the desert.

The observation that crystalline MOF structures melt into a liquid of identical composition to the parent framework led to the discovery of a new category of glass, distinct from well-known inorganic, organic, and metallic glasses. This prompted an international team of researchers to investigate, mixing even more complex materials to try and combine the properties of several different 'hybrid' glasses in the same material.

They used Pair Distribution Function (PDF) measurements on the X-ray Pair Distribution Function (XPDF) beamline (I15-1), combined with electron microscopy, and differential scanning calorimetry, to examine the structure of MOF glassy mixtures, to see whether they mix 'intimately', or if the separate components remain within their own 'domains'. This shows whether the resulting properties come from a fully integrated compound, or from the separate domains, or even from the edges between different domains.

Their results showed that the basic metal-organic ligand connectivity of the crystalline MOF state remains unaffected in each of the individual glass domains present in the material. This is important, as it provides confirmation that the glass is made of domains of MOF structures.

Metal-organic frameworks (MOFs) are fast becoming dominant in research into new materials. These three-dimensional structures are formed from the self-assembly of inorganic nodes, and organic bridging ligands, into highly ordered networks with exceptionally high internal surface areas (>7000 m<sup>2</sup> g<sup>-1</sup>). These 'molecular sponges' possess huge, record-breaking porosities; in some cases, the internal surface area of 1 g of a MOF is the same as one-and-a-half football fields. Many applications have therefore been proposed for MOFs, including, for example, H<sub>2</sub>, CO<sub>2</sub>, and CH<sub>4</sub> gas storage and separations, ion conduction, catalysis, and water harvesting<sup>1</sup>. Commercial (crystalline) MOF

products available include those for the prevention of fruit ripening, and the storage of toxic gases in the semiconductor industry.

The term MOF has predominantly referred to crystalline compounds, which are characterised primarily through crystallography. Glasses are amorphous compounds, meaning they contain no long-range atomic order. Due to this, they do not display Bragg diffraction, and cannot be characterised through traditional crystallographic tools.

We recently made liquids from a MOF family<sup>2</sup>. These liquids can be quenched

to form glasses, which are the first new family of glasses, in terms of their dominant chemical bonding, found since metallic glasses in the 1970s<sup>3</sup>. These MOF glasses possess an identical short-range order (i.e. atomic bonding below 6 angstroms) to their crystalline cousins, though their structures are far more complex to characterise.

In our quest for ever-greater complexity, we mixed two amorphous MOF components together with the aim of forming a new glass, which allowed us to investigate how these new materials behaved. We were particularly interested in the possibility of forming a single material containing 'interlocking' non-crystalline ('glassy') MOF domains, or, as we termed them, 'MOF blends'.

High temperature reactions between mixtures of some specific

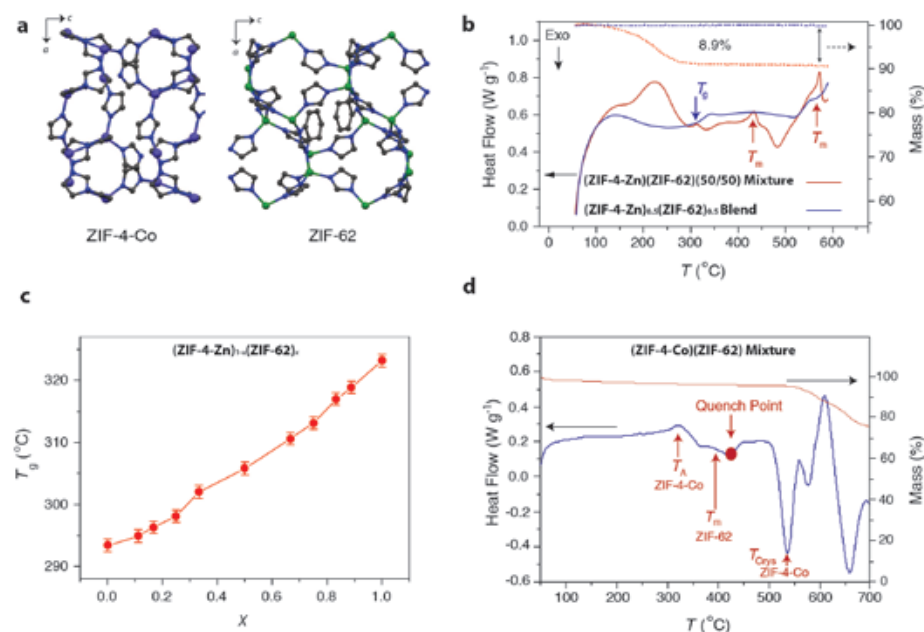


**Figure 1:** (a) Unit cells of crystalline ZIFs, ZIF-4-Co and ZIF-62. N—dark blue, C—grey, Zn—green, Co—purple. (b) Thermogravimetric analysis (red dotted curve) and differential scanning calorimetry data (red solid curve) for (ZIF-4-Zn)(ZIF-62)(50/50). The blue curves represent data on reheating of the glass that forms upon quenching, i.e., (ZIF-4-Zn)<sub>0.5</sub>(ZIF-62)<sub>0.5</sub>. (c) The glass transition of a sample series of (ZIF-4-Zn)<sub>1-x</sub>(ZIF-62)<sub>x</sub>. (d) Differential scanning calorimetry (blue curve) and thermogravimetric analysis (red curve) of the physical mixture (ZIF-4-Co)(ZIF-62)(50/50).

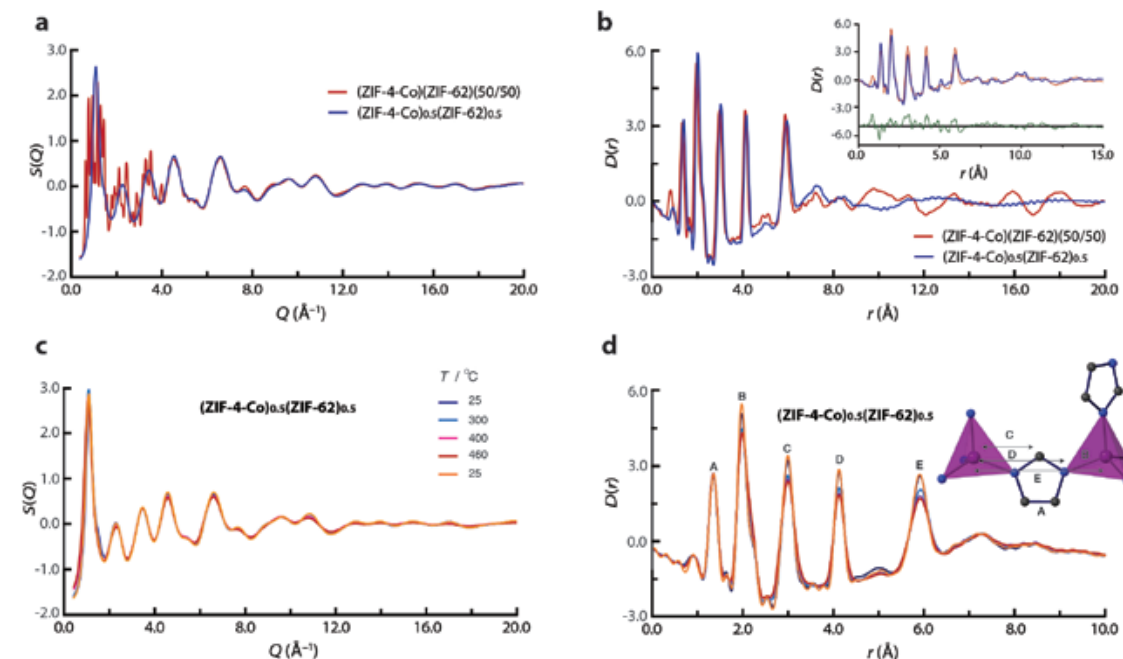


**Figure 2:** (a) X-ray structure factors  $S(Q)$  of the physical mixture of crystalline MOFs and the blended glass, i.e. (ZIF-4-Co)(ZIF-62)(50/50) and (ZIF-4-Co)<sub>0.5</sub>(ZIF-62)<sub>0.5</sub>. (b) Corresponding X-ray pair distribution functions,  $D(r)$ , along with (inset) refinement of (ZIF-4-Co)(ZIF-62)(50/50) against the published structures of ZIF-62 and ZIF-4-Co. (c) Variable temperature  $S(Q)$  of (ZIF-4-Co)<sub>0.5</sub>(ZIF-62)<sub>0.5</sub> upon heating. (d) Corresponding pair distribution functions  $D(r)$  of (ZIF-4-Co)<sub>0.5</sub>(ZIF-62)<sub>0.5</sub> upon heating. The atom pairs that contribute most of the intensity are labelled in peaks (A-E), indicated in the structural fragment.

MOFs, namely ZIF-4 [M(Im)<sub>2</sub>] and ZIF-62 [Zn(Im)<sub>1.75</sub>(blm)<sub>0.25</sub>] (M = Co<sup>2+</sup>, Zn<sup>2+</sup>, Im: C<sub>3</sub>H<sub>3</sub>N<sub>2</sub><sup>-</sup>, blm: C<sub>7</sub>H<sub>5</sub>N<sub>2</sub><sup>-</sup>), were investigated (Fig. 1). Previously, it had been observed that, upon heating, both ZIF-4-Zn and ZIF-4-Co undergo a transition to a high-density amorphous phase, and then to a dense crystal upon heating to 300 °C and 450 °C, respectively. The dense zinc framework melts at 550 °C, unlike the dense cobalt crystal, which remains intact until thermal decomposition at ca. 570 °C. ZIF-62 remains in the room temperature crystalline structure until it melts at 410 °C<sup>4</sup>.

*In situ* Small and Wide Angle X-ray Scattering (SAXS, and WAXS) measurements were made while heating the two MOFs together. These showed that one component formed a liquid, while the other turned into an amorphous solid. The measurements also showed that the particles coalescence, confirming, along with differential scanning calorimetry results, that the two MOF components had blended together – in a manner seen in pure organic polymers, but not previously observed in MOFs.

However, these data crucially provided no information on the extent of metal-ligand bonding within the glass, and hence couldn't determine the extent to which the original MOF structures were retained within each domain. High resolution PDF data obtained on the glass, along with the mixture of the two phases prior to melting, demonstrated clearly that the metal-ligand-metal connectivity reminiscent of all MOFs, was retained (Fig. 2).

Specifically, whereas the X-ray structure factor  $S(Q)$  of a simple mixture of (ZIF-4-Co)(ZIF-62)(50/50) contained Bragg diffraction, that of (ZIF-4-Co)<sub>0.5</sub>(ZIF-62)<sub>0.5</sub>, processed to form an amorphous MOF blend, did not. This rules out small regions of crystallinity in the glass. These data were converted to the corresponding Pair Distribution Functions (PDFs). Interatomic distances at 1.3, 2, 3, 4 and 6 Å were common to both crystal and blend samples, indicating a common local structure and connectivity, and consistent with previous conclusions on near-identical short-range order between crystal, and glass, MOFs.

These prototypical MOF blends are categorised as 'compatible polymer blends', because they have chemically compatible interactions between the two components, and a single glass transition<sup>5</sup>. Future interesting areas of research will be in (i) generating an immiscible blend with two or more  $T_g$ s, (ii)

using the techniques illustrated here to produce functional multi-domain glass structures, and (iii) understanding further the reactivity and behaviour of the liquid state. PDF techniques, and I15-1 in particular for our group, will play a pivotal role in the visualisation of these complex hybrid structures.

### References:

1. Furukawa H. *et al.* The chemistry and applications of metal-organic frameworks. *Science*. **341**, (2013). DOI: 10.1126/science.1230444
2. Gaillac R. *et al.* Liquid metal-organic frameworks. *Nat. Mater.* **16**, 1149–1154 (2017). DOI: 10.1038/nmat4998
3. Bennett T. D. *et al.* Liquid, glass and amorphous solid states of coordination polymers and metal-organic frameworks. *Nat. Rev. Mater.* **3**, 431–440 (2018). DOI: 10.1038/s41578-018-0054-3
4. Longley L. *et al.* Liquid phase blending of metal-organic frameworks. *Nat. Commun.* **9**, 2135 (2018). DOI: 10.1038/s41467-018-04553-6
5. Alemán J. *et al.* Definitions of terms relating to the structure and processing of sols, gels, networks, and inorganic-organic hybrid materials (IUPAC Recommendations 2007). *Pure and Applied Chemistry* **79**, 1801 (2007). DOI: 10.1351/pac200779101801

### Funding acknowledgement:

Royal Society. China Scholarship Council and the Elite Research Travel Scholarship from the Danish Ministry of Higher Education and Science. EU Horizon 2020 programme under the SINE2020 project Grant No. 654000. European Research Council under the European Union's Seventh Framework Program (No. FP7/2007-2013)/ERC Grant Agreement No. 291522-3DIMAGE. Leverhulme Trust project Breaking the non-convexity barrier, EPSRC grant EP/M00483X/1, EPSRC centre EP/N014588/1 and from CHIPS (Horizon 2020 RISE project grant). EPSRC grant EP/L016516/1 for the Cambridge Centre for Analysis. The Cantab Capital Institute for the Mathematics of Information.

### Corresponding authors:

Thomas Bennett, University of Cambridge, tdb35@cam.ac.uk and David Keen, STFC ISIS Facility, david.keen@stfc.ac.uk

## Solving the single-crystal structure of mixed-layer hexaferrites, for potential use in data storage

**Related publication:** Delacotte C., Whitehead G. F. S., Pitcher M. J., Robertson C. M., Sharp P. M., Dyer M. S., Alaria J., Claridge J. B., Darling G. R., Allan D. R., Winter G. & Rosseinsky M. J. Structure determination and crystal chemistry of large repeat mixed-layer hexaferrites. *IUCr* **5**, 681–698 (2018). DOI: 10.1107/s2052252518011351

**Publication keywords:** Large repeat hexaferrites; Mixed-layer structural models; Polytypes; Stacking sequences; Defects; Magnetic properties

**H**exaferrites are an important class of magnetic oxides with applications in data storage and electronics, and have been the subject of numerous studies since their discovery in the 1950s. They are iron (III)-based oxides with highly modular crystal structures, formed of building blocks that can be stacked in different sequences to form a large variety of unique structures. The large size of the resulting structures makes it difficult to analyse them with atomic resolution, but the important functional properties of the hexaferrite family led a team of researchers to investigate the single-crystal growth and structural determination of very large unit cell mixed-layered hexaferrite materials.

The team grew a series of complex hexaferrite crystals, and solved their atomic-level crystal structure using high-resolution synchrotron X-ray diffraction, electron diffraction, and imaging methods, and their physical characterisation by magnetometry. X-ray diffraction data from the Small-Molecule Single-Crystal Diffraction beamline (I19) allowed the team to successfully determine the single-crystal structures of nine hexaferrite materials, all with very large unit cell parameters. The structures include a new hexaferrite stacking sequence, with the longest lattice parameter of any hexaferrite to have its structure fully determined.

Hexaferrites are a class of iron (III)-based oxides with hexagonal, trigonal, or rhombohedral lattices, and have been extensively studied for their applications as magnets, particularly in recording and data storage devices, as well as in electrical components such as antennas<sup>1-4</sup>. All hexaferrites are ferrimagnetic, having high magnetic ordering temperatures due to localised Fe<sup>3+</sup> cations, and strong Fe<sup>3+</sup>-O-Fe<sup>3+</sup> antiferromagnetic superexchange interactions. The family of hexaferrites contains many varieties; the most studied being the BaFe<sub>12</sub>O<sub>19</sub> M-type lattice, followed by BaM<sub>2</sub>Fe<sub>16</sub>O<sub>27</sub> (W-type), Ba<sub>2</sub>M<sub>2</sub>Fe<sub>12</sub>O<sub>22</sub> (Y-type), Ba<sub>3</sub>M<sub>2</sub>Fe<sub>24</sub>O<sub>41</sub> (Z-type), Ba<sub>4</sub>M<sub>2</sub>Fe<sub>28</sub>O<sub>46</sub> (X-type), and Ba<sub>4</sub>M<sub>2</sub>Fe<sub>36</sub>O<sub>60</sub> (U-type) where typically M = Co<sup>2+</sup>, Zn<sup>2+</sup>, Fe<sup>2+</sup>, Mg<sup>2+</sup>, or Mn<sup>2+</sup><sup>5</sup>. To add further complexity to this fascinating system, each family contains a subgroup of more complex mixed-layer structures formed from the regular stacking of M and Y unit blocks, the M<sub>p</sub>Y<sub>n</sub> series, giving rise to a large number of different stacking sequences with hexagonal c parameters up to 1577 Å. These M and Y structural unit blocks are themselves built from the R, S, and T blocks (Fig. 1), which are distinguished by the stacking of their close-packed oxygen layers. In the R and T sub-blocks, the oxygen layers are in hexagonal close packing while they are in cubic close packing in the S sub-blocks. Two types of oxygen layers are present: one with a barium substitution (the {BaO<sub>3</sub>} layers), and one without (the {O<sub>4</sub>} layers).

The availability of modern characterisation methods opens the possibility of accessing new complex stacking sequences, and associated properties, that lie beyond those that could be studied and understood with previously available tools. Our recent work at I19 focussed on mixed-layer hexaferrites constructed from different ratios and permutations of M- and Y- blocks, and we have now reported full structural refinement of nine mixed-layer materials belonging to the M<sub>2</sub>Y<sub>3</sub>, M<sub>2</sub>Y<sub>4</sub>/M<sub>4</sub>Y<sub>8</sub>, M<sub>2</sub>Y<sub>5</sub>, M<sub>2</sub>Y<sub>7</sub>, M<sub>2</sub>Y<sub>8</sub>, M<sub>2</sub>Y<sub>9</sub> series (Table 1) from single-crystals in the Ba-Fe-Zn-O system. To aid in our characterisation, we determined their structures crystallographically, combining transmission electron microscopy techniques (electron diffraction and high-resolution imaging) with single-crystal X-ray diffraction data collected on I19 in order to refine complete structural models. The single-crystal X-ray refinement of the several previously reported hexaferrite systems allowed us to propose a model for the observed cation ordering within the entire MY hexaferrite series based

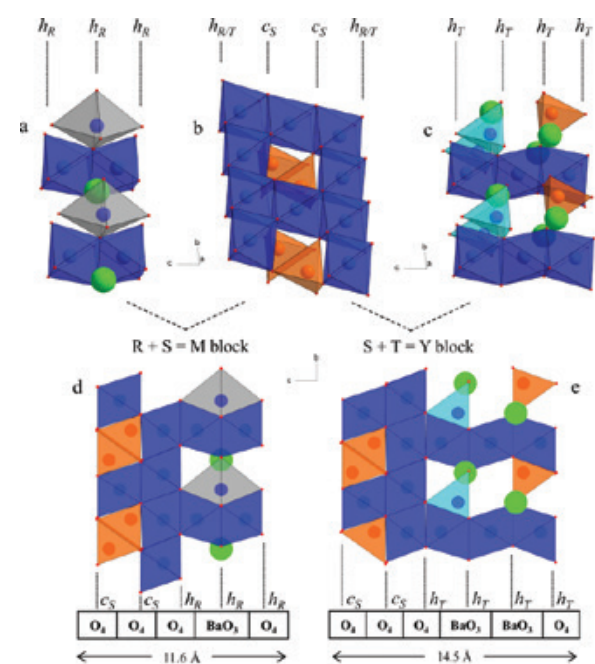


**Figure 1.** A 3-D view of the R (a), S (b), and T (c) sub-blocks along with the projections of the M (d) and Y (e) blocks. Colour coding: dark blue: Fe<sup>3+</sup> octahedra, grey: Fe<sup>3+</sup> bipyramids, light blue: Fe<sup>3+</sup> tetrahedral, orange: Fe<sup>2+</sup>/Zn<sup>2+</sup> tetrahedra. The h and c notation refer to hexagonal and a cubic packing of the oxygen layers whereas each subscript letter corresponds to the sub-block types. The anion-layer stacking and c dimension of the M and Y unit blocks are also highlighted. This figure has been reprinted with permission from the original publication: *IUCr* (2018), **5**, 681–698.

on electrostatic potential calculations enabled by the precisely determined structures. The ability to handle large cells on I19 allowed us to realise a new stacking sequence within the M<sub>4</sub>Y<sub>8</sub> series, with a complex structure that corresponds to the largest repeat known for an oxide material within the Inorganic Crystal Structure Database (ICSD).

**Table 1:** Synthesis and single-crystal growth of target hexaferrites in this study. The level of complexity of the mixed layered compounds required the use of (N)<sub>x</sub> nomenclature where N refers to the number of anion layers of the stacking sequence, and x to the x-fold repeat of this stacking sequence within a complete unit cell.

Series	c axis (Å)	Space Group	Stacking Sequence	Number of anion layers	Refined compositions
M <sub>2</sub> Y <sub>3</sub>	200.135(3)	R $\bar{3}m$	(MYMY <sub>2</sub> ) <sub>3</sub>	(28) <sub>3</sub> =84	Ba <sub>8</sub> Fe <sub>60</sub> Zn <sub>6</sub> O <sub>104</sub>
M <sub>2</sub> Y <sub>4</sub> / M <sub>4</sub> Y <sub>8</sub>	81.2388(8)	P6 <sub>3</sub> /mmc	(MY) <sub>2</sub>	(17) <sub>2</sub>	Ba <sub>10</sub> Fe <sub>72</sub> Zn <sub>8</sub> O <sub>126</sub>
	243.5953(9)	R $\bar{3}m$	(MYMY <sub>3</sub> ) <sub>3</sub>	(34) <sub>3</sub> =102	
M <sub>2</sub> Y <sub>5</sub>	487.184(2)	R $\bar{3}m$	(MYMY <sub>2</sub> MYMY <sub>4</sub> ) <sub>3</sub>	(68) <sub>3</sub> =204	Ba <sub>8</sub> Fe <sub>42</sub> Zn <sub>5</sub> O <sub>74</sub>
	95.725(1)	P $\bar{3}m1$	(MYMY <sub>4</sub> ) <sub>1</sub>	(40) <sub>1</sub>	
M <sub>2</sub> Y <sub>7</sub>	287.187(7)	R $\bar{3}m$	(MY <sub>2</sub> MY <sub>3</sub> ) <sub>3</sub>	(40) <sub>3</sub> =120	Ba <sub>8</sub> Fe <sub>34</sub> Zn <sub>9</sub> O <sub>96</sub>
	374.176(1)	R $\bar{3}m$	(MYMY <sub>6</sub> ) <sub>3</sub>	(52) <sub>3</sub> =156	
M <sub>2</sub> Y <sub>8</sub>	417.644(1)	R $\bar{3}m$	(MY <sub>3</sub> MY <sub>3</sub> ) <sub>3</sub>	(58) <sub>3</sub> =174	Ba <sub>9</sub> Fe <sub>60</sub> Zn <sub>8</sub> O <sub>107</sub>
M <sub>2</sub> Y <sub>9</sub>	461.224(1)	R $\bar{3}m$	(MY <sub>4</sub> MY <sub>5</sub> ) <sub>3</sub>	(64) <sub>3</sub> =192	Ba <sub>10</sub> Fe <sub>66</sub> Zn <sub>9</sub> O <sub>118</sub>

The structural refinement of the large unit cells observed in this study was indeed challenging due in part to the long hexagonal repeats, where reflection overlap was prevalent when using the in-house diffractometers (Fig. 2a). Thus, to solve these structures, synchrotron instrumentation was required, enabling the use of a 300 mm detector distance, and the acquisition of well-separated reflections (Fig. 2b). I19 data collections were essential, and allowed the determination of these mixed-layer structures. The mixed-layer structural models were then solved and refined with synchrotron X-ray diffraction data.

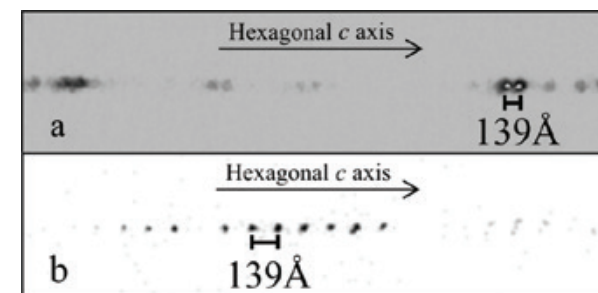


**Figure 2.** A set of observed single-crystal X-ray reflections for the (58)<sub>3</sub> hexaferrite collected using an in-house diffractometer with a detector distance of 137 mm (a) and the same crystal measured at I19 with the 300 mm detector distance (b). Both frames illustrate the 139 Å primitive repeat of the (58)<sub>3</sub> hexaferrite. This figure has been reprinted with permission from the original publication: *IUCr* (2018), **5**, 681–698.

Highlighted in this report is a new mixed-layer hexaferrite stacking sequence within the M<sub>4</sub>Y<sub>8</sub> series, the (68)<sub>3</sub> hexaferrite. The structure solution of the (68)<sub>3</sub> compound yielded a rhombohedral symmetry (space group Rm) with lattice constants: a = 5.8721(1) Å, c = 487.184(2) Å and a (MYMY<sub>2</sub>MYMY<sub>4</sub>)<sub>3</sub> sequence, as seen in Fig. 3.

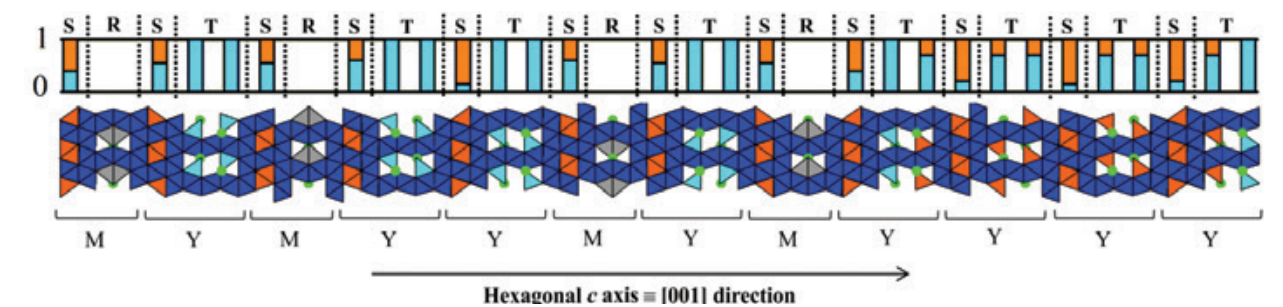


**Figure 3.** Partial projection of the (68)<sub>3</sub> hexaferrite structural model corresponding to a single MYMY<sub>2</sub>MYMY<sub>4</sub> sequence. There is a three-fold repeat of the sequence shown in order to generate the full unit cell, where subsequent repeats are translated in plane by (2/3, 1/3). In this representation, tetrahedral (light blue), octahedral (dark blue), and bipyramidal (grey) iron environments are shown; tetrahedral mixed iron/zinc sites are illustrated in orange and barium atoms in green. The histogram indicates proportions of iron (light blue) and zinc (orange) occupancy in the tetrahedral sites. This figure has been reprinted with permission from the original publication: *IUCr* (2018), **5**, 681–698.

### References:

- Obradors X. *et al.* Magnetic transitions in Pr<sub>2</sub>NiO<sub>4</sub> single crystal. *J. Appl. Phys.* **70**, 6329–6331 (2002). DOI: 10.1063/1.349958
- Liu X. *et al.* Research on La<sup>3+</sup>-Co<sup>2+</sup>-substituted strontium ferrite magnets for high intrinsic coercive force. *J. Magn. Magn. Mater.* **305**, 524–528 (2006). DOI: 10.1016/j.jmmm.2006.02.096
- Stergiou C. A. *et al.* Y-type hexagonal ferrites for microwave absorber and antenna applications. *J. Magn. Magn. Mater.* **405**, 54–61 (2016). DOI: 10.1016/j.jmmm.2015.12.027
- Özgür Ü. *et al.* Microwave ferrites, part 1: fundamental properties. *J. Mater. Sci. Mater. Electron.* **20**, 789–834 (2009). DOI: 10.1007/s10854-009-9923-2
- Pullar R. C. Hexagonal ferrites: A review of the synthesis, properties and applications of hexaferrite ceramics. *Prog. Mater. Sci.* **57**, 1191–1334 (2012). DOI: 10.1016/j.pmatsci.2012.04.001

### Funding acknowledgement:

Engineering and Physical Sciences Research Council (grant No. EP/N004884/1).

### Corresponding author:

Craig Miles Robertson, University of Liverpool,  
Craig.Robertson@liverpool.ac.uk

## Spectroscopy Group

Sofia Díaz-Moreno, Science Group Leader

**T**he Spectroscopy Group consists of four beamlines: the Microfocus Spectroscopy beamline (I18) the Core Extended X-ray Absorption Fine Structure (EXAFS) beamline (B18), and the two independently operating branches of the Versatile X-ray Absorption Spectroscopy (XAS) beamline, I20-Scanning and I20-EDE (Energy Dispersive EXAFS). These spectrometers are highly complementary, most notably in the energy ranges they cover, the size of their focussed beam spots, and the time resolutions they are able to reach. The complementarity of these facilities means that they can support research across many different scientific disciplines, from chemistry and catalysis through to materials science, condensed matter physics, environmental and life science, and cultural heritage. Over the last year more than 160 experiments were performed using the Spectroscopy Group beamlines.

Aside from supporting a very vibrant user programme, many technical developments have also been implemented on the beamlines over the last 12 months. Several developments have improved the detection characteristics of the beamlines, through the integration of new detectors and the development of new data acquisition electronics. Additionally, the year has seen a range of new sample environment equipment added to the beamline inventories, such as a new plug flow reactor for B18, and a helium cryostat to be used on I20.

### I18 update

The Microfocus Spectroscopy beamline (I18) uses a  $2 \times 2 \mu\text{m}^2$  beam to examine heterogeneous material on the micrometre scale using a variety of techniques such as X-ray Fluorescence (XRF), X-ray Absorption Near Edge Structure (XANES) spectroscopy and X-Ray Diffraction (XRD).

In the last year, I18 continued to benefit from the recent developments made on the new mapping perspective that is used to collect XRF maps and benefitted from the simultaneous use of the two Vortex-ME4 detectors. To address the existing bottleneck for diffraction studies, in terms of data collection rates, I18 is aiming to integrate a new 2D detector, Excalibur (Fig. 1). Excalibur is a Medipix-based detector that allows fast data collection, which will enable XRD mapping and tomography measurements to be collected up to two orders of magnitude faster than with the current setup. The detector will be installed and integrated within the control and data acquisition systems of I18 over the next six months, and will be ready for user operation by the end of the year.

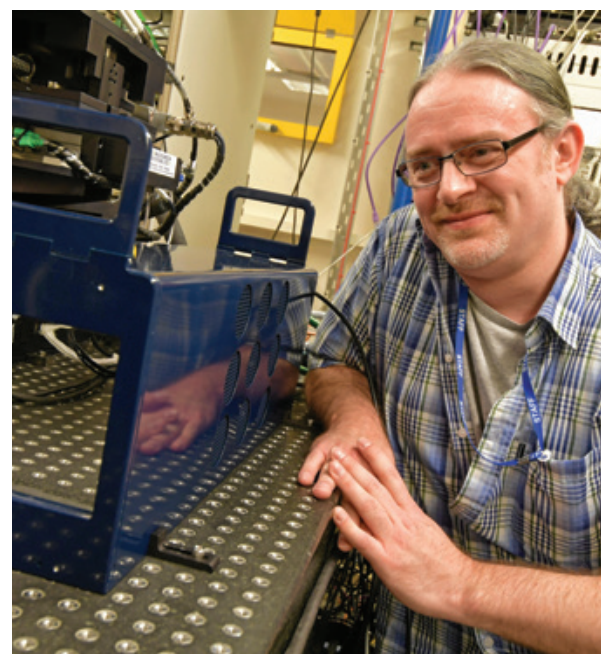


Figure 1: Senior Detector Scientist, Scott Williams, with the Excalibur detector on I18.

In addition, a novel X-ray beam position monitor has been developed, which will be installed on the beamline in the coming months. The device will enable the monitoring of the beam motions at a position close to the sample. This information will make it possible to identify and improve the optical components responsible for the beam movement e.g. monochromator vibration, mirror drift, and enable a reduction in the beam size at the sample position to below  $1 \mu\text{m}$ .

### B18 update

The Core EXAFS beamline, B18, is characterised by a wide energy range, a focused beam and a continuous scanning monochromator. These characteristics allow for efficient collection of XAS data on all elements heavier than phosphorus. The availability of a flexible experimental space, combined with a large range of sample environment equipment, make this beamline ideal to perform experiments *in situ* and under *operando* conditions.

The implementation of a simple fluorescence mapping tool has enabled new experiments to be performed at B18, particularly for the study of heterogeneous systems. Although initially developed for the study of fossils, the mapping tool has been particularly useful for the study of precious artefacts such as cannonballs recovered from the wreck of the Mary Rose. The studies performed at B18 have helped to unravel the corrosion mechanisms in the cannonballs and their interaction with the preservative treatments used for their conservation.

Upgrades to the beamline have included the development of a new plug-flow reactor with improved temperature control, and a multiple-sample cryostat for liquid nitrogen temperatures compatible with the soft X-ray end station. This latter device will be introduced into the user programme in the next allocation period.

The fluorescence capabilities of B18 will be further increased by the integration of the newly developed Xspress-4 read-out electronics with the beamline's existing germanium detector (Fig. 2). Xspress-4 digital pulse processor is an in-house development of Diamond's Detector Group that significantly improves the efficiency of the data acquisition in terms of both maximum count rate and resolution. These improved characteristics will directly translate into faster acquisition times that will not only enhance the capability of the beamline for the study of processes under operation conditions, but will also enable the study of more dilute samples with a large background signal that would otherwise saturate the detector.

### I20 update

The Scanning branch of I20 (I20-Scanning) exploits the high flux provided by the wiggler source through two different end stations. The XAS end station uses a 64 element monolithic germanium detector with the Xspress-4 read-out system to examine the structure of very low concentration samples. The X-ray Emission Spectroscopy (XES) end station uses a spectrometer based on a 1 m Rowland circle geometry to perform high-energy resolution studies of the electronic structure of samples.

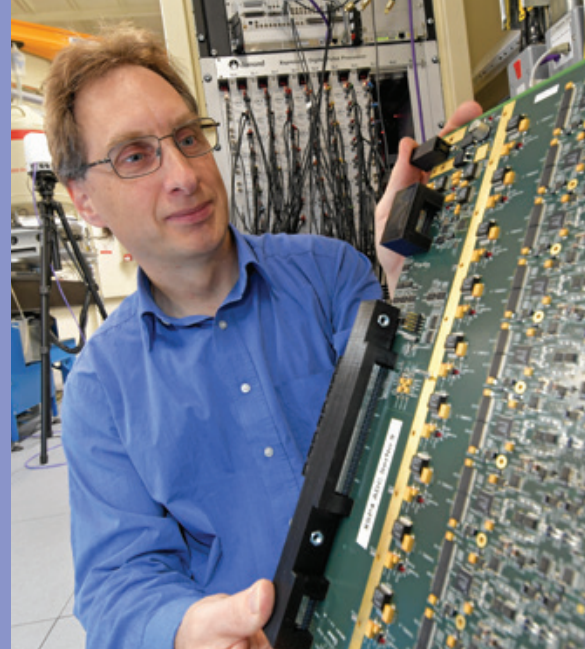


Figure 2: Senior Electronics Engineer, Graham Dennis, with the Xspress-4 digital pulse processor on I20.

The development project for a new monochromator for I20-Scanning has progressed significantly over the last year. The vibration and cooling performance of a new wider first crystal has been tested extensively using a spare axis, mimicking the conditions of the beamline. This new crystal was installed in the beamline monochromator in March 2019, substantially improving the cooling characteristics of the device. It is anticipated that the performance of the new system will inform the design of an entirely new monochromator for I20-Scanning that will be better able to exploit the high photon flux delivered by the wiggler source, and extend the energy range of the beamline up to 34keV.

The XES end station has benefitted from the installation of a four-element Medipix pixel detector, replacing the single element Medipix. This larger detector enables the detection of the diffracted fluorescence signal from the crystal analyser in a more straightforward manner, and eases the challenge of aligning the spectrometer. The use of the large Medipix detector has approximately halved the time needed to set-up the spectrometer and thus improved the efficiency of the beamline. To fully exploit the capabilities of the XES end station, a new closed cycle helium cryostat capable of reaching temperatures as low as 5K has been purchased. We expect to be able to make this cryostat available to the user community this year.

The Energy Dispersive EXAFS (EDE) branch of I20 uses a polychromator to perform XAS experiments in a dispersive geometry. It is designed for *in situ* and *operando* studies with time resolutions ranging from seconds down to milliseconds or even microseconds.

The popularity of user experiments on the I20-EDE branch that use different sample environments has continued to grow over the year. Using a bespoke sample cell, an experiment combining X-ray absorption and infrared spectroscopies, was performed to study a catalyst under *operando* conditions with a time resolution of 100 ms, while the beamline's stopped-flow system was used to study oxide precipitation with a time resolution as low as 20 ms. In addition, the high pressure programme on the line has developed, with a number of users studying systems under high pressure in diamond anvil cells using both traditional EDE and turbo-XAS, which is a complementary sequential data acquisition mode. Materials at pressures up to 20 GPa have been examined.

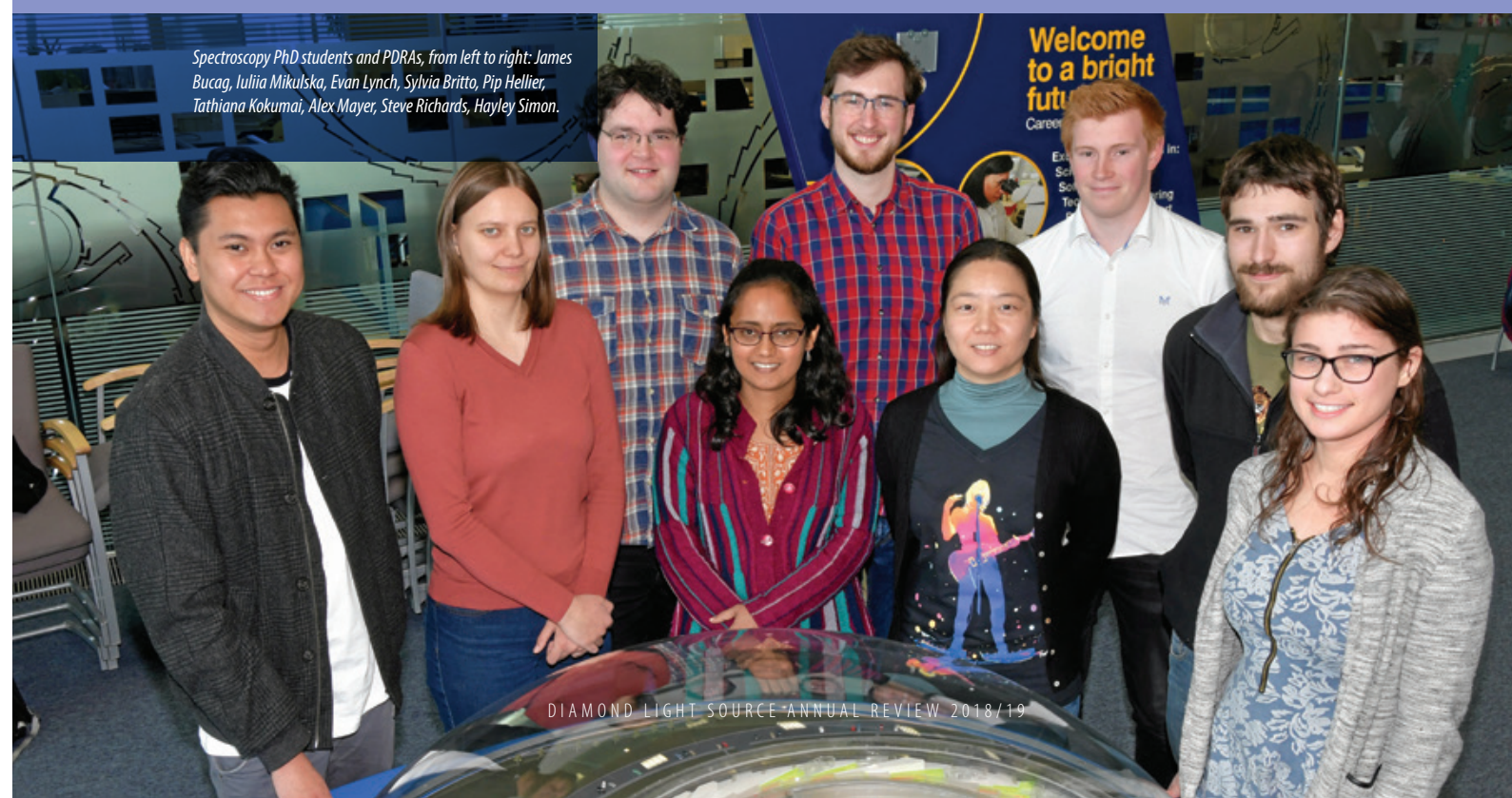
### Community support and development

As part of our on-going role to support the development of the spectroscopy user community, the group organises and runs an annual three day XAS workshop that typically takes place in March. This workshop covers a brief introduction to the spectroscopy beamlines at Diamond, as well as methods to process and analyse spectroscopy data. The event is always in very high demand. In 2018, 82 applications were received whilst in 2019, the number of applications increased to 153. Venue limitations and required staff to student ratios limit the successful applications to no more than 25 to 30 participants.

Last February, the group also held a one-day meeting for Diamond's spectroscopy PhD students. This meeting provided a welcome opportunity for the students to talk about their research projects with the other students and scientists in the group.

This year the Spectroscopy Group has also organised and hosted a workshop in September to canvas ideas to support the developing case for Diamond-II. The workshop was well attended by spectroscopy users from the main scientific disciplines covered by the beamlines: chemistry and catalysis, energy materials, bioscience and Earth and environment. The workshop highlighted several new research areas that will be made possible by the realisation of Diamond-II, and these new ideas were used as the foundation for the spectroscopy section of the scientific case for Diamond-II.

Spectroscopy PhD students and PDRAs, from left to right: James Bucag, Iulia Mikulska, Evan Lynch, Sylvia Britto, Pip Hellier, Tathiana Kokumai, Alex Mayer, Steve Richards, Hayley Simon.



## Atomic insights into new fast-charging lithium-ion battery materials

**Related publication:** Griffith K. J., Wiaderek K. M., Cibir G., Marbella L. E. & Grey C. P. Niobium tungsten oxides for high-rate lithium-ion energy storage. *Nature* **559**, 556–563 (2018). DOI: 10.1038/s41586-018-0347-0

**Publication keywords:** Lithium-ion battery; X-ray absorption spectroscopy; Niobium; Tungsten; Metal oxide; Energy storage

The increasing energy storage needs of electric vehicles and mobile devices is driving research into higher performance batteries. One particular challenge for some applications is safely charging/discharging fast enough, and most materials that offer both high power and fast charging require nanoparticles that are expensive to make and difficult to produce in large quantities.

In order to understand the battery performance of new large-scale battery materials containing niobium and tungsten, a team from the University of Cambridge studied the changes in each metal individually. They used the Core X-ray Absorption Spectroscopy (XAS) beamline (B18) to investigate the chemical changes that occur in their new niobium tungsten oxide batteries to understand how these elements are able to store an unexpectedly large quantity of energy. B18 is designed for XAS measurements, which can distinguish each type of ion and the changes that occur to its chemical state during reaction in a battery.

Their results showed that both niobium and tungsten ions are able to store 'extra' charge in the battery, beyond what is usually expected, and that they work together. This is different from many battery materials containing multiple types of ion, where they are usually not active at the same time and some are not active at all. The new battery material is designed to be used as the negative electrode (anode), and to work with any of the many positive electrodes (cathodes) that are used in commercial lithium-ion batteries.

Advanced batteries are required as the world moves toward electric vehicles, intermittent renewable energy sources, and increasingly power-intensive portable electronics and 'smart' devices. Modern lithium-ion batteries contain a positive electrode made of a metal oxide and a negative electrode made of graphite. For safety reasons, the use of graphite limits how fast these can recharge or how much power they can deliver. A new negative electrode, in combination with a standard positive electrode, could enable a high-performance lithium-ion battery that can recharge in just a few minutes, depending on the size of the device, which would facilitate new technologies and accelerate the transition away from fossil fuels.

In order for a battery to charge in minutes, the electrode materials inside must allow lithium-ions to move quickly. In practice, the arrangement of atoms in most materials – known as the crystal structure – does not allow sufficient lithium-ion mobility and so the particle size of these materials is reduced down to the nanoscale to shorten the distance that lithium has to travel. However, there is a practical problem with this strategy. Around 100,000,000 kilograms

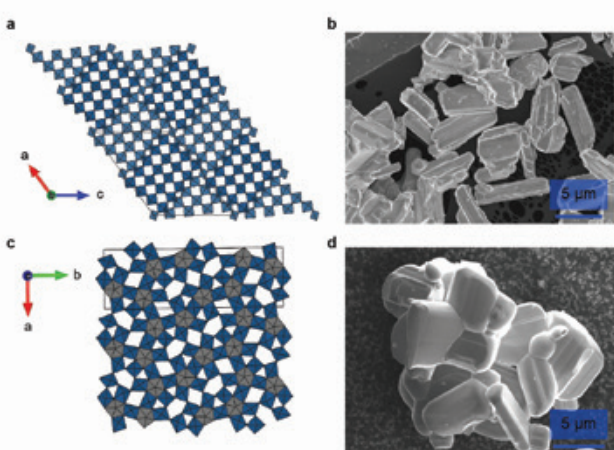


**Figure 1:** Crystal structure and electron microscope image of two niobium tungsten oxides; (a) structure of  $\text{Nb}_{16}\text{W}_5\text{O}_{55}$ ; (b) image of  $\text{Nb}_{16}\text{W}_5\text{O}_{55}$ ; (c) structure of  $\text{Nb}_{18}\text{W}_{16}\text{O}_{93}$ ; (d) image of  $\text{Nb}_{18}\text{W}_{16}\text{O}_{93}$ . The polyhedra in (a) and (c) represent a metal atom at the centre and oxygen atoms at the corners.  $\text{Nb}_{16}\text{W}_5\text{O}_{55}$  has tunnels along the *b*-axis and  $\text{Nb}_{18}\text{W}_{16}\text{O}_{93}$  has tunnels along the *c*-axis; the crystallographic indices are given.

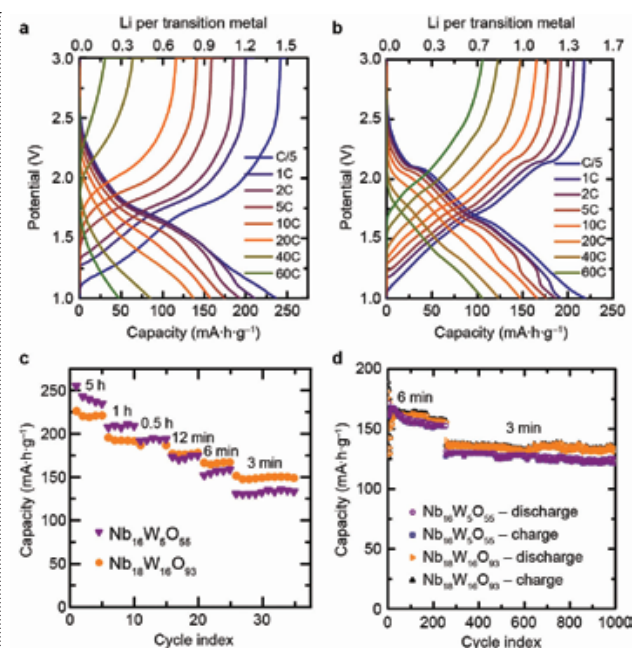


**Figure 2:** Electrochemistry curves and battery performance of two niobium tungsten oxides; (a) discharge and charge curves of  $\text{Nb}_{16}\text{W}_5\text{O}_{55}$ ; (b) discharge and charge curves of  $\text{Nb}_{18}\text{W}_{16}\text{O}_{93}$ ; (c) charge storage capacity for a given discharge/charge time; (d) charge storage capacity for 1000 cycles at 6 min and 3 min rates. In 3 min, the niobium tungsten oxides can reach 60–70% of the charge that is accessible in 5 h and they can retain >90% of their capacity for 1000 cycles.

of graphite are used in batteries annually and this number is expected to triple by 2025; but nanomaterials can be expensive to produce and difficult to scale-up. Conversely, this work involves the discovery of niobium tungsten oxides as a family of materials that exhibit high-rate battery performance with large-scale particles from scalable synthesis methods.

The arrangements of atoms in niobium tungsten oxide compounds are extremely complicated and were the subject of an extraordinary effort by crystallographers, in the 1960s (Fig. 1)<sup>1,2</sup>. This was purely fundamental science at the time. However, thanks to their complex structures, the compounds

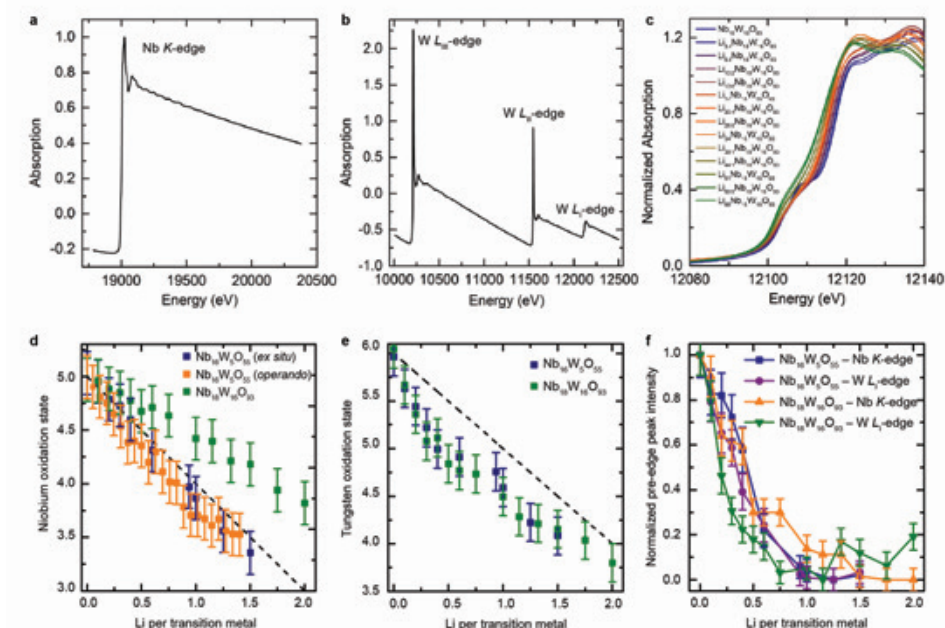


**Figure 3:** X-ray absorption spectroscopy; (a) X-ray absorption by niobium atoms and (b) tungsten atoms in  $\text{Nb}_{16}\text{W}_5\text{O}_{55}$ ; (c) tungsten  $L_{2,3}$  absorption edge of  $\text{Li}_x\text{Nb}_{16}\text{W}_{16}\text{O}_{93}$  at different lithium contents; (d) evolution of the niobium and (e) tungsten oxidation state with lithium insertion; (f) quantification of changes in the characteristic pre-edge feature. Increased lithium storage is associated with a decrease in the pre-edge feature (e.g. (c) at 12,108 eV) and a negative shift in the position of the absorption edge (e.g. (c) at 12,114 eV). From these changes, information on the chemical oxidation state and the symmetry of niobium and tungsten can be extracted. Panel (c) shows an example spectral dataset for the tungsten  $L_{2,3}$ -edge of  $\text{Nb}_{16}\text{W}_5\text{O}_{55}$ ; analogous datasets were collected for all tungsten  $L$ -edges and the niobium  $K$ -edge of both  $\text{Nb}_{16}\text{W}_5\text{O}_{55}$  and  $\text{Nb}_{18}\text{W}_{16}\text{O}_{93}$  and these data were used to obtain the results in panels (d–f).

$\text{Nb}_{16}\text{W}_5\text{O}_{55}$  and  $\text{Nb}_{18}\text{W}_{16}\text{O}_{93}$  are capable of storing a large quantity of lithium with rapid insertion and extraction in large particles that are simple to produce and easily scalable. Electrochemical testing was performed on electrodes comprising the niobium tungsten oxides at different applied currents and for up to 1000 discharge/charge cycles (Fig. 2). The electrodes demonstrated that it is possible to store more than one lithium ion for each metal cation (i.e.  $\text{Nb}^{5+}$ ,  $\text{W}^{6+}$ ), which means that the batteries are able to store more charge. This rather unusual phenomenon is known as multielectron redox and raised interesting questions about the role of the metals.

To understand the chemistry that enables high charge storage capacity, it was necessary to separate the functional role of niobium vs. tungsten. For this role, X-ray Absorption Spectroscopy (XAS) was performed at beamline B18 at Diamond Light Source. XAS is an advanced characterisation technique that can easily distinguish between different elements and follow the chemical and atomic structural evolution that occurs during a reaction such as that of a niobium tungsten oxide with lithium. High-resolution data were acquired on B18 at the niobium  $K$ -edge and tungsten  $L_{2,3}$ ,  $L_{2,3}$  and  $L_{2,3}$ -edges for the niobium tungsten oxide host compounds and after electrochemical lithium insertion up to as much as two lithium ions per metal centre (Fig. 3). In addition, a series of spectra were recorded for niobium and tungsten model compounds in different oxidation states that were used as reference spectra for comparison to the electrode materials. The samples were measured in transmission mode, illuminating the entire large particles and ensuring that the results were representative of the whole sample rather than just the surface. Like most partially-discharged battery materials, the samples are sensitive to air and thus a special transfer apparatus was built by beamline scientists with 3D printed components and used to move the samples from an inert argon glovebox to the beamline and to encapsulate an inert helium atmosphere during data collection.

Tracking the absorption of X-rays at different states of charge led to the discovery that niobium and tungsten ions store charge simultaneously and both elements undergo multielectron redox and thus contribute to the high storage capacity of the new materials. Chemical insights from XAS were combined with lithium diffusion measurements from pulsed field gradient nuclear magnetic resonance spectroscopy and operando crystal structure analysis from X-ray

diffraction during high-rate battery cycling. In conclusion, this multifaceted investigation provided a wholistic picture for advanced battery performance whereby these metal ions store excess charge, lithium is able to travel through the material with nearly liquid-like mobility, and the atomic structure undergoes minimal volume changes, thus minimal strain as it incorporates lithium. This research provides new electrode candidates for advanced battery technologies and proves that it is possible to achieve fast charging and high power operation with easily-produced large particles. The insights into the mechanism of operation also outline a strategy for future material discovery and design by identifying the key features of high-rate compounds.

## References:

- Roth R. S. et al. Multiple phase formation in the binary system  $\text{Nb}_2\text{O}_5\text{--WO}_3$ . II. The structure of the monoclinic phases  $\text{WNb}_{12}\text{O}_{33}$  and  $\text{W}_5\text{Nb}_{16}\text{O}_{55}$ . *Acta Crystallogr.* **19**, 32–38 (1965). DOI: 10.1107/S0365110x65002724
- Stephenson N. C. A structural investigation of some stable phases in the region  $\text{Nb}_2\text{O}_5\text{--WO}_3\text{--WO}_3$ . *Acta Crystallogr. Sect. B Struct. Crystallogr. Cryst. Chem.* **24**, 637–653 (1968). DOI: 10.1107/S0567740868002979

## Funding acknowledgement:

The Winston Churchill Foundation of the United States, a Herchel Smith Scholarship (University of Cambridge), and the Science and Technology Facilities Council (STFC) Futures Early Career Award. EPSRC grant EP/M009521/1. European Union's Horizon 2020 research and innovation programme under the Marie Skłodowska–Curie grant agreement number 750294 and a Charles and Katharine Darwin Research Fellowship. This research also used resources of the Advanced Photon Source (GUP40466, GUP41657, GUP47967), a US Department of Energy (DOE) Office of Science User Facility operated for the DOE Office of Science by Argonne National Laboratory under contract number DE-AC02-06CH11357.

## Corresponding author:

Dr. Kent J. Griffith, Northwestern University, kent.griffith@northwestern.edu

## Tumour penetration by novel precious-metal anticancer drug candidate

**Related publication:** Sanchez-Cano C., Romero-Canelón I., Geraki K. & Sadler P. J. Microfocus x-ray fluorescence mapping of tumour penetration by an organo-osmium anticancer complex. *J. Inorg. Biochem.* **185**, 26–29 (2018). DOI: 10.1016/j.jinorgbio.2018.04.014

**Publication keywords:** Organometallic metallodrugs; 3D spheroids; Tumour penetration; Elemental mapping; X-ray fluorescence

Some of the most effective cancer treatments involve platinum-based drugs, but resistance to platinum compounds is increasing and there is an urgent need to find alternatives. A team from the University of Warwick has discovered a new osmium-based (Os-based) anti-cancer agent, FY26, which exhibits high potency against a range of cancer cell lines and is capable of overcoming platinum resistance. Before it can be tested in clinical trials, the team needs to understand fully how it works.

Tumours are complex systems that show a low level of irrigation by blood vessels. Poor penetration can limit the ability of a drug to reach the interior of a tumour, which is of vital importance for the success of most anti-cancer agents. The researchers wanted to know how FY26 would behave in tumours, and in particular if the drug would be able to penetrate easily into their core. To investigate, they used the Microfocus Spectroscopy beamline (I18) which can resolve individual cells within a model tumour (a collection of closely packed cancer cells known as a spheroid) and has high sensitivity to detect the drug at low concentrations.

The resulting X-ray fluorescence maps allowed the team to conclude that FY26 is capable of efficiently reaching the inner core of a model tumour, with drug penetration directly related to exposure time. They found that the drug also altered the distribution of zinc and calcium, which can play a role in cancer cell death, providing new insights into the mechanism of FY26-induced cell death.

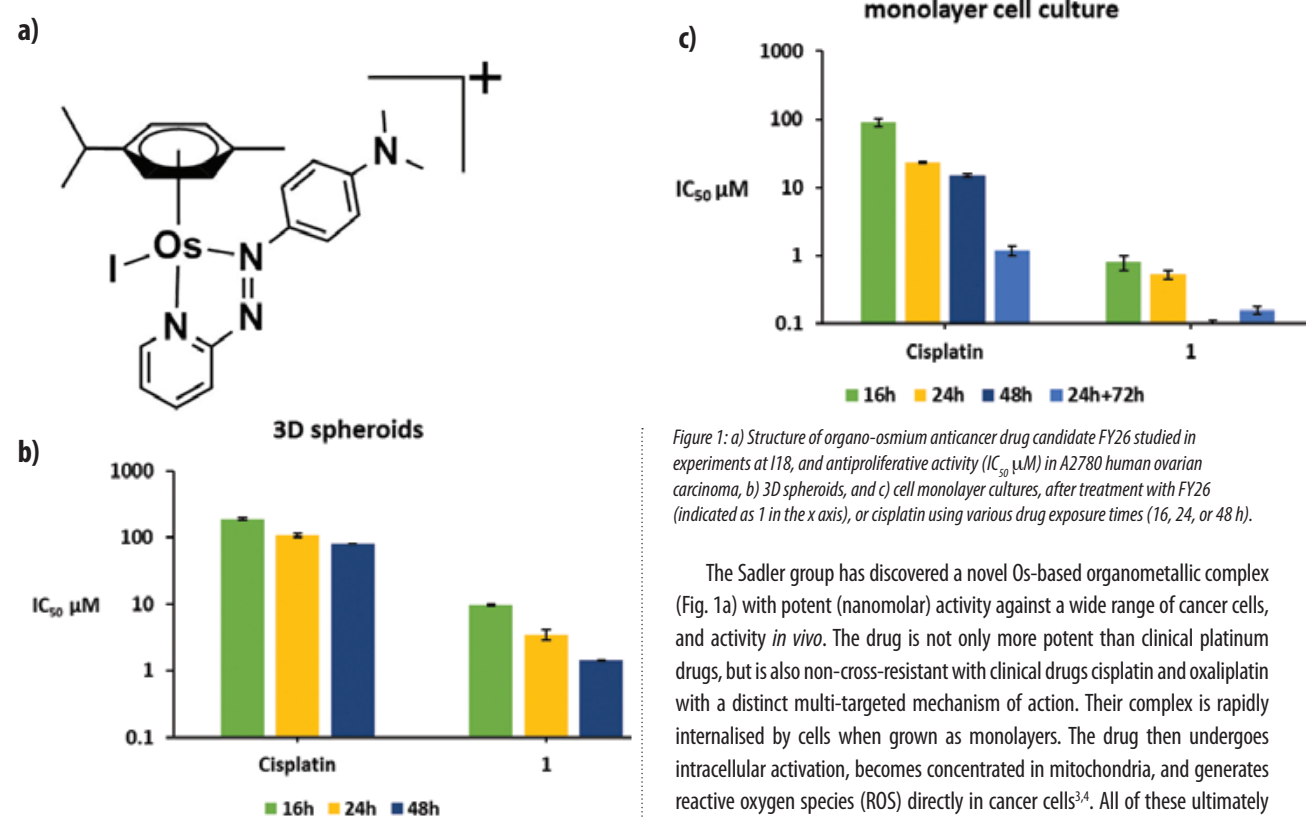


**Figure 1:** a) Structure of organo-osmium anticancer drug candidate FY26 studied in experiments at I18, and antiproliferative activity ( $IC_{50}$   $\mu M$ ) in A2780 human ovarian carcinoma, b) 3D spheroids, and c) cell monolayer cultures, after treatment with FY26 (indicated as 1 in the x axis), or cisplatin using various drug exposure times (16, 24, or 48 h).

The Sadler group has discovered a novel Os-based organometallic complex (Fig. 1a) with potent (nanomolar) activity against a wide range of cancer cells, and activity *in vivo*. The drug is not only more potent than clinical platinum drugs, but is also non-cross-resistant with clinical drugs cisplatin and oxaliplatin with a distinct multi-targeted mechanism of action. Their complex is rapidly internalised by cells when grown as monolayers. The drug then undergoes intracellular activation, becomes concentrated in mitochondria, and generates reactive oxygen species (ROS) directly in cancer cells<sup>3,4</sup>. All of these ultimately lead to the initiation of a unique cell death process, which is different from apoptosis, but unknown until now.

However, many types of cancers involve the formation of solid tumours. Thus anticancer drugs need to be capable of penetrating into their core to achieve an effective antineoplastic effect<sup>5</sup>. This can be difficult to achieve due to low vascularisation of tumours, amongst other factors. Therefore, it is vital to investigate drug candidates in tumour models other than 2D monolayer cell cultures, to obtain reliable information on their overall anticancer properties. 3D spheroids are easily-constructed solid tumour models which can be cultured with good control over their size. As such, they are extremely useful for initial *in*

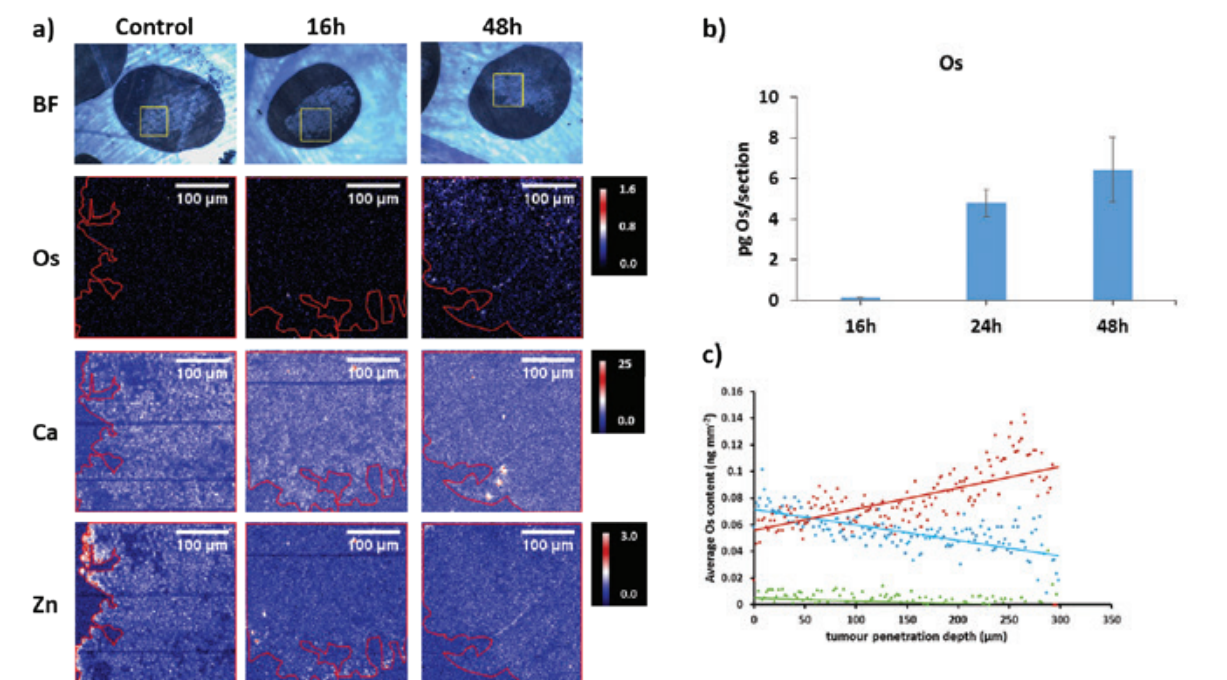


**Figure 2:** a) Bright field images and XRF elemental maps of Os, Ca and Zn in human ovarian carcinoma spheroid sections treated with organo-osmium anticancer drug FY26 for 0, 16 or 48 h ( $2 \times 2 \mu m^2$  step size, 1 s dwell time; Scale bar  $100 \mu m$ ; Calibration bar  $ng mm^{-2}$ ). Yellow squares indicate areas of the spheroid studied using XRF. Red areas indicate limits of the spheroids. b) Total Os content (pg/section), and c) Average Os content ( $ng mm^{-2}$ ) as a function of distance from spheroid surface, after treatment for 16 h (green), 24 h (blue) or 48 h (red) with the drug.

*in vitro* studies of tumour growth inhibition and drug penetration.

Interestingly, this Os-based drug candidate is also highly effective (more so than cisplatin) in inhibiting the growth of 3D spheroids created from human ovarian carcinoma cells. Moreover, increases in the drug exposure time lead to comparable increases in antiproliferative activity, both in 2D and 3D cultured cells (Fig. 1b). This suggests that FY26 is capable of penetrating into spheroids in an efficient time-dependent way.

X-ray fluorescence (XRF) at the I18 microprobe beamline at Diamond Light Source has been used to probe the penetration properties of our drug and its effect on the distribution of natural metal ions. 3D spheroids tumour models were treated with a therapeutically relevant (and therefore low) concentration of the complex for different times (0, 16, 24 and 48 h), fixed, embedded in resin and sectioned in 500 nm thick sections. Then, elemental distribution were determined from XRF elemental maps, using a beam focused down to a  $2 \times 2 \mu m^2$  subcellular size (for highest resolution), and with the irradiation energy fixed at 12 keV (to achieve excitation of the Os  $L_{III}$ -edge).

These maps confirm the presence of Os in samples treated with the drug. FY26 complex is capable of penetrating into the tumour core, and remains there for longer than expected. Furthermore, the measurements show that both tissue penetration and accumulation of Os is directly related with the time of spheroid exposure to the drug (Fig. 2). In contrast, cell monolayers showed maximum uptake after 24 h incubation, followed by a rapid decrease in the amount of Os inside cells during the next 48 h. These differences in the accumulation kinetics of FY26 between cell monolayers and 3D tumour models may result from more effective efflux from cell monolayers, or slow diffusion of the drug into tissue-like samples.

Treatment of spheroids with the Os drug also leads to extensive changes in Zinc (Zn) and Calcium (Ca) distribution, from being discretely localised in untreated samples to being more widely distributed in treated spheroids (Fig. 2a). This change in distribution is time-dependent. After 16h exposure to the drug, some Zn and Ca are still discretely localised in certain areas of the spheroids, whereas after 24 or 48 h incubation, they are more evenly distributed. The changes observed in the Zn and Ca maps of spheroids are in good agreement with those observed for monolayer cultured cells treated with the drug<sup>2</sup>. Overall,

these alterations confirm the presence of nuclear damage with Ca release from the endoplasmic reticulum (ER), possibly indicating immunogenic cell death, which remains to be further elucidated.

Overall, these microfocus X-ray fluorescence experiments on beamline I18 provide new insights into the interaction of a promising organo-osmium anticancer drug candidate with solid tumours. XRF maps show that the Os drug penetrates efficiently into tumour spheroids, although more complicated models would be required to mimic the heterogeneous nature of solid tumours. Interestingly, such studies could also be made using the I18 microprobe, on real tumours extracted from animal models treated with this drug candidate. Nevertheless, the results highlight the potential of this organo-osmium complex as a candidate for further development as a clinical drug to treat platinum resistant tumours, a current clinical need.

### References:

- <https://www.who.int/news-room/fact-sheets/detail/cancer>
- Kelland L. The resurgence of platinum-based cancer chemotherapy. *Nat. Rev. Cancer* **7**, 573–584 (2007). DOI: 10.1038/nrc2167
- Needham R. J. *et al.* In-Cell Activation of Organo-Osmium(II) Anticancer Complexes. *Angew. Chemie - Int. Ed.* **56**, 1017–1020 (2017). DOI: 10.1002/anie.201610290
- Sanchez-Cano C. *et al.* Synchrotron X-Ray Fluorescence Nanoprobe Reveals Target Sites for Organo-Osmium Complex in Human Ovarian Cancer Cells. *Chem. - A Eur. J.* **23**, 2512–2516 (2017). DOI: 10.1002/chem.201605911
- Minchinton A. I. *et al.* Drug penetration in solid tumours. *Nat. Rev. Cancer* **6**, 583 (2006). DOI: 10.1038/nrc1893

### Funding acknowledgement:

The SXRF experiments were performed in the frame of Diamond Light Source proposal SP13478. The authors thank CRUK/EPSRC (Grant No. C53561/A19933), EPSRC (Grant No. EP/F034210/1) and Wellcome Trust (Grant No. 107691/Z/15/Z) for support.

### Corresponding authors:

Prof Peter J. Sadler, University of Warwick, p.j.sadler@warwick.ac.uk and Dr Carlos Sanchez-Cano, CIC biomaGUNE, csanchez@cicbiomagune.es

## Identifying active iron sites for NO<sub>x</sub> pollution control in porous matrices

**Related publication:** Beale A. M., Greenaway A. G., Kroner A. B., Lezcano-González I., Agote-Arán M., Hayama S. & Díaz-Moreno S. Operando HERFD-XANES/XES studies reveal differences in the activity of Fe-species in MFI and CHA structures for the standard selective catalytic reduction of NO with NH<sub>3</sub>. *Appl. Catal. A Gen.* **570**, 283–291 (2018). DOI: 10.1016/j.apcata.2018.11.026

**Publication keywords:** NH<sub>3</sub>-SCR; NO; Fe-containing zeolites; HERFD-XANES; XES

**D**iesel is the fuel of choice for heavy goods vehicles, but diesel combustion generates nitrogen oxides (NO<sub>x</sub>) that are known to be harmful to human health; NO<sub>x</sub> has been estimated to lead to 38,000 premature deaths globally each year. Selective catalytic reduction with ammonia (NH<sub>3</sub>) is a widely-applied technology for converting NO<sub>x</sub> emissions from diesel engines into harmless nitrogen gas and water.

Iron-based microporous materials are known to be active catalysts for NO<sub>x</sub> removal, but it is difficult to know which combination of iron species and porous structure give the best performance – once this is known, it is possible to develop a more efficient catalyst or process.

A team of researchers from University College London, the Research Complex at Harwell, and Diamond Light Source investigated iron-containing zeolites, an important class of microporous materials known to catalyse the NO<sub>x</sub> reduction when the NO<sub>x</sub> is combined with NH<sub>3</sub> and a small amount of heat is applied. The NO<sub>x</sub> reduction with NH<sub>3</sub> results in the formation of harmless nitrogen and oxygen gases.

They used the X-ray Spectroscopy beamline (I20-Scanning) to collect high-resolution X-ray Absorption Near Edge Structure (XANES) and X-ray Emission Spectroscopy (XES) spectra, which allowed them to extract detailed chemical information from the features of the X-ray absorbing element.

Their results suggested that isolated octahedral iron (Fe<sup>3+</sup>) species on H-ZSM-5 are highly active under the conditions studied. In contrast, isolated tetrahedral Fe<sup>3+</sup> sites present in Silicalite-1 exhibited lower redox properties, leading to a reduced NO conversion. Clusters and large Fe<sub>3</sub>O<sub>4</sub> particles on H-SSZ-13 exhibited low selective catalytic reduction activity.

Nitrogen oxides (NO<sub>x</sub>) are one of the major sources of air pollution produced from engines during fuel combustion processes. Today, selective catalytic reduction (SCR) of NO with ammonia (NH<sub>3</sub>-SCR) is a widely applied technology for converting NO<sub>x</sub> emissions from diesel engines into harmless N<sub>2</sub> and H<sub>2</sub>O<sup>1</sup>. Fe-containing microporous materials are among the most active catalysts for NH<sub>3</sub>-SCR. Much research has been devoted to investigating the relationship between structure and activity of these materials. This is, however, challenging, mostly due to the presence of many different types of Fe species (i.e. isolated species, oligomers, or large particles)<sup>2</sup>. Catalyst improvement for the control of NO<sub>x</sub> emissions relies on a better understanding of the effect of Fe speciation on the catalytic activity, as well as further insight into the NH<sub>3</sub>-SCR reaction mechanism. To this end, a set of Fe/zeolites (~0.5 wt. %) were prepared using different microporous materials as support. The supports studied were H-ZSM-5 (MFI structure, Si/Al = 15), H-SSZ-13 (CHA structure, Si/Al = 15), and Silicalite-1 (MFI structure, Si/Al = ∞). Ultraviolet-visible (UV-Vis) spectroscopy (Fig. 1a) revealed different Fe speciation for each microporous support: Fe/H-ZSM-5 comprised isolated Fe<sup>3+</sup> species with both octahedral (Oh) and tetrahedral (Td)

geometries, Fe/Silicalite-1 prepared with Fe citrate (Fe/S1-T-citr) contained highly dispersed Fe species, mainly in tetrahedral coordination, while Fe/Silicalite-1 prepared with ferric nitrate (Fe/S1-T-nitr) presented increased amounts of Fe<sub>3</sub>O<sub>4</sub> clusters and Fe<sub>2</sub>O<sub>3</sub> particles. Fe/H-SSZ-13 catalyst meanwhile contained mainly large Fe<sub>3</sub>O<sub>4</sub> particles. Comparison of the catalytic activity of these materials (Fig. 1b) revealed Fe/H-ZSM-5 to be the most active at these temperatures. The structure and behaviour of Fe species under real reaction conditions, particularly in Fe-ZSM-5, was then probed by High Energy Resolution Fluorescence Detected X-ray Absorption Near Edge Structure (HERFD-XANES), and X-ray Emission Spectroscopy (XES) recorded on beamline I20-Scanning<sup>3</sup>.

In order to obtain an in-depth understanding of the nature and behaviour of the different types of Fe species, HERFD-XANES and XES spectra were recorded under a number of gas compositions (chosen to mimic the conditions that the catalyst experiences in the field): 1) 20% O<sub>2</sub> in He flow at 500 °C after activation, 2) 0.1% NO in He at 200 °C, 3) 1% NH<sub>3</sub> in He at 200 °C and, 4) SCR conditions (5000 ppm NO, 5000 ppm NH<sub>3</sub> and 5% O<sub>2</sub> in He) at 300 °C; the last condition being nowadays more commonly described as under *operando*. Fig. 2a shows

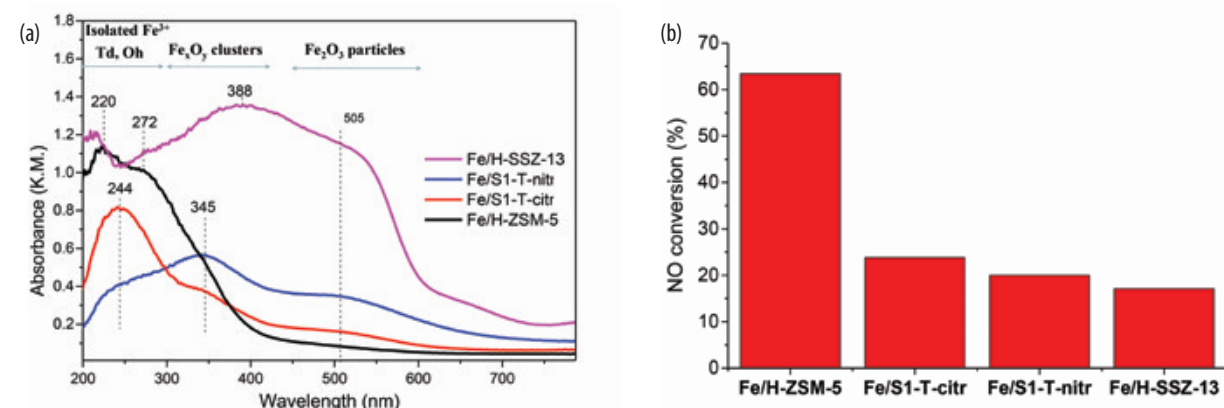


Figure 1: (a) UV-vis absorption spectra of Fe/zeolites (0.5 wt. %) synthesised using different zeolite topologies and Fe precursors, and (b) NO conversion of Fe/zeolites after 1 h of NH<sub>3</sub>-SCR under 5000 ppm NO, 5000 ppm NH<sub>3</sub> and 5% O<sub>2</sub> flow at 300 °C, GHSV = 35000 h<sup>-1</sup>.

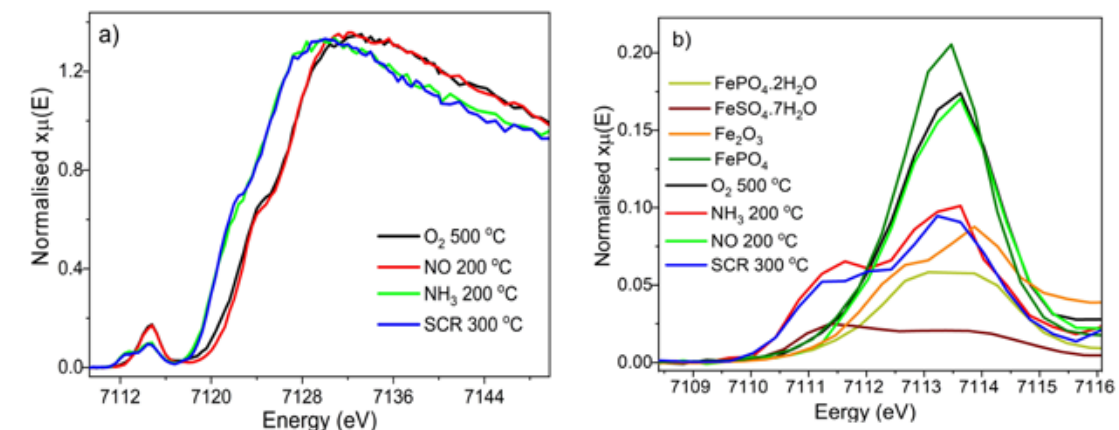


Figure 2: Fe K-edge HERFD-XANES spectra collected for Fe/H-ZSM-5 after activation in 20% O<sub>2</sub>/He (500 °C), under 0.1% NO/He and 1% NH<sub>3</sub>/He (200 °C), and under SCR conditions (5% O<sub>2</sub>, 5000 ppm NO, 5000 ppm NH<sub>3</sub> in He, 300 °C); (a) General features for the catalyst spectra, and (b) comparison of the pre-edge features for the Fe reference model compounds indicated in the figure and the catalyst.

the HERFD-XANES spectra collected for the most active and responsive catalyst (Fe/H-ZSM-5), while Fig. 2b compares the pre-edge features with those for reference compounds with known Fe speciation; this comparison allows to evaluate the local geometry and the chemical state of Fe species in the samples<sup>4</sup>.

The HERFD-XANES data reveal a dynamic chemical state of Fe in Fe/H-ZSM-5 that changes with gas atmosphere. The pre-edge features of the catalyst before reaction suggests the presence of mainly isolated Fe<sup>3+</sup> species with both Oh and Td species. Small changes in the XANES spectrum can be observed when flowing NO, which has previously been attributed to NO adsorption onto Fe<sup>3+</sup> centres, leading to a partial Fe reduction (i.e. oxidative addition of NO). In the presence of reductive gases, however, bigger changes are observed; the pre-edge is seen to shift to lower energies under NH<sub>3</sub> (centroid position goes from 7113.41 to 7112.95 eV), indicating reduction to Fe<sup>2+</sup> – probably due to ammonia

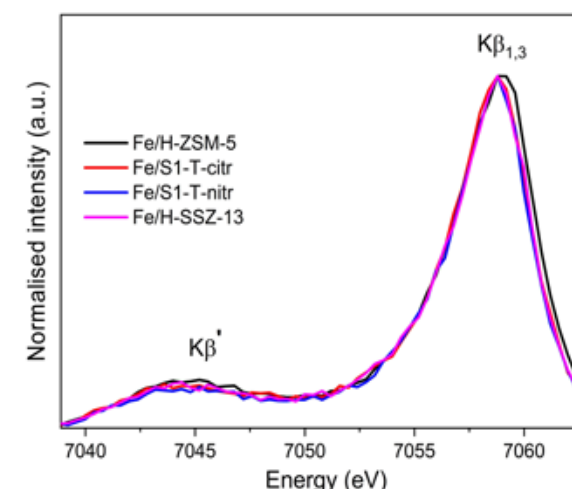


Figure 3: Kβ XES mainlines for Fe/zeolites acquired at room temperature after the activation (20% O<sub>2</sub>/He flow, 2 h at 500 °C).

coordination to the metal, and donation of the free electron pair of the nitrogen, resulting in the formation of Fe<sup>2+</sup>-NH<sub>2</sub> complexes. A similar shift is observed under NH<sub>3</sub>-SCR conditions, and is consistent with reoxidation of Fe<sup>2+</sup> to Fe<sup>3+</sup> being a slow step in the reaction process. Note that during reaction, a mass spectrometer was used to verify that the catalyst was actively reducing NO<sub>x</sub>.

In addition to the HERFD-XANES data discussed above, Kβ XES spectra were also acquired. Fig. 3 shows the Kβ' and Kβ<sub>1,3</sub> mainlines (3p → 1s transitions of the absorbing atom) for the Fe/zeolites (recorded at room temperature after calcination). All the spectra present a well-defined Kβ' feature, indicating they constitute high-spin complexes. For metal complexes with the same spin-state, the centroid of the Kβ<sub>1,3</sub> feature can be correlated with the covalent (vs. ionic) character of the metal-ligand bond; it has been reported that Kβ<sub>1,3</sub> emission

shifts to higher energies with increasing ionic character. In Fig. 3, it appears that all the spectra seem identical although the Kβ<sub>1,3</sub> peak in the Fe/H-ZSM-5 sample is slightly shifted to higher energies (i.e. Kβ<sub>1,3</sub> maxima at 7059.15 eV while for the rest of the references is at 7058.78 eV). Such a shift may be indicative of a different, more ionic, metal-ligand bond character with respect to the other samples. This could be a consequence of the fact that Fe is providing charge compensation of the framework AlO<sub>4</sub><sup>-</sup> charge. This is not the case of Fe/Silicalite-1 catalysts as these materials do not contain framework Al, while for Fe/H-SSZ-13 the majority of the species present are Fe<sub>2</sub>O<sub>3</sub> particles.

Fe/H-ZSM-5 gives higher NH<sub>3</sub>-SCR activity, this can be attributed to the isolated Oh Fe<sup>3+</sup> species with enhanced redox behaviour. The presence of framework Al appears to promote the formation of such species at ion exchange sites, probably providing charge compensation facilitating Fe redox activity. The absence of spectral changes in Fe/Silicalite-1 catalysts points that Td Fe<sup>3+</sup> species barely interact with the reactants, showing no reduction. The activity in these samples is attributed to the presence of Fe clusters/particles. These observations suggest that the reducibility of Fe, and its capacity to coordinate with reactant gases, is important for realising low-temperature activity, which is essential during cold-start/idling of vehicles. Copper (Cu) based catalysts are usually the choice for low temperature SCR; they show 100% NO conversion already at 200 °C, while Fe-based catalysts require at least 300 °C. Nonetheless, since Fe is cheaper than Cu, there is now an opportunity to understand or effect the reducibility of Fe to realising low(er) temperature activity of these catalysts for NO<sub>x</sub> removal.

### References:

- Beale A. M. *et al.* Recent advances in automotive catalysis for NO<sub>x</sub> emission control by small-pore microporous materials. *Chem. Soc. Rev.* **44**, 7371–7405 (2015). DOI: 10.1039/C5CS00108K
- Brandenberger S. *et al.* The state of the art in selective catalytic reduction of NO<sub>x</sub> by ammonia using metal-exchanged zeolite catalysts. *Catal. Rev. - Sci. Eng.* **50**, 492–531 (2008). DOI: 10.1080/01614940802480122
- Diaz-Moreno S. *et al.* I20; The Versatile X-ray Absorption spectroscopy beamline at Diamond Light Source. *J. Phys. Conf. Ser.* **190**, 12038 (2009). DOI: 10.1088/1742-6596/190/1/012038
- Boubnov A. *et al.* Identification of the iron oxidation state and coordination geometry in iron oxide- and zeolite-based catalysts using pre-edge XAS analysis. *J. Synchrotron Radiat.* **22**, 410–426 (2015). DOI: 10.1107/S1600577514025880

### Funding acknowledgement:

EPSRC (EP/K007467/1); Diamond Light Source; Johnson Matthey Plc.

### Corresponding author:

Prof Andrew M. Beale, University College London, andrew.beale@ucl.ac.uk

## Soft Condensed Matter Group

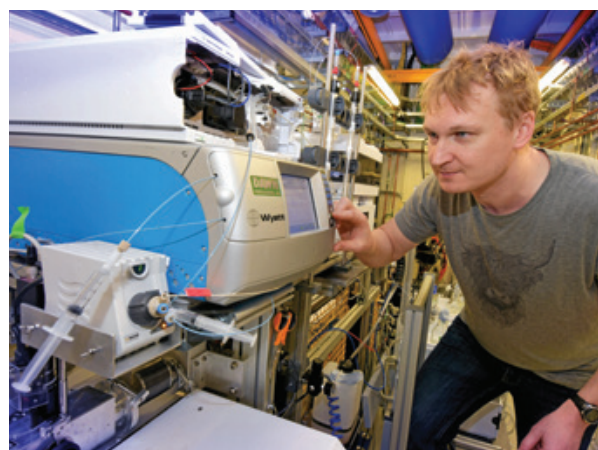
Robert Rambo, Science Group Leader

**T**he Soft Condensed Matter (SCM) Group provides the infrared (IR) and Circular Dichroism (CD) microspectroscopy and both Small and Wide Angle X-ray Scattering (SAXS and WAXS) capabilities of Diamond. The group comprises of four beamlines: High Throughput SAXS (B21), the Multimode Infrared Imaging And Microspectroscopy (MIRIAM) beamline (B22), SAXS and Diffraction (I22) and the CD beamline (B23). This unique portfolio of beamlines can analyse a range of samples that include two-dimensional thin films (photovoltaics), living mammalian cells, three-dimensional matrices (e.g. metal-organic frameworks, gels and waxes) and nano-particles in non-crystalline states. The SCM Group maintains a dedicated laboratory space for visiting users. The laboratory houses vital equipment for sample preparation and analysis such as a centrifuges, a biosafety level 2 facility, spectroscopy equipment and the ability to work with different gases. B21, I22 and B23 now offer mail-in services for SAXS and CD measurements through UAS announcements to our user community. In addition, both B22 and B23 continue to offer off line access to IR microscopy and imaging, and CD spectroscopy.

In the last year, the SCM Group had a record number of publications across the beamlines participating in 141 scientific papers spanning a breadth of topics including food, geology, space, microfluidics, polymers, graphene, green and life sciences.

The Diamond-II upgrade, which aims to reduce the emittance and size of the accelerated electrons, will be transformative to the facility, particularly for the SCM Group. For B21, we anticipate a nearly 100x increase in power, producing at least  $10^{15}$  photons per second on the sample in a special 'pink' beam mode, allowing for the possibility to probe within the microsecond regime. For B22, the change in source and optics is expected to provide up to four-fold higher photon flux density in the already diffraction limited microbeam at the sample and, combined with currently under commissioning novel IR adaptive optics system, to shape the illumination for full-field IR imaging over a field of view double of that currently possible. The targeted stability increase in the Diamond-II source should provide a nearly 10-fold increase in signal-to-noise for IR microanalysis, and especially for the ongoing dedicated user call for IR nanospectroscopy beamtime, uniquely worldwide in Synchrotron IR photothermal mode. Finally, for B23, the new source will be aimed at driving down the spatial resolution of the beam. B23 has been pioneering a new capability called CD-imaging that maps the chiral information of materials across 2-dimensional surfaces. Currently, B23 provides mapping at  $50 \mu\text{m}^2$  spatial resolution and the upgrade seeks to reduce this down to  $\sim 1 \mu\text{m}^2$ .

In planning for Diamond-II, the SCM Group hosted a two-day workshop where we invited speakers to facilitate discussions about the new science capabilities enabled by Diamond-II. The meeting was a great success, attracting a diverse group of scientists.



Principal Beamline Scientist, Nathan Cowieson, on beamline B21.

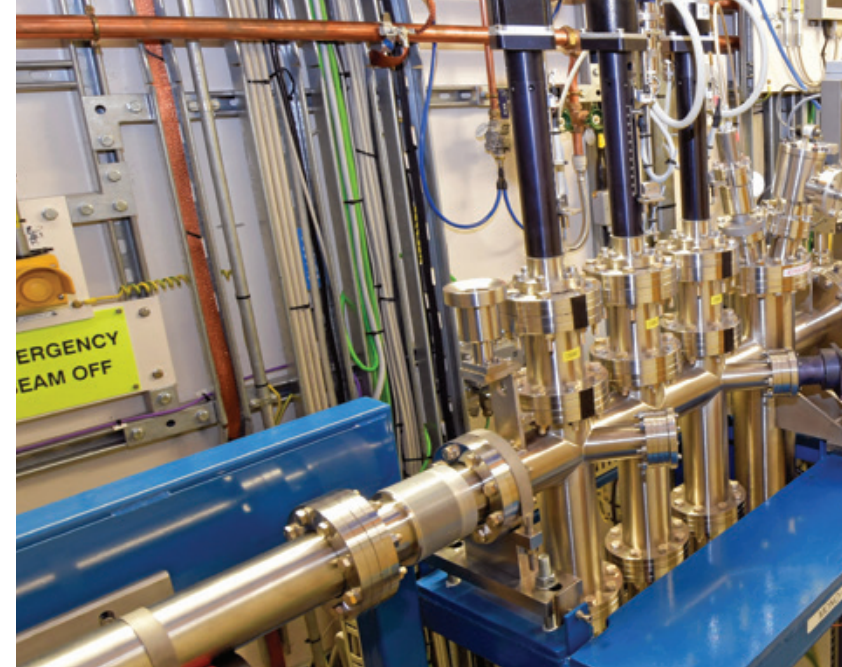
### B21 update

The High Throughput SAXS beamline (B21) is dedicated to the study of noncrystalline, randomly oriented particles. SAXS measurements can be made on any type of sample and in any physical state. There is strong demand for so-called BioSAXS from the life science community since such measurements provide the opportunity to study biological machines in conditions that are comparable to their liquid, hydrated environment. This ability complements the many solid-state studies performed at Diamond using X-ray crystallography and cryo-electron microscopy. The B21 end station is most commonly configured to run high-throughput batch-mode experiments using either the bioSAXS sample delivery robot or the High-Performance Liquid Chromatography (HPLC) instrument for inline size-exclusion chromatography (SEC) coupled SAXS but can also be configured for low-throughput, manually loaded samples.

B21 underwent a major rebuild of its experimental hutch, installing the 'module 8' camera. This upgrade saw retirement of our original Pilatus 2M detector where B21 now uses the state-of-the-art, in vacuum Eiger 4M detector from Dectris. The in vacuum system removes the large Kapton window that formed the observation window for the old 2M detector. In the old configuration, the window created a nearly 12 mm gap between the detector and the beamstop, where the scattered X-rays would travel through the Kapton material, nylon membrane and air gap before being read by the detector. In the new, windowless design the X-rays are no longer impeded by window materials and the beamstop is now positioned within a couple of millimetres of the detector face – thereby improving our accessible low- $q$  (scattering vector) SAXS measurement. In addition, the new detector provides pixels that are  $\sim$ half the size of the old detector, nearly doubling the information in a SAXS measurement. These changes produced substantial decreases in the instrumentation noise at the smallest scattering angles. The plan for B21 in 2019 is to pursue a new mirror mechanism to improve the focus, provide a high band-pass, 'pink beam' and an entirely windowless path for the X-ray beam from monochromator to samples.

### B22 update

The Multimode Infrared Imaging and Microspectroscopy (MIRIAM) beamline (B22) is used to assess the molecular composition and microscopic spatial distribution of a sample at the highest, optically-achievable resolution. B22 operates two end stations that are dedicated to confocal IR microspectroscopy and IR imaging, with a suite of single and array detectors that cover the whole IR range. B22 is used for a wide variety of applications such as the analysis of inorganic-organic combinations and polymers, as well as studying live cancer cells under the IR microprobe for in situ drug response, for example. The beamline had a record year in publications that included



“This unique portfolio of beamlines can analyse a range of samples...”

The Optics Hutch on I22.

showing how IR microspectroscopy can be used to identify stem cells in endometrial tissue to out-of-this world investigations of volatiles in the solar system. Terahertz (THz) spectroscopy has proved particularly prolific in high impact publications, particularly exploiting the unique broadband capability of synchrotron radiation for measuring the real and imaginary part of dielectric function in new material science across the entire IR to THz range, for example.

In 2018, B22 published a world first for micro photoacoustic IR spectroscopy (microPAS). Unlike laser source, the microphotoacoustic with synchrotron IR enables seamless spectral coverage for efficient Fourier Transform IR (FTIR) spectroscopy with micrometric spatial resolution of molecular composition across organic and inorganic samples. The microPAS method was developed in collaboration with the Canadian Light Source and Dr. Luca Quaroni (Krakow Univ. Poland). In addition, the beamline continues to provide a dedicated call (now the 2<sup>nd</sup>) for IR nanospectroscopy in hot thermal mode (AFM IR). This cutting edge method is particularly suitable for molecular analysis of submicron to micron scale biomaterial with exceptional 100 nm resolution (i.e. up to 100 times below the IR wavelength scale). The in progress, high-speed chopper upgrade will provide a nearly 3x improvement in the optical modulation frequency plus extra stability. Operating between 50 to 200 kHz with less than 1% jitter, the new chopper will give a significant improvement to benefit AFM-coupled nanospectroscopy in terms of resolution and spectral acquisition speed and quality.

### B23 update

Operational since 2009, the Circular Dichroism (CD) beamline (B23) uses circularly polarised light to characterise the structure of complex materials in solution and in solid-state films. Many molecular systems have a handedness (chirality) to them akin to our right and left hands. This molecular handedness will differentially absorb light that is either right-polarised or left-polarised and at B23, measurements are made that precisely quantify how much of each type of polarised light is absorbed by the sample. In thin films, quantification of the polarisation at micron resolution can inform on how materials prefer to orient themselves and for biological samples, CD spectra can be used to demonstrate conformational changes, drug binding or instabilities in a protein.

B23 is at the forefront of a new CD Imaging (CDi) technology. CDi exploits the highly collimated synchrotron light beam for scanning thin-films and surfaces of solid materials. Unlike absorption methods, CDi can inform on the local chiral structure of the material limited by the spatial resolution of the scanning beam and the precision of the rotating gratings. Dr Giuliano Silligardi, B23 PBS, has secured funding for a dedicated Mueller-Matrix Polarimeter (MMP) instrument to be installed in autumn 2019 that will improve CDi measurements of solid state films by extracting the linear

dichroism and linear and circular birefringence contributions from that of CD, otherwise seen as polarisation distortion artefacts. Current CDi measurements require manual manipulation of the sample to make several measurements of the material in different orientations. The MMP will allow all necessary measurements to be performed at once, thereby revealing the information that each polarisation can provide. Many thin-film materials are made from polymers and these polymers will preferentially form a handedness structure such as a helix. Currently, the chiral homogeneity of these supramolecular structures throughout the material cannot be interrogated efficiently using non-destructive methods. CDi will provide a complementary method to high-resolution microscopy for material science.

### I22 update

The Small Angle Scattering and Diffraction beamline (I22) offers combined Small and Wide Angle X-ray Scattering (SAXS and WAXS) studies on a range of low order biological and synthetic samples. I22 excels at providing structural information on partially ordered materials ranging from bone and thin-films to large helical structures such as collagen.

The I22 PBS, Dr Nick Terrill, in collaboration with Prof Michael Rappolt from the School of Food Science and Nutrition at the University of Leeds, was awarded an Engineering and Physical Sciences Research Council (EPSRC) grant to build an offline SAXS facility to be located at Diamond and managed by the SCM Group. The Multi-User Facility for SAXS/WAXS (DL-SAXS) will allow independent development/testing of sample environments prior to beamtime, and provides an additional SAXS instrument for experiments.

I22 continues to provide a highly competitive SAXS/WAXS instrument and has completed phase 1 of a Beam Conditioning Optics (BCO) upgrade project. The project will significantly improve data quality through a completely embedded microfocus mechanism, providing variable beamsizes, energy and evacuated flight tube. The new optical layout has significantly reduced divergence and will provide access to much lower  $q$  (scattering vectors) than previously available. In the past, I22 was limited to providing microfocus experiments at only 14 keV, the new set up will allow lower energy microfocus experiments with the main beamline SAXS camera, on a case-by-case basis. I22 has recorded a flux of  $5.6 \times 10^{10}$  photons/sec in a  $10 \mu\text{m} \times 10 \mu\text{m}$  micro-focused beam at 14 keV, very similar to the old system but with significantly reduced backgrounds, hugely improved  $q$ -range and lower divergence. The new set-up provides demagnification and focusing of the primary beam down to this minimum spot size. The microfocus sample stages are still available for accurate sample positioning, and with the completion of the BCO upgrade in late 2019, a new inline microscope capability for all modes will be available.

## Investigating the structure of the synaptonemal complex

**Related publication:** Duncie J. M., Dunne O. M., Ratcliff M., Millán C., Madgwick S., Usón I. & Davies O. R. Structural basis of meiotic chromosome synapsis through SYCP1 self-assembly. *Nat. Struct. Mol. Biol.* **25**, 557–569 (2018). DOI: 10.1038/s41594-018-0078-9

**Publication keywords:** Meiosis; Chromosome structure; Double-strand break; Chiasmata; Synaptonemal complex; SYCP1; Self-assembly

Cell division is a fundamental process for all organisms. In higher-ordered organisms such as humans, the production of egg and sperm cells for reproduction requires a specialised process of cell division called meiosis. Here, our genes, which are organised into chromosomes, must be equally divided between the two new cells that arise from division. Facilitating this segregation is a special protein structure called the synaptonemal complex (SC). The SC provides the necessary 3D framework for crossover formation, ensuring the correct chromosomal segregation into haploid germ cells. Although the SC was discovered in 1956, its molecular structure has remained unknown. An international team of researchers sought to uncover the underlying structure of the human SC through studies on the self-assembly mechanism of SYCP1, its principal protein component.

To do so, the researchers needed to establish the solution structure of obligate unassembled SYCP1 molecules through analysis of their two structural domains. Having established that the C-terminal self-assembly site of SYCP1 undergoes protonation-induced assembly from a dimer to a tetramer in solution, and solved its tetrameric crystal structure, the researchers also needed to determine the structure of the dimeric conformation, and test whether the tetrameric conformation in solution matches the crystal structure.

Therefore, the researchers performed Size-Exclusion Chromatography Small Angle X-ray Scattering (SEC-SAXS) at the High Throughput SAXS beamline (B21). SEC-SAXS analysis accurately determines the principal dimensions (length and width) of an elongated molecule. It provided a simple and robust means for determining the structure of the principal coiled-coil regions of SYCP1.

In combination with other data, their findings led to a model for SYCP1 self-assembly in which obligate tetramers form a supramolecular lattice through staggered N-terminal head-to-head assembly in the midline coupled with C-terminal back-to-back assembly on the chromosome axis.

During meiosis, homologous chromosome pairs are brought into close synapsis along their entire length through assembly of a zipper like structure, the synaptonemal complex (SC). The SC has a characteristic appearance in electron micrographs, in which the two chromosome axes are held 100 nm apart by a series of transverse filaments that meet in a midline electron-dense

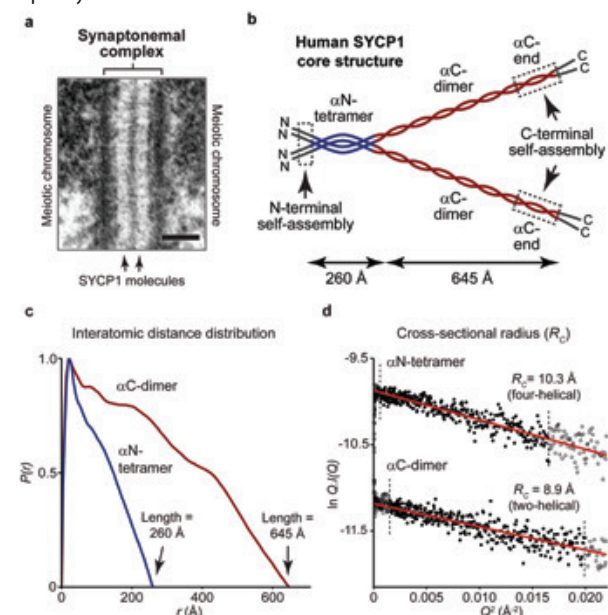


**Figure 1:** SEC-SAXS analysis of SYCP1  $\alpha$ N-tetramer and  $\alpha$ C-dimer. (a) Electron micrograph of the mammalian synaptonemal complex (SC), reproduced from Kouznetsova *et al.* Scale bar, 100 nm. (b) The SYCP1 core structure consists of an N-terminal four helical bundle ( $\alpha$ N-tetramer) that splays into two C-terminal coiled-coiled dimers ( $\alpha$ C-dimer). Self-assembly sites at its N- and C-terminal ends are indicated (dashed boxes). (c) SEC-SAXS  $P(r)$  distributions for  $\alpha$ N-tetramer (blue) and  $\alpha$ C-dimer (red). The maximum interatomic distances, which correspond to the coiled-coil length, are indicated. (d) SEC-SAXS Guinier analysis of the radius of gyration of the cross-section ( $R_c$ ); the linear fit is highlighted in black and is demarcated by dashed lines ( $Q R_c < 1.3$ ).

structure (Fig. 1a)<sup>1,2</sup>. SC transverse filaments are formed of elongated SYCP1 protein molecules, facing in opposite directions, with their C-termini bound to chromosome axes and their N-termini meeting head-to-head in the midline<sup>3,4</sup>. Human SYCP1 contains 976 amino acid residues, which encode a predicted coiled-coil structural core of almost 700 amino acids, flanked by unstructured N- and C-termini. However, the structure of SYCP1 and its mechanism of assembly between meiotic chromosomes remained unknown.

The coiled-coil constitutes a simple but highly diverse and prevalent protein fold that is characterised by the intertwining of  $\alpha$ -helical chains, and frequently provides architectural rigidity, often serving to impose function-critical distances between flanking sequences. Small Angle X-ray Scattering (SAXS) provides a robust means for determining the principal dimensions (i.e. length and width) of asymmetric, elongated/rod-like molecules in solution, and hence is particularly well-suited to characterising coiled-coils. In the present study, size-exclusion chromatography coupled to SAXS (SEC-SAXS), performed at B21, was used as a powerful and invaluable tool in defining the geometry and orientation of the principal coiled-coiled regions of SYCP1.

Analysis by circular dichroism and size-exclusion chromatography multi-angle light scattering (SEC-MALS) revealed that the SYCP1 core can be dissected into a 155-residue N-terminal  $\alpha$ -helical tetramer ( $\alpha$ N-tetramer), and a 424-residue C-terminal  $\alpha$ -helical dimer ( $\alpha$ C-dimer; Fig. 1b). SEC-SAXS was utilised to determine the principle dimensions of these putative coiled-coils. As is typical for elongated molecules, the SAXS pair-distance ( $P(r)$ ) distribution functions (describing the relative spread of interatomic distances within the molecule) were positively skewed for  $\alpha$ N-tetramer and  $\alpha$ C-dimer (Fig. 1c). The  $P(r)$  distribution indicates the maximum dimension of the molecule, which for a coiled-coil may be directly interpreted as its length.  $\alpha$ N-tetramer and  $\alpha$ C-dimer showed  $P(r)$  maximum dimensions of 260 and 645 Å, which closely match their theoretical lengths as extended coiled-coils. Determination of the cross-sectional radius of gyration ( $R_c$ ) reveals the thickness of elongated molecules and thereby indicates the number of helices within a coiled-coil. SAXS data for  $\alpha$ N-tetramer

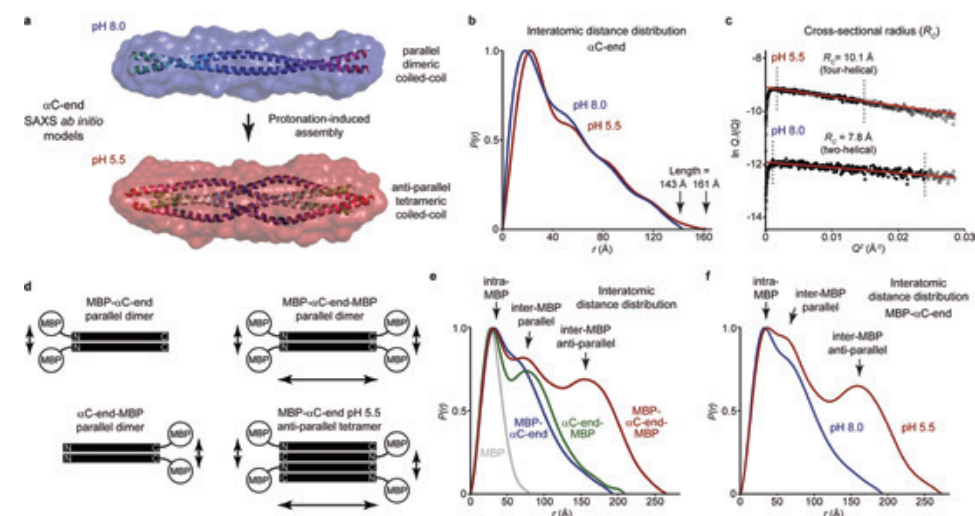


**Figure 2:** SEC-SAXS analysis of SYCP1  $\alpha$ C-end. (a) SEC-SAXS *ab initio* molecular envelopes for SYCP1  $\alpha$ C-end at pH 8.0 and 5.5 with docked dimeric coiled-coil and the  $\alpha$ C-end tetrameric crystal structure (PDB accession 6F63). (b) SEC-SAXS  $P(r)$  distributions and (c) Guinier analysis of the radius of gyration of the cross-section ( $R_c$ ) of  $\alpha$ C-end at pH 8.0 (blue) and 5.5 (red). (d) Schematic representing predicted configurations of  $\alpha$ C-end MBP-fusions with arrows indicating inter-MBP distances. (e-f)  $P(r)$  distributions for (e)  $\alpha$ C-end MBP-fusions at pH 8.0 and (f) MBP- $\alpha$ C-end at pH 8.0 and 5.5. Peaks representing intra- and inter-MBP distances are indicated.

and  $\alpha$ C-dimer revealed  $R_c$  values of 10.3 and 8.9 Å, which are consistent with the presence of four and two helices within their cross-sections (Fig. 1d). Thus, SAXS analysis revealed that  $\alpha$ N-tetramer and  $\alpha$ C-dimer comprise extended four-helical bundles and dimeric coiled-coils, respectively. These findings underpin a model for the structure of unassembled SYCP1 in which an N-terminal tetramer forks

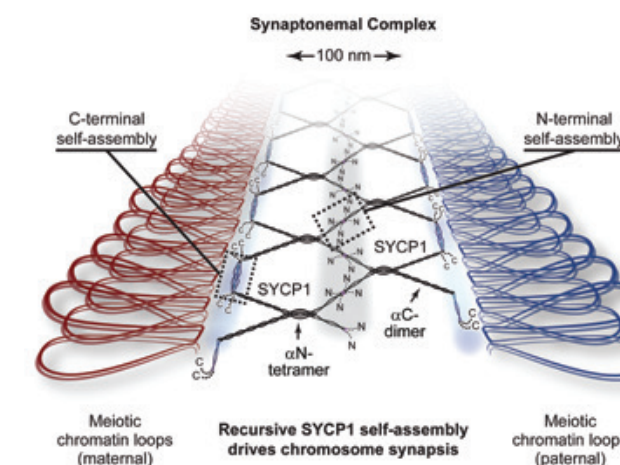


**Figure 3:** Meiotic chromosome synapsis by SYCP1. Bifurcating SYCP1 tetramers undergo recursive assembly to produce a potentially limitless proteinaceous lattice between homologous chromosomes. The lattice is created by a staggered and opposing arrangement of SYCP1 molecules adjoined through self-assembly sites encoded by sequences at N- and C-terminal ends of its elongated structural core.

at its C-terminus, splaying apart as two elongated dimeric coiled-coils (Fig. 1b).

The C-terminal end of  $\alpha$ C-dimer (referred to as  $\alpha$ C-end; Fig. 1b) was determined through SEC-MALS to undergo a protonation-dependent dimer-to-tetramer transition in solution (triggered by reducing pH from 8.0 to 5.5). The crystal structure of tetrameric  $\alpha$ C-end revealed an anti-parallel coiled-coil (PDB accessions 6F63 and 6F64), whilst its dimeric structure remained unknown. SEC-SAXS analysis at pH 8.0 and 5.5 determined shapes that closely match the dimensions of a theoretical dimeric coiled-coil and the tetrameric crystal structure, respectively (Fig. 2a). In support of this, they showed similar  $P(r)$  maximum dimensions, indicating that the extended structure of tetrameric  $\alpha$ C-end is replicated in its dimeric conformation (Fig. 2b). Further, the respective  $R_c$  values of 7.8 and 10.1 Å suggest the presence of two and four helices within their cross-sections (Fig. 2c). Next, to determine the orientation of the helices (i.e. head-to-head or head-to-tail alignment) within the two  $\alpha$ C-end conformations, further SAXS studies were performed that placed large protein markers (maltose-binding protein, MBP) on the ends of the helices (Fig. 2d). This was achieved through SAXS analysis of maltose-binding protein (MBP)-fusions (Fig. 2d). The dominance of globular structure within scattering data leads to clear inter-MBP

peaks within  $P(r)$  distributions, which determine how they are orientated by the coiled-coil, with short or long inter MBP distances indicating a parallel or anti-parallel setting, respectively<sup>5</sup>. Single MBP fusions of  $\alpha$ C-end at pH 8.0 revealed short inter-MBP distances, with long distances observed only in a double N- and C-terminal fusion, indicating that the dimeric conformation of  $\alpha$ C-end is parallel (Fig. 2e). In contrast, a single MBP fusion at pH 5.5 demonstrated both short and long inter-MBP peaks, indicating that the tetrameric conformation contains both parallel and anti-parallel chains (Fig. 2f). Thus, SAXS analysis revealed that  $\alpha$ C-end forms a parallel dimeric coiled-coil that undergoes protonation-dependent assembly into an anti-parallel tetramer that matches the crystal structure. The  $\alpha$ C-end tetramer binds to DNA, suggesting a coordinated mechanism for its assembly on the chromosomal axis.

These findings, in combination with biophysical and crystallographic data revealing a distinct self-assembly mechanism for the SYCP1 N-terminus, led to a model for SYCP1 supramolecular assembly into a potentially limitless proteinaceous lattice between meiotic chromosomes (Fig. 3). This model represents the culmination of the described experiments, and could not have been established without the SAXS data collected at B21.

### References:

- Zickler D. *et al.* Recombination, pairing, and synapsis of homologs during meiosis. *Cold Spring Harb. Perspect. Biol.* **7**, 1–28 (2015). DOI: 10.1101/cshperspect.a016626
- Kouznetsova A. *et al.* Meiosis in Mice without a Synaptonemal Complex. *PLoS ONE* **6**(12): e28255 (2011). DOI: 10.1371/journal.pone.0028255
- De Vries F. A. T. *et al.* Mouse Sycp1 functions in synaptonemal complex assembly, meiotic recombination, and XY body formation. *Genes Dev.* **19**, 1376–1389 (2005). DOI: 10.1101/gad.329705
- Sauer M. *et al.* Elucidation of synaptonemal complex organization by super-resolution imaging with isotropic resolution. *Proc. Natl. Acad. Sci.* **112**, 2029–2033 (2015). DOI: 10.1073/pnas.1414814112
- Dunne O. M. *et al.* Molecular structure of human synaptonemal complex protein SYCE1. *Chromosoma* (2019). DOI: 10.1007/s00412-018-00688-z

### Funding acknowledgement:

Grants BIO2015-64216-P and MDM2014-0435-01 (MINECO, Spanish Ministry of Economy and Competitiveness). MINECO BES-2015-071397 scholarship associated to the Structural Biology Maria de Maeztu Unit of Excellence. Wellcome Trust Career Re-entry Fellowship (062376). Fellowship jointly funded by the Wellcome Trust and Royal Society (grant number 104158/Z/14/Z).

### Corresponding author:

Dr Owen Davies, Newcastle University, owen.davies@newcastle.ac.uk

## A novel dynamic flow system for chemical analysis of live biological cells

**Related publication:** Doherty J., Raoof A., Hussain A., Wolna M., Cinque G., Brown M., Gardner P. & Denbigh J. Live single cell analysis using synchrotron FTIR microspectroscopy: Development of a simple dynamic flow system for prolonged sample viability. *Analyst* **144**, 997–1007 (2019). DOI: 10.1039/c8an01566j

**Publication keywords:** Live cells; Infrared spectroscopy; Dynamic flow; Water correction; Ovarian cancer

**A**nalysing cells on a cell-by-cell basis using infrared microspectroscopy can reveal important biochemical information, providing insight into diseases, and drug-cell interactions. However, for visible and infrared microscopy, the cells have to be preserved and dried; also, water is a strong infrared absorber and obscures the spectrum of the cells under investigation. Analysing dried fixed cells reduces the relevance of the results since they are not in their natural environment.

Researchers investigated building a sample environment that would allow the cells to be kept alive in water during infrared microspectroscopy analysis. The sample chamber needed an amount of water small enough to not be a major problem, but large enough to allow the correct flow of nutrients to the cells, to keep them alive for a prolonged period of time. It also had to be temperature-controlled.

They carried out their work on the Multimode Infrared Imaging And Microspectroscopy (MIRIAM) beamline (B22), modifying a commercially-available liquid sample holder with a narrow gap for the cells to sit in, and just enough water to stay alive, without inducing mechanical stress. They also used a special hydrophobic pen to draw a channel in the chamber that allowed the nutrients to flow through the chamber and keep the cells alive. They tested the dynamic system by introducing a labelled molecule and monitoring the uptake by the cells, and also by looking at temperature-induced degradation of cells. Their tests were successful, and the dynamic cell system is now available to other infrared users of Diamond Light Source.

The study of biological cells using micro-Fourier Transform Infrared (micro-FTIR) spectroscopy has historically been limited to the use of fixed, dried samples. While there are clear benefits to this type of sample preparation, for example the ability to return to the same sample for repeat measurement, chemical fixatives are known to affect various cellular structures, limiting the interpretation of data obtained<sup>1</sup>.

Cell dehydration can affect the position, intensity, and ratio of bands across the spectrum, in particular DNA bands that become harder to distinguish from

those of proteins, RNA, and carbohydrates. In contrast, studies of living cells provide biological detail that was previously lost when using fixed samples, especially when live cell analysis has been combined with the increased infrared (IR) brilliance of a synchrotron radiation (SR) source<sup>2</sup>.

The study of living cells, however, presents a range of challenges to bioanalysts. Live cells require an aqueous environment to remain viable for any significant length of time, and water presents two significant problems for IR spectroscopists. Firstly, the strength of the water absorption prevents

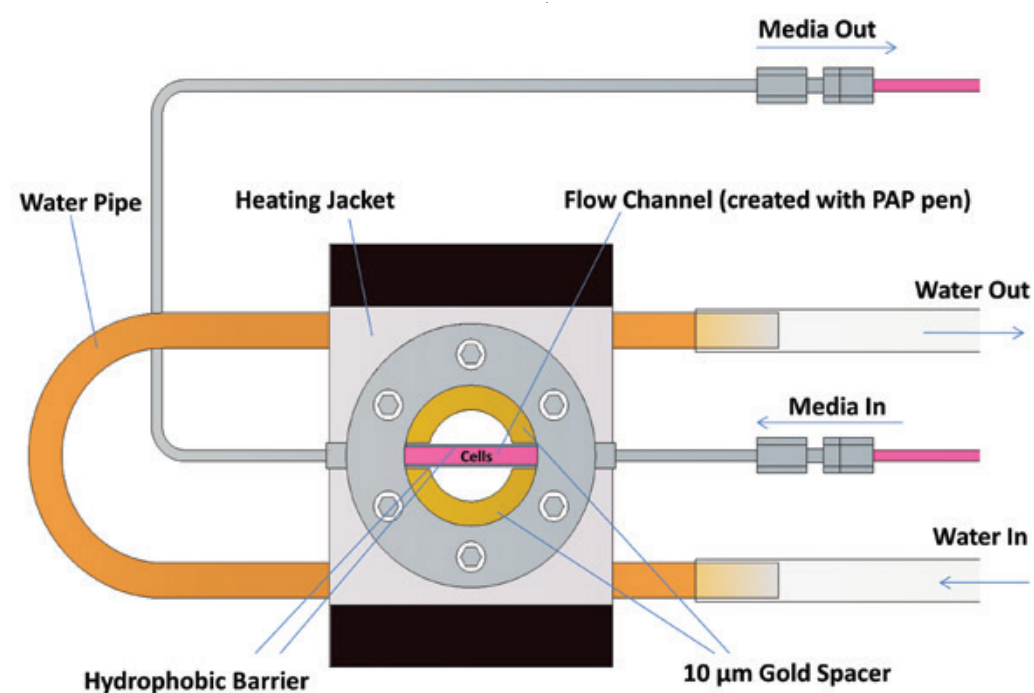


Figure 1: Diagram of the assembly of the modified liquid sample holder. The heating jacket is shown around the sample chamber, and the inlet and outlet flow from the sample holder is indicated. Inside the sample chamber, the 10 µm spacer, hydrophobic barriers and the flow channel are all highlighted.

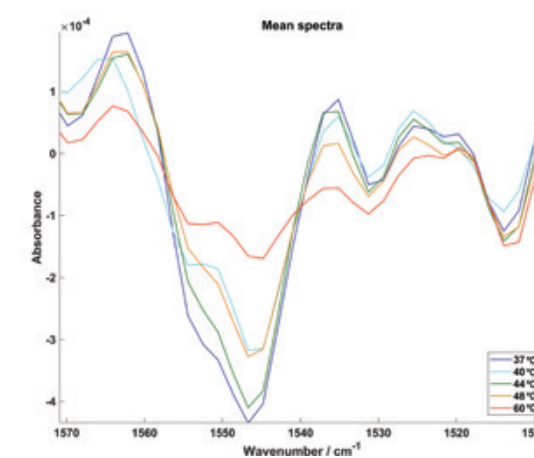


Figure 2: Second derivative mean spectra (1500–1580  $\text{cm}^{-1}$  region) of SKOV3 cells, indicating the changes around the Amide II band as a function of increasing temperature.

sufficient IR from reaching the sample to give a good signal and consequently produce high-quality data. Secondly, the position of the O–H bending and stretching modes, at  $\sim 1650$  and  $3000\text{--}3500$   $\text{cm}^{-1}$  respectively, obscures key biological information relating to protein and lipid bands. This makes the extraction of biochemical information difficult<sup>1</sup>.

In a recent publication, a collaborative team from the groups of Dr J. L. Denbigh (University of Salford), Prof P. Gardner (University of Manchester), and Dr G. Cinque (Diamond Light Source), have developed a liquid sample chamber for live cell analysis that balances the requirements of a water layer that is thin enough for the transmission of infrared radiation, but thick enough to keep the cells fully hydrated in a constant flow of nutrients, enabling them to be studied for up to 24 hours<sup>3</sup>.

The sample chamber is based on a modified commercial (Harrick) liquid sample holder, consisting of two 2 mm thick  $\text{CaF}_2$  windows separated with a 10 µm metal spacer. The spacer has been modified to allow liquid (in this case cell culture media) to flow through the chamber. A key feature of the design is the creation of a  $\sim 2$  mm channel on the bottom window, using a PAP pen which deposits a hydrophobic barrier to direct the flow over the cells (Fig. 1). The cells under study are deposited on to the bottom  $\text{CaF}_2$  window, in the channel, prior to the assembly of the rest of the chamber. The sample chamber is fitted with a temperature-controlled heating jacket to maintain the cells at 37 °C, or to cool/heat the sample as required. The cell culture media is delivered to the sample chamber using a Hamilton Syringe connected to a syringe pump.

In this study, it was important to demonstrate the capabilities of the sample environment, and this was achieved using two types of test IR measurement; one monitoring the heat-induced denaturing of cells, and another looking at uptake of an important dietary fatty acid implicated in cancer progression. For both studies, data were collected in transmission mode using the 36 $\times$  objective/condenser optics on a (Bruker) Hyperion 3000 microscope coupled to a Vertex 80 FTIR spectrometer on B22 at Diamond. This used a liquid-nitrogen cooled mercury-cadmium-telluride high sensitivity 50 micron pitch detector<sup>4</sup>. The raw spectra were subjected to an *ad hoc* water correctional algorithm that enabled the single cell spectrum to be recovered from the substantial water background<sup>5</sup>.

Fig. 2 shows the second derivative of infrared spectra from SKOV3 ovarian cancer cells in media, being subjected to thermal stress. In particular, the collapse of Amide II-related bands at 60 °C between 1547 and  $\sim 1520$   $\text{cm}^{-1}$  is a significant structural change, and consistent with published work on temperature-induced denaturing of proteins.

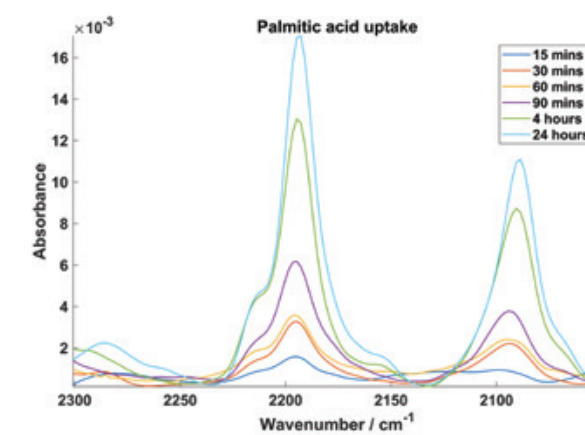


Figure 3: Mean microFTIR spectra of deuterated palmitic acid uptake in cells at each incubation time.

Monitoring of the uptake of deuterated palmitic acid (D31PA) over time involved the collection of a large number of spectra ( $\sim 200$ ) from single SKOV3 ovarian cancer cells over the course of several hours, while the sample was maintained in a healthy condition in the dynamic flow system. Fig. 3 shows the infrared spectra of the  $\text{CD}_2/\text{CD}_3$  symmetric and asymmetric stretches as a function of cell exposure. As can be seen, D31PA is observed after just 15 minutes and continues to build up in the cell over a 24 hour period.

By demonstrating cell viability up to 24 hours, we have shown that the dynamic flow chamber is potentially suitable for a range of live cell applications of IR microspectroscopy monitoring cellular changes following exposure to a stimulus. Combined with effective water correction, and the brilliance of SR, we have acquired high-quality micro-FTIR spectra from living cells over any extended period of time. This paves the way for further dynamic flow studies of cells at the MIRIAM beamline.

### References:

- Doherty J. *et al.* Single-cell analysis using Fourier transform infrared microspectroscopy. *Appl. Spectrosc. Rev.* **52**, 560–587 (2017). DOI: 10.1080/05704928.2016.1250214
- Diem M. *et al.* Monitoring the reversible B to A-like transition of DNA in eukaryotic cells using Fourier transform infrared spectroscopy. *Nucleic Acids Res.* **39**, 5439–5448 (2011). DOI: 10.1093/nar/gkr175
- Doherty J. *et al.* Live single cell analysis using synchrotron FTIR microspectroscopy: Development of a simple dynamic flow system for prolonged sample viability. *Analyst* **144**, 997–1007 (2019). DOI: 10.1039/c8an01566j
- Cinque G. *et al.* Multimode infrared imaging and microspectroscopy (MIRIAM) beamline at diamond. *Synchrotron Radiat. News* **24**, 24–33 (2011). DOI: 10.1080/08940886.2011.618093
- Doherty J. *et al.* Increased optical pathlength through aqueous media for the infrared microanalysis of live cells. *Anal. Bioanal. Chem.* **410**, 5779–5789 (2018). DOI: 10.1007/s00216-018-1188-2

### Funding acknowledgement:

Diamond Light Source; University of Manchester; KidsCan Children's Cancer Research.

### Corresponding author:

Dr Joanna Denbigh, University of Salford, j.l.denbigh@salford.ac.uk

## A step towards earlier detection of multiple sclerosis

**Related publications:** Shaharabani R., Ram-On M., Talmon Y. & Beck R. Pathological transitions in myelin membranes driven by environmental and multiple sclerosis conditions. *Proc. Natl. Acad. Sci.* **115**, 11156–11161 (2018). DOI: 10.1073/pnas.1804275115; Shaharabani R., Ram-On M., Avinery R., Aharoni R., Arnon R., Talmon Y. & Beck R. Structural Transition in Myelin Membrane as Initiator of Multiple Sclerosis. *J. Am. Chem. Soc.* **138**, 12159–12165 (2016). DOI: 10.1021/jacs.6b04826

**Publication keywords:** SAXS; Phase transition; Myelin; Multiple sclerosis; Lamellar phase; Inverted hexagonal phase; Membrane; Lipids

Using Diamond Light Source's Small Angle Scattering & Diffraction beamline (I22), I911-SAXS at MAX IV Laboratory, SWING at SOLEIL synchrotron, and P12 at EMBL BioSAXS, a team of researchers from Tel Aviv University and the Technion-Israel Institute of Technology mapped, for the first time, the delicate and complicated force balance between the myelin sheath constituents and their effect on the myelin structure.

It is well known that fatty, membranous materials (such as lipids) can organise into a variety of shapes (phases), including stacked sheets (lamellae), tubes, or cubes, to name a few. Controlling these phases is essential to proper function. This new information will allow the researchers to identify critical components involved in neurodegenerative diseases such as multiple sclerosis (MS).

MS is an autoimmune disease resulting in the destruction of myelin, a fatty substance that insulates nerves and increases the speed at which signals travel between nerve cells. MS affects more than 2.3 million people worldwide and has no cure. By investigating the microscopic structure of myelin membrane under various conditions, the researchers were able to identify the critical conditions that alter the myelin structure. Their results showed a phase transition from a healthy stack of lamellas to a diseased inverted hexagonal phase as a result of the altered lipid stoichiometry, myelin basic protein content, and environmental conditions such as salinity and temperature. Myelin lipid composition, and the physiological environmental conditions, are critical for myelin to function properly, and the results demonstrate that these conditions should be contemplated as alternative routes for MS early detection.

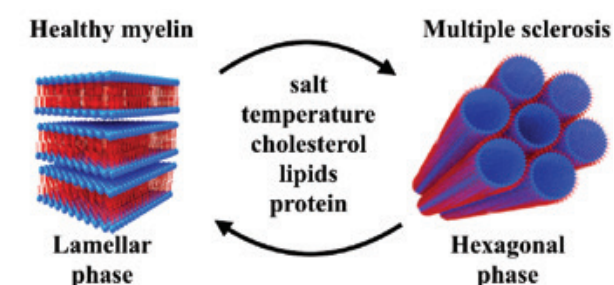


Figure 1: Schematic summary of the conditions resulting in phase transition in healthy and diseased myelin.

The myelin sheath, a repeating lipid-protein multilamellar structure, acts as an electrical insulator by forming a capacitor surrounding the axon, insuring fast nerve conduction<sup>1</sup>. The myelin membrane is composed of multiple lipid types, and the myelin basic protein (MBP). MBP facilitates binding of the myelin sheath to the underlying cytoplasmic membrane presumably through a charge-charge interaction where the positively-charged protein binds to the negatively-charged membranes acting as an intermolecular adhesion glue<sup>2,3</sup>.

Multiple sclerosis (MS) is an autoimmune disease resulting in myelin destruction. Currently, over 2.3 million people are affected by MS, while its etiology or cure are still elusive<sup>2,3</sup>. Previous *in vivo* studies correlated MS with changes in lipid composition and MBP deficiency<sup>3</sup>. Using Small Angle X-ray Scattering (SAXS), we recently evaluated the structural consequences of lipid and protein compositions at altered environmental conditions<sup>4,5</sup>. In particular, the structures of healthy (i.e. normal lipid composition) and diseased myelin (i.e. modified lipid composition) states were addressed (Fig. 1).

In Fig. 2 we show high-resolution synchrotron SAXS patterns, taken at I22, of normal and modified lipid compositions with and without the inclusion of MBP. The scattering profiles are composed of Bragg reflections overlaid on the

membrane form-factor signal. Multilamellar and hexagonal phases reflections are found at wave-vectors:  $q_{L(00n)} = \frac{2\pi n}{d_L}$  and  $q_{H(hkl)} = \frac{4\pi}{\sqrt{3}a_H} \sqrt{h^2 + hk + k^2}$  respectively. Here,  $n$ ,  $h$ , and  $k$  are the Miller integers,  $d_L$  and  $a_H$  represent the real-space unit-cell length of the lamellar and hexagonal phase respectively.

In the absence of MBP, normal lipid composition (Fig. 2, red line) results in one lamellar phase with unit-cell spacing of  $d_L = 113$  Å, while the modified lipid composition (Fig. 2, black line) results in coexistence of lamellar and inverted hexagonal ( $H_{II}$ ) phases with unit-cell lengths of  $d_L = 123$  and  $a_H = 90$  Å respectively<sup>4</sup>. The addition of MBP, however, results in phase transition for both lipid compositions. In the modified lipid composition (Fig. 2, blue line), the  $H_{II}$  phase quickly demolished and the SAXS signal results in a single lamellar

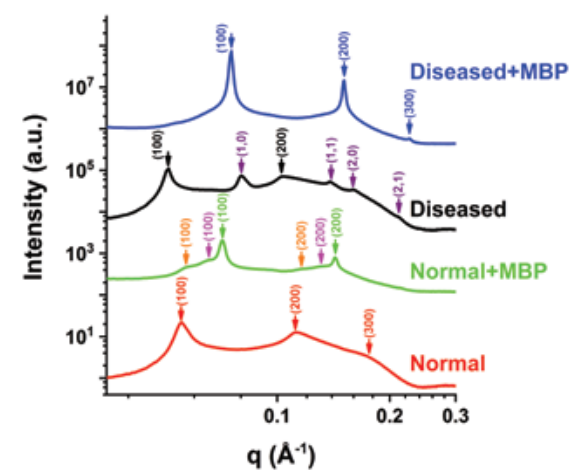


Figure 2: Normal and modified lipid compositions with and without MBP. Normal lipid composition only (red curve), normal lipid composition with 20% w/w MBP (green curve), modified lipid composition only (black curve), modified lipid composition with 20% w/w MBP (blue curve). For clarity of representation the scattering patterns are shifted in the intensity-axis.

phase with a unit-cell length of  $d_L = 84$  Å (above 7 wt% MBP content). For the normal lipid composition (Fig. 2, green line), the one lamellar phase in the absence of the protein transitions into three correlation peaks, indicating three unit-cell distances.

The dominant peak corresponds to the unit-cell length of the membrane (above 7 wt% MBP,  $d_L = 88$  Å, green arrow in Fig. 2), while the two shallow peaks correspond to in-plane MBP organisation within the membrane leaflets (Fig. 2, orange and pink arrows). These findings highlight that MBP is crucial for stabilising the membrane to form functional lamellar structures. Moreover, MBP causes the leaflets to adhere to one another, and flattens the membranes, counteracting local negative curvatures. In the absence of the protein, we expect that the normal lipid composition will be susceptible to structural phase transitions due to local changes in the membrane curvature.

*In vivo*, the environmental conditions are highly regulated and controlled. Potassium and sodium are essential for proper action potential along the myelinated axons. Calcium and zinc ions have the same oxidation state, yet they have different biological functions in the body, such as signal transduction pathways, and the induction of protein-protein interactions. Due to the fact that the myelin membrane is close to a structural phase transition, we addressed the effects of altered environmental conditions on the cytoplasmic myelin membrane structures<sup>5</sup>.

Changing the monovalent ion type or its concentration results in structural changes above a critical concentration,  $C^*$  (Fig. 3a-b). Above  $C^*$ , the lamellar unit-cell length ( $d_L$ ) decreases with increasing concentration for both monovalent ions (Fig. 3a-b, square symbols). In contrast, the hexagonal phase unit-cell length ( $a_H$ ) shows an opposite trend (Fig. 3a-b, hexagonal symbols), where  $a_H$  increases slightly with increasing monovalent salt concentration (Fig. 3a). This phenomenon occurs for both monovalent salts, and persists until  $C^*$ , at which point  $a_H$  becomes salt independent, and the lamellar phase is well ordered. Importantly, exchanging sodium with potassium ions exhibits the same pathological coexisting  $H_{II}$  phase even for healthy lipid composition above (Fig. 3b).

The divalent ions results are dramatically different. Here, we find that the structures are much more ion-specific (Fig. 3c-d). For example, the inverted hexagonal phases differ in the unit-cell length sizes at saturation with  $a_H$  ( $Mg^{2+} > a_H$  ( $Ca^{2+}) > a_H$  ( $Zn^{2+}$ ). Moreover, above a critical concentration,  $C^*(Zn^{2+}) = 5$  mM  $< C^*(Ca^{2+}) = 7$  mM  $< C^*(Mg^{2+}) = 9$  mM, we find a coexisting dense lamellar phase ( $d_d$ ). This new phase has the same unit-cell length for all ion types and lipid compositions ( $d_d \sim 64$  Å). Moreover, above  $C^*$ , we find no changes in the hexagonal unit-cell lengths (Fig. 3, hexagonal symbols). Surprisingly, here we find that even the normal lipid composition exhibits coexisting of inverted hexagonal phases, similar to the diseased state.

In order to study myelin vulnerability, we measured its structure in the context of membrane self-assembly by SAXS. From a physical perspective, the competing forces between the lipids determine the nanoscopic structure and the macroscopic mesophase, discussed in detail in ref<sup>4,5</sup>. In these studies, we identified several factors that tend to destabilise the lamellar phase, and induce the formation of the inverted hexagonal phase. Minor alterations of the environmental conditions can drive structural instabilities and the formation of the  $H_{II}$  phase. Lower salinity and low temperature are favorable for healthy lamellar phase up to about physiological condition.

In summary, even healthy myelin lipid composition is on the verge of a structural phase transition. The phase transition can be linked as a possible trigger for the outbreak of MS. In the process of phase transition from lamellar into the  $H_{II}$  phase, the membrane undergoes large undulations typical to the

increase in local curvatures<sup>5</sup>. These undulations can induce spontaneous pores, resulting in the vulnerability of the membrane to an attack by the immune system. Therefore, changes in lipid composition, depletion of MBP, or local environmental modification near the myelin, whether by ion type or ion concentration, can result in pathological phase transition that characterises the diseased state.

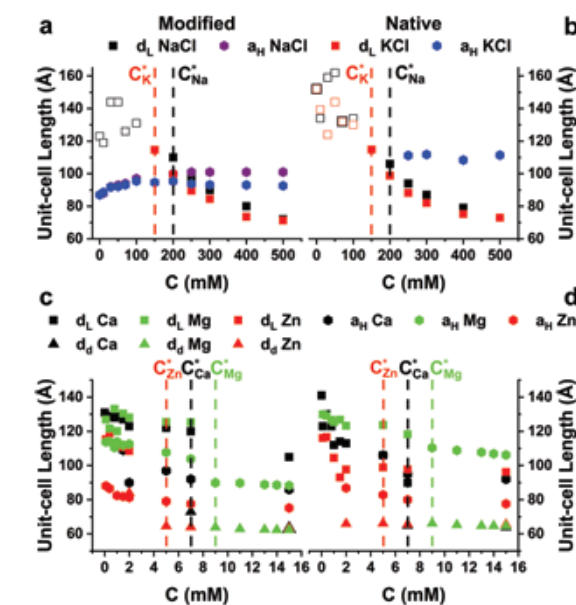


Figure 3: Normal and modified lipid compositions for different divalent ions concentration (C). Modified (a, c) and normal (b, d) lipid concentration for different monovalent (a, b) and divalent (c, d) ion concentrations. Dashed lines indicate  $C^*$ .

### References:

- Wood D. D. *et al.* Is the myelin membrane abnormal in multiple sclerosis? *J. Membr. Biol.* **79**, 195–201 (1984). DOI: 10.1007/BF01871058
- Ohler B. *et al.* Role of lipid interactions in autoimmune demyelination. *Biochim. Biophys. Acta - Mol. Basis Dis.* **1688**, 10–17 (2004). DOI: 10.1016/j.bbdis.2003.10.001
- Boggs J. M. *et al.* Interaction forces and adhesion of supported myelin lipid bilayers modulated by myelin basic protein. *Proc. Natl. Acad. Sci.* **106**, 3154–3159 (2009). DOI: 10.1073/pnas.0813110106
- Shaharabani R. *et al.* Structural Transition in Myelin Membrane as Initiator of Multiple Sclerosis. *J. Am. Chem. Soc.* **138**, 12159–12165 (2016). DOI: 10.1021/jacs.6b04826
- Shaharabani R. *et al.* Pathological transitions in myelin membranes driven by environmental and multiple sclerosis conditions. *Proc. Natl. Acad. Sci.* **115**, 11156–11161 (2018). DOI: 10.1073/pnas.1804275115

### Funding acknowledgement:

The work was supported by the Israel Science Foundation (571/11 and 550/15), and the Sackler Institute for Biophysics and the Abramson Center for Medical Physics at Tel Aviv University. Travel grants to the synchrotron were provided by BioStruct-X.

### Corresponding authors:

Rona Shaharabani, Tel Aviv University, ronasa@tauex.tau.ac.il and Roy Beck, Tel Aviv University, roy@tauex.tau.ac.il

## Cancer cells hijack human body systems in order to spread

**Related publication:** Sakhnevych S. S., Yasinska I. M., Bratt A. M., Benlaouer O., Gonçalves Silva I., Hussain R., Siligardi G., Fiedler W., Wellbrock J., Gibbs B. F., Ushkaryov Y. A. & Sumbayev V. V. Cortisol facilitates the immune escape of human acute myeloid leukemia cells by inducing latrophilin 1 expression. *Cell. Mol. Immunol.* **15**, 994–997 (2018). DOI: 10.1038/s41423-018-0053-8

**Publication keywords:** Cancer; Leukaemia (blood/bone marrow cancer); Anti-tumour immunity; Immune escape

**A**cute myeloid leukaemia (AML) is a rapid and often fatal disease. The disease originates in the body's system for producing white blood cells, where diseased AML cells (in common with many other types of cancer) will interfere with healthy human cytotoxic lymphoid cells, the body's natural defence system against cancerous cells.

Understanding how cancer cells manipulate the various human body systems for survival, proliferation, and disease progression is crucial for developing immunotherapy treatments for cancer, which would allow the patient's own immune system to fight and cure the disease. In order to understand how cancer cells 'hijack' the body's processes, a team of researchers used Synchrotron Radiation Circular Dichroism (SRCD) spectroscopy on the Circular Dichroism beamline (B23) to study the interactions of the AML cell-specific receptor with its natural ligand, commonly present in the blood and surface of the endothelium. The AML cell-specific receptor determines the activity of one of the crucial immune evasion pathways operated by malignant cells, particularly AML cells.

The human steroid hormone cortisol is often referred to as the 'stress hormone', but it has a wide variety of roles in the body, including helping to control blood sugar levels, regulate metabolism, reduce inflammation, and assist with memory formulation. The researchers found that AML cells used cortisol to increase surface presence of latrophilin 1, a receptor that facilitates secretion of immune suppression factors.

Acute myeloid leukaemia (AML) is a blood/bone marrow cancer which originates from human myeloid cell precursors, and rapidly develops into a systemic disease. AML cells can interact with cytotoxic immune cells of lymphoid lineage, such as natural killer (NK) cells and cytotoxic T cells (CTCs). AML cells can interact permanently with NK and CTC cells, thereby impairing the anti-cancer activity of these crucial immune cells. Unlike many other types of cancer cells, AML cells can promote anti-cancer activity not only during direct interaction with NK cells/CTCs, but also indirectly, by secreting immunosuppressive proteins like galectin-9, and its receptor and possible trafficker Tim-3 (T cell immunoglobulin and mucin domain containing protein 3). This pathway finally leads to impairing anti-cancer activity of NK cells, killing of CTCs, and even downregulation of their biochemical activation<sup>1</sup>. Our recent studies have shown that AML cells express a cell surface protein called latrophilin 1 (LPHN1), which is normally found in neurons, and also in haematopoietic stem cells (HSCs)<sup>1,2</sup>. LPHN1 expression is repressed during HSC maturation, unless they undergo malignant transformation and become AML cells.

We found that cortisol, a small molecular weight steroid hormone (Fig. 1) produced by the adrenal cortex, can upregulate expression of LPHN1 in AML cells<sup>3</sup>, producing a significant increase in LPHN1 protein levels. Interestingly, cortisol levels are significantly increased in the blood plasma of AML patients compared to healthy donors. Respectively, galectin-9 levels in the blood plasma of AML patients was dramatically high compared to healthy individuals.

Further investigation has demonstrated that the LPHN1 ligand, FLRT3, is present in human blood plasma. Interestingly, its molecular weight and levels were similar in the blood plasma of healthy donors and AML patients. This means that healthy blood contains the LPHN1 ligand, which may be used for other, unidentified purposes. We studied the interaction of LPHN1 and FLRT3 using SRCD spectroscopy, and characterised LPHN1 conformational changes

with its high-affinity binding partners. This determined the next experimental set-ups, which led to investigation/confirmation of FLRT3-LPHN1 interactions in tissue culture and *ex vivo* systems.

Obtained results allowed us to confirm the hypothesis that human AML cells do not repress the expression of LPHN1. In order to keep LPHN1 levels high, AML cells must recruit cortisol. Cortisol is one of the master regulators of carbohydrate metabolism in the human body that will increase blood plasma glucose levels under stress.

The interaction of LPHN1 with FLRT3 contributes to the capability of AML cells to recruit complex body systems to 'work for' cancer progression. Our results have shown that cortisol upregulates LPHN1 expression, leading to more receptors available in the AML cells. The increased receptors correlates with decreased blood plasma glucose levels since malignant cells, normally lacking oxygen, become more dependent on glycolysis. Also, increasing the number of white blood cells decreases the number of red blood cells, making use of cytosolic degradation of glucose for obtaining energy more systemic. These alterations result in increased cellular glucose uptake. This normally leads to upregulation of secretion of the corticotropin-releasing hormone (CTRH) by the hypothalamus<sup>4</sup>. CTRH induces production and secretion of the adrenocorticotropic hormone (ACTH) by the pituitary gland<sup>4</sup>. ACTH upregulates cortisol biosynthesis and secretion of cortisol by the adrenal cortex. Cortisol is then used by AML cells for the purpose of upregulation of LPHN1 expression on the genomic level. Importantly, in healthy human white blood cells, and other cell types, cortisol is unable to induce LPHN1 expression, possibly because of gene repression. Interaction of AML cell-associated LPHN1 with blood plasma-based or endothelial FLRT3 facilitates the secretion of galectin-9 and Tim-3. The latter protects AML cells against immune attack, which could otherwise be performed by NK cells as well as cytotoxic T cells. The concept of such a recruitment of human body systems by AML cells is summarised in Fig 1.

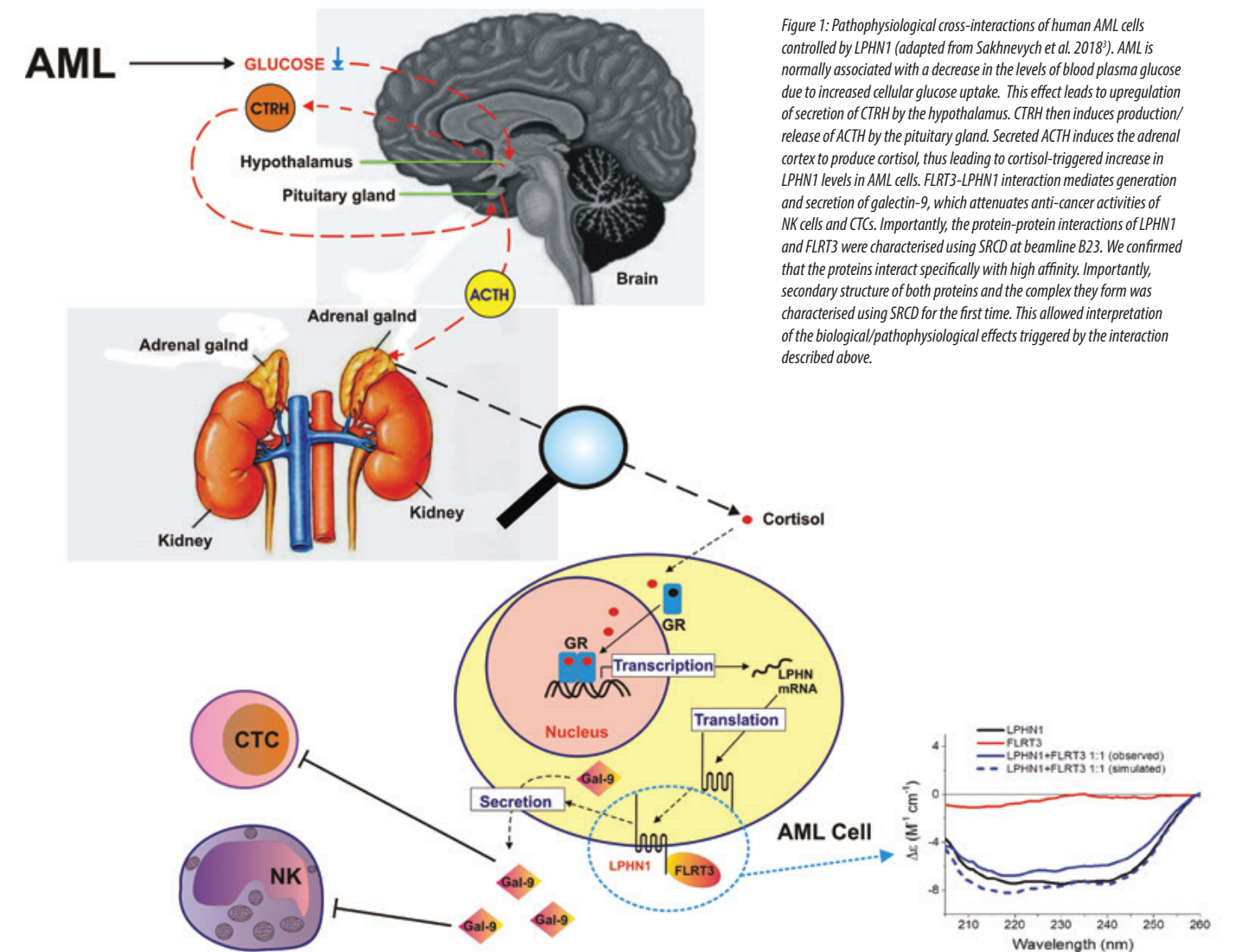


**Figure 1:** Pathophysiological cross-interactions of human AML cells controlled by LPHN1 (adapted from Sakhnevych et al. 2018<sup>3</sup>). AML is normally associated with a decrease in the levels of blood plasma glucose due to increased cellular glucose uptake. This effect leads to upregulation of secretion of CTRH by the hypothalamus. CTRH then induces production/release of ACTH by the pituitary gland. Secreted ACTH induces the adrenal cortex to produce cortisol, thus leading to cortisol-triggered increase in LPHN1 levels in AML cells. FLRT3-LPHN1 interaction mediates generation and secretion of galectin-9, which attenuates anti-cancer activities of NK cells and CTCs. Importantly, the protein-protein interactions of LPHN1 and FLRT3 were characterised using SRCD at beamline B23. We confirmed that the proteins interact specifically with high affinity. Importantly, secondary structure of both proteins and the complex they form was characterised using SRCD for the first time. This allowed interpretation of the biological/pathophysiological effects triggered by the interaction described above.

### References:

- Gonçalves Silva I. et al. The Tim-3-galectin-9 Secretory Pathway is Involved in the Immune Escape of Human Acute Myeloid Leukemia Cells. *EBioMedicine* **22**, 44–57 (2017). DOI: 10.1016/j.ebiom.2017.07.018
- Sumbayev V.V. et al. Expression of functional neuronal receptor latrophilin 1 in human acute myeloid leukaemia cells. *Oncotarget* **7**: 45575–45583 (2016). DOI: 10.18632/oncotarget.10039
- Sakhnevych S. S. et al. Cortisol facilitates the immune escape of human acute myeloid leukemia cells by inducing latrophilin 1 expression. *Cell. Mol. Immunol.* **15**, 994–997 (2018). DOI: 10.1038/s41423-018-0053-8
- Tabata I. et al. Effect of low blood glucose on plasma CRF, ACTH, and cortisol during prolonged physical exercise. *J. Appl. Physiol.* **71**, 1807–1812 (2017). DOI: 10.1152/jappl.1991.71.5.1807

### Funding acknowledgement:

This work was supported by a Daphne Jackson Trust postdoctoral fellowship (to IMY), University of Kent Faculty of Sciences Research Fund (to VVS).

### Corresponding authors:

Dr Vadim Sumbayev, University of Kent, v.sumbayev@kent.ac.uk and Dr Rohanah Hussain, Diamond Light Source, rohanah.hussain@diamond.ac.uk

## Phase III Overview

**With 32 beamlines in operation (including those in optimisation and commissioning modes), the end of the 2018/19 Financial Year saw the close of the third phase of construction at Diamond. A 33<sup>rd</sup> beamline, DIAD, is scheduled to begin initial operations in 2020. An overview of the activities and progress of DIAD and the final Phase III beamlines is outlined below.**

Beamline	PBS	Status	First User
I05 - Angle-Resolved PhotoEmission Spectroscopy (ARPES)	Cephise Cacho	Operational	2013
B21 - High Throughput SAXS	Nathan Cowieson	Operational	2013
I08 - Scanning X-ray Microscopy (SXM)	Burkhard Kaulich	Operational	2014
B24 - Cryo-TXM	Maria Harkiolaki	Optimisation	2015
I23 - Long-Wavelength Macromolecular Crystallography	Armin Wagner	Optimisation	2016
I15-1 - XPDF	Christine Beavers	Operational	2016
I02-2 - Versatile MX <i>in situ</i> (VMXi)	Dave Hall (acting)	Commissioning	2016
B07 - Versatile Soft X-ray (VERSOX)	Georg Held	Operational	2017
I14 - Hard X-ray Nanoprobe	Paul Quinn	Optimisation	2017
I21 - Inelastic Soft X-ray Scattering	Kejin Zhou	Optimisation	2017
I02-1 - Versatile MX micro (VMXm)	Gwyndaf Evans	Commissioning	2018
DIAD - Dual Imaging and Diffraction	Christina Reinhard (acting)	Construction	2020

### I05 - Angle-Resolved Photoemission Spectroscopy (ARPES)

I05 is a facility dedicated to the study of electronic structures by ARPES. This technique is applied to materials with exotic electronic ground states such as unconventional superconductors, solids exhibiting charge and spin density waves, excitonic insulators and non-Fermi liquids. Operational since 2014, the high-resolution branch has contributed to a number of research areas, including the discovery of Weyl semimetal behaviour in tantalum arsenide (TaAs), and studies of iron-based superconductors, such as iron selenide (FeSe). The Nano-ARPES branch is also now operational, enabling investigators to understand not only the electronic structure on a macroscopic scale, but also to establish the real space distribution of those states with sub-micrometre resolution.

### B21 - High Throughput Small-Angle X-ray Scattering (SAXS)

SAXS is used to study particles in solution on B21. SAXS provides a resolution-limited, structural snapshot of the sample and can be used to study slow processes, such as fibre formation. B21 underwent a major rebuild of its experimental hutch, installing the 'module 8' camera. In the new, windowless design the X-rays are no longer impeded by window materials and the beamstop is now positioned within a couple of millimetres of the detector face. In addition, the new detector provides pixels that are ~half the size of the old detector, nearly doubling the information in a SAXS measurement. The plan for B21 in 2019 is to pursue a new mirror mechanism to improve the focus, provide a high band-pass, 'pink beam' and an entirely windowless path for the X-ray beam from monochromator to sample.

### I08 - Scanning X-ray Microscopy (SXM)

I08 is used for morphological, elemental and chemical speciation on a broad

range of organic-inorganic interactions in a 250-4400 eV photon energy range and sample investigations under ambient or cryogenic conditions, which is unique for an SXM facility. The main activity on I08 over the past year has been designing, constructing and testing various aspects of a new soft X-ray spectro- and tomo-ptychography branchline (J08). This new branchline is expected to be available for experiments in early 2020 and will provide spatial resolutions down to a few nm, providing a step change in imaging performance.

### B24 - Full Field Cryo-Transmission X-ray Microscope (Cryo-TXM)

B24 is a full field transmission microscope designed specifically to meet the rising demand for tomographic imaging of biological specimens under near physiological conditions. The technique bridges the resolution gap that exists between electron microscopy (EM) and conventional light microscopy and allows acquisition of tomographic data from both native and fluorescent-labelled samples. A full user programme was delivered from April 2018 at B24 and the interest from user groups continues to grow steadily. The X-ray microscope has benefitted from the incorporation and full commissioning of a 25 nm zone plate, which is currently available to users. The integration of a bespoke cryo fluorescence super resolution module is also in high demand and has been developed to offer both cryoStructured Illumination microscopy (cryoSIM) and dSTORM allowing data collection beyond the diffraction limit.

### I23 - Long-Wavelength Macromolecular Crystallography

I23 is a unique facility dedicated to directly solving the crystallographic phase problem from native proteins. It is the first macromolecular crystallography (MX) beamline internationally optimised for the long-wavelength region. I23 can access the absorption edges of calcium, potassium and chlorine allowing

unambiguous identification of the nature of these atoms even at low resolution. Over the next few years, we will be able to give further insight into binding of these important elements in biology, information which remains elusive in cryo-EM. In the coming months, significant improvements to the beamline will be made to facilitate user mode and, to optimise best use of time on I23, adaptors for the I23 sample holders have been developed that enable fast sample screening on beamline I03.

### I15-1 - X-ray Pair Distribution Function (XPDF)

The XPDF beamline is dedicated to producing high quality X-ray scattering data for Pair Distribution Function (PDF) analysis. Operational since 2017, I15-1 has illuminated samples from diverse fields, from Earth sciences to pharmaceuticals, as well as material science and chemistry. Ultimately, it provides data collection and analysis software to allow non-expert users to study the local structure of crystalline, amorphous solids, and liquids. In spring 2020, a sample-changing robot and an upgraded detector will be installed on the beamline. This upgrade will be a synergistic addition to the existing auto-processing infrastructure, and will allow users to collect better data with less manual intervention.

### I02-2 - Versatile MX *in situ* (VMXi)

VMXi is the first beamline of its kind solely dedicated to data collection directly from crystallisation experiments *in situ*. The beamline has the facility to store thousands of user crystallisation experiments and features an automated transfer between sample storage and the beamline, as well as highly automated data collection and analysis. Through 2018, significant upgrades have been made that enable VMXi to progress to a full user programme, with the beamline being the test bed for the first 2nd generation Eiger2 X detector (4M), which is capable of collecting data at very fast rates with extremely high count rates. A new sample viewing system, and improved alignment configuration, now enable accurate automatic collection of data sets from many 10s, if not 100s of crystals per hour. Early experiments with serial crystallography delivery methods have been trialled and will add a further strength to the beamline capabilities in the coming years.



The VMXi team on the beamline, from left to right: Juan Sanchez-Weatherby, James Sandy, Halina Mikolajek.

### B07 - Versatile Soft X-rays (VERSOX)

VERSOX gives users the ability to carry out studies of catalysts under gas-phase reaction conditions or investigations in atmospheric science and biology with samples under native conditions such as liquid environments. The beamline is in the process of installing a second branch, to enable high-throughput X-ray Photoelectron Spectroscopy (XPS) measurements on multiple samples, and Near-edge Extended X-ray Absorption Fine Structure (NEXAFS) spectroscopy in ambient-pressure environments up to several bar. Together with the Near

Ambient Pressure XPS/NEXAFS capabilities of the existing branch, the beamline will cover a wide range of non-vacuum sample environments for soft X-ray experiments. It thus provides excellent opportunities to study the electronic and structural properties of materials relevant to science areas, such as atmospheric chemistry, pharmaceuticals, catalysis, or cultural heritage, etc. Future development plans include expanding the sample environment capabilities to enable studies of solid-liquid interfaces and liquid surfaces.

### I14 - Hard X-ray Nanoprobe

At over 185m long I14 is a scanning probe beamline that uses X-ray fluorescence and diffraction techniques to determine the structure and composition of a wide range of materials. It offers a small beam of 60 – 200 nm for high resolution imaging, which allows for the possibility of studying micron scale samples, such as biological cells, in greater detail and also allows users to study the role of nanoparticles in a range of areas such as catalysis and the environment. I14 has entered its second year of operation and has developed and expanded its capabilities in X-ray fluorescence, diffraction and X-ray Absorption Near Edge Structure (XANES) mapping. The integration of the Excalibur detector on I14 now enables diffraction data to be acquired at sampling times down to 10 ms. For XANES mapping there have been a number of developments in automated drift correction to improve data quality. The beamline is still in its optimisation phase and new techniques and facilities such as ptychography are in development, and an increasing emphasis on *in situ* studies is driving a number of developments in this area.

### I21 - Inelastic Soft X-ray Scattering

I21 is a dedicated Resonant Inelastic Soft X-ray Scattering (RIXS) facility that produces highly monochromatised, focused and tunable (250-3000 eV) X-ray beams. It is suited to investigate the electronic, magnetic and lattice dynamics of samples, particularly those with magnetic and electronic interactions. I21 accepted first users in October 2017 and has been operating in optimisation mode with ~50% of available beamtime allocated to the user programme. Towards the end of 2018, the beamline spectrometer was transformed from a discrete-port setup to a continuous-rotation configuration allowing, amongst other things, studies of emergent phenomena throughout the Brillouin zone.

### I02-1 - Versatile MX micro (VMXm)

VMXm performs atomic structure determination for studies where large crystals are difficult to produce or suffer from weak diffraction. This is a common challenge for protein complexes and other flexible biological macromolecules. The smallest X-ray beam size measured to date on VMXm is currently 0.4 x 1.2 µm, and uniquely combines scanning electron microscopy with X-ray diffraction, to allow the smallest protein crystals to be aligned into the X-ray beam and small wedges of rotation data to be recorded. First user experiments were carried out on VMXm in October 2018. Further commissioning and optimisation will take place throughout 2019.

### DIAD - Dual Imaging and Diffraction

DIAD is based on an innovative X-ray optical concept to allow the study of *in situ* processes with both imaging and diffraction simultaneously, enabling the user to take measurements of a live process as it evolves. The beamline has completed construction of the Optics Hutch and took first light in December 2018. Next to a standard tomography setup, a mechanical test-rig for diffraction and tomography will be one of the main instruments to allow *in situ* experiments for a variety of scientific disciplines such as engineering and materials science, biomaterials and hard tissues, geology and mineralogy, and soil plant interactions. The commissioning activities and construction of the experimental end station are ongoing with first users expected in early-mid 2020.

## Integrated Facilities and Collaborations

**D**iamond Light Source is uniquely placed; with a large number of scientific collaborations and integrated facilities on site, Diamond is a powerful resource for advancing research and allowing for growth. These complementary assets continue to allow us to be a leading facility enabling inter- and multi-disciplinary research.

Our collaborations have gone from strength to strength, growing and expanding their remit over the last few years, with 2018 being no exception. With new funding and the evolution of research partnerships, our collaborations have powered world-changing projects this year across many disciplines.

Diamond's integrated facilities have continued to expand and improve, allowing more in-depth and longer-term research to take place, truly taking advantage of the expertise here on campus. The official launch of eBIC, with Nobel Prize winner Richard Henderson, was a real demonstration of the excitement in the scientific community around Diamond's complementary facilities.

### Integrated Facilities

#### The electron Bio-Imaging Centre (eBIC)

eBIC is the first high-end cryo-electron microscopy (cryo-EM) facility worldwide to be embedded in a synchrotron, and its user operations mirror the well-established synchrotron beamline model. eBIC was established following the initial award of a £15.6 million grant from the Wellcome Trust, the Medical Research Council (MRC), and the Biotechnology and Biological Sciences Research Council (BBSRC). After successful review by the Scientific Advisory Committee (SAC) in 2018, eBIC is now fully integrated into Diamond's core programme. The partnerships, and the unique location of eBIC at Diamond, enable scientists to combine their techniques with many of the other cutting-edge approaches that the synchrotron offers.

eBIC provides scientists with state-of-the-art experimental equipment and expertise in the field of cryo-EM, for both single particle analysis and cryo-electron tomography. For the academic user programme, eBIC houses four Titan Krios microscopes, a Talos Arctica, and a Scios cryo-FIB/SEM. In addition, a partnership with the University of Oxford allows users to access a Krios in high-containment located at Oxford.

The last 12 months have marked several key developments for eBIC, including the official opening of the facility by Nobel Prize winner Dr Richard

Henderson, who won in 2017 for developing the cryo-EM technique. Dr Henderson noted that, "coupling [cryo-EM] techniques with the capabilities at Diamond creates a unique environment that will help keep the UK at the forefront of world-leading science". The opening, held with Thermo Fisher Scientific, established eBIC as a 'one-stop shop' for structural biology, and one of the largest cryo-EM sites in the world.

The collaboration with Thermo Fisher further expands Diamond's cryo-EM offerings by providing two new dedicated microscopes and professional cryo-EM services designed exclusively for the pharmaceutical industry. New instruments have been installed, including a Thermo Scientific Glacios Cryo-EM and a Thermo Scientific Krios Cryo-EM at eBIC and the industrial programme is now underway.

eBIC also held a number of successful workshops over the last year, including the 'Cryo-EM Sample Preparation Workshop' in October 2018, which focussed on teaching new cryo-EM users how to prepare samples for imaging in a three-day, intensive hands-on course. This was supported by the electron microscopy facility at the Astbury Biostructure laboratory at the University of Leeds, the Institute of Structural and Molecular Biology at Birkbeck College, the Division of Structural Biology at the University of Oxford (STRUBI), MRC Laboratory of Molecular Biology, Thermo Fisher Scientific, Leica Biosystems, TTP Labtech, CryoSol-World, and Quorum Technologies.



The official opening of eBIC, September 2018. From left to right: Richard Henderson, MRC Laboratory of Molecular Biology, Dan Shine, Thermo Fisher Scientific, Andrew Harrison, Dave Stuart and Katie Cunnea, Diamond Light Source.



Researchers from the National Graphene Institute at the University of Manchester were the first users of ePSIC. From left to right: Lan Nguyen, Sarah Haigh and Aidan Rooney.

The Scios cryo-focused ion beam scanning electron microscope at eBIC also took its first users in October 2018. During this first commissioning allocation period (Oct 18 - Mar 19) the peer review panel chose three groups to work at eBIC on the Scios. Additionally, eBIC director Dr Peijun Zhang gave 15 presentations at international meetings, including the American Association for the Advancement of Science (AAAS) annual meeting, speaking with a panel of world-leading scientists on 'Infectious Disease; Pushing the Boundaries of Physiology', where she presented her work in interrogating HIV-1 on a new level.

To date, eBIC has produced 65 user publications, and held its first user meeting in April 2019 in Nottingham in collaboration with CCP-EM and their Spring Symposium.

#### The electron Physical Science Imaging Centre (ePSIC)

ePSIC at Diamond is a national centre for aberration-corrected transmission electron microscopy. Since its opening in 2017, researchers from around the world have brought their samples to ePSIC to image their atomic structure with sub-ångström resolution.

The two transmission electron microscopes which make up the centre, a JEOL ARM 200 and a JEOL GRAND ARM 300, were brought to Diamond through collaboration with Johnson Matthey and the University of Oxford respectively. In early 2019, Dr Chris Allen was appointed as Principal Electron Microscopist at ePSIC, having run the Oxford side of the collaboration for the previous three years.

The ARM 200 is a state-of-the-art probe-corrected analytical microscope capable of imaging, electron energy loss spectroscopy and X-ray spectroscopy at atomic resolution. It is aligned at accelerating voltages (incident electron beam energies) of 80 and 200 keV.

The ARM 300 is a dedicated imaging instrument aligned across a wide range of accelerating voltages (30 - 300 keV). This enables the experimental conditions to be carefully tailored to the specific sample being studied. The ARM300 is both probe- and imaging-corrected and has numerous detectors including a fast

direct electron detector, which can operate at up to 2000 fps. This detector is used for both fast movie acquisition when operating in broad-beam Transmission Electron Microscopy (TEM) mode and for the collection of large arrays of far-field diffraction patterns (4D-STEM) when operating in focused probe STEM mode. These combined capabilities have enabled ePSIC to become an international leader in cutting-edge material science electron microscopy and is a unique resource within the UK.

With *in situ* sample holders, users at ePSIC can perform variable temperature measurements from 100 to 1,600 K to directly image the atomic structure of materials during thermally driven transitions. This *in situ* capability will be expanded upon over the coming year with the arrival of a new holder, which will allow simultaneous temperature control and electrical biasing of the sample.

The state-of-the-art instrumentation available at ePSIC has attracted both established electron microscopists looking to develop new techniques and scientists with limited previous electron microscopy experience interested in understanding the atomic structure of their samples. The collaboration of the expert staff at ePSIC with this wide range of users is helping to bring cutting-edge microscopy techniques to the wider material science community.

#### The Membrane Protein Laboratory (MPL)

The MPL is a well-established, state-of-the-art facility that enables membrane protein research, and was established to assist researchers investigating proteins that are embedded in the membranes that coat thousands of cells in the body. It provides the tools, resources and know-how that allows scientists from around the world to visualise their protein of interest on the atomic scale.

In 2018, the facility moved into the Research Complex at Harwell (RcAH) to contribute to and take advantage of the Harwell Cell and Structural Biology Partnership. Dr Andrew Quigley, MPL Facilities Coordinator, notes: "With the RcAH located next to the synchrotron we will continue to maintain our close proximity to the beamlines, allowing MPL staff and users to collaborate closely with beamline staff to create a highly productive working environment."

Membrane proteins make up about a third of the human genome, in fact, we have over 7,000 membrane proteins in our bodies, of which many are important drug targets with over half of current commercially available small-molecule drugs targeting membrane proteins. Understanding the structure of these is essential for helping scientists to understand how they work, any associated disease mechanisms, and in the development of new medicines. Dr Quigley continues: “We have traditionally grown membrane protein crystals, an extremely difficult step on the way towards solving a membrane proteins structure. Having a dedicated laboratory with cutting-edge equipment close to the experimental stations where membrane protein structures can be solved, greatly enhances scientists’ ability to successfully crystallise membrane proteins and further our understanding of these important drug targets. Recently with the cryo-EM revolution, a new method has been opened up providing an alternative route towards solving the structure of these difficult to work with proteins. Undoubtedly, the close proximity of the MPL and eBIC will greatly enhance our ability to understand the structures of membrane proteins by cryo-electron microscopy.”

The MPL is open to user applications from anywhere in the world, and proteins crystallised here have been used in experiments in other facilities. Two forthcoming papers will describe work supported by the MPL that has led to a series of successful X-ray Free Electron Laser (XFEL) data collection visits to SACLA-Japan by a team of scientists from the National Physical Laboratory (NPL), Diamond (I24 and XFEL teams) and collaborators from the University of Oxford (Department of Biochemistry).

Recently published work in *Nature Communications*<sup>1</sup> details a collaboration between a worldwide team of scientists and the MPL that has led to the structure of a Sodium coupled sialic acid symporter, an important energy source used by many pathogenic bacteria which has an additional role in helping bacteria to evade the immune response. Also, research published in the journal *Methods*<sup>2</sup> in collaboration with the MPL discussed various approaches, methods and techniques that can be used to support successful membrane protein crystallisation, and also reviews membrane protein serial crystallography, including data collection and management from multiple membrane protein crystals.

#### References:

1. Wahlgren W. Y. *et al.* Substrate-bound outward-open structure of a Na<sup>+</sup>-coupled sialic acid symporter reveals a new Na<sup>+</sup> site. *Nat. Commun.* **9**, 1753 (2018). DOI: 10.1038/s41467-018-04045-7
2. Birch J. *et al.* The fine art of integral membrane protein crystallisation. *Methods* **147**, 150–162 (2018). DOI: <https://doi.org/10.1016/j.ymeth.2018.05.014>

#### XChem

Diamond’s XChem facility specialises in X-ray structure-accelerated, synthesis-aligned fragment medicinal chemistry. Integrated into the I04-1 beamline and nearby Lab XChem, it offers a highly streamlined process for full X-ray screening experiments. XChem allows up to 1,000 compounds to be screened individually in less than a week (including 40 hours of unattended beamtime). The process covers soaking, harvesting automatic data collection, and data analysis.

This year has seen some exciting developments for the XChem facility. The team collected their 100,000<sup>th</sup> crystal in October 2018, only three and a half years since the inception of the XChem programme. Alongside this exciting milestone, the XChem computational team released the alpha version of their Fragalysis software; a web-interface tool which reviews XChem hits and generates the next follow up series.

Other developments this year included an expanded lab space and capacity, to meet the MX users’ higher demands on the facility, as well as increased XChem beamtime. A dedicated XChem support team has been put in place to assist with research. Additionally, XChem Block Access Group (BAG) access has been rolled out in the user programme, and the first XChem BAG user came during April 2019.

From Spring 2019, XChem users will be able to run even faster gridscreens and X-ray scans using new beamline electronic controls including the Zebra signal controls box, similar to Diamond’s other MX beamlines, further integrating XChem within the MX workflows. This is happening alongside continuous improvements to dataset delivery times; already these have increased from 18 to 22 datasets per hour in January 2019, and will see a further increase to around 30 datasets per hour in a new, fast, fully automated X-ray centring mode in the spring 2019 period.

#### XFEL Hub

Funded initially by the Wellcome Trust and the Biotechnology and Biological Research Council (BBSRC), the XFEL Hub at Diamond aims to provide expertise and support to the UK community engaged in XFEL-related research; from experimental conception to beamtime proposals, through sample preparations and testing, to XFEL data collection, analysis, and publication.

Now in its third year of activity (from October 2015), the XFEL Hub at Diamond underwent a comprehensive external international review, as well as a review by the Diamond Science Advisory Committee (SAC). The results of those reviews were very positive, which has stabilised the group within Diamond, and will allow the Hub to continue to provide travel assistance to the UK life scientists who are awarded XFEL beamtime around the world.

In addition to this, Principal Beamline Scientist for the XFEL Hub, Dr Allen M. Orville, received two five-year grants, which will help to further enable time-resolved structural biology research at storage ring beamlines like Diamond’s I24 and VMXi, XFELs, and with cryo-EM methods. In addition to these overarching goals, the Wellcome Investigator Award in Science will support up to four PDRA’s over the course of the grant, who will contribute toward research and development efforts in biophysics, serial MX, computational, and/or instrumentation. The Royal Society Wolfson Fellowship will provide for a four-year PhD studentship that will exploit synergistic sample delivery and manipulation method between XFEL and cryo-EM communities.

The XFEL Hub has achieved a number of exciting research successes<sup>1,2</sup>, and an in-depth story and podcast appeared in *Chemical & Engineering News*. As another example, during four 12-hour shifts in December 2018 at the Linac



Nadisha Gamage, Research Technician, working in the MPL.

Coherent Light Source (LCLS) / Macromolecular Femtosecond Crystallography (MX) Instrument, the XFEL Hub and its collaborators collected 54 datasets of correlated time-resolved serial femtosecond crystallography (tr-SFX) and time-resolved X-ray emission spectroscopy (tr-XES) from about 12 types of metalloenzymes. Producing diffraction data to better than 1.3 Å resolution and consuming less than 1 mg of enzyme per dataset, this was, to our knowledge, a record for productivity at the instrument. Additionally, the XFEL Hub and its contributors also received and executed two beamtimes at SACLA in February 2019, wherein they installed and used the acoustic tape drive system at SACLA for pump-probe tr-SFX, which also correlated with tr-XES. About 20 tr-SFX datasets were collected from three different phytochromes that exploited five different illumination schemes.

#### References:

1. Wiedorn M. O. *et al.* Megahertz serial crystallography. *Nat. Commun.* **9**, 4025 (2018). DOI: 10.1038/s41467-018-06156-7
2. Kern J. *et al.* Structures of the intermediates of Kok’s photosynthetic water oxidation clock. *Nature* **563**, 421–425 (2018). DOI: 10.1038/s41586-018-0681-2

#### Collaborations

##### University of Manchester at Harwell

The University of Manchester at Harwell is a unique structure for national laboratory science that provides a transformative resource for the university in Manchester and the facilities in Harwell. The collaboration has created a portal for university researchers to access world-class research that builds upon the longstanding relationship with Diamond and now also includes the facilities of the Science and Technology Facilities Council (STFC), including the ISIS neutron source and the Scientific Computing Department (SCD).

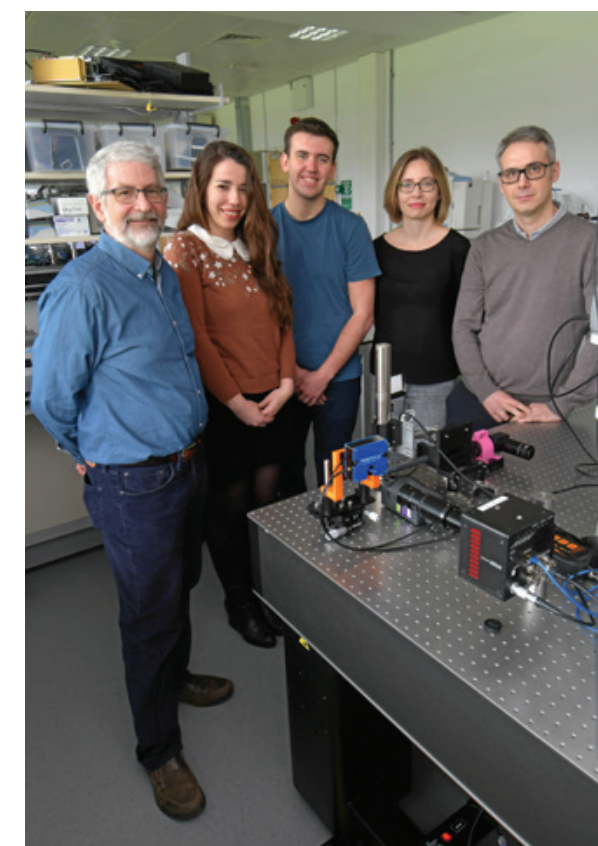
It has created a baseline structure to support and strengthen access for The University of Manchester and other university researchers. This is being extended across all central facility research in partnership with Diamond and STFC. There is also a cadre of Fellows based under this umbrella, at Harwell and in Manchester, to lead and develop themes within schools across the Faculty of Science and Engineering. They forge the link to Harwell and bring new users from the faculty to Diamond, stimulating research. Future collaborations with the Rosalind Franklin Institute (RFI), the Faraday Institution (FI) and the Ada Lovelace Centre (ALC), developing in parallel at Harwell, will place ten fellows within this year.

The University of Manchester at Harwell is a unique opportunity to bring new users to the synchrotron and advance strategically important research themes within a multidimensional science-space. Collaborators are excited to work with Diamond to exploit our world-class and expanding research tools to add to the resource base in national facilities science.

##### UK Catalysis Hub

Catalysis is a core area of contemporary science, engineering and technology that has substantial economic and societal impact, and is of significance to the UK’s Industrial Strategy, making it a strong area of focus for Diamond. The physical home of the UK Catalysis Hub – a national network with over 35 collaborating universities – is located next to Diamond at the Research Complex at Harwell (RCaH). It provides a platform for researchers to work collectively, and to gain frequent access to the synchrotron, alongside other facilities at Harwell.

The UK Catalysis Hub was established in 2013 with funding from the Engineering and Physical Sciences Research Council (EPSRC). An additional £14 million in funding from the EPSRC was committed in October 2018. The Hub seeks to coordinate, promote and advance the UK catalysis research portfolio.



The XFEL Hub team from left to right: Allen Orville, Anka Lucic, Bradley Davy, Agata Butryn, Pierre Aller.

The project has four new interrelated themes:

- Core
- Optimising, Predicting and Designing New Catalysts
- Catalysis at the Water Energy Nexus
- Catalysis for the Circular Economy and Sustainable Manufacturing

The Hub promotes a ‘whole system’ approach to the study of catalysis combined with high throughput, which allows optimal experiments to be carried out which shorten the path to development of commercially useful products and promote the UK catalysis effort and expertise on a global stage.

One of the main continued benefits of the Catalysis Hub is sustained access to a synchrotron radiation source. Professor Andrew Dent, Diamond’s Deputy Director of Physical Sciences, explains, “The UK Catalysis Hub has a Block Allocation Group (BAG) on the X-ray Absorption Spectroscopy (XAS) beamline B18 at Diamond. The Hub coordinates the experiments they perform in that time, which allows them to more effectively carry out their research.”

This access route increases the efficiency of data acquisition and allocates small amounts of time for proof of concept investigations and rapid access for *in situ* and *ex situ* applications before a full study starts. Applications are judged by a panel of expert academics and beamline scientists, who consider (i) the quality of the underpinning science, (ii) the likely success of the experiments, (iii) bringing in new users of synchrotron radiation, and (iv) coordinating time effectively to maximise efficiency. This opportunity is open to every academic working in catalysis in the UK.

Prof Dent concludes: “Diamond’s strong partnership with the Hub is emphasised with links to their Spring and Winter Conferences and its involvement in workshops that we have run exploring future research opportunities. We will continue to grow this great relationship, as it is helping to provide key science areas for opportunities such as the proposed Diamond-II upgrade.”

# Machine Operation and Development

Richard Walker, Technical Director

In 2018/19, our 12<sup>th</sup> year of operations, a total of 208 days (4,992 hours) were scheduled for beamline operations, 203 days of User Mode, and five beamline start-up days. The majority of the beam delivery was in standard multibunch mode (900 bunch train) or “hybrid” mode (686 bunch train + a single bunch) with total current of 300 mA. In addition, there was one day in May 2018 of “low-alpha” mode to produce short bunches (3.5 ps rms). All beamline operations were carried out in top-up mode.

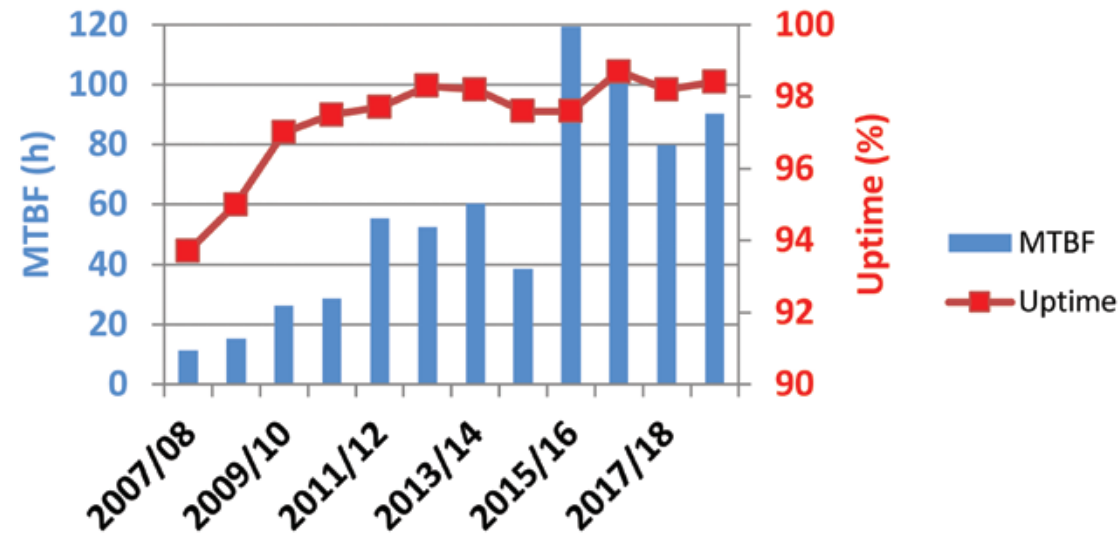


Figure 1: Mean Time Between Failures (MTBF) and Uptime by operating year.

The annual operating statistics are shown in Fig. 1. The Mean Time Between Failures (MTBF) for the year was 90.3 hours, an improvement over the previous year and our 4<sup>th</sup> successive year, exceeding the target minimum of 72 hours. The overall uptime (beam delivered as a percentage of scheduled hours) also remained high at 98.4%.



Figure 2: The girder with the 10-pole wiggler (the black object in the centre of the picture) in place of the “missing sextupole” installed in the storage ring. The wiggler is shown in its withdrawn position and was later moved over the vacuum vessel which can be seen behind the wiggler.

## 'Missing sextupole' scheme

The 'missing sextupole' scheme, described in last year's Review, involved the removal of one of the sextupole magnets in the storage ring to enable a

short 10-pole wiggler magnet to be installed as the radiation source for the Dual Imaging and Diffraction (DIAD) beamline. Following thorough testing of this mode of operation during Machine Development periods, by switching off the sextupole as well as all of its corrector functions, the machine was run permanently in that mode from April 2018 onwards. In the June 2018 shutdown, the relevant two girders were taken out of the machine and replaced with pre-assembled girders with the sextupole magnet removed and with the required new vacuum vessels. In the following August shutdown, the wiggler magnet was then installed (see Fig. 2). The new front-end was completed in the November shutdown which enabled “first light” to be achieved in the DIAD Optics Hutch in December.

## Radiofrequency (RF) upgrades

A number of upgrades of the RF systems, which provide power to the electron beam in the three accelerators, are underway, aimed at improving reliability and increasing resilience against failure.

In the linear accelerator (linac), procurement is underway of additional “SLED” cavities that will be added to the linac accelerating structures to boost the power, which will mean that if either of the two klystron RF power supplies fails, we will still be able to operate at the same linac energy of 100 MeV, and so preserve injection into the booster synchrotron.

In the booster synchrotron we have installed a second RF cavity and are in the process of installing a solid-state amplifier to power it. We will then have complete redundancy of the RF systems in the booster.

In the storage ring we have installed two normal conducting cavities of the EU higher-order mode damped design to provide a partial back-up in case of

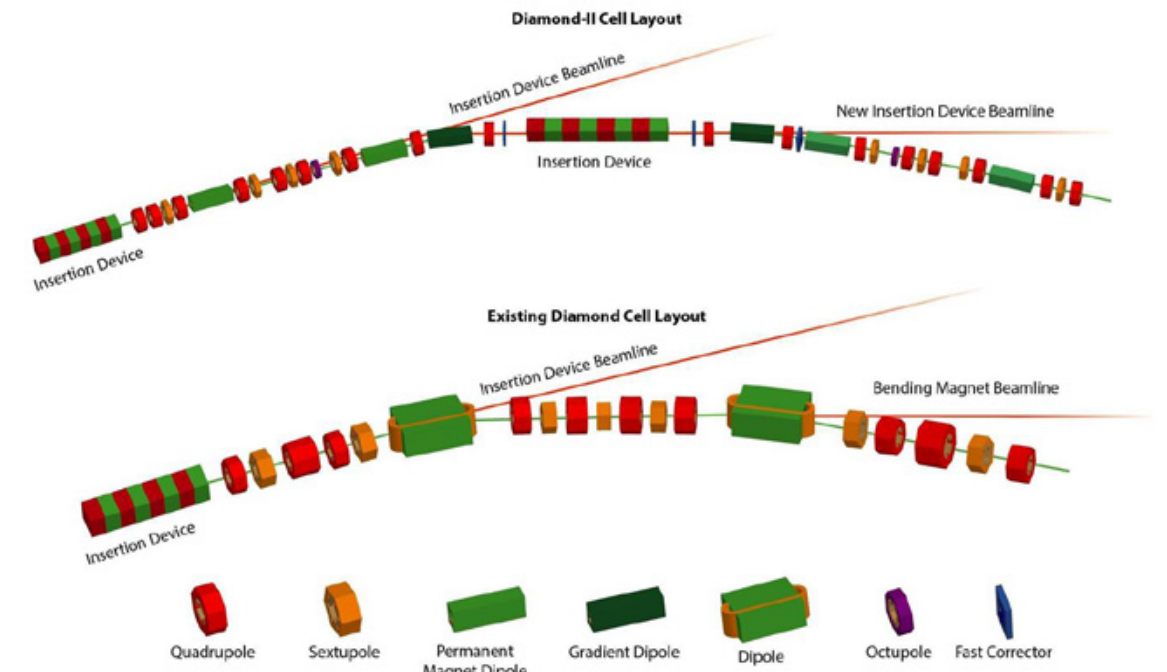


Figure 3: Layout of one cell of the existing ring (lower) and the proposed M-H6BA lattice for Diamond-II (upper).

failure of one of the two main superconducting cavities. One is operational and the second is currently being conditioned. A third cavity is being procured for installation in 2020 which will allow the ring to be operated, albeit at reduced current, even in the case of failure of both superconducting cavities or the cryoplat.

## Diamond-II

Studies for a possible upgrade to Diamond started in 2013, but were intensified during this year following the decision to produce a Conceptual Design Report (CDR) by the end of March 2019. Rather than pursue the lowest possible emittance, as other light source upgrades are targeting, the design of Diamond-II differs significantly in two ways: firstly, by the inclusion of additional “mid-straight”, which allow the creation of additional insertion device beamlines, and secondly by an increase in ring energy to 3.5 GeV, which despite increasing the emittance, results in significantly higher brightness in the medium and hard X-ray range. Fig. 3 shows a schematic layout of one cell of the proposed lattice, M-H6BA, a modified hybrid six bend achromat, compared to that of the current ring. The six bending magnets are clearly seen, as well as the additional insertion device, in the new mid-straight. This lattice produces an emittance of 160 pm at 3.5 GeV, a factor 20 lower than the current machine. Thanks to the increase in ring energy however the brightness increases by a factor of 70 at 25 keV.

## New synchrotron main air compressors

Compressed air plays an important part in the function of Diamond, being used throughout the facility, in the accelerator tunnels (e.g. vacuum valves), in beamlines (e.g. air pads), laboratories, external buildings, plant rooms, etc. The reliability and stability of the compressed air system is crucial for stable performance of the machine and beamlines – without it, there would be no beam.

As the existing fixed speed air compressors were showing their age and were not very energy efficient, a decision was taken in 2018 to replace these compressors with new 75 kW oil-free rotary screw variable speed air compressors (see Fig. 4). Each of the two new compressors can deliver a

maximum of 12.3 m<sup>3</sup>/minute of clean (oil free) compressed air at 7 Bar, at a much more stable pressure than previously and with an electrical consumption saving of £17k/yr.



Figure 4: One of the two new variable speed drive air compressors.

## Optics and Metrology Group

Kawal Sawhney, Optics and Metrology Group Leader

The Optics and Metrology Group continues to provide expert guidance that serves Diamond's diverse beamlines and other synchrotrons<sup>1-13</sup>. For Diamond-II, by simulating the effects of the source's increased brightness on the beamline optics, we are ensuring that the beamlines will receive the greatest possible benefit. In metrology, we are developing new *ex situ* capabilities in micro-stitching interferometry and continuously improving our current techniques. Moreover, we are strengthening our at-wavelength characterisation of optics by using X-ray speckle tracking, ptychography, and crystal topography. Our work on novel optics and detectors, described below, has already been applied successfully to Diamond's beamlines.

### Optics for variable beam sizes

VMXm is a new beamline at Diamond, which is designed to produce a variable size micro-focused beam for rapid data collection on large molecule biological samples in crystalline form such as proteins. The requirements for the focused beam at the sample are that the focused intensity should be high and the beam size should be switchable in a range of sizes from under 0.5  $\mu\text{m}$  to over 5  $\mu\text{m}$  on a time scale of less than one second to enable high-speed data collection and to minimise radiation damage of the samples. This required use of a high aperture double mirror system (Kirkpatrick-Baez) to focus the X-ray beam from the undulator source to the sample position.

The vertically focusing mirror was a novel design developed by the Optics Group to provide a variable focused beam size. The mirror has a basic elliptical shape with a glancing incidence angle of 3 mrad and provides a high demagnification to give sub-0.5  $\mu\text{m}$  focal spot. The mirror was, however, split into seven lanes, running the length of the mirror. The profile of the reflecting surface in each lane was a modification of the basic elliptical shape and calculated to generate a smooth symmetrical intensity distribution at the sample position, with full width at half maximum varying in sequence from 0.4  $\mu\text{m}$  (lane 1) to 8  $\mu\text{m}$  (lane 7). The change in beam size was achieved by translating the mirror to illuminate a different lane with the X-ray beam. Initial testing of the multilane mirror was carried out on the Diamond Test beamline (B16)<sup>6</sup>. Following first beam, the mirror was installed on the VMXm beamline and alignment was performed using wavefront sensing. The initial measurements showed a focused beam size of 0.41  $\mu\text{m}$  using lane 1 of the mirror and beam-sizes in sequence 0.97, 1.42, 2.5, 4.7, 6.7, 8.7  $\mu\text{m}$  for the remaining lanes (Fig. 1).

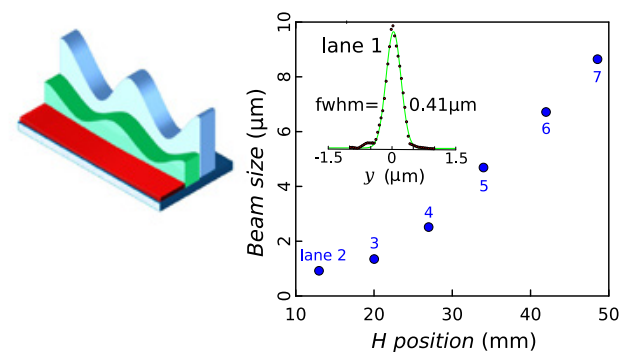


Figure 1: (Left) Schematic of the multilane mirror – the schematic shows only three lanes whereas the mirror installed on VMXm has seven lanes. (Right) Measured beam-size (fwhm) at sample position on VMXm beamline as the mirror is translated across lanes 2 to 7 and inset, the measured beam profile for mirror lane 1.

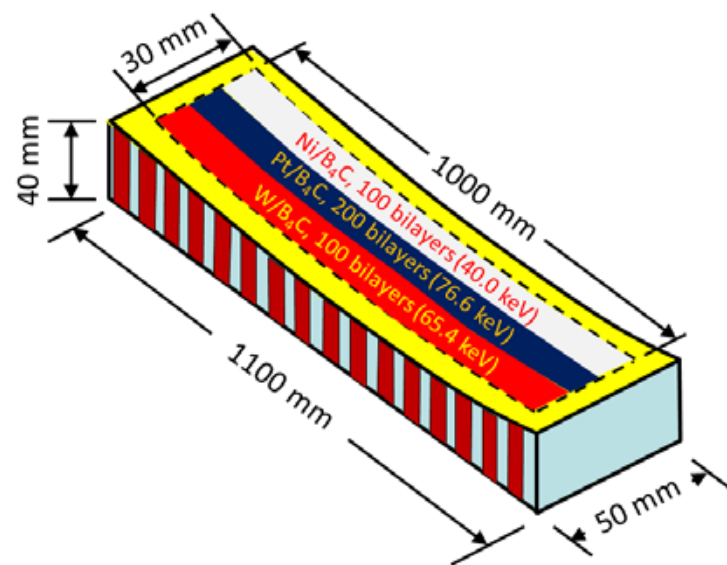


Figure 2: Schematic of the Diamond I15-1 multilayer-coated bimorph mirror.

### Multilayer-coated bimorph mirror for focusing high-energy X-rays

Diamond's X-ray Pair Distribution Function (XPDF) beamline I15-1 presented the Optics and Metrology Group with a unique challenge. A wiggler X-ray beam with a large cross-section (11.0 mm H  $\times$  4.4 mm V) and photon energy  $\geq 40$  keV had to be focused into a spot 680  $\mu\text{m}$  H  $\times$  20  $\mu\text{m}$ , or smaller, at a distance continuously variable over nearly 1 m. The energy selection and horizontal focusing are performed together by a set of three bent Laue crystals, one for each energy 40.0 keV, 65.4 keV and 76.6 keV. However, the tight vertical focus demanded a precisely deformable optic of large aperture that would introduce extremely low phase errors throughout its operating range of focal distances. Neither lenses nor conventional mirrors could fulfil these needs with the high-energy X-rays used on I15-1. Instead, a multilayer-coated bimorph mirror of 1 m active length (Fig. 2), the first on a synchrotron beamline, was installed. Three parallel, laterally graded, multilayer stripes were deposited: Ni/B<sub>2</sub>C for 40.0 keV, W/B<sub>2</sub>C for 65.4 keV and Pt/B<sub>2</sub>C for 76.6 keV. Each has a Bragg angle of 4.2 mrad, permitting a sufficient aperture. The bimorph has 16 actuators, allowing not only almost ideal elliptical shaping of the reflecting surface, but also correction of waviness and gravitational sag. Vertical focal sizes of 13  $\mu\text{m}$  FWHM (full width at half maximum) have been achieved and waviness has been reduced to 0.5  $\mu\text{m}$  rms (root-mean-square). The relative rms error of the multilayer spacing over the mirror length is below 0.17%. Peak reflectivity at all points exceeds 70%.

### White beam X-ray imaging system

The high flux of the white X-ray beam from third generation synchrotron light sources can significantly benefit the fast developing field of high-speed X-ray imaging, while the degradation of the scintillator screen due to high flux brings technical challenges to the existing X-ray imaging systems. To solve this issue, we have designed and established a novel white beam X-ray imaging system at beamline B16 by embedding the scintillator in a flowing inert-gas environment. The X-ray imaging system (Fig. 3) has demonstrated excellent performance under the exposure of white beam over days. The spatial resolution and field of view can be adjusted continuously by varying the positions of the lens and the camera using the motorised stages.

The new X-ray imaging system has been combined with a fly-scan tomography stage with a ZEBRA system. It enabled the data acquisition time for one tomography to decrease from hours down to less than 30 seconds by taking advantage of the intense white beam. The fast tomography setup has been routinely used at B16 for various applications such as biological tissues, functioning metals and geological samples. Recently, combined with the X-ray speckle imaging technique, we have employed the fast fly-scan tomography system for investigating Moon rocks recovered during the Apollo Missions. It has allowed us to swiftly and effectively collect 3D information of olivine inside the lunar rock in much more detail than ever before.

#### References:

- Sawhney K. *et al.* Development of pseudo-perfect x-ray optics using refractive compensators. *AIP Conf. Proc.* **2054**, 060003 (2019). DOI: 10.1063/1.5084634
- Alcock S.G. *et al.* Dynamic adaptive X-ray optics. Part I. Time-resolved optical metrology investigation of the bending behaviour of piezoelectric bimorph deformable X-ray mirrors. *J. Synchrotron Rad.* **26**, 36-44 (2019). DOI: 10.1107/S1600577518015965
- Alcock S.G. *et al.* Dynamic adaptive X-ray optics. Part II. High-speed piezoelectric bimorph deformable Kirkpatrick-Baez mirrors for rapid variation of the 2D size and shape of X-ray beams. *J. Synchrotron Rad.* **26**, 45-51 (2019). DOI: 10.1107/S1600577518015965
- Zhou T. *et al.* Optimized alignment of X-ray mirrors with an automated speckle-based metrology tool. *Rev. Sci. Instrum.* **90**, 021706 (2019). DOI: 10.1063/1.5057712
- Sutter J.P. *et al.* A novel, 1 m long multilayer-coated piezo deformable bimorph mirror for focusing high-energy X-rays. *AIP Conf. Proc.* **2054**, 030005 (2019). DOI: 10.1063/1.5084568

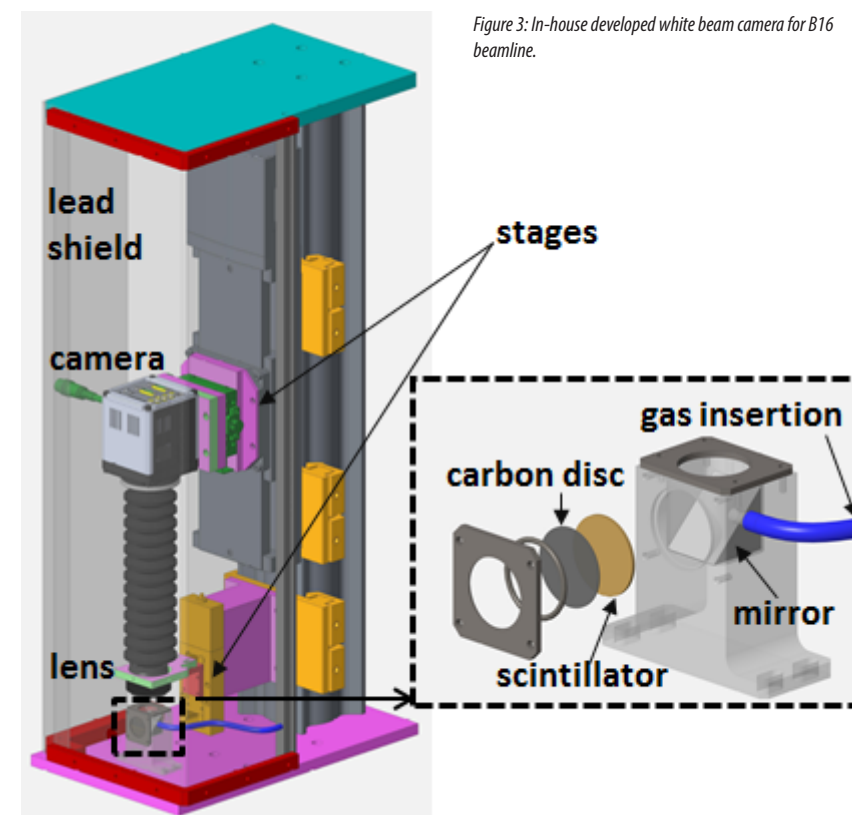


Figure 3: In-house developed white beam camera for B16 beamline.

- Laundy D. *et al.* Optical elements for dynamically broadening the focus of micro-focus optics at synchrotron x-ray sources. *AIP Conf. Proc.* **2054**, 060006 (2019). DOI: 10.1063/1.5084637
- Hand M. *et al.* Compensation of x-ray mirror distortion by cooling temperature control. *AIP Conf. Proc.* **2054**, 060044 (2019). DOI: 10.1063/1.5084675
- Sutter J.P. *et al.* Ideal Cartesian oval lens shape for refocusing an already convergent beam. *AIP Conf. Proc.* **2054**, 030007 (2019). DOI: 10.1063/1.5084570
- Alcock S.G. *et al.* High-speed adaptive optics using bimorph deformable x-ray mirrors. *Rev. Sci. Instrum.* **90**, 021712 (2019). DOI: 10.1063/1.5060737
- Wang H. *et al.* X-ray phase-contrast imaging with engineered porous materials over 50 keV. *J. Synchrotron Rad.* **25**, 1182-1188 (2018). DOI: 10.1107/S1600577518005623
- Zhou T. *et al.* Development of an X-ray imaging system to prevent scintillator degradation for white synchrotron radiation. *J. Synchrotron Rad.* **25**, 801-807 (2018). DOI: 10.1107/S1600577518003193
- Zhou T. *et al.* Auto-alignment of X-ray focusing mirrors with speckle-based at-wavelength metrology. *Optics Express* **26**, 26961-26970 (2018). DOI: 10.1364/OE.26.026961
- Zhou T. *et al.* Single-shot X-ray dark-field imaging with omnidirectional sensitivity using random-pattern wavefront modulator. *Appl. Phys. Lett.* **113**, 091102 (2018). DOI: 10.1063/1.5047400

## Detector Group

Nicola Tartoni, Detector Group Leader

The major achievements of the Detector Group in the past year were the consolidation of the Excalibur detectors<sup>1</sup>, which now run very reliably with the ODIN-DAQ framework<sup>2</sup>, the release of the Xspress4 pulse processor to the users of beamline I20<sup>3</sup>, the full characterisation of the second demonstrator of small pitch Ge detector, the conceptual design of the arc-detector for beamline I15-1, and substantial progress with the Tristan project.

The Tristan project can be considered the most innovative detector system that the Detector Group is currently developing. Tristan is based on the Timepix3 read-out ASIC which works in event driven mode (time stamp and location of an event sent out for any occurrence)<sup>4</sup>, rather than in frame based mode. The time stamping capabilities of Timepix3 make it, conceptually, a very good detector for time resolved experiments.

The first module of the Tristan detector was assembled, mounted in the appropriate frame to make up the so called Tristan1M. Following that, a first test was carried out at beamline I19 with the full infrastructure in place. One Tristan module is made up of 16 Timepix3 chips, organised in an 8x2 matrix, which are bonded to a monolithic silicon sensor. The total sensitive area is approximately 113.8 mm x 28.3 mm. The module mounted on the mechanical framework of Tristan1M is shown in Fig. 1.

The data from the 16 chips of one module are acquired and formatted by the FEMII card, which was developed by the Science and Technology Facilities Council (STFC) under the CfI programme, and which is used in the Xspress4 pulse processor, and in the Arc-detector for beamline I15, which is under development. The FEMII card sends the data to a Linux server through a 10 Gbit/s fibre optics link. The Linux server runs the ODIN-DAQ framework as data acquisition software and sends the data to storage through an Infiniband connection. The data are stored in HDF5 format.

When the first test of the Tristan1M was carried out at I19, all the data infrastructure was in place and was working correctly. The test consisted of recording the diffraction pattern from a crystal which was rotated 360° around its axis. Fig. 2 shows the image which is reconstructed from all recorded events during a complete revolution of the crystal around its axis. The data validation is in progress and we are preparing the next test that will consist of data from a dynamic experiment pump and probe experiment.

At the same time the development of the Tristan10M (10 modules in a 2x5 matrix for a total of 160 ASICs running in parallel) is in its final stage. After the production of the modules, the assembly of the full detector and final development of the software will follow.

Another important ongoing project is the development of an arc-detector for I15-1 based on CdTe sensors and Medipix3RX. The project is at the conceptual stage. Most of the concepts have been defined and we are starting the detailed design of some parts. The detector will consist of an array of monolithic CdTe sensors with a format of 256 x 768 pixels with 55 micron pitch. Each sensor is bonded to three Medipix3RX ASICs to make up a hybrid. Twenty-four hybrids are then arranged in an arc as shown in the sketch in Fig. 3. The 24 hybrids will cover 110°. The system will then drive 72 ASICs in parallel. Two FEMII cards will be the read-out electronics that will be located in a rack a few metres apart from the detector head. The data channel between the detector

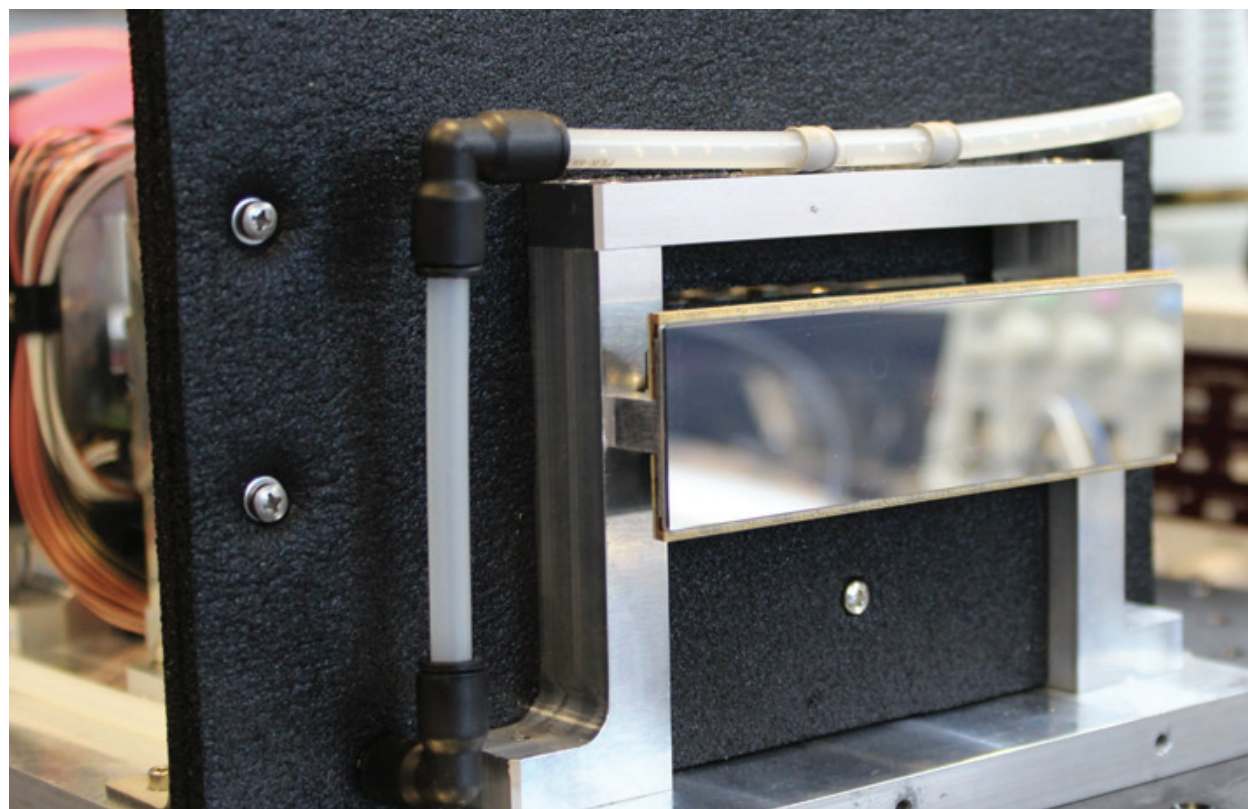


Figure 1: The 1 million pixels sensor module mounted on the Tristan1M framework, ready to be powered up for operations.

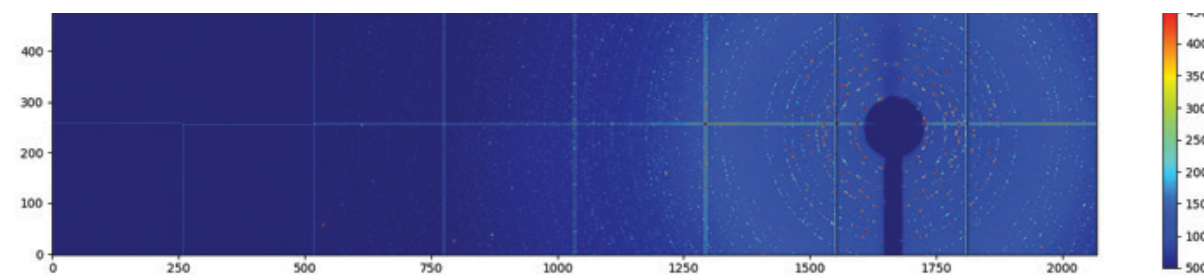


Figure 2: Reconstructed diffraction image of the events due to single crystal diffraction which are recorded by Tristan. The test was carried out at I19.

head and the FEMII cards will be made out of fibre optics links generated by a number of ancillary small FPGA cards located on the arc.

The Xspress4 pulse processor proved to be very successful as a read-out system of the 64-element Ge detector of I20 and very popular with the beamline users. Therefore, it was decided to build another system to read-out the 36-element Ge detector of B18 that uses the same technology and therefore expected to give the same improvement in performance.

The Xspress4 pulse processor was also used to read-out the 19-element Ge detector demonstrator currently under evaluation by the Detector Group. The Xspress4 proved to be effective also with this detector and enabled read-out in parallel to all the 19 channels, both in laboratory tests and in tests at the Test beamline B16. The cross-talk correction characteristics of Xspress4 worked effectively also with a detector using a different technology with respect to those in use at I20 and B18. This proved that the Xspress4 can be applied to a variety of detector systems. A patent granted to the Xspress4<sup>5</sup> recognises this concept as highly innovative.

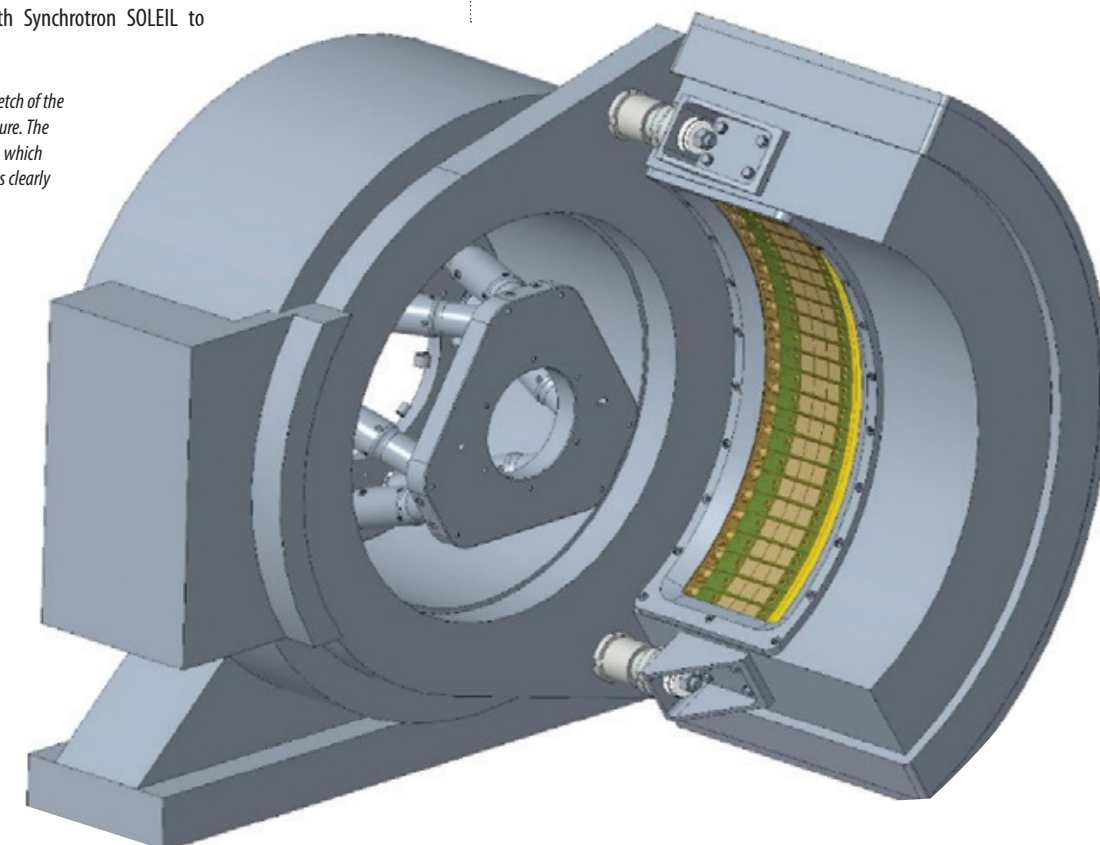
Further developments of the firmware of the pulse processor together with its time stamping capabilities, and the channel to channel communication capability, enabled it to reject the charge shared events of the demonstrator. In summary, this development proved that the Xspress4 can be used as a read-out platform for future multi-element Ge detectors, should Diamond wish to upgrade this technology. Currently we are pursuing a collaboration with Synchrotron SOLEIL to

further develop the demonstrator, and to develop higher segmentation Ge detectors for X-ray Absorption Fine Structure (XAFS) experiments.

### References:

1. Tartoni N. *et al.* Excalibur: A three million pixels photon counting area detector for coherent diffraction imaging based on the Medipix3 ASIC. *IEEE Nuclear Science Symposium Conference Record* 530–533 (2012). DOI: 10.1109/NSSMIC.2012.6551164
2. Yendell G. *et al.* Odin - a Control and Data Acquisition Framework for Excalibur 1M and 3M Detectors. *ICALEPS2017 Proceedings* (2018). DOI: 10.18429/JACoW-ICALEPCS2017-TUPHA212
3. Dennis G. *et al.* First results using the new DLS Xspress4 digital pulse processor with monolithic segmented HPGe detectors on XAS beamlines. *AIP Conference Proceedings* 2054, 060065 (2019). DOI: 10.1063/1.5084696
4. Yousef H. *et al.* Timepix3 as X-ray detector for time resolved synchrotron experiments. *Nucl. Instruments Methods Phys. Res. Sect. A Accel. Spectrometers, Detect. Assoc. Equip.* 845, 639–643 (2017). DOI: 10.1016/j.nima.2016.04.075
5. United States patent no. 10,168,438 B2.

Figure 3: Engineering sketch of the I15-1 arc detector structure. The layout of the 24 hybrids, which cover an angle of 110°, is clearly visible.



## Scientific Software, Controls and Computation

Mark Heron, Head of Scientific Software Controls and Computation

The past year brought a major organisational change within Diamond, with all Software and Computing groups brought together under one new management structure, to create the department for Scientific Software, Controls and Computation. This new department is structured as seven groups: Scientific Computing, Data Analysis, Data Acquisition, Beamline Controls, Accelerator Controls, Web Applications and Electronic Systems. This change recognises the importance of software, computing and control systems to the scientific output from Diamond; the up-and-coming challenges Diamond faces from Big Data as a consequence of the new detectors; and the need to develop the organisation to fully exploit the scientific opportunities of Big Data.

The new structure further positions Diamond well for the developments needed for software and computing in preparation for Diamond-II, which will produce data rates and data volumes far in excess of Diamond. Some initial considerations of the detectors in the Diamond-II era indicate raw data rates in Petabytes (PB) per hour as being credible. These data rates will make acquisition and analysis very challenging and require new solutions such as Machine Learning to be able to effectively analyse the data. At these data rates, the growth of data volumes will substantially exceed the increases in computing due to technological progress (Moore's law giving a doubling on computing power every two years), and so will require developments in the storage and compute resource available on-site and off-site.

To ensure that these challenges are met, a medium term strategy for Scientific Software Controls and Computation is now being developed. Following an external review in the summer of 2019, it will be presented to the Science Advisory Committee in the autumn.

The following are examples of some of the exciting developments across the broad range of science software and computing which are taking place within the Scientific Software, Controls and Computation department.

### Implementing the next generation of High Performance Computing (HPC) at Diamond

The increasing demands for data acquisition and subsequent data processing are driving Diamond to not only invest in new, additional, computational capacity on-premise, but to also explore the use of the cloud.

On 1<sup>st</sup> March 2019, the newly named Hamilton cluster, after the NASA scientist Margaret Hamilton, entered its production life and is now collecting data for the first time. A year long process of procurement and installation brings into service a new data centric HPC computing platform for the acquisition and analysis of scientific data. Doubling existing storage and compute capabilities on-premise to a total of approximately 16PB of storage,



Scientific Software, Controls and Computation (SSCC) Management Team, from left to right: Joe Handford, Simon Lay, Austen Rose, Mark Heron, Alun Ashton, Andrew Richards, and Ulrik Pedersen.



The new Hamilton cluster provided by Lenovo for data acquisition and data processing.

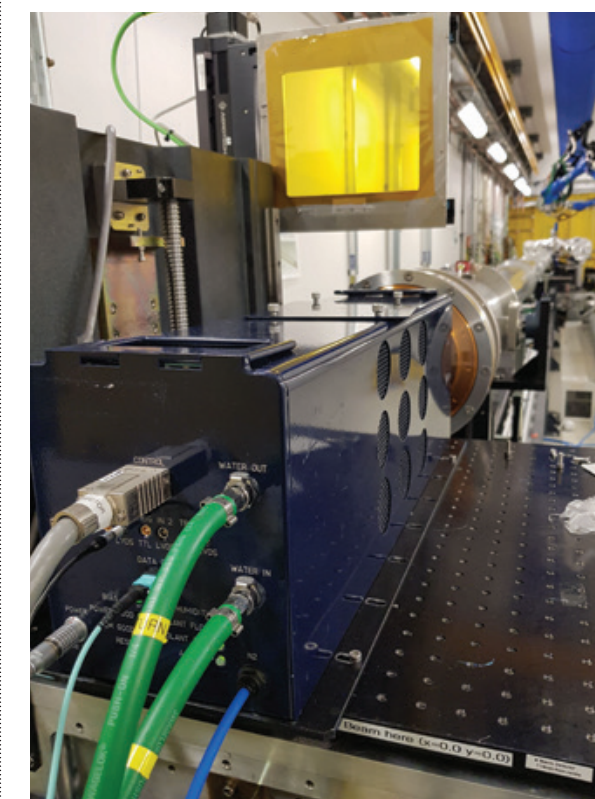
5,000 computing cores and 200 GPUs of compute power, this new system will enable researchers to keep up with the ever increasing data rates from new detectors and the increasing volumes of data for post-processing.

Although the new system is in place, the time taken to implement and deploy new systems, and the increasing demands for post-processing capability when users have returned home to their institutes, mean that Diamond is also beginning the move to using cloud based computational resources. Feasibility studies are already underway with major commercial cloud providers and locally as part of the Science and Technology Facilities Council (STFC) funded IRIS e-Infrastructure project. Using OpenStack technology, IRIS provides distributed compute and storage capabilities at STFC Rutherford Appleton Laboratories, and the universities of Cambridge and Manchester. In determining how best to provide post-processing services for users of Diamond, the Scientific Computing Team are developing proof of concept services in 2019 to leverage the growing opportunity that cloud computing presents and looking at how best to present to end users such cloud based data analysis services. The use of cloud techniques is introducing concepts into the on-premise infrastructure already, such as the use of containerisation (both Docker and Singularity) and looking at how future on-premise infrastructure may become more virtualised or abstracted from the end user. This will facilitate more transparent high performance computer hardware upgrades in the future and ensure Diamond can leverage new technologies emerging from various companies in the most efficient way, to sustain the increasing data rates from detectors across Diamond.

### Odin High Performance Detector readout

Odin is a software framework for Data Acquisition (DAQ) and Control of high-performance detector systems. It is the result of a close collaboration between STFC Technology Department and Diamond's Beamline Controls Group over several years. The software framework provides a highly scalable DAQ software pipeline to capture data from the latest and fastest new detectors, and is designed to cater for further developments in fast detectors. Easy integration and roll-out to beamlines is supported through the EPICS area Detector interface that most imaging detectors at Diamond use.

The Odin software has been deployed on beamlines I13 and I14 to control and capture data from the Excalibur 3M detectors to support Ptychography imaging experiments. This improved the maximum possible framerate from around 50 frames per second (fps) to over 100fps while also improving the overall reliability. On Macromolecular Crystallography beamlines, the Odin framework now supports readouts from three new Eiger detectors. The first two being Eiger 4M's on beamline B21 and VMXi and the third an Eiger2 16M on beamline I04.



Beamline I13 detector, with Odin readout.

The Odin software framework has been designed from the start to scale and grow as new detectors produce ever-increasing data rates. This is achieved by a parallel architecture which allows more nodes to be added to process the data streams in parallel. The next generation of detectors developed at Diamond all use Odin with development and testing phases already in place. These are Tristan a new large-angle time resolved detector based on the Timepix sensor; and Percival, a collaborative development of a Complementary Metal Oxide Semiconductor (CMOS) sensor, for low energy applications. In both cases, the Odin framework delivers continuous readout in multi-gigabytes of data per second.

## PandABox: Flexible triggering for continuous scanning

PandABox is a collaborative development project between Synchrotron SOLEIL and Diamond; with SOLEIL responsible for the hardware and Diamond for the firmware and software. It provides a highly flexible solution to enable new hardware synchronisation techniques in sample scanning. PandABox was a key component in speeding up scanning of samples delivered by the Mapping Project, improving scanning rates from 5Hz up to 300Hz on some beamlines. Some recent developments will enable 10kHz scanning to be delivered in areas like the Ptychography project.

PandA uses the latest system-on-chip Field Programmable Gate Array (FPGA) technology where a powerful FPGA fabric, Central Processing Unit (CPU) and peripherals are all functionally on the same chip. This is connected to a range of digital and analogue input/output (I/O), allowing connections to detectors, motion stages, diodes and Diamond's timing system. To provide ease of use it is configured via a web page that allows logic blocks to be rewired at run time to produce new applications without having to rebuild the firmware in the FPGA.

Diamond has worked with Quantum Detectors to commercialise PandA and so other institutes can benefit from the platform. To further aid this, the hardware, firmware and software are open source allowing external contributors to help make PandABox even better in the future.

## Adding mapping to generic data acquisition application

Diamond's Generic Data Acquisition (GDA) system, used on the majority of beamlines, is a Java based Client Server Application that provides beamline experiment orchestration, data collection and real-time data visualisation managed through a customisable Graphical User Interface and Python syntax scripting environment.



PandABox: Flexible triggering for continuous scanning.

In 2018 the Data Acquisition Group continued to develop a consolidated and streamlined scripting syntax to shield users from the differences between software and hardware controlled scanning. Simple software controlled scans and more complex hardware scans can now both be specified using an intuitive syntax. This enables users to seamlessly move from slower software scans to faster hardware scans, thereby enabling greater experiment capabilities through recording higher resolution data in the same or shorter periods of time. The range of available scan maps was further extended to include those appropriate to support new science areas such as Ptychography. Initial tests of the Ptychography technique using the new spiral path yielded an order of magnitude improvement in resolution.

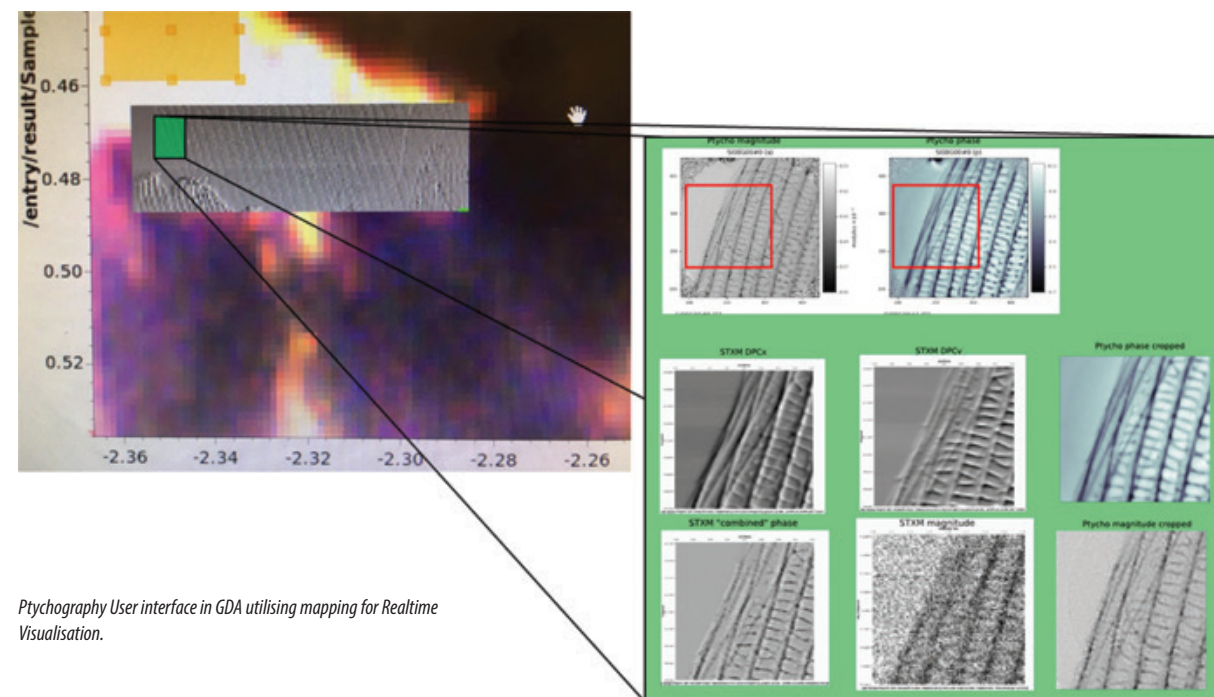
The consolidated scan syntax development work represents a first step in achieving one of the goals of the strategic roadmap for GDA, this being to insulate clients from the Server implementation providing a well-defined but extensible interface. In 2019 the team will be building on this initial work by adding a secure REST API and publish/subscribe message bus to the GDA server. Isolating clients from the GDA server implementation will make GDA a product that can be more easily adopted outside of Diamond and also facilitate the move to a web-based GDA Client. The message bus will make it easy to dynamically change the available auto-processing applications, and have per scan auto-processing queued with the scan request.

## Machine learning to accelerate our understanding of viruses

In order to study the life stage of viruses, scientists working in our state-of-the-art electron Bio-Imaging Centre (eBIC) have collected a three-dimensional snapshot of rheovirus particles replicating inside mammalian cells 12 hours post-infection. This data was acquired using Cryo-Electron Tomography, a technique in which a thin slice of frozen material is tilted through a range of angles in the microscope and a sequence of images are recorded. These images are then reconstructed into the 3D volume using computational techniques.

To extract useful information from this data, we have turned to a crowdsourcing model and called on people of all ages around the world to help speed up the analysis. This methodology not only allows us to find where the viruses are present in the cell and what life stage they are at, but it also engages the public with the science carried out at Diamond. In addition, these data annotations will prove valuable for training machine learning models. Once these models are trained, further data analysis and the resulting findings will be much quicker to achieve.

As part of this, we have teamed up with The Zooniverse ([www.zooniverse.org](http://www.zooniverse.org)), a platform that encourages and enables curious minds to contribute to scientific research projects. Our project entitled 'Science Scribbler: Virus



Ptychography User interface in GDA utilising mapping for Realtime Visualisation.

Factory' does not require any specialised training or expertise and is open to all ages. In the first task, Virus Picker, a randomly selected window of the data is presented to the citizen scientist and they simply have to click on any virus particles that they see in this image. The data is recorded in the Zooniverse database for us to download and analyse at a later date. To ensure the data is robust, each data window is shown to five annotators before being retired from the workflow. Thanks to the hard work of all the contributors, this stage is now complete.

The second task, Virus Classifier, takes the individual virus particles selected from the first workflow and presents them to the volunteer. The task of the citizen scientist in this scenario is to classify the virus into the correct life-

stage category according to information provided to them in a key that shows representative examples.

This is just the first of a number of projects that have been planned for hosting on The Zooniverse over the next three years and has been made possible through a collaboration with the Department of Structural Biology at the University of Oxford and by funding from the Wellcome Trust. Already, incredibly useful information on the location and life stage of every single virus particle in a host cell dataset is streaming in from all four corners of the globe. This will pave the way to more powerful data analysis pipelines and result in important scientific insights that will help us understand the infection and replication mechanisms of these pathogens.



Mark Basham, Senior Software Scientist, during the launch of 'Science Scribbler: Virus Factory'.

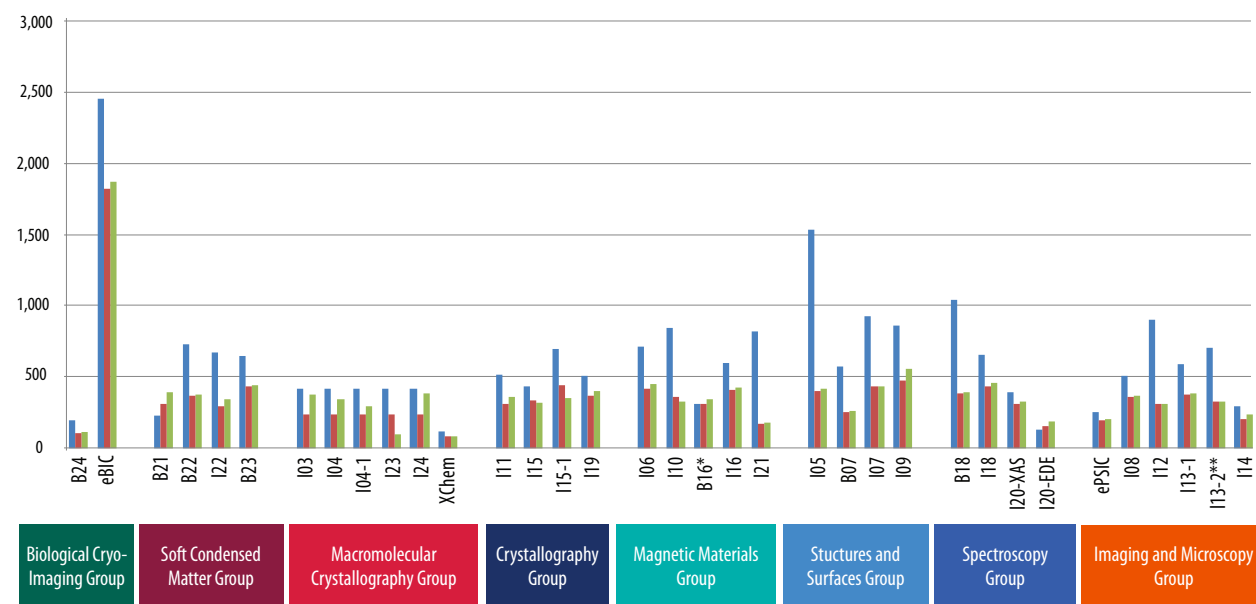
## Key Facts and Figures

### Facility usage

In our twelfth year of operations (1st April 2018 to 31st March 2019), we received 1,788 proposals for experiments on our instruments via peer reviewed access routes, requesting a total of 22,117 shifts. After peer review, 1,191 proposals were awarded beamtime. This resulted in 12,497 experimental shifts being awarded across 30 beamlines and eight electron microscopes. We welcomed 6,332 onsite user visits from academia across all instruments, with an additional 4,459 remote user visits.

In the past 12 months, Diamond has continued to review its reporting method on facility usage. Our new reporting tool is continuously being developed and improved and allows us to report more precisely and more consistently. As a result, some of the reporting criteria and results in this review have evolved compared to previous years.

### User shifts requested, awarded and delivered by group, beamline and electron microscope 2018/19

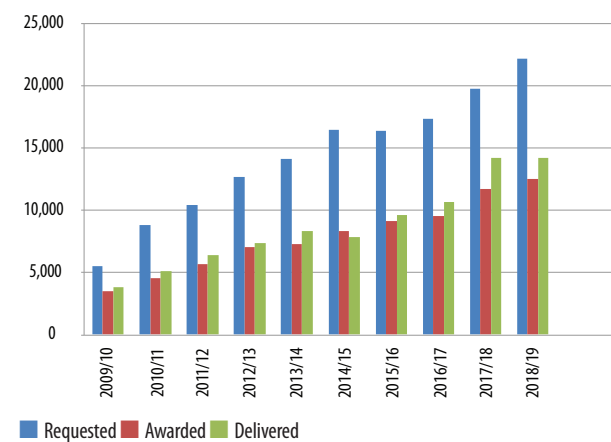


■ Requested ■ Awarded ■ Delivered

\* B16 is an optical testing beamline with only 50% of beamtime for users.

\*\* I13-2 Provides 35% of the available shifts to the Diamond Manchester Collaboration: these shifts are not included in this section.

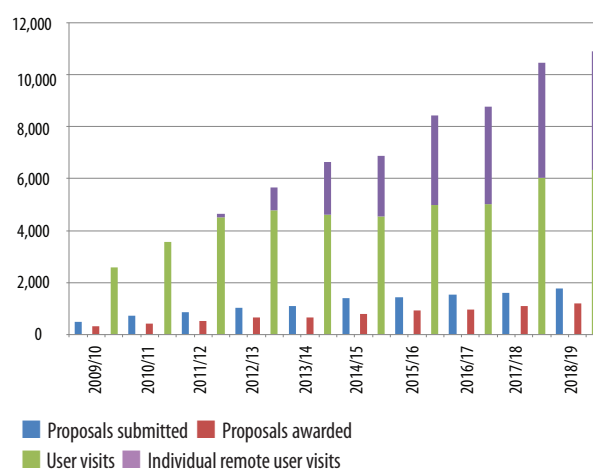
### Total user shifts requested, awarded and delivered



■ Requested ■ Awarded ■ Delivered

Various improvements have been made regarding the count of requested shifts for rapid access as well as regarding the count of requested shifts for proposals requesting more than one instrument.

### Total numbers of proposals and users per year

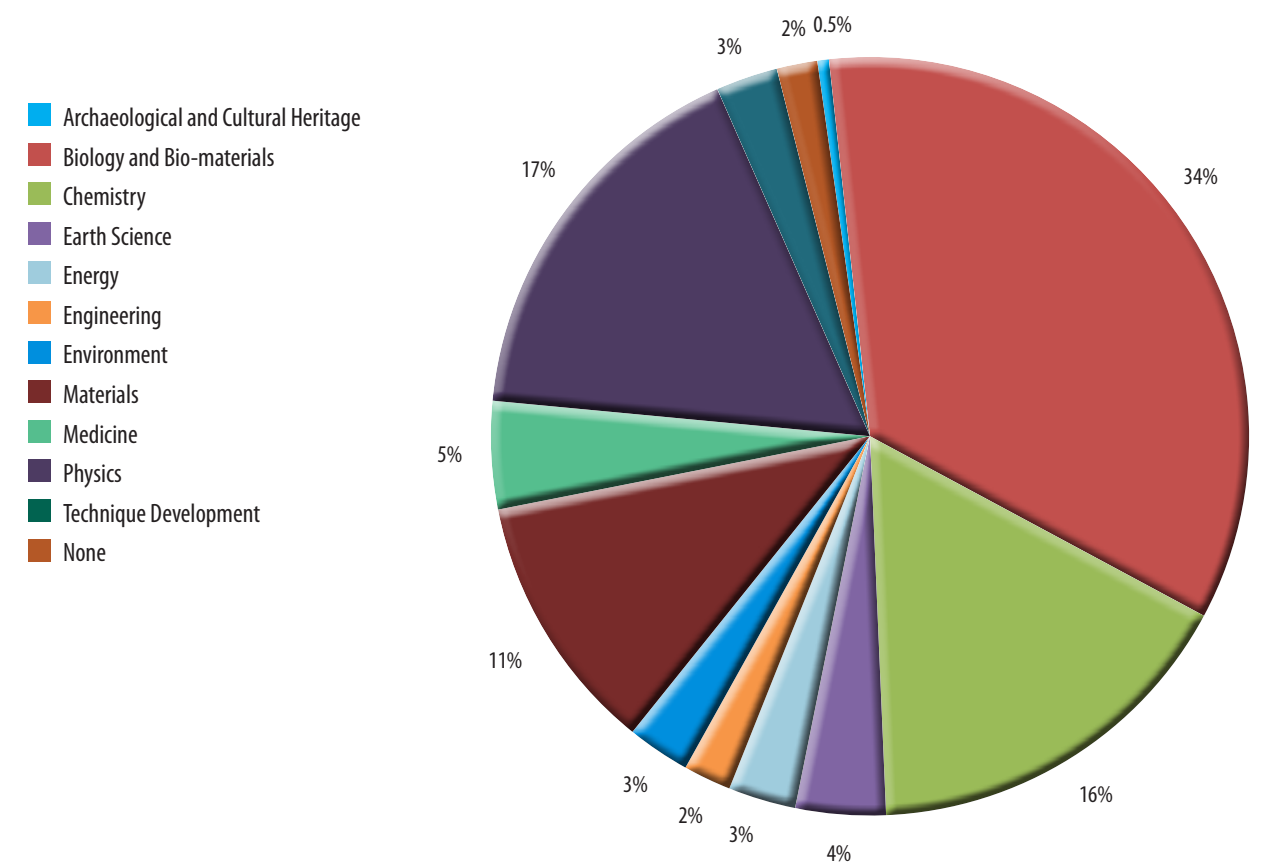


■ Proposals submitted ■ Proposals awarded  
■ User visits ■ Individual remote user visits

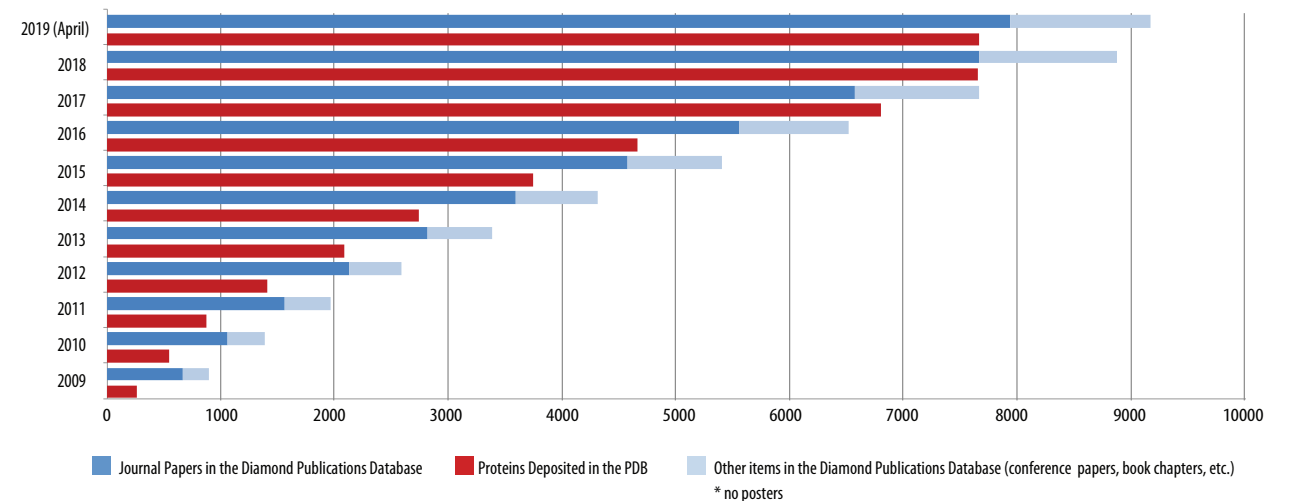
Members of staff visiting as part of peer reviewed access routes are now included in the count for user visits. In-house research is still excluded from this report.

## Proposals by discipline and research theme

### Experimental shifts scheduled by Diamond by main subject area for 2018/19



### Cumulative number of items in Diamond Publications Database by our scientists and users and cumulative number of protein structures solved



■ Journal Papers in the Diamond Publications Database ■ Proteins Deposited in the PDB ■ Other items in the Diamond Publications Database (conference papers, book chapters, etc.)

\* no posters

### Machine performance

	2009/10	2010/11	2011/12	2012/13	2013/14	2014/15	2015/16	2016/17	2017/18	2018/19
Total no. operational beamlines by end FY	17	19	20	22	24	25	26	28	31	32*
Scheduled hours of machine operation	5712	5808	6000	5832	5976	5808	5928	5688	6072	5904
Scheduled hours of user operation	4728	4728	5064	4872	5088	4944	5040	4584	5160	4992
Machine uptime %	97.0	97.5	97.7	98.3	98.2	97.6	97.6	98.7	98.2	98.4
Mean time between failures (hours)	26.2	28.5	55.4	52.4	60.3	38.6	119.4	103.1	79.9	90.3

\* Across all access routes.

## Industrial Liaison

Elizabeth Shotton, Head of Industrial Liaison

**The industrial user programme continues to flourish. Over the past year, we have seen record growth that has, in turn, led to expansion of both the team and the services available for our clients. Over 150 clients worldwide are making regular use of Diamond's facilities, and the team have been particularly industrious over the last year, supporting over 600 different experimental sessions, twice the number of the previous year.**

Our industrial users have diversified their use of the wide range of facilities available at Diamond. The majority of our clients continue to represent the life science sector, in particular structural biology; however, as research and development in this area grows increasingly complex, driven by diverse and challenging targets, a multi-technique approach can be helpful to gain understanding.

As Diamond matures, the expansion and development of expertise and complementary facilities have become increasingly important to both our academic and industrial users. The Industrial Liaison service offer for integrated structural biology provides a synergistic approach, where our clients can access both world leading technology and talent across Macromolecular Crystallography (MX), fragment based drug discovery, Small Angle X-ray Scattering (SAXS) and cryo-electron microscopy (cryo-EM) techniques. Co-location of these advanced characterisation facilities at Diamond, supported by expert staff, leads to rapid technique development, streamlined sample handling processes and increased opportunities for innovation in all fields.

Cryo-EM in particular is an area of growth, as the popularity of the technique as an alternative route to high resolution structural information from hard-to-crystallise systems is rapidly increasing, far outstripping the availability of high-end microscopes. Few structural biology groups in industry yet have access to their own instruments, and specialist expertise is needed to fully exploit the power of the technique. Access to Diamond's industrial cryo-EM service can therefore provide expert advice on experiment design, sample preparation, data collection and analysis; ideal for those starting out with cryo-EM or experienced users with complex problems to solve.

Perhaps our most significant collaboration of 2018 was entering into partnership with Thermo Fisher Scientific to provide two new dedicated microscopes for industrial use, based at Diamond. The new instruments installed at eBIC (electron BioImaging Centre) include a Thermo Scientific Glacios Cryo Transmission Electron Microscope (TEM) and a Thermo Scientific Krios G3i Cryo-TEM. Access to both a Glacios and a Krios at one location optimises productivity and time-to-result because of the designed-in connectivity between the two instruments. Scientists are able to first pre-screen samples on the Glacios to find the best quality samples before advancing to the higher resolution imaging on the Krios. These additional microscopes create further capacity for both industrial and academic cryo-EM experiments at Diamond. The partnership with Thermo Fisher has cemented eBIC's position as one of the largest and most advanced cryo-EM sites in the world, embedded in a hub of complementary advanced synchrotron based methods for advancing our understanding and treatment of viruses and diseases.

A key aspect of the partnership is the joint provision of the key expertise needed to exploit these resources fully, and offer professional cryo-EM services in sample preparation, cryo-EM screening and high-end data collection, designed exclusively for the pharmaceutical industry. The two new microscopes are staffed by dedicated industrial liaison scientists. Additional staff will join the team during 2019 to further enhance our service.

Fragment-based lead discovery is a drug discovery process that has revolutionised the pharmaceutical industry, providing valuable and cost-effective insights for rational drug design in the early stages. Rather than focusing on a few large complex compounds, it explores a larger part of the

existing chemical space from the drug targets of interest, providing new entry routes for the development of lead compounds. The unique XChem facility for X-ray structure-accelerated, synthesis-aligned fragment medicinal chemistry, established at Diamond in partnership with the Structural Genomics Consortium (SGC), provides a streamlined, secure and effective route to fragment screening.

Over the past few years, both academic and industrial user demand has soared and left us with insufficient capacity to meet the needs of our community, driving the need for expansion and growth. We gained funding to create an identical parallel facility dedicated for industrial client campaigns and we are delighted to report that over the last year the XChem for Industry facility has been commissioned and is fully operational. We now have a dedicated Industrial Liaison Scientist taking responsibility for XChem for Industry campaigns.

The co-location of the XChem for Industry laboratory and the I04-1 beamline significantly reduces the time to structural determination. The unique processes, tailored software and automated systems allow seamless data tracking from initial crystal cultivation through to data analysis. It is now possible to screen up to 700 compounds in a single day. On the 18<sup>th</sup> October 2018, the XChem facility on beamline I04-1 diffracted its 100,000<sup>th</sup> crystal dataset since inception in 2014, with data from an industrial client. This amazing achievement is even more remarkable in that 50,000 of those crystals were collected in a single year, highlighting the efficiency gains from optimisation of the facility.

While structural biology is a major part of the work of the Industrial Liaison Office (ILO), there has also been growth in the industrial use of the physical science beamlines over the past year. The team have been working with colleagues across the Science and Technology Facilities Council (STFC) in a major funding scheme helping UK based companies access high tech scientific facilities and knowledge to fast-track solutions to industrial challenges. The Bridging for Innovators (B4I) programme helps companies overcome product, manufacturing or process performance issues to accelerate productivity. Two companies have recently been awarded funding under the B4I scheme to use Diamond to help with their productivity challenges. The first company aims to use imaging and diffraction techniques to characterise battery materials and the second company will gain valuable insight from cryo-soft X-ray tomography to probe interactions of novel vaccines with cells. The B4I programme is open until 2021 so we look forward to collaborating with a wide range of companies to lower barriers to innovation throughout the scheme's lifetime.

Continuing the theme of collaboration, the ILO has supported a range of activities for Newton Fund partnerships with Indonesia and Thailand. The Newton Fund's aim is to develop a science and innovation partnership that promotes the economic development and welfare of collaborating countries. Indonesian visiting scientist Ferensa Oemry has joined the ILO for a year to gain experience of X-ray Absorption Spectroscopy (XAS) as part of the Newton Fund partnership with Indonesia and has participated in beamtime experiments.

In November 2018, Elizabeth Shotton, Head of Industrial Liaison, and Rachel Freeman, Industrial Liaison Marketing Manager, travelled to Thailand to deliver a training workshop at the Synchrotron Light Research Institute, Thailand. Paul Collier from Johnson Matthey provided a valuable industrial perspective to the workshop, which focused on developing marketing skills for industrial engagement with interactive sessions. The ILO team were impressed with the enthusiasm of their Thai counterparts in embracing the marketing activities wholeheartedly and perhaps a little surprised by the level of competitiveness exhibited by all teams in pursuit of the prize – a Diamond mug!



Ailsa Powell, Industrial Liaison Scientist, in the XChem for Industry lab.



Celebrating the Thermo Fisher Scientific agreement during the official launch of eBIC. Left to right: Dave Stuart, Diamond Light Source, Rishi Matadeen, Dan Shine and Raymond Schrijver, Thermo Fisher Scientific, Jason van Rooyen and Elizabeth Shotton, Diamond Light Source.

## Engaging with Diamond Light Source

Communications and Engagement Team

Over the past year Diamond has continued to engage in a range of activities, linking the wide variety of science and engineering at the facility with a diverse range of audiences. Our staff have reached many publics, helping to communicate the breadth of research and technology undertaken at Diamond, as well as supporting and learning from our users, and helping to train and develop the next generation.

In total over the past year, Diamond has welcomed **6,065** visitors to the facility, including; **1,456** for scientific and technical events, **635** undergraduate and postgraduate visitors, **3,176** school students and members of the public, and **779** VIPs and Stakeholders.

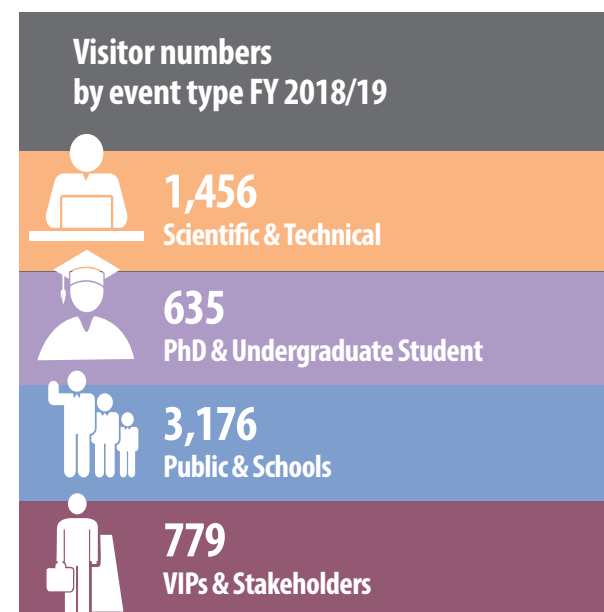
The majority of public visitors attend an event run as part of our core programme, many attending one of our increasingly popular Inside Diamond open days or regular community group visits, which give members of the public a chance to go inside the synchrotron as well as visiting one of our beamlines and engaging with our staff.

“Everyone was so welcoming, personable and keen to help.”

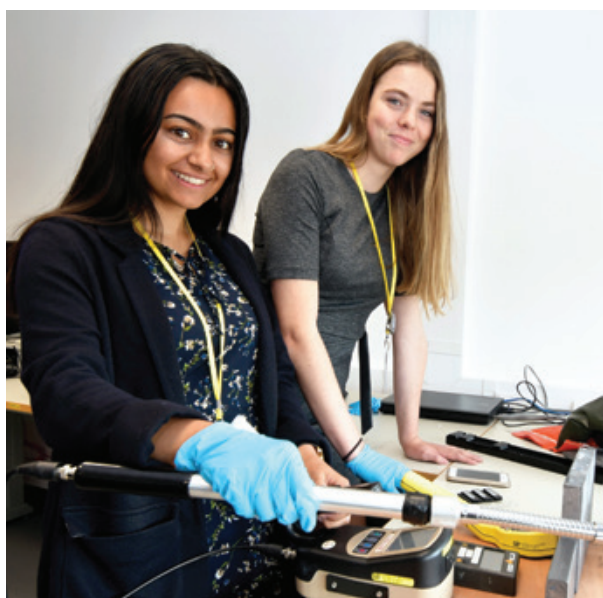
“A wonderful opportunity to see public engagement done really well.”

### visitors to recent Inside Diamond open days

For school/college level students we hosted a range of events for different ages and subjects. As well as hosting general schools open days, we ran more tailored events on areas including particle physics, computing, engineering and science. Diamond also continued to support a school level work experience programme, with 24 students being welcomed for a week of talks and activities based around a specific project to complete, and invited to give a talk on it at the end of the week. The projects were arranged and supported by staff in areas across the organisation.



Diamond continues to collaborate closely with the engagement teams at the Science and Technology Facilities Council (STFC) and across the rest of the campus, to offer visitors access to a wider range of events and experiences. The Particle Physics masterclass events for A-level students, and the Stargazing event for the general public, brought over 1,000 people onto the campus and gave the opportunity for staff across site to offer a wide range of hands-on activities to visitors. Away from site, Diamond continues to travel further afield to reach a geographically and culturally diverse range of audiences.



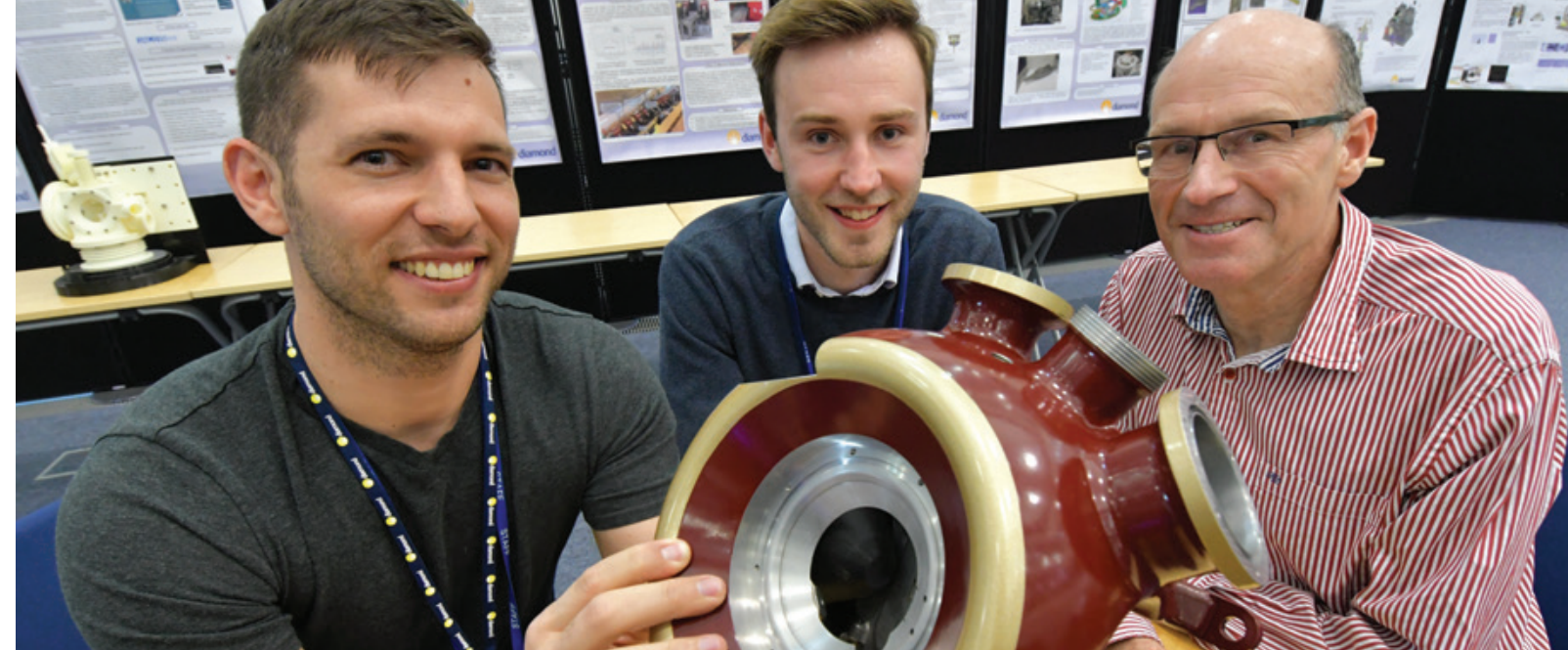
Students Miya Manzur and Eloise Thompson working in the Health Physics lab during Diamond's work experience week.

This year also saw the initial stages of an exciting project developing Diamond's first visible light beamline (VISR), which will offer fantastic opportunities to highlight experimental techniques and experiments to visitors. In summer 2019, we will be running an undergraduate project to develop this beamline and to maximise its usage, for both visitors and as a training tool.

### Higher Education engagement

Diamond is committed to training, encouraging and inspiring the next generation of scientists and engineers, and our links and support for higher education continue to offer students a range of opportunities to engage with and learn from world-leading staff and resources.

An additional 20 students started joint PhD studentships this year, while 17 completed their studies. Diamond currently supports 81 students altogether. These placements are co-funded with a range of universities and other world-leading research facilities, giving students access to a wide breadth of resources and expertise. The popularity of these programmes continues to increase; in 2018 we saw a 93% rise in proposals for new PhD projects, and in 2019 this went up by an additional 35%. Following the selection process, we look forward to an additional 19 students joining later in 2019.



Pablo Sanchez Navarro, Frankie Bailey and Stewart Scott look at a 3D printed prototype vacuum vessel, to be used on beamline VMXm, during the Early Career Engineering School.

Our undergraduate placements continue to be in high demand. In June 2018 we welcomed 14 undergraduates for the summer and another 10 to complete 12 month Year in Industry projects, in subject areas across the facility. 2019 has seen no let-up in demand for these placements and from the 843 applicants we look forward to welcoming 25 new undergraduate students in June.

The demand for student visits remains high and Diamond supported 22 visits from undergraduate and postgraduate groups, offering a range of access, talks and training.

### Scientific workshops and conferences

Diamond runs a broad portfolio of workshops, meetings and conferences tailored towards the needs of our staff and user community, with whom we continue to train, inform and learn from. In summer 2018, we ran

Date	Event	Participants
18 - 20 April 2018	Diagnos-F1069tics Experts of European LightSources (DEELS) & TW-DULER (Topical Workshop on Diagnostics for Low Emittance Rings)	34
25 April 2018	Visit from Institute of Physics conference	25
1 - 4 May 2018	INSTRUCT Model Building Icknield Workshop	25
15 - 16 May 2018	Diamond-II Coherence Workshop	40
4 - 5 June 2018	Small Angle Scattering Training School	47
13 June 2018	Visit from the Institution of Engineering and Technology (IET)	30
19 June 2018	Clever Characterisation for Smarter Formulations 3	60
25-26 June 2018	M4DE and Advanced Alloys CDTs	30
25 - 27 June 2018	RIXS/REXS workshop	81
16 - 19 July 2018	British Zeolite Association Annual Meeting	
16 August 2018	MRC-KHIDI UK-Korea Symposium	95
27 August - 1 September 2018	BCA Summer School	50
3 - 7 September 2018	SR2A - Synchrotron Radiation and Neutrons in Art & Archaeology	56
3 - 4 September 2018	Diamond-II - Crystallography	59
10 - 11 September 2018	Diamond-II - MX + Soft Condensed Matter	131

two biennial student workshops: the BCA-CCP4 (British Crystallographic Association-CCP4) Summer School and the SR (Synchrotron Radiation) School, which saw an intake of over 120 students combined. Both residential courses targeted postgraduate students and provided broad-based introductions to key synchrotron techniques, helping to prepare the next generation of synchrotron users. In the autumn we piloted a five-day Early Career Engineering School that aimed to provide 60 engineers from around the world with a basic grounding in a range of areas specific to working at a light source.

With the prospect of the Diamond-II upgrade on the horizon, we ran a series of scientific workshops in September 2018 to directly engage with our academic and industrial user communities in order to explore how Diamond-II could best support research and innovation. The numerous useful discussions were fed into the Diamond-II Science Case.

Date	Event	Participants
13 September 2018	Diamond-II - Magnetic Materials + Structures & Surfaces	78
16 - 21 September 2018	Synchrotron Radiation School	75
18 - 19 September 2018	Diamond-II - Biological Cryo-Imaging + Imaging & Microscopy + Spectroscopy	145
1 October 2018	Early Career Scientist Symposium	80
2 - 4 October 2018	Cryo-EM Sample Workshop	32
9 - 10 October 2018	I19 Remote Access Training	20
12 - 16 November 2018	Early Career Engineering School	60
2 - 8 December 2018	Diamond - CCP4 workshop	50
28 January 2019	Oxfordshire EPICS Meeting	20
29 January 2019	Aberration-corrected PEEM at Diamond	39
18 - 19 February 2019	CCPEM Relion Workshop	31
26 - 27 February 2019	Opportunities for high-pressure research at Diamond	75
27 - 28 February 2019	MX BAG Training	35
11 - 13 March 2019	XAS workshop	35
14 March 2019	STFC Coordinated Additive Manufacture programme meeting	23
14 - 15 March 2019	Hyperspy Workshop	25
25 - 26 March 2019	Imaging BioPro Workshop	60
27 - 28 March 2019	START launch event	60

## Governance and Management

**D**iamond Light Source Ltd was established in 2002 as a joint venture limited company funded by the UK Government via the Science and Technology Facilities Council (STFC), now under UK Research & Innovation (UKRI), and by the Wellcome Trust, owning 86% and 14% of the shares respectively. Diamond now employs almost 700 scientists, engineers, technicians and support staff from 39 countries worldwide. The Chief Executive and Directors are advised by committees representing key stakeholder groups, including the Science Advisory Committee (SAC), Diamond User Committee (DUC), and Diamond Industrial Science Committee (DISCo).

Diamond is free at the point of access for researchers accessing Diamond via peer review, and provided the results are published in the public domain for everyone's benefit. Allocation of beamtime is via a peer review process to select proposals on the basis of scientific merit and technical feasibility. Eight peer review panels meet twice a year to assess the proposals submitted for each six-month allocation period. Diamond also welcomes industrial researchers through a range of access modes including proprietary research.

### Board of Directors

#### Prof Sir Adrian Smith (Chairman)

Director, Alan Turing Institute

#### Prof Andrew Harrison

Chief Executive Officer, Diamond Light Source

#### Marshall Davies

Business Advisor, Science and Technology Facilities Council

#### Prof Michael Fitzpatrick

Pro-Vice-Chancellor, Coventry University

#### Prof Mark Thomson

Executive Chair, Science and Technology Facilities Council

#### Prof Mike Turner

Acting Director, Wellcome Trust Science Division

#### Andrea Ward

Director of Finance & Corporate Services, Diamond Light Source

#### Prof Keith Wilson

Professor of Chemistry, University of York

#### Company Secretary

Andrew Richards, Diamond Light Source

As at April 2019

### Executive



**Prof Andrew Harrison** took the helm as CEO of Diamond Light Source in January 2014. He was previously Director General of the Institut Laue-Langevin neutron source in Grenoble, France, where he had worked since 2006. With a background as an inorganic chemist and Professor of Solid State Chemistry at the University of Edinburgh, Prof Harrison brings a wealth of experience of scientific leadership to the organisation.



**Prof Laurent Chapon** joined Diamond as Director of Physical Sciences in 2016 from the Institut Laue-Langevin in Grenoble, France. Whilst there, Prof Chapon was Senior Fellow and Leader of the Diffraction Group for over five years. He is an expert in materials science as well as X-ray and neutron diffraction techniques. His principal interests include transmission metal oxides, frustrated oxides, and multiferroics.



**Prof David Stuart** is MRC Professor of Structural Biology at the University of Oxford, and Joint Head of the Division of Structural Biology at the Department of Clinical Medicine. He was appointed Director of Life Sciences at Diamond in 2008. His principal research interests include the structure of viruses and viral proteins as well as cellular proteins, especially those that interact with viruses.



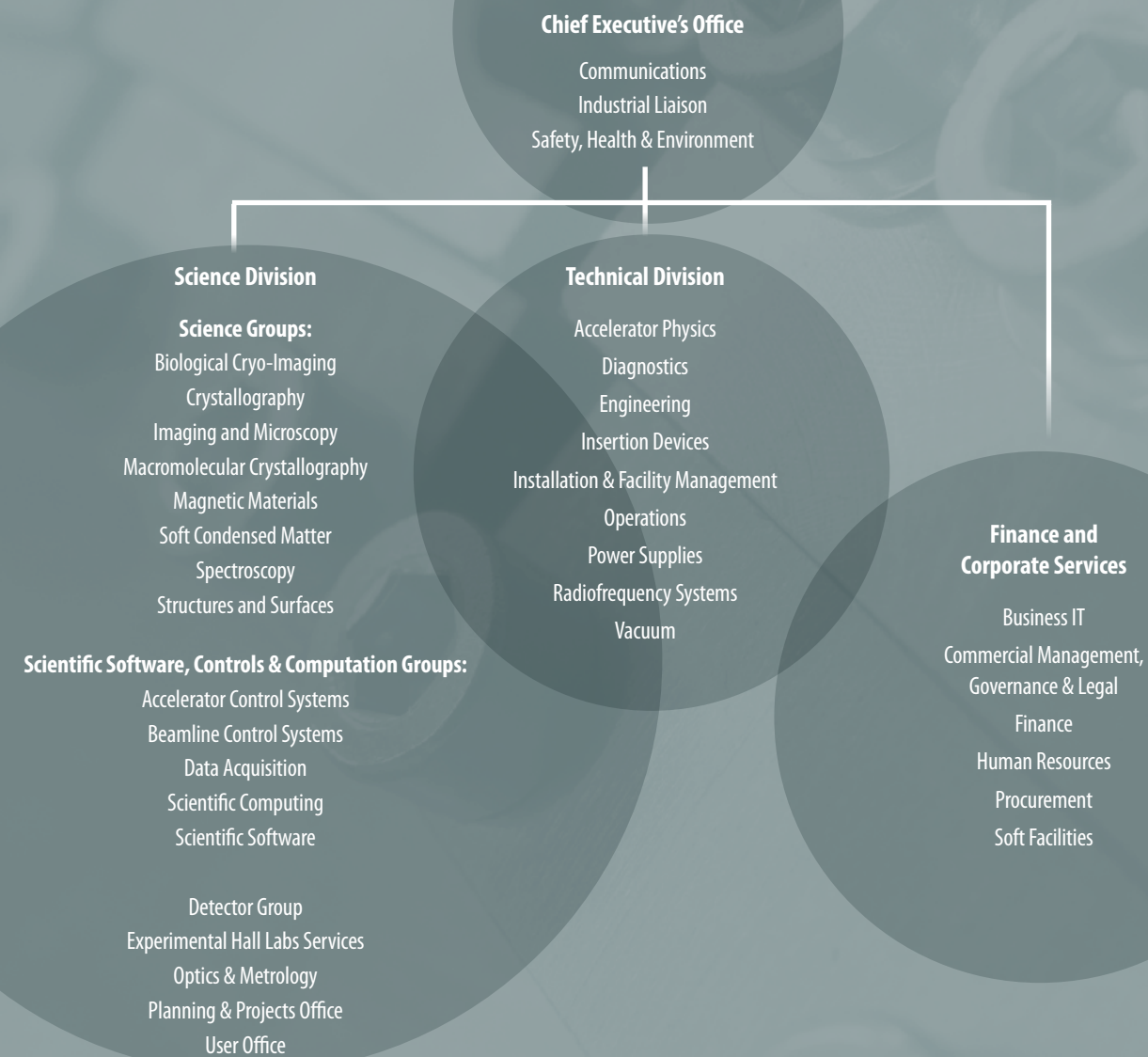
**Prof Richard Walker** joined Diamond Light Source as Technical Director in January 2002. He was previously Director of the Light Sources Division at Sincrotrone Trieste in Italy, and prior to that he was a key member of the Daresbury Laboratory SRS team. He is a visiting Professor of Physics at the University of Oxford.



**Andrea Ward** joined Diamond as Director of Finance and Corporate Services in 2019, with 15 years' experience as a Senior Finance professional. During a 12-year tenure at Vertex Pharmaceuticals, she worked with the Board to lead finance and procurement functions in Europe, later moving to Canada with the business to assist with acquisition and commercialisation opportunities. Andrea has also worked at ResMed and the Ontario Lottery and Gaming Corporation.

## Staffing and Financial Information

### Outline Organisational Chart



### Summary of Financial Data

	2008/09	2009/10	2010/11	2011/12	2012/13	2013/14	2014/15	2015/16	2016/17	2017/18	2018/19
Operating Costs £m	28.4	30.5	33.5	36.5	39.9	42.5	44.5	54.6	56.9	62.8	64.5
Total Staff (Year End)	369	401	419	438	481	507	534	582	609	639	680
Capital Expenditure – Operations £m	4.5	5.7	8.6	5.1	8.0	7.5	6.2	8.0	10.5	12.8	17.4
Phase II £m	25.5	22.0	16.2	9.9	2.8	0.8	0.2	0.0	0.0	0.0	0.0
Phase III £m	0.1	0.3	3.0	10.3	14.2	17.2	23.7	20.6	11.5	3.7	1.0
Other capital projects £m							4.8	5.6	7.3	4.3	5.3

Figures up to and including 2014/15 exclude VAT, thereafter figures include VAT.

## Committee Membership

**The Scientific Advisory Committee (SAC)** advises the CEO and the Science Directors on the scientific and technical questions impacting the specification, design, commissioning and operation of the facility; experimental and user support facilities, and opportunities for scientific exploitation.

**Dr Andrew Thompson (Chair)**  
SOLEIL (France)

**Dr Tom Hase (Vice-Chair)**  
University of Warwick (UK)

**Dr John Barker**  
Evotec (DISCo Representative)

**Dr Nick Brooks**  
Imperial College (UK) – (Chair of the DUC)

**Dr Bridget Carragher**  
New York Center for Structural Biology (USA)

**Prof John SO Evans**  
University of Durham (UK)

**Prof Peter Hatton**  
University of Durham (UK)

**Prof Philip Hofmann**  
Aarhus University (Denmark)

**Prof Ken Lewtas**  
Lewtas Science & Technologies  
(DISCo Representative)

**Dr Adrian Mancuso**  
European XFEL

**Dr Lisa Miller**  
Brookhaven National Lab/NSLS-II (USA)

**Prof Arwen Pearson**  
The Hamburg Centre of Ultrafast Imaging (Germany)

**Dr Jörg Raabe**  
PSI (Switzerland)

**Prof Mary Ryan**  
Imperial College (UK)

**Prof Christian Schroer**  
DESY (Germany)

**Prof Sam Shaw**  
University of Manchester (UK)

**Prof Titia Sixma**  
Netherlands Cancer Institute (Netherlands)

**Prof Moniek Tromp**  
University of Amsterdam (Netherlands)

**The Diamond Industrial Science Committee (DISCo)** advises the CEO and Directors on opportunities for industry to be engaged in research at Diamond, industrial research priorities that will help shape operational strategy, including the best way to exploit the current suite of beamlines and to develop the case for investment in future beamlines, and to develop best practice for industrial engagement.

**Dr Malcolm Skingle (Chair)**  
GlaxoSmithKline

**Dr John Barker**  
Evotec

**Dr Andrew Barrow**  
Rolls-Royce

**Prof David Brown**  
Charles River Laboratories

**Dr Paul Collier**  
Johnson Matthey

**Dr Rob Cooke**  
Heptares Therapeutics

**Dr Cheryl Doherty**  
GlaxoSmithKline

**Prof Peter Dowding**  
Infineum

**Prof Jonathan Hyde**  
NNL

**Prof Ken Lewtas**  
Lewtas Science & Technologies

**Dr John Pollard**  
Vertex Pharmaceuticals (Europe) Ltd

**Dr Richard Storey**  
AstraZeneca

**Dr Ian Tucker**  
Unilever

**The Diamond User Committee (DUC)** has been set as a platform for discussion between Diamond and the user community of matters relating to the operation and strategy of Diamond.

**Dr Nick Brooks (Chair)**  
Imperial College London

**Dr Arnaud Basle**  
University of Newcastle

**Dr Gavin Bell**  
University of Warwick

**Dr Ann Chippindale**  
University of Reading

**Dr Sean Connell**  
CIC bioGUNE

**Dr Tim Knowles**  
University of Birmingham

**Dr Gareth Law**  
University of Manchester

**Dr Marcus Newton**  
University of Southampton

**Prof Colin Pulham**  
University of Edinburgh

**Prof Andrea Russell**  
University of Southampton

**Dr Laura Spagnolo**  
University of Glasgow

**Dr Neil Telling**  
Keele University

**Dr Andrew Thomas**  
The University of Manchester





Diamond Light Source Ltd  
Harwell Science & Innovation Campus  
Didcot, Oxfordshire OX11 0DE  
Tel: +44 (0)1235 778 639  
Fax: +44 (0)1235 778 499  
[www.diamond.ac.uk](http://www.diamond.ac.uk)

Acknowledgement:  
We would like to thank the authors and all  
colleagues who contributed to this publication.



Printed on Forest Stewardship  
Council (FSC) accredited paper stock.

Published May 2019